

FABRICATION OF ADVANCED ELECTRODE
MATERIALS FOR ELECTROCHEMICAL
SUPERCAPACITOR APPLICATIONS

FABRICATION OF ADVANCED ELECTRODE
MATERIALS FOR ELECTROCHEMICAL
SUPERCAPACITOR APPLICATIONS

By RYAN YUK YEUNG POON, B.ENG

A Thesis Submitted to the School of Graduate Studies in Partial Fulfillment
of the Requirements for the Degree Doctor of Philosophy

Ph.D. Thesis
McMaster University

Ryan Yuk Yeung Poon
Materials Science and Engineering

McMaster University DOCTOR OF PHILOSOPHY (2019) Hamilton,
Ontario (Materials Science and Engineering)

TITLE: Fabrication of Advanced Electrode Materials for Electrochemical
Supercapacitor Applications

AUTHOR: Ryan Yuk Yeung Poon, B.Eng. (McMaster University, Canada)

SUPERVISOR: Dr. Igor Zhitomirsky, Distinguished Engineering Professor,
Ph.D., P.Eng.

NUMBER OF PAGES: CCXVI, 216

Lay Abstract

In modern society, the demand for clean and renewable energy have grown drastically and there is a need in development of advanced energy storage devices. Currently, the most common energy storage devices are batteries or conventional capacitors. Batteries can store a large amount of energy, however they are limited by their low power performance. Capacitors can charge and discharge rapidly, but the amount of energy stored is relatively low. Other than batteries and capacitor, electrochemical supercapacitors are emerging energy storage devices that offer the advantages of high power and energy density, fast charge-discharge and long lifetime.

The objective of this work was to develop advanced nanocomposite electrode materials for electrochemical supercapacitor applications. New colloidal processing strategies have been developed and advanced dispersants were employed for the fabrication of high performance nanocomposites for electrochemical supercapacitor applications. The results presented in this work showed exceptional performances compared to literature data and paved a new way for further developments.

Abstract

Electrochemical supercapacitors (ESs) are currently under development for electronics and automotive applications due to their hybrid properties inherited from batteries and capacitors. ESs exhibit higher power densities than batteries and energy densities than capacitors, and offer long cyclic life and rapid charge-discharge suitable for many applications. A promising candidate of electrode materials is manganese dioxide (MnO_2), which has the advantages of high theoretical capacitance, low cost and environmentally friendly. However, the low electronic and ionic conductivities of MnO_2 have limited its performance for practical applications. It has been demonstrated in literature that composite materials, which consist of conductive additives such as multi-walled carbon nanotubes (MWCNTs) and MnO_2 can address this problem, however further investigations are required to produce ESs with superior performance for real-world applications.

In this dissertation, novel colloidal fabrication techniques have been developed and advanced dispersants were employed to fabricate advanced nanocomposite electrodes. MnO_2 -MWCNTs composite electrode was fabricated with use of multifunctional dispersant. The multifunctional dispersant cetylpyridinium chloride (CPC) showed good dispersion of MWCNTs and capability of forming complex with the precursor of MnO_2 , which improved the homogeneity of the composite and generated unique morphology. The MnO_2 -MWCNTs composite electrode fabricated exhibited remarkable areal capacitance at high active mass loadings. New scalable fabrication technique was developed for MnO_2 -MWCNTs by using high solubility sodium permanganate (NaMnO_4) precursor. The

fabricated composite electrode showed superior performance compared to electrodes fabricated by other colloidal techniques at similar mass loading. Liquid-liquid extraction was employed to address the problem of particles agglomeration upon drying. Bio-inspired advanced extractor lauryl gallate (LG) was used for liquid-liquid extraction of particles. LG has organic catechol group allowed for strong adsorption on inorganic particles. Using LG as an advanced extractor has facilitated the transfer of particles from aqueous to organic phase to prevent agglomeration associated with drying procedure and improved mixing with MWCNTs. Advanced dispersants from bile acid salts and charged aromatic dyes families such as sodium taurodeoxycholate (TDS) and tolonium chloride (TL) were used as MWCNTs dispersants, to fabricate composite electrode with alternative metal oxides such as Mn_3O_4 and V_2O_3 . Furthermore, 3,4-dihydroxybenzaldehyde (DHB) was investigated as a dispersing agent for Mn_3O_4 and used to fabricate Mn_3O_4 -MWCNTs composite electrode with TL by Schiff base formation. Mn_3O_4 offers the advantages of small particle size compared to MnO_2 , and can be converted to MnO_2 by electrochemical cycling to enhance capacitive performance. V_2O_3 was considered as an alternative to MnO_2 due to its metallic conductivity at room temperature. An activation procedure has been developed, which promoted the formation of capacitive V_2O_5 surface layer on conductive V_2O_3 to increase capacitance. The advanced dispersants have shown excellent dispersion of MWCNTs in aqueous solutions at low concentrations and facilitated the formation of homogeneous composite with Mn_3O_4 and V_2O_3 . Activation procedures were developed for the Mn_3O_4 and V_2O_3 composite electrodes, and the electrodes with high active mass loadings showed exceptional performance after activation.

Acknowledgement

First and foremost, I would like to thank my supervisor Dr. Igor Zhitomirsky for his guidance and constant support throughout my Ph.D. study. You have always been a kind, patience, euthanasic and hardworking supervisor, and have inspired me to carry out high quality research to complete my Ph.D. and this dissertation. You are someone that I look up to, and I feel extremely lucky to be one of your students.

I would also like to thank my committee members Dr. Kish and Dr. Kitai, for their valuable inputs and suggestions, and made me realize it is important to know my own weaknesses in research and life. There are also many technicians and staff who helped me in the past few years as well, and I would like to thank Dr. Britten, Victoria Jarvis, Chris Butcher, Danielle Covelli, Doug Culley, Xiaogang Li, Ed McCaffery and Mary-Anne Bechamp for their assistance and support.

It was my pleasure to be part of the Zhitomirsky group, and I have enjoyed the time we spent together and the discussions we had about our research and daily life. I would like to thank Jordan Milne, Amanda Clifford, Ri Chen, Aseeb Syed, Cameron Wallar, Mustafa Ata, Haoyu Fan, Pamela Liang, Mohamed Nawwar, Heyfer Zhao and Jessica Liu for their help with research, coursework and daily life.

I am incredibly grateful for the endless love and support from my family. Thank you, mom and dad, for your continuous support of my decision, and for sharing your experience in life with me. To my sister and brother, Stephanie and Andrew, thank you for always being there for me and help me through my problems.

Last but not least, I would like to thank my love Michele Tsang. I could not have achieved my goals without your encouragement, and I am glad to have you by my side all these years. Thank you for your unconditional love and support in both my academic and personal life.

Declaration of Academic Achievements

This dissertation was used to fulfill the requirements of the degree Doctor of Philosophy. The major research project was conducted from September 2016 to August 2019. The results of this dissertation were published in 6 papers in peer-reviewed journals, which were listed below:

1. **R. Poon** and I. Zhitomirsky, “Supercapacitor electrode with high active mass loading”, *MRS Communications*, vol.8, no. 3, pp. 1135-1138, 2018.
2. **R. Poon**, X. Zhao, M.S. Ata, A. Clifford and I. Zhitomirsky, “Phase transfer of oxide particles for application in thin films and supercapacitors”, *Ceramics International*, vol. 43, no.11, pp. 8314-8320, 2017.
3. **R. Poon** and I. Zhitomirsky, “High areal capacitance of Mn_3O_4 -carbon nanotube electrodes”, *Materials Letters*, vol. 215, pp.4-7, 2018.
4. C.J. Wallar[≡], **R. Poon**[≡] and I. Zhitomirsky, “High areal capacitance of V_2O_3 -carbon nanotube electrodes”, *Journal of the Electrochemical Society*, vol. 164, no. 14, pp. A3620-A3627, 2017. (≡: Authors contribute equally to this publication)
5. W. Liang[≡], **R. Poon**[≡] and I. Zhitomirsky, “Zn-doped FeOOH-polypyrrole electrodes for supercapacitors”, *Materials Letters*, vol. 1, no. 1, pp. 124-133, 2019. (≡: Authors contribute equally to this publication)
6. **R. Poon**[≡], W. Liang[≡] and I. Zhitomirsky, “ Mn_3O_4 and $(\text{ZnFe})\text{OOH}$ composites for supercapacitors with high active mass”, *Metallurgical and Materials Transaction A*, Accepted. (≡: Authors contribute equally to this publication)

In addition to the work presented above, I have also contributed to 9 papers that are published and submitted in peer-reviewed journals and are not covered in this dissertation.

7. **R. Poon** and I. Zhitomirsky, “Application of Cyrene as a solvent and dispersing agent for fabrication of Mn_3O_4 -carbon nanotube supercapacitor electrodes”, *Colloid and Interface Science Communications*, Submitted.
8. R. Chen, **R. Poon**, R. Sahu, I. Puri and I. Zhitomirsky, “ MnO_2 -carbon nanotube electrodes for supercapacitors with high active mass loadings”, *Journal of Electrochemical Society*, vol. 164, no.7, pp. A1673-A1678, 2017.
9. M.S. Ata, **R. Poon**, A. Syed, J. Milne and I. Zhitomirsky, "New developments in non-covalent surface modification, dispersion and electrophoretic deposition of carbon nanotubes", *Carbon*, vol. 130, pp. 584-598, 2018.
10. C.J. Wallar, D. Luo, **R. Poon** and I. Zhitomirsky, “Manganese dioxide-carbon nanotube composite electrode with high active mass loading for electrochemical supercapacitors”, *Journal of Materials Science*, vol. 52, no.7, pp.3687-3696, 2016.
11. T. Zhang, X. Zhao, **R. Poon**, A. Clifford, R. Mathews and I. Zhitomirsky, “Synthesis and liquid-liquid extraction of non-agglomerated $\text{Al}(\text{OH})_3$ particles for deposition of cellulose matrix composite films”, *Journal of Colloid and Interface Science*, vol. 508, pp.49-55, 2017.
12. X. Zhao, A. Clifford, **R. Poon**, R. Mathews and I. Zhitomirsky, "Carboxymethyl cellulose and composite films prepared by electrophoretic deposition and liquid-liquid particle extraction", *Colloid and Polymer Science*, vol.296, no.5, pp.927-934 2018.
13. R.M.E. Silva, **R. Poon**, J. Milne, A. Syed and I. Zhitomirsky, “New developments in liquid-liquid extraction, surface modification and agglomerate-free processing of inorganic particles”, *Advances in Colloid and Interface Science*, vol. 261, pp. 15-27, 2018.
14. M. Nawwar, **R. Poon**, R. Chen, R. Sahu, I. Puri and I. Zhitomirsky, “High areal capacitance of Fe_3O_4 -decorated carbon nanotubes for supercapacitor electrodes”, *Carbon Energy*, vol. 1, no. 1, pp. 124-133, 2019.

15. M. Nawwar, **R. Poon**, R. Sahu, I. Puri and I. Zhitomirsky, “Spinel-spinel ceramic supercapacitor prepared using multifunctional dispersant-capping agent-charge transfer mediator”, *Ceramics International*, Submitted.

Table of Contents

Lay Abstract	III
Abstract	IV
Acknowledgement	VI
Declaration of Academic Achievements.....	VIII
List of Figures.....	XIV
List of Tables	XXV
List of Abbreviations and Symbols	XXVI
Chapter 1 Introduction.....	1
Chapter 2 Literature Review	5
2.1 Fundamental and parameters of capacitors and supercapacitors	5
2.2 Supercapacitors – Electrochemical double layer capacitors & pseudocapacitors	6
2.3 Principles of energy storage in pseudocapacitors	11
2.4 Carbon materials for EDLCs applications	16
2.4.1 Activated Carbon (AC)	16
2.4.2 Graphene-based materials	18
2.4.3 Carbon nanotubes.....	20
2.5 Metal oxides & hydroxides as electrode materials	23
2.5.1 Positive electrode	23
2.5.1.1 Ruthenium dioxide (RuO ₂).....	23
2.5.1.2 Manganese dioxide (MnO ₂).....	25
2.5.1.3 Vanadium pentoxide (V ₂ O ₅).....	29
2.5.1.4 Nickel oxide (NiO) & nickel hydroxide (Ni(OH) ₂).....	31
2.5.1.5 Cobalt oxide (Co ₃ O ₄) & cobalt hydroxide (Co(OH) ₂).....	33
2.5.2 Negative Electrodes.....	35
2.5.2.1 Iron Oxide (Fe ₂ O ₃) and oxy-hydroxide (FeOOH)	35
2.5.2.2 Vanadium nitride (VN).....	37
2.6 Configurations and types of ES	40
2.7 Electrolytes of supercapacitors	43
2.7.1 Aqueous Electrolytes.....	44
2.7.2 Organic Electrolytes	45
2.7.3 Ionic Liquids	46
2.7.4 Solid /Quasi-Solid-State Electrolytes	46
2.8 Dispersion of metal oxides and carbon nanotubes for composite fabrication ...	48
2.9 References	61
Chapter 3 Objectives.....	70
Chapter 4 Supercapacitor electrodes with high active mass loading	71
4.1 Abstract	72

4.2	Introduction.....	72
4.3	Experimental Procedure.....	74
4.4	Results and Discussion.....	76
4.5	Conclusions.....	82
4.6	Acknowledgements.....	82
4.7	Supplementary Materials.....	83
4.8	References.....	88
Chapter 5 Zn-doped FeOOH-polypyrrole electrodes for supercapacitors.....		91
5.1	Abstract.....	92
5.2	Introduction.....	93
5.3	Experimental Procedure.....	94
5.4	Results and Discussion.....	95
5.5	Conclusions.....	101
5.6	Acknowledgements.....	101
5.7	Supplementary Materials.....	102
5.8	References.....	105
Chapter 6 Phase transfer of oxide particles for application in thin films and supercapacitors.....		106
6.1	Abstract.....	107
6.2	Introduction.....	108
6.3	Experimental Procedure.....	110
6.4	Results and Discussion.....	113
6.5	Conclusions.....	125
6.6	Acknowledgements.....	126
6.7	References.....	127
Chapter 7 High areal capacitance of Mn₃O₄-carbon nanotube electrodes.....		132
7.1	Abstract.....	133
7.2	Introduction.....	134
7.3	Experimental Procedure.....	135
7.4	Results and Discussion.....	136
7.5	Conclusions.....	141
7.6	Acknowledgements.....	141
7.7	Supplementary Materials.....	142
7.8	References.....	143
Chapter 8 Mn₃O₄ and (ZnFe)OOH composites for supercapacitors with high active mass.....		144
8.1	Abstract.....	145
8.2	Introduction.....	146
8.3	Experimental Procedure.....	148
8.4	Results and Discussion.....	149
8.5	Conclusions.....	160

8.6	Acknowledgements	160
8.7	References	161
Chapter 9 Fabrication of high areal capacitance Mn₃O₄-Carbon nanotube composite electrode by Schiff base formation		164
9.1	Abstract	165
9.2	Introduction	166
9.3	Experimental Procedure	168
9.4	Results and Discussion	170
9.5	Conclusions	177
9.6	References	178
Chapter 10 High areal capacitance of V₂O₃-carbon nanotube electrodes		182
10.1	Abstract	183
10.2	Introduction	184
10.3	Experimental Procedure	187
10.4	Results and Discussion	190
10.5	Conclusions	207
10.6	Acknowledgements	207
10.7	References	208
Chapter 11 Conclusions and Future Works		214

List of Figures

Figure 1.1: Ragone plot showing power and energy densities for different energy storage devices. Reprinted with permission from Royal Society of Chemistry [2]	1
Figure 2.1: Schematic of simple electrostatic capacitor. Reprinted with permission from Wiley Books. [11].....	5
Figure 2.2 Schematics of EDLC at discharged and charged state. Reprinted with permission from Elsevier. [12]	7
Figure 2.3: Double layer in (a) Helmholtz model, (b)Gouy-Chapman model, and (c) Stern model. Reprinted with permission from Plenum Pub. Corp. [13]	8
Figure 2.4: Equivalent circuit diagram of C_{dl} in Stern model. Reprinted with permission from Plenum Pub. Corp. [13].....	8
Figure 2.5: Schematic of Grahame model. Reprinted with permission from Plenum Pub. Corp. [13].....	9
Figure 2.6: Schematic of pseudocapacitive systems identified by Conway. Reprinted with permission from Royal Society of Chemistry. [20]	11
Figure 2.7: Coverage vs. potential for positive and zero g value. Reprinted with permission from Plenum Pub. Corp. [13].....	13
Figure 2.8: Pseudocapacitive systems and their Nernst equations. Reprinted with permission from Plenum Pub. Corp. [13]	15
Figure 2.9: Comparison of carbon materials based on their properties in EDLCs. Reprinted with permission from Royal Society of Chemistry. [23]	16

Figure 2.10: Schematic of porous structure of activate carbon. Reprinted with permission from Journal of Electrochemical Society. [24]	17
Figure 2.11: Schematic of the conductive pathways in graphene electrodes of different orientations. Reprinted with permission from Royal Society of Chemistry. [28]	18
Figure 2.12: Atomic structure of carbon nanotubes of different chirality, and their corresponding chiral vectors projected on a graphene sheet. Reprinted with permission from Royal Society of Chemistry. [25].....	20
Figure 2.13: Schematic of tree-root model for anhydrous and hydrous RuO ₂ . Reprinted with permission from American Chemical Society. [41].....	24
Figure 2.14: Different crystal structure of MnO ₂ . Reprinted with permission from American Chemical Society. [45].....	26
Figure 2.15: Cyclic voltammograms of different phases of MnO ₂ . Reprinted with permission from American Chemical Society. [45].....	26
Figure 2.16: Specific capacitance of MnO ₂ electrode containing (a) 0 wt.%, (b) 10 wt.% and (c) 20 wt.%. Reprinted with permission from Elsevier. [53]	29
Figure 2.17: TEM image of PPy@V ₂ O ₅ core-shell structure provided by Qu et al. Reprinted with permission from John Wiley and Sons.[59].....	31
Figure 2.18: CVs for (A) pure α -FeOOH-MWCNTs and (B) α -FeOOH-PPy-MWCNTs composite electrode by Chen et al. Reprinted with permission from Journal of Electrochemical Society. [84].....	36

Figure 2.19: CVs of composite consist of 80% PPy-20%MWCNTs with PPy:FeOOH ratio of (A) 7:2 and (B) 7:3 by Fan et al. Reprinted with permission from Taylor & Francis. [85]	37
Figure 2.20: Specific capacitance vs. cycle number for VN electrodes under different conditions by Choi et al. Reprinted with permission from John Wiley and Sons. [86].....	38
Figure 2.21: Capacitance retention of flexible asymmetric device fabricated using VN and VO _x nanowires. Reprinted with permission from American Chemical Society. [87]	39
Figure 2.22: Working voltage window of different active materials in aqueous electrolytes. Reprinted with permission from John Wiley and Sons. [88].....	41
Figure 2.23: Effects of electrolytes on performance of ESs. Reprinted with permission from Royal Society of Chemistry. [92]	43
Figure 2.24: Schematic of surface charge of particles as a function of pH.	49
Figure 2.25: Schematic of total potential energy vs. separation distance with contributions from van der Waals attraction and electrostatic repulsion.[102]	51
Figure 2.26: Total potential energy vs. separation distance of two spherical particles of different $\kappa - 1$ values.[102].....	52
Figure 2.27: Chemical structure of (A) CA, (B) TCA, (C) PCA and (D) DCA.	53
Figure 2.28: Adsorption mechanism of CA suggested by Ata et al., which involved (a) bidentate chelating bonding, (b) inner sphere bidentate bridging bonding, (c) outer sphere bidentate bridging bonding and (d) adsorption by carboxylic group. Reprinted with permission from RSC Publishing. [106].....	54

Figure 2.29: Weight % of SDS vs. weight % of CNTs adapted from Vigolo et al. Reprinted with permission from The American Association for the Advancement of Science. [110]	56
Figure 2.30: Chemical structures of some BAS, including (A) cholic acid sodium salts (CAS), (B) deoxycholic acid sodium salts (DCAS) and (C) taurocholic acid sodium salts (TCAS).	58
Figure 2.31: Chemical structure of (A) BDS, (B) NTS, (C) ITR and (D) ITT. Reprinted with permission from Taylor & Francis. [123]	60
Figure 4.1: XRD pattern of MnO ₂ powder.	77
Figure 4.2: SEM image of MnO ₂ -NT composite; arrows show examples of elongated particles.	78
Figure 4.3: (a, b) CVs at different scan rates and (c, d) C _g and C _s versus scan rate for MnO ₂ -NT electrodes with AM of (a, c) 42 mg cm ⁻² and (b, d) 61 mg cm ⁻² .	80
Figure 4.4: (a) Nyquist plot of complex impedance and (b, c) frequency dependences of components of complex capacitance for MnO ₂ -NT electrodes with AM of 42 and 61 mg cm ⁻² .	81
Figure 4.5: Extraction of MWCNT from the aqueous phase (bottom) to the 1-butanol phase (top).	83
Figure 4.6: (a) Aqueous mixture of cetylpyridinium permanganate and MWCNT, (b) phase transfer and formation of mixed suspension of MnO ₂ and MWCNT in the 1-butanol phase.	83

Figure 4.7: High magnification SEM image of the MnO₂-MWCNT composite material. The diameter of the MWCNT in the middle of the picture is significantly larger, compared to the diameter of original MWCNT (13 nm).....84

Figure 4.8: Transmission electron microscopy (TEM) (JEOL, JEM 1200 EX TEMSCAN) image of MnO₂-MWCNT composite.....84

Figure 4.9: (a) CVs at different scan rates, (b) specific capacitance, calculated from the CV data versus scan rate, (c) Nyquist plot of complex impedance and (d) frequency dependencies of the components of complex capacitance, calculated from the impedance data for MnO₂-MWCNT electrodes with mass loading of 51 mg cm⁻².....85

Figure 4.10: Specific capacitance, calculated from CV data at 2 mV s⁻¹ versus mass loading for MnO₂-MWCNT electrodes.86

Figure 4.11: Galvanostatic charge-discharge behavior at different current densities for MnO₂-MWCNT electrodes with mass loadings of (a) 42 and (b) 61 mg cm⁻².....87

Figure 5.1: (A–D) CVs at scan rates of (a) 2, (b) 5 and (c) 10 mV s⁻¹ and (E,F) CS and Cm versus scan rate for (A, E(a)) FC, (B, E(b)) 8ZFC, (C, E(c)) 12ZFC, (D,F) 12ZFCPC. ...96

Figure 5.2: Capacitance retention versus cycle number for (A)(a) FC (b) 8ZFC (c) 12ZFC (B) 12ZFCPC.97

Figure 5.3: (A) CVs at scan rates of (a)2, (b) 5 and (c) 10 mV s⁻¹, and (B) CS and Cm versus scan rate for MC.....98

Figure 5.4: Testing data for (A,B) 12ZFC-MC and (C,D) 12ZFCPC-MC cells: (A,C) CVs at scan rates of (a)2, (b) 5 and (c) 10 mV s⁻¹, and (B,D) CS and Cm, inset shows LEDs powered by a supercapacitor module..... 100

Figure 5.5: (A) CVs at scan rates of (a) 2, (b) 5 and (c) 10 mV s ⁻¹ and (B) C _s and C _m versus scan rate for 12ZFCPC.....	102
Figure 5.6: (A) Nyquist plot of complex impedance, and frequency dependences of (B) C _s ' and (C) C _s '' for (a) FC, (b) 8ZFC, (c) 12ZFC.....	102
Figure 5.7: (A) Nyquist plot of complex impedance, and frequency dependence of (B) C _s ' and (C) C _s '' for 12ZFCPC.....	103
Figure 5.8: (A) Nyquist plot of complex impedance, and frequency dependence of complex capacitance (B) C _s ' and (C) C _s '' for MC.....	103
Figure 5.9: Nyquist plot of complex impedance, and frequency dependence of complex capacitance (B) C _s ' and (C) C _s '' for asymmetric 12ZFCPC-MC device.....	103
Figure 5.10: Galvanostatic charge-discharge for asymmetric 12ZFCPC-MC device at current densities of (a) 3, (b) 5, (c) 7 and (d) 10 mA cm ⁻²	104
Figure 6.1: X-ray diffraction patterns of (a) titania and (b) Mn ₃ O ₄ , prepared by chemical	114
Figure 6.2: SEM images of (a) Mn ₃ O ₄ and (b) titania powders.....	114
Figure 6.3: (A) Chemical structure of R'-CHO, (B) chemical structure of H ₂ NR'', (C) Schiff base reactions between H ₂ NR'' and R'-CHO, adsorbed by (a) chelation or (b) bridging of metal atoms (M) on the particle surface, (D) schematic of extraction, involving (a) modification of particles with R'-CHO during synthesis and (b) extraction by Schiff base formation, (E) (a) synthesized titania, modified with R'-CHO, (b) extracted titania.	115
Figure 6.4: FTIR spectra of (a) H ₂ NR'', (b) R'-CHO, (c) titania, extracted by Schiff base	117

Figure 6.5: Particle size distribution for (a) titania and (b) Mn_3O_4 , extracted by Schiff base	118
Figure 6.6: SEM image of a titania-PVB film.	118
Figure 6.7: (A) Chemical structure of GR, (B) GR adsorption on a particle surface by (a) chelation and (b) bridging of metal atoms (M) on a particle surface, (C) schematic of extraction, involving (a) synthesis and precipitation of particles and (b) extraction using GR adsorption at the liquid-liquid interface, (D) (a) precipitated Mn_3O_4 and (b) Mn_3O_4 extraction by adsorbed GR.....	119
Figure 6.8: FTIR spectra of (a) GR, (b) titania, extracted using GR and (c) Mn_3O_4 extracted	121
Figure 6.9: Particle size distribution for (a) titania and (b) Mn_3O_4 , extracted by adsorbed GR.	121
Figure 6.10: CV at a scan rate of 10 mV s^{-1} , C_s and C_m versus scan rate for the composite Mn_3O_4 –MWCNT electrode.....	123
Figure 6.11: (A) Nyquist plot of complex impedance, (B) C_s' and (C) C_s'' versus frequency for the composite Mn_3O_4 –MWCNT electrode.	123
Figure 7.1: (A) X-ray diffraction pattern of as-prepared Mn_3O_4 , (B) SEM image of Mn_3O_4 -MWCNT electrode material.....	137
Figure 7.2: (A) CVs at a scan rate of 20 mV s^{-1} and (B) capacitance versus scan rate dependences for (a) 1 st , (b) 3 rd and (c) 5 th TP for Mn_3O_4 -MWCNT electrode.	138
Figure 7.3: Nyquist plot of complex impedance and frequency dependences of (B) C_s' and (C) C_s'' after (a) 1 st , (b) 3 rd and (c) 5 th TP for Mn_3O_4 -MWCNT composite electrode.....	139

Figure 7.4: XPS spectra of Mn ₃ O ₄ -MWCNT composite (A) as-prepared and (B) after 5 th TP.....	140
Figure 7.5: Chemical structure of TD.	142
Figure 7.6: 1 g L ⁻¹ MWCNT suspensions, containing 1 g L ⁻¹ TD (left) and without TD (right).	142
Figure 8.1: XRD pattern of as-precipitated powder, arrows show peaks, corresponding to JCPDS file 024-0734.	149
Figure 8.2: (A) CVs at scan rates of (a) 2, (b) 5 and (c) 10 mV s ⁻¹ and (B) CS and Cm for Mn ₃ O ₄ -CNT electrode.	150
Figure 8.3: (A) Nyquist plot of complex impedance, and frequency dependence of complex capacitances (B) CS' and (C) CS'' for Mn ₃ O ₄ -CNT electrode.	151
Figure 8.4: (A,B) SEM images and (C,D) XPS spectra for Mn ₃ O ₄ -CNT electrode: (A,C) as prepared and (B,D) after testing.	152
Figure 8.5: Capacitance retention of Mn ₃ O ₄ -MWCNT electrode during cycling.	153
Figure 8.6: (A,B,C) CVs at scan rates of (a) 2, (b) 5 and (c) 10 mV s ⁻¹ and (D) CS and Cm for (A,D(a)) FeOOH-CNT, (B,D(b)) (Fe,Zn)OOH-CNT and (C,D(c)) (Fe,Zn)OOH-CNT-PNT electrodes.	154
Figure 8.7: Capacitance retention during cycling for (a) FeOOH-CNT (b) (Fe,Zn)OOH-CNT (c) (Fe,Zn)OOH-CNT-PNT electrode.	155
Figure 8.8: (A-D) Nyquist plot of complex impedances at (A)-0.8, (B)-0.5, (C)-0.3 V, and (D)+0.1 V vs. SCE for (a) (Fe,Zn)OOH-CNT (b) (Fe,Zn)OOH-CNT-PNT electrodes; (E,F)	

frequency dependence of complex capacitances (E) C_s' and (F) C_s'' for (a) (Fe,Zn)OOH-CNT (b) (Fe,Zn)OOH-CNT-PNT electrode at fixed potential of +0.1 V vs. SCE..... 156

Figure 8.9: CVs at a scan rate of 20 mVs⁻¹ for (a) (Fe,Zn)OOH-CNT-PNT electrode and (b) Mn₃O₄-CNT electrode..... 157

Figure 8.10: (A) CVs at scan rate of (a) 2, (b) 5 and (c) 10 mV s⁻¹ and (B) C_s and C_m for device, fabricated using Mn₃O₄-CNT and (Fe,Zn)OOH-CNT-PNT as positive and negative electrodes, respectively. 158

Figure 8.11: Capacitance retention during cycling of the device fabricated using Mn₃O₄-CNT and (Fe,Zn)OOH-CNT-PNT as positive and negative electrodes, respectively and (inset) LED bulbs powered by two devices connected in series..... 159

Figure 9.1: XRD pattern of Mn₃O₄ with addition of DHB after synthesis. 170

Figure 9.2: Adsorption of DHB on Mn atom by (A) chelating and (B) bridging mechanisms. 171

Figure 9.3: FTIR spectra of (a) pure Mn₃O₄, (b) Mn₃O₄-DHB, and (c) pure DHB..... 172

Figure 9.4: Chemical structure of (A) DHB and (B) TL, and (C) Schiff base formation between R'-CHO and R''-NH₂..... 173

Figure 9.5: (A) CVs at scan rate of (a) 2, (b) 5 and (c) 10 mV s⁻¹, and (B) C_s and C_m versus scan rates for Mn₃O₄-MWCNT composite electrode after the 4th activation procedure. 174

Figure 9.6: (A) Nyquist plot of complex impedance and frequency dependences of (B) C_s' and (C) C_s'' of Mn₃O₄-MWCNT composite electrode after the 4th activation procedure. 174

Figure 9.7: (A) CVs at scan rate of (a) 2, (b) 5 and (c) 10 mV s^{-1} , and (B) C_s and C_m versus scan rates for Mn_3O_4 -MWCNT composite electrode fabricated with DHB during synthesis. 176

Figure 9.8: (A) Nyquist plot of complex impedance and frequency dependences of (B) C_s' and (C) C_s'' of Mn_3O_4 -MWCNT composite electrode fabricated with DHB during synthesis. 176

Figure 10.1: SEM images of as-received MWCNT 189

Figure 10.2: SEM images of (A) $\text{V}_2\text{O}_3(\text{r})$, (B) $\text{V}_2\text{O}_3(\text{m})$, (C) $\text{V}_2\text{O}_3(\text{r})$ -MWCNT composite before testing, (D) $\text{V}_2\text{O}_3(\text{r})$ -MWCNT composite after testing (scale bar = 2 μm). 191

Figure 10.3: (A) Schematic of LG adsorption on $\text{V}_2\text{O}_3(\text{r})$ and MWCNT, (B,C) sedimentation tests for (B) 1 g L^{-1} V_2O_3 , (C) 1 g L^{-1} MWCNT in a water-ethanol solvent (50 vol.% ethanol) (a) without LG and (b) in the presence of 0.5 g L^{-1} LG. 192

Figure 10.4: Charge-discharge behavior of $\text{V}_2\text{O}_3(\text{r})$ -MWCNT composites, prepared using LG, at current densities of (a) 3, (b) 5, (c) 7 and (d) 10 mA cm^{-2} 193

Figure 10.5: CVs for consecutive cycling at (A) 50, (B) 100, (C) 5 and (D) 2 mV s^{-1} for $\text{V}_2\text{O}_3(\text{r})$ -MWCNT composites, prepared using LG 194

Figure 10.6: (A) CVs at scan rates of (a) 5, (b) 10 and (c) 20 mV s^{-1} and (B) C_g and C_s versus scan rate for $\text{V}_2\text{O}_3(\text{r})$ -MWCNT composites, prepared using LG, after AP. 195

Figure 10.7: (A,B) CVs at scan rates of (a) 5, (b) 10 and (c) 20 mV s^{-1} for (A) $\text{V}_2\text{O}_3(\text{r})$ and (B) $\text{V}_2\text{O}_3(\text{r})$ -MWCNT composite, prepared without LG, (C) C_g and C_s versus scan rate for (a) $\text{V}_2\text{O}_3(\text{r})$ and (b) $\text{V}_2\text{O}_3(\text{r})$ -MWCNT composite, prepared without LG after AP. 197

Figure 10.8: (A) Nyquist plot of complex impedance, (B,C) frequency dependences of components of complex capacitance (B) C_s' and (C) C_s'' , calculated from the EIS data for $V_2O_3(r)$ -MWCNT composites, prepared using LG, before AP.198

Figure 10.9: (A) Nyquist plot of complex impedance, (B,C) frequency dependences of components of complex capacitance (B) C_s' and (C) C_s'' , calculated from the EIS data for $V_2O_3(r)$ -MWCNT composites, prepared using LG, after AP.199

Figure 10.10: Capacitance retention versus cycle number for $V_2O_3(r)$ -MWCNT composites, prepared using LG, after AP.200

Figure 10.11: X-Ray diffraction patterns of (A) $V_2O_3(r)$, (B, C) $V_2O_3(r)$ -MWCNT composites: (A, B) before AP and (C) after AP.201

Figure 10.12: XPS data for (A) $V_2O_3(r)$, (B, C) $V_2O_3(r)$ -MWCNT composites: (A, B) before AP and (C) after AP.....201

Figure 10.13: (A) CVs at scan rates of (a) 5, (b) 10 and (c) 20 $mV s^{-1}$ and (B) C_g and C_s versus scan rate for $V_2O_3(m)$ -MWCNT composites, prepared using LG, after AP.203

Figure 10.14: (A) Nyquist plot of complex impedance, (B,C) frequency dependences of components of complex capacitance (B) C_s' and (C) C_s'' , calculated from the EIS data for $V_2O_3(m)$ -MWCNT composites, prepared using LG, before AP.203

Figure 10.15: (A) Nyquist plot of complex impedance, (B,C) frequency dependences of components of complex capacitance (B) C_s' and (C) C_s'' , calculated from the EIS data for $V_2O_3(m)$ -MWCNT composites, prepared using LG, after AP.204

Figure 10.16: Capacitance retention versus cycle number for $V_2O_3(m)$ -MWCNT composites, prepared using LG, after AP.205

List of Tables

Table 2.1 Summary of literature capacitance of graphene-based composite materials for flexible supercapacitor application. Reprinted with permission from American Chemical Society. [30].....	19
Table 4.1: Capacitances calculated from the CV data versus scan rates for MnO ₂ -MWCNT electrodes with different mass loadings.....	86

List of Abbreviations and Symbols

A, mA (unit)	Ampere, milliamp
AC	Activated Carbon
AM	Active mass
AP	Activation procedure
BAS	Bile acid salts
BDS	Sodium benzene-1,3-disulfonate
BET	Brunauer–Emmett–Teller
C, μC (unit)	Coulomb, microcoulomb
C	Capacitance
C^+/R^+	Cationic species in electrolyte
C^*	Complex differential capacitance
C_{+ve}	Capacitance of positive electrode
C_{-ve}	Capacitance of negative electrode
C_{Cell}	Overall cell capacitance
C_{Diff}	Capacitance from diffuse layer
C_{dl}	Capacitance from double layer
C_{g}	Gravimetric capacitance
C_{H}	Capacitance from Helmholtz plane
C_{H}^+	Concentration of H^+ in underpotential deposition
C_i	Concentration of counter ions of type i
C_{IH}	Capacitance from inner Helmholtz plane
C_{OH}	Capacitance from outer Helmholtz plane
C_{s}	Areal capacitance
C_{s}'	Real component of complex capacitance
C_{s}''	Imaginary component of complex capacitance
CA	Caffeic acid

CAS	Cholic acid sodium salts
CNTs/NT	Carbon nanotubes
CPC	Cetylpyridinium chloride
CV	Cyclic voltammetry or cyclic voltammogram
CVD	Chemical Vapor Deposition
DCA	2,4-dihydroxycinnamic acid
DCAS	Deoxycholic acid sodium salts
DHB	3,4-dihydroxybenzaldehyde
DI	Deionized
DLS	Dynamic light scattering
DLVO	Derjaguin-Landau-Verwey-Overbeek
DOPA	L-3-4,dihydroxyphenylalanine
e^-	Electron
ϵ_0	Permittivity of vacuum
E	Electrode potential
E°	Standard electrode potential
E_{Total}	Total energy stored in capacitor
EDLC	Electrochemical double layer capacitor
EIS	Electrochemical impedance spectroscopy
EPD	Electrophoretic deposition
ES	Electrochemical supercapacitor
EV	Ethyl violet
f	Frequency
F	Faraday constant
F, mF, μ F (unit)	Farad, millifarad, microfarad
FTIR	Fourier-transform infrared spectroscopy
g, mg, μ g (unit)	Gram, milligram, microgram

g	Interaction energy between noble metal and adsorbed species in underpotential deposition
GPE	Gel polymer electrolytes
GR/LG	Lauryl Gallate
h (unit)	Hour
Hz, mHz, kHz (unit)	Hertz, millihertz, kilohertz
I	Current
IEP	Isoelectric point
ILs	Ionic Liquids
ITR	Potassium indigotrisulfonate
ITT	Potassium indigotetrasulfonate
K (unit)	Temperature in Kelvin
k	Boltzmann constant
L, mL (unit)	Liter, milliliter
LTO	Lithium titanate ($\text{Li}_4\text{Ti}_5\text{O}_{12}$)
m	Mass of active materials
m, cm, μm , nm (unit)	Meter, centimeter, micrometer, nanometer
M	Molar concentration
MWCNTs	Multi-walled carbon nanotubes
NTS	1,3,(6,7)-naphthalenetrisulfonic acid
Q	Charge stored
q_H	Charge associated with adsorption of H^+
P	Maximum power
P(SSA-MA)	poly(4-styrenesulfonic acid-co-maleic acid) sodium salts
PCA	<i>p</i> -courmaric acid
PELLI	Particles extraction through a liquid-liquid interface

PPy	Polypyrrole
PTFE	Polytetrafluoroethylene
PVB	Poly(vinyl butyral-co-vinyl alcohol-co-vinyl acetate)
PV	Pyronin Y
Q	Charge stored
R	Resistance
R	Gas constant
r	Radius of spherical particles
R _{cap}	Resistance of capacitor
RHE	Reversible hydrogen electrode
S	Area of electrode
S	Separation distance of spherical particles
s (unit)	Second
SCap	Supercapacitor
SCE	Saturated calomel electrode
SDS	Sodium dodecyl sulfate
SEM	Scanning electron microscopy
SSE	Solid state electrolyte
SWCNT	Single-walled carbon nanotube
T	Temperature
TCA	<i>trans</i> -cinnamic acid
TCAS	Taurocholic acid sodium salts
TD	Sodium taurodeoxycholate
TEABF ₄	Tetraethylammonium tetrafluoroborate
TEM	Transmission electron microscopy
TL	Tolonium chloride
TP	Testing procedure

V	Voltage
V_{Max}	Maximum voltage
V_{Min}	Minimum voltage
W (unit)	Watt
Wh (unit)	Watt hour
wt%	Weight percentage
ω	Angular frequency
X	Fraction of ion occupancy in lattices
XPS	X-ray photoelectron spectroscopy
XRD	X-ray diffraction
z	Number of electrons transferred in redox reactions
Z^*	Total impedance
Z'	Real component of impedance
Z''	Imaginary component of impedance
Z_i	Valence of counter ions of type i
$\delta m/Rm$	Ratio of active material mass to current collector mass
ΔV	Voltage window
$^{\circ}C$ (unit)	Temperature in Celsius
θ_H	Surface coverage of H^+ in underpotential deposition
[Ox]	Concentration of oxidized species
[Red]	Concentration of reduced species
Φ_A	Van der Waals attraction potential
Φ_R	Electrostatic repulsion potential
$\frac{1}{\kappa}$	Debye-Huckel screening strength or double layer thickness

Chapter 1 Introduction

Climate change and global warming caused by rapid economic development have become a major problem in the world, and in respond the demand for alternative energy sources and high performance energy storage devices have surged drastically[1]. In our society, the common energy storage devices are capacitors and batteries, which are used in small electronics, electric or hybrid vehicles, and many other applications.

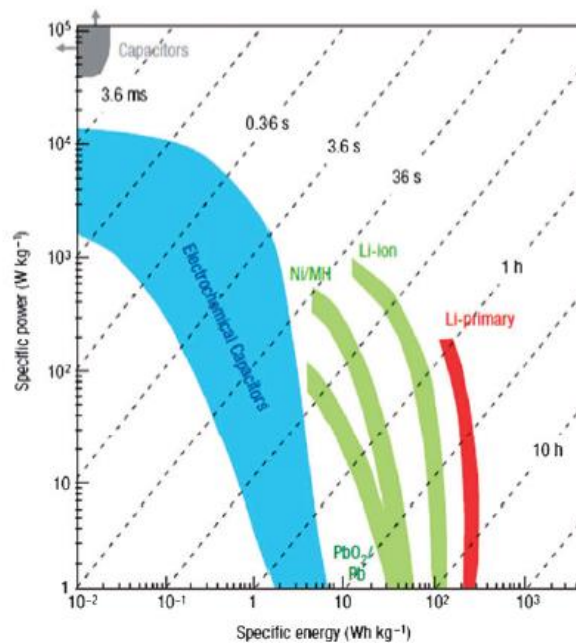


Figure 1.1: Ragone plot showing power and energy densities for different energy storage devices. Reprinted with permission from Royal Society of Chemistry [2]

Figure 1.1 is a Ragone plot, where different energy storage devices are plotted based on their power and energy densities. Electrochemical supercapacitors (ESs) are emerging energy storage devices that offer a balance of power and energy performance, and bridging the gap between conventional capacitors and batteries. ESs also possess other advantages

such as long cyclic life and ability to charge-discharge rapidly, making them suitable for applications neither capacitors or batteries can achieve. Currently, ESs are used for electric vehicles in conjunction with batteries, which have shown to reduce overall size of power source, improve life time and reduce energy loss of batteries [3]–[5].

ESs can be classified into two types by their charge-discharge mechanism, electrochemical double layer capacitors (EDLCs) and pseudocapacitors. The mechanism for the EDLCs involves non-faradic double-layer charge storage on electrodes surface. Pseudocapacitors utilize fast and reversible faradic charge transfer on the surface and near surface of electrode materials for charge storage. Current commercially available ESs have capacitance in the range of microfarad to thousands farad, which are significantly higher than conventional capacitors. Active materials for ESs electrodes that are commonly used are carbon materials (activated carbon, carbon nanotubes, carbon fibers etc.), conducting polymers (polyaniline, polypyrrole, polythiophene etc.) and metal oxides and hydroxides (RuO_2 , MnO_2 , V_2O_5 etc.).

Metal oxides and hydroxides have shown promising results as active materials of ESs, which involve faradic charge storage and show higher energy density than EDLCs. Among all metal oxides, RuO_2 is one of the first metal oxides investigated as an active material for pseudocapacitor. It has high intrinsic electrical and ionic conductivities and good electrochemical reversibility, and its hydrous form exhibits capacitance over 600 F g^{-1} in $0.5 \text{ M H}_2\text{SO}_4$ electrolyte in potential window up to 1 V vs. SCE (standard calomel electrode) [6]. Despite the exceptional performance of RuO_2 electrode, they were never commercialized due to high cost of RuO_2 and the use of strong acidic electrolyte.

To reduce the cost and improve safety of ESs, investigations have been focusing on other metal oxides with appreciable potential window in neutral aqueous electrolytes, such as MnO_2 , Co_3O_4 , V_2O_5 and NiO [1]. MnO_2 is another promising candidate as an active material in ESs, which has low cost and exhibits pseudocapacitance over a wide potential window in neutral aqueous electrolytes. MnO_2 was first investigated by Lee and Goodenough as an active material in 1999, and the capacitances recorded was above 200 F g^{-1} without degradation over 100 cycle in 2M KCl electrolyte and potential window of -0.2 to + 1.0 V vs. SCE [7]. However, MnO_2 suffers from low electrical and ionic conductivities, and high capacitance can only be realized for thin film electrodes[8]. Numerous attempts have been done to address this problem, either by the mean of metal ions doping (Co, Al, Cu)[9], [10] or fabricating composites consist of carbon-based materials with high surface area and conductivity. Multi-walled carbon nanotubes (MWCNTs) are commonly used as conductive additives due to their low percolation threshold. In order to fabricate homogeneous composites, metal oxides and carbon nanotubes must be dispersed using appropriate dispersants. Therefore, the development of co-dispersants and multi-functional dispersants are crucial for the fabrication of high performance composite electrodes.

The primary objective of this work was the development of new colloidal techniques for fabrication of composite electrodes. In these techniques, advanced extractors and dispersants were investigated, and they have successfully reduced particles agglomeration and allowed efficient dispersion of constituents in composites. These strategies have resulted in improved mixing of active materials, and the electrodes fabricated exhibited remarkable capacitances and good rate performance at high active mass loadings.

Advanced dispersants were also employed for fabrication of composite electrodes with alternative metal oxides such as Mn_3O_4 and V_2O_3 . With an appropriate electrochemical activation procedure, both metal oxide composites have shown promising results as active materials for ESs applications. Advanced electrodes were used for the fabrication of asymmetric ESs devices, which showed good performance in enlarged voltage windows.

Chapter 2 Literature Review

2.1 Fundamental and parameters of capacitors and supercapacitors

Before going into details of ESs, a short summary of capacitor should be reviewed as they are similar in terms of parameters and general operating mechanisms.

Figure 2.1 is a schematic of an electrostatic capacitor, which consists of two conductive plates separated by a dielectric plate. The conductive plates are initially electrically neutral, and when a voltage is applied electrons will start to travel from the positive plate to the negative plate until the potential difference between the plate are the same as the source. The two plates are now positively and negatively, and the amount of charge stored is given by Eq.2.1, where Q is the charge stored, V is voltage between plates and C is capacitance of the dielectric capacitor.

$$Q = CV \tag{2.1}$$

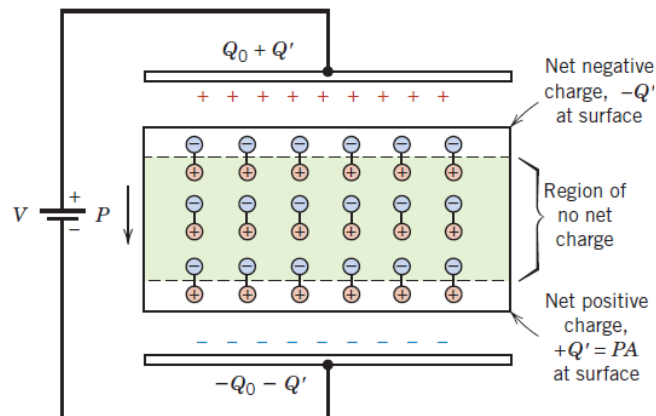


Figure 2.1: Schematic of simple electrostatic capacitor. Reprinted with permission from Wiley Books. [11]

For an electrostatic capacitor, its capacitance is dependent on the dielectric constant ϵ_r , contact areas between plates A and the thickness of dielectric d shown in Eq.2.2.

$$C = \epsilon_0 \epsilon_r \frac{A}{d} \quad 2.2$$

The equation shows that the amount of charge stored in a capacitor is proportional to voltage, and the total energy and maximum power stored in a capacitor is governed by Eq.2.3 and Eq. 2.4.

$$E_{Total} = C \int_{V_{Min}}^{V_{Max}} V dV = \frac{1}{2} CV^2 \quad 2.3$$

$$P = IV = \frac{V^2}{4R_{cap}} \quad 2.4$$

These equations also apply to ESs, indicating the performance of capacitor can be enhanced by increasing the capacitance of active materials, expanding the operating voltage window and reducing internal resistance of capacitors.

2.2 Supercapacitors – Electrochemical double layer capacitors & pseudocapacitors

ESs can be classified into two categories, based on the charge storage mechanism[1]: (i) electrochemical double layer capacitors (EDLCs) and (ii) pseudocapacitors.

In EDLCs, the charge-discharge mechanism originated from pure electrostatic charge accumulation and separation at the electrode/electrolyte interface on two electrodes as shown in Figure 2.2, and the capacitance arises from such interface is called double layer capacitance(C_{dl}) [12]. Similar to conventional capacitors, EDLCs consist of positive and

negative electrodes immersed in an electrolyte but offer a higher capacitance per volume by using high surface area porous carbon materials as active materials.

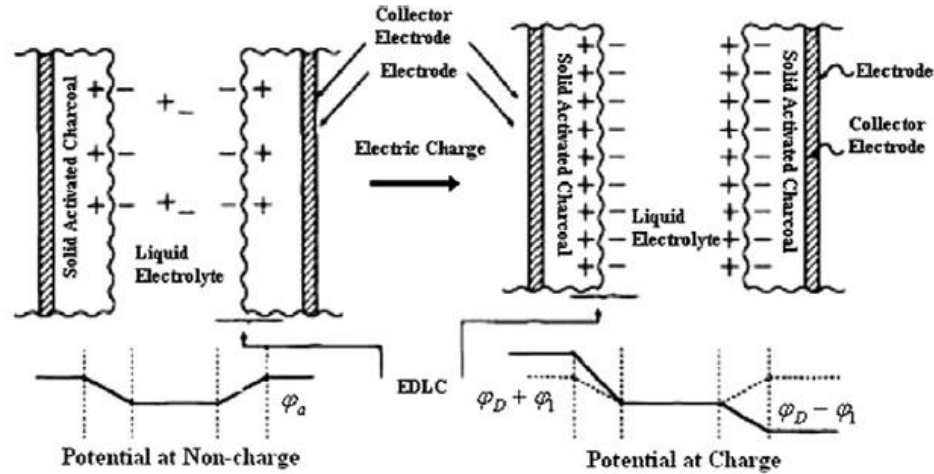


Figure 2.2 Schematics of EDLC at discharged and charged state. Reprinted with permission from Elsevier. [12]

In order to understand the charge storage mechanism, the origin and models of double layer should be discussed. The concept of double layer was first modeled by von Helmholtz, and the model included two layers of opposite charges with an atomic level separation distance. Figure 2.3(a) is a schematic of Helmholtz model, where the charged electrode surface is covered by a static array of compacted ions. After Helmholtz model was proposed, Gouy & Chapman realized that the ions in electrolyte would not only be subjected to static electric field on the surface of electrode, but also thermal fluctuation according to Boltzmann principle. Therefore, Gouy-Chapman have improved the Helmholtz model by assuming ions as point charges and account for the thermal fluctuation shown in Figure 2.3.b. However, the assumption of point charge ions led to the failure of Gouy-Chapman model

due to incorrect potential near electrode surface and overestimated the C_{dl} . To address the overestimation of C_{dl} , Stern model shown in Figure 2.3.c, broke down C_{dl} into two components: an inner layer that obeys Langmuir's adsorption isotherm, and region beyond such layer is treated as a diffuse region of distributed charge similar to Gouy-Chapman model.

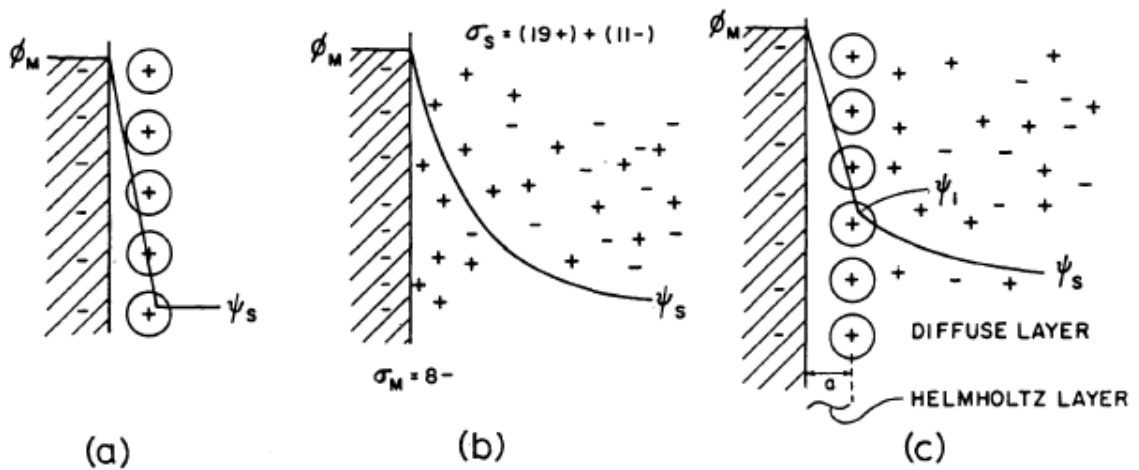


Figure 2.3: Double layer in (a) Helmholtz model, (b)Gouy-Chapman model, and (c) Stern model. Reprinted with permission from Plenum Pub. Corp. [13]

Using Stern model, the equivalent circuit diagram of C_{dl} can be represented by Figure 2.4, and the contribution of Helmholtz (C_H) and diffuse layer($C_{Diff.}$) capacitance can be related to C_{dl} by Eq.2.5.

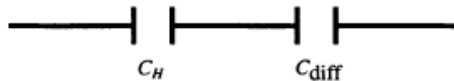


Figure 2.4: Equivalent circuit diagram of C_{dl} in Stern model. Reprinted with permission from Plenum Pub. Corp. [13]

$$\frac{1}{C_{dl}} = \frac{1}{C_H} + \frac{1}{C_{Diff.}} \quad 2.5$$

Overall, the Stern model has generated a much more completed picture of double layer compared to Helmholtz and Gouy-Chapman model by distinguishing the contribution of capacitance from Helmholtz layer and diffuse layer. Grahame model further refined the Stern model, by accounting for properties of cations and anions in electrolyte such as ionic radii of ions and polarizability.[13] The most important distinction in Grahame model is the distances of closest approach for cations and anions to electrodes surface, since cations are typically smaller than anions and retain a solvation shell due to ion-solvent interaction[13]. The solvation shell of cations causes cations to be further away from the electrode surface, compared to anions. The difference in distance of closest approach for cations and anions have broke down Helmholtz layer into inner and outer Helmholtz layers shown in Figure 2.5.

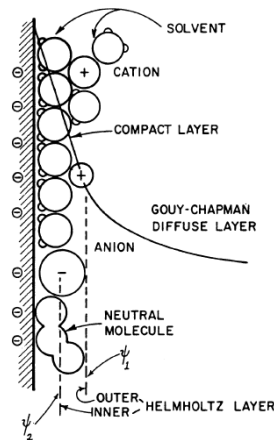


Figure 2.5: Schematic of Grahame model. Reprinted with permission from Plenum Pub. Corp. [13]

As a result of such difference in distance, the C_{dl} in positive polarization (positive charged surface) is higher than in negative polarization due to larger separation distance. Therefore, Eq.2.5 can be rewritten as Eq.2.6, to account of the capacitance contribution from inner (C_{IH}) and outer (C_{OH}) Helmholtz layers.

$$\frac{1}{C_{dl}} = \frac{1}{C_{IH}} + \frac{1}{C_{OH}} + \frac{1}{C_{Diff}} \quad 2.6$$

In commercial EDLCs, porous carbon materials are typically used as active materials, which have surface areas in the range of 500-3000 m² g⁻¹[14]. It has been demonstrated in literature that these carbon-based electrodes exhibited C_{dl} between 15-50 μF cm⁻² in aqueous electrolytes[15]. Taking an average value of C_{dl} as 30 μF cm⁻² and surface area of 1000 m² g⁻¹, the theoretical capacitance of such carbon material is 300 F g⁻¹. However, the actual attainable capacitances for carbon-based materials is often below 50 F g⁻¹, due to limited electrolyte access in pores and low electrical conductivity[16]–[18]. Despite the low attainable capacitance of active materials, EDLCs operate in a pure electrostatic fashion and do not involve phase change allowed them to have extremely long cyclic life. The operating voltage window of aqueous EDLCs is limited to about 1.4 V to prevent decomposition of water molecules, and with organic electrolytes EDLCs can operate up to 3.5 to 4 V[15]. Even though EDLCs with organic electrolytes give higher energy density, the electrolyte resistance is higher in organic electrolytes and reduce the power density[15].

2.3 Principles of energy storage in pseudocapacitors

In EDLCs, energy storage is based on charge accumulation on the surface of electrode. In pseudocapacitors, energy is stored by fast and reversible redox reactions at the surface of active materials. Compared to EDLCs, pseudocapacitors offer 10 to 100 times higher capacitance because charge storage is not limited to surface only, but also the near surface region where ions can diffuse into[19]. However, the slow faradic process hindered the power performance of pseudocapacitors compared to EDLCs.

Pseudocapacitance arise when electrode potential is dependent logarithmically on the extent of reactions, involve charge transfer across the double layer[13]. Conway has identified faradic systems that can give rise to pseudocapacitance: (i) underpotential deposition system, (ii) redox pseudocapacitance and (iii) intercalation pseudocapacitance[20].

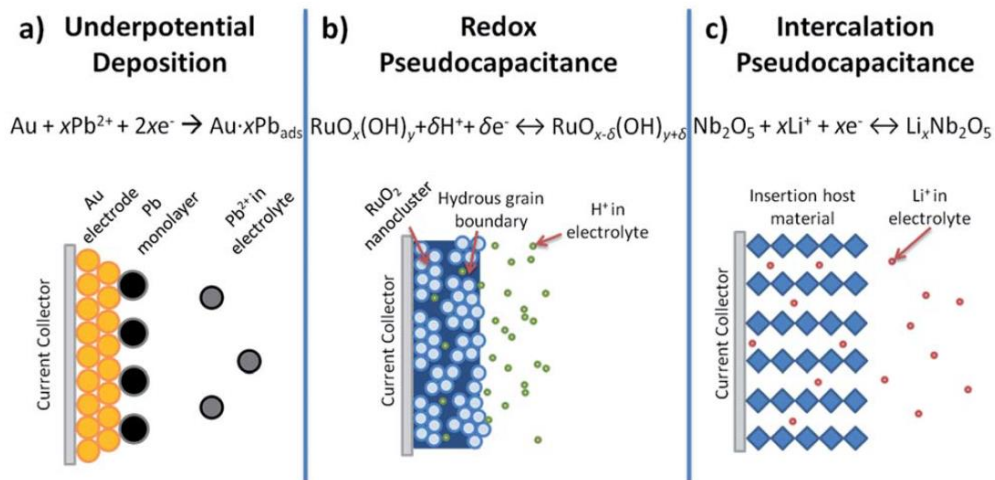


Figure 2.6: Schematic of pseudocapacitive systems identified by Conway. Reprinted with permission from Royal Society of Chemistry. [20]

From the thermodynamic point of view, pseudocapacitance can be related to potential by Eq.2.7 where α is some property of system, proportional to amount of charge passed[13].

$$\frac{\alpha}{1 - \alpha} = K \exp \frac{VF}{RT} \quad 2.7$$

In the under potential deposition system, charge is stored by potential-dependent adsorption of adatoms (H, Pb, Cu) onto metal (Pt, Au, Ag) surface[15]. For H-Pt system, 2-dimensional surface reactions are involved, and Eq.2.7 can be rewritten as Eq.2.8 where θ_H is the fractional surface coverage of H on Pt and C_{H^+} is the concentration of H^+ ions assuming the electrosorption obeys Langmuir isotherm.

$$\frac{\theta_H}{1 - \theta_H} = K C_{H^+} \exp \frac{VF}{RT} \quad 2.8$$

This equation indicated there is such range of potential correspond to a range of θ_H , and the capacitance can be defined by Eq.2.9.

$$C_\phi = q_H \frac{d\theta_H}{dV} = \frac{q_H F}{RT} \theta_H (1 - \theta_H) \quad 2.9$$

From Eq.2.9, the maximum capacitance $\frac{q_H F}{4RT}$ can be reached when $\theta_H = 0.5$. Using $q_H \sim 210 \mu\text{C cm}^{-2}$, the maximum achievable capacitance for H-Pt system is approximately $2200 \mu\text{F cm}^{-2}$ [15]. However, this capacitance was derived using Langmuir isotherm with no interactions between adatoms and metals, and Boudart chemisorption typically resulted in change in surface electron distribution[13]. Therefore, Conway and Gileadi considered an adsorption isotherm with interaction energy term $g\theta$ to accommodate for the interactions.

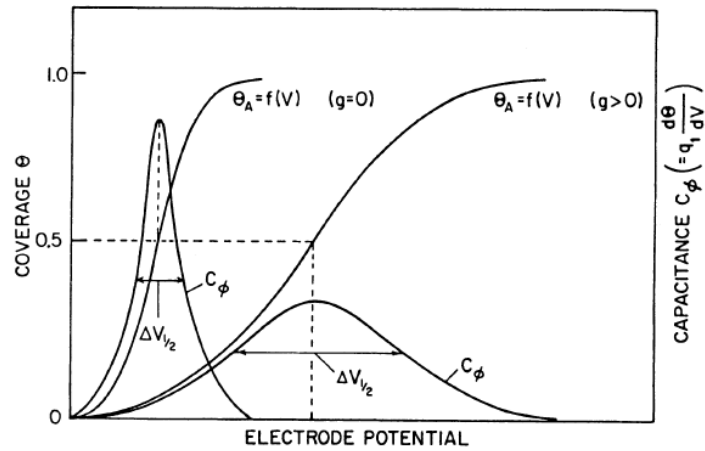


Figure 2.7: Coverage vs. potential for positive and zero g value. Reprinted with permission from Plenum Pub. Corp. [13]

To account of the interaction energy, Eq.2.9 can be modified to Eq.2.10 where maximum capacitance is achieved when $\theta_H = 0.5$, but span over a larger potential range shown in Figure 2.7.

$$C_{\phi} = \frac{q_H F}{RT} \frac{\theta_H (1 - \theta_H)}{1 + g \theta_H (1 - \theta_H)} \quad 2.10$$

Despite the substantial pseudocapacitance arise from underpotential deposition, the high cost of noble metal substrates has limited their applications[19]. However, the concept of chemisorption and interaction energy can still be applied for redox and intercalation pseudocapacitance systems.

In redox pseudocapacitance, ions are electrochemically adsorbed onto surface of active materials accompanied with faradic charge transfer[20]. Metal oxides and conducting polymers are examples of redox pseudocapacitive materials, and the adsorption of ions is achieved by the charge compensation in redox reactions.

For any redox reaction, it can be described using the general chemical equation of Eq.2.11, where Ox and Red are the oxidized and reduced species.



Using Eq.2.11, the Nernst equation of such system can be written as Eq.2.12, where [Ox] and [Red] represent the concentration of oxidized and reduced species.

$$E = E^{\circ} + \frac{RT}{zF} \ln \frac{\mathfrak{R}}{1 - \mathfrak{R}}, \mathfrak{R} = \frac{[Ox]}{[Ox] + [Red]} \quad 2.12$$

$$\frac{\mathfrak{R}}{1 - \mathfrak{R}} = \exp \frac{\Delta E z F}{RT} \quad 2.13$$

By manipulating the Nernst equation Eq.2.13 shows a form resemble Eq.2.7, but with the property of concern of the extent of redox reactions. Therefore, similar conclusion can be made that the potentials follow a logarithmical relation with the extent of redox reactions. Toupin et al. have demonstrated such potential dependence in MnO₂ thin and thick film electrodes by X-ray photoelectron spectroscopy (XPS), where MnO₂ oxidation state changes with potential for thin film electrode[21]. Another interesting finding of Toupin et al. was that the oxidation state of MnO₂ thick film did not vary with potential which they concluded the charge storage mechanism was similar to carbon electrode, and only a thin layer of MnO₂ was involved in the process and electrochemically active[21].

The intercalation pseudocapacitance is also based on redox reactions, arise when ions intercalate into tunnels or layers active materials accompanied by faradic charge transfer without crystallographic phase change, but involve redox reactions in a 3-dimensional structure rather than 2-dimensional surface in redox pseudocapacitance. Similar to

underpotential deposition and redox pseudocapacitance, the extent of intercalation can be related to a range of potential by Eq.2.14, where X is the fraction of ion occupancy in lattices.

$$\frac{X}{1-X} = \exp \frac{\Delta E z F}{RT} \quad 2.14$$

Overall, Figure 2.8 shows a summary of pseudocapacitive systems and their corresponding Nernst equations, and the key idea of this section is the logarithmic relations between potential and capacitance give rise to pseudocapacitance.

	System Type	Essential Relations
(a)	Redox system: Ox + ze ⇌ Red	$E = E^0 + \frac{RT}{zF} \ln \mathfrak{R}/(1 - \mathfrak{R})$ $\mathfrak{R} = [\text{Ox}]/([\text{Ox}] + [\text{Red}]) \quad \mathfrak{R}/(1 - \mathfrak{R}) = [\text{Ox}]/[\text{Red}]$
(b)	Intercalation system: Li ⁺ into "MA ₂ "	$E = E^0 + \frac{RT}{zF} \ln X/(1 - X)$ X = occupancy fraction of layer lattice sites (e.g., for Li ⁺ in TiS ₂)
(c)	Underpotential deposition M ^{z+} + S + ze ⇌ S·M (S ≡ surface lattice sites)	$E = E^0 + \frac{RT}{zF} \ln \theta/(1 - \theta)$ θ = 2-dimensional site occupancy fraction

Note: (b) and (c) can be regarded as mixing of occupied (X or θ) sites with unoccupied sites, (1 - θ) or (1 - X).
 Also θ + (1 - θ) = 1 or X + (1 - X) = 1.

Figure 2.8: Pseudocapacitive systems and their Nernst equations. Reprinted with permission from Plenum Pub. Corp. [13]

2.4 Carbon materials for EDLCs applications

In section 2.2, it was mentioned that performance of EDLCs is governed by the structure and the surface area of active materials. Carbon materials have advantages such as high surface area, good conductivity, high thermal stability, excellent corrosion resistance and controllable porous structure make them excellent candidate as active materials in EDLCs and additives in pseudocapacitors[22]. Figure 2.9 is a summary of different carbon materials and their related properties for EDLCs.

Material	Activated carbon	Templated carbon	Carbide-derived carbon	Carbon aerogel	Carbon fiber	Graphene	VA-CNT	Graphene oxide
Price	Low	High	Medium	Medium	Medium	Medium	High	High
Scalability	High	Low	Medium	Medium	High	Medium	Low	Low
Surface area [$\text{m}^2 \text{g}^{-1}$]	~2000	<4500	<3200	<700	<200	2630 ^a	1315 ^a	~500
Conductivity	Low	Low	Medium	Low	Medium	High	High	Variable
Gravimetric capacitance	Medium	High	High	Medium	Low	Medium	Low	Low
Volumetric capacitance	High	Low	High	Low	Low	Medium	Low	Low

^a Theoretical values.

Figure 2.9: Comparison of carbon materials based on their properties in EDLCs. Reprinted with permission from Royal Society of Chemistry. [23]

2.4.1 Activated Carbon (AC)

Activated carbon (AC) powders are the most widely used electrode materials in EDLCs due to their high surface area and low cost. The porous structure of AC is generated by the oxidation of carbon precursor, such as high temperature oxidation or chemical oxidation by strong acid or base[24]. The pores can be classified in three categories illustrated in Figure 2.10: (i) macropores (larger than 50 nm), (ii) mesopores (2~50 nm), and (iii) micropores (< 2 nm)[24].

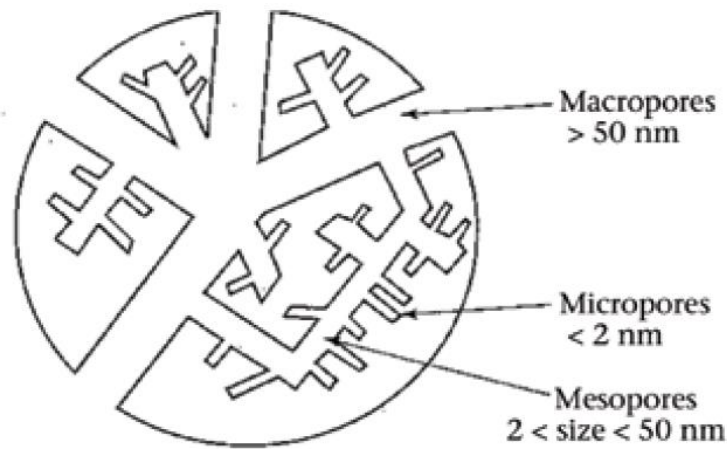


Figure 2.10: Schematic of porous structure of activate carbon. Reprinted with permission from Journal of Electrochemical Society. [24]

By controlling the oxidizing environment of AC, the porous structure can gives AC high specific area up to $3000 \text{ m}^2 \text{ g}^{-1}$ [25]. Generally, larger surface area should result in higher capacitance due to increased charge accumulation on surface, but the AC electrode fabricated resulted in $< 10 \mu\text{F cm}^{-2}$. It was realized that not all surface area is accessible to electrolyte, and smaller pores restrict the motion of electrolyte ions resulted in poor capacitive behaviour. Other factors such as pore size distribution, geometry and structure, electrical and ionic conductivities and surface defects can also affect the performance of AC in EDLCs significantly. It has been demonstrated that AC exhibits higher capacitance in aqueous electrolyte ($100\sim 300 \text{ F g}^{-1}$) compare to organic electrolyte ($< 150 \text{ F g}^{-1}$).[25] This phenomenon can be explained by larger effective size of organic ions compare to the ones in aqueous, but the surface tension and wettability of electrolyte on AC surface play an important role as well.

2.4.2 Graphene-based materials

Graphene is a 2-dimensional monolayer of graphite, which has low density, good conductivity, high mechanical strength and chemical stability, and high surface area.[26] Such unique properties of graphene have attracted and driven the development of graphene-based electrodes for batteries and ESs application. The theoretical capacitance of graphene can reach 550 F g^{-1} , which is the highest intrinsic capacitance achievable by carbon materials[26]. Recent studies have shown that graphene electrodes can achieve specific capacitance of 117, 135 and 99 F g^{-1} in H_2SO_4 , aqueous and organic electrolytes respectively[26], [27]. Compared to AC and carbon nanotubes, the accessible surface area does not depend on the pore distribution, but rather the degree of agglomeration of graphene monolayers[27]. Due to the 2-dimensionality of graphene, the orientation of the monolayers also plays an important role in conductivity.

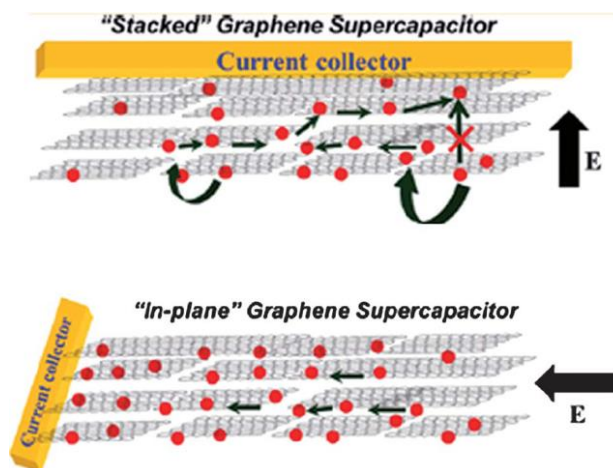


Figure 2.11: Schematic of the conductive pathways in graphene electrodes of different orientations. Reprinted with permission from Royal Society of Chemistry. [28]

Figure 2.11 shows two different geometries and the corresponding conductive pathway of graphene electrodes. In the stacked geometry, the random orientation of graphitic layers restricted the complete utilization of electrochemical surface area, whereas in plane geometry allow electrolyte access to all surface and resulted in improved capacitance[28]. The extraordinary mechanical properties of graphene have also gained significant interest in the emerging field of flexible ESs[29]. The high strength of graphene can reinforce the electrode structure to mechanical bending and twisting, and in conjunction with polymeric gel electrolyte graphene have yielded remarkable capacitance in the range of 100 – 250 F g⁻¹. [30] Graphene nanocomposite of carbon materials, metal oxides and conducting polymers have also been investigated, and the results are summarized in Table 2.1.

electrode material(s)	current collector	binder	highest specific capacitance	current density (Ag ⁻¹)	capacitance basis	areal mass loading (cm ²)	types of electrolyte
rGO/carbon black	Au-coated PET		79 F g ⁻¹	1	whole electrode	1	PVA/H ₂ SO ₄
mesoporous graphene/PTFE	coin cell	PTFE	100–250 F g ⁻¹	1		1.3 (coin cell)	celgard membrane/EMIMBF ₄
graphene/PANI			261 F g ⁻¹	0.38	active material		PVA/H ₃ PO ₄
graphene/PANI nanofibers			210 F g ⁻¹	0.30	whole electrode		filter paper/H ₂ SO ₄
PPy/graphene			237 F g ⁻¹	0.01 V s ⁻¹ (CV)	whole electrode		KCl
rGO/cMWCNT–CFP/PPy			82.4 F g ⁻¹	0.5	active material		PAAK/KCl
multilayer rGO	Au-sputtered		247.3 F g ⁻¹	0.176	whole electrode	0.4	PVA/H ₃ PO ₄
MnO ₂ -coated graphene fiber			9.1–9.6 mF cm ⁻²	2 × 10 ⁻⁴ μA	whole electrode		PVA/H ₂ SO ₄
β-Ni(OH) ₂ / graphene	Au-coated PET		3304 μF cm ⁻²	0.1/m ²	area of single electrode	1	PVA/KOH
laser-scribed rGO			4.04 mF cm ⁻²	1	whole electrode		PVA/H ₂ SO ₄
graphene-coated MnO ₂			29.8 F g ⁻¹	1.5 mA/cm ²	whole electrode		membrane separator/Na ₂ SO ₄
CNT-Mn ₃ O ₄ / graphene			72.6 F g ⁻¹	0.5	active material		PAAK/KCL
IL-CMG/RuO ₂ -IL-CMG			167 F g ⁻¹	1	active material		PVA/H ₂ SO ₄
graphene-cellulose nanofibers aerogel			203 F g ⁻¹	0.7	active material	0.02	PVA/H ₂ SO ₄
MnO ₂ /rGO	CNF	ethylene glycol			active material	28	PVA/NaNO ₃

Table 2.1 Summary of literature capacitance of graphene-based composite materials for flexible supercapacitor application. Reprinted with permission from American Chemical Society. [30]

2.4.3 Carbon nanotubes

Carbon nanotubes (CNTs) are long cylindrical carbon and can be thought of graphene sheet “rolled” into a cylinder according to the chiral vector. CNTs have advantages such as nanometer size distribution, high aspect ratio and surface area, low resistivity and high stability, which make CNTs suitable as active materials for EDLCs[31]. Unlike other carbon materials, CNTs have interconnected mesopores which utilize all accessible surface area[32]. Figure 2.12 is a schematic showing the structure of CNTs, and three types of CNTs are categorized based on chirality. The three types of CNTs are zig-zag, chiral and armchair configurations, and the chirality gives rise to metallic property of zig-zag and chiral configuration, and semiconducting property for armchair configuration[33].

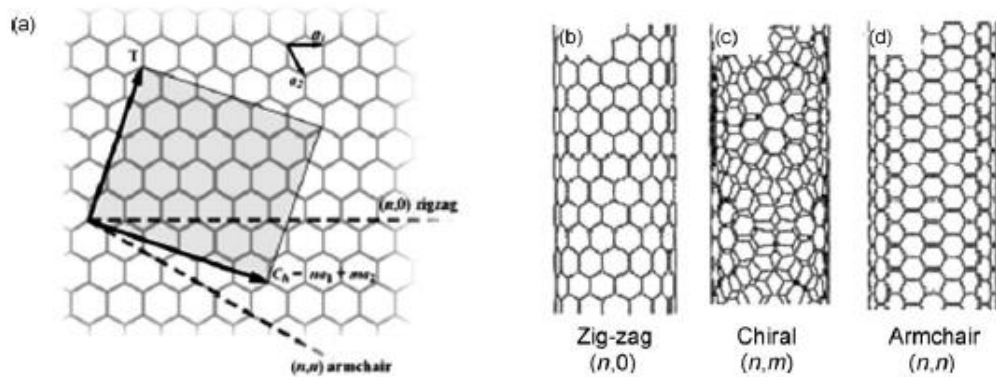


Figure 2.12: Atomic structure of carbon nanotubes of different chirality, and their corresponding chiral vectors projected on a graphene sheet. Reprinted with permission from Royal Society of Chemistry. [25]

CNTs are usually available in the form of single-walled (SWCNTs) or multi-walled (MWCNTs), and both have been extensively studied to investigate their potentials as active materials and conductive additives for composite materials. In 1997, Niu et al. first

attempted to fabricate CNTs electrode for EDLC, using catalytic decomposition of hydrocarbons to grow MWCNTs and followed by a surface functionalization process using nitric acid to increase redox activity. The functionalized MWCNTs resulted in a surface area of $430 \text{ m}^2 \text{ g}^{-1}$ and a specific capacitance of 102 F g^{-1} in a sulfuric acid electrolyte[34]. In another study by An et al., MWCNTs produced via arc-discharge process was annealed at high temperature and used to fabricate electrodes. It was found that heating MWCNTs at high temperature below $1000 \text{ }^\circ\text{C}$ can increase the specific surface area and reduce average pore diameter, which improved graphitization and capacitance of MWCNTs electrodes. By increasing the annealing temperature from $600 \text{ }^\circ\text{C}$ to $800 \text{ }^\circ\text{C}$, the specific capacitance increased from 138 F g^{-1} to 158 F g^{-1} [35]. The performance of CNTs electrode is affected by factors such as surface area, pore distribution and conductivity, which can be improved by surface functionalization, high temperature oxidization or doping. CNTs have shown promising results as electrode materials, however the high production cost of CNTs has become one of the major drawbacks for mass productions.

Despite the high cost of CNTs, the low percolation threshold of CNTs makes them an ideal conductive additive for ESs applications. Sandler et al. and Battisti et al. have investigated the percolation threshold for composite where CNTs were used as conductive fillers for insulating polymeric matrices[36], [37]. In Sandler et al.'s approach[36], chemical vapor deposition (CVD) grown MWCNTs were incorporated in epoxy matrices with a MWCNTs loading ranged from $0.001 - 1 \text{ wt}\%$. It was demonstrated that $0.005 \text{ wt}\%$ MWCNTs loading was sufficient to allow good electrical conduction[36]. For Battisti et al.'s procedure[37], they prepared unsaturated polystyrene-MWCNTs nanocomposite with MWCNTs loading

in the range of 0 – 0.3 wt%. Using a statistical percolation model with experimental data, the percolation threshold of MWCNTs in this case was determined to be 0.026 wt% [37]. The quality of MWCNTs dispersion is an important factor in the processing step of nanocomposite fabrications, as it governs the effectiveness of conductivity improvement [37]. Therefore, dispersion of MWCNTs is a crucial parameter in fabrication of high performance nanocomposites with good electrical conductivity.

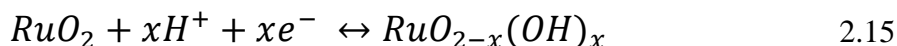
2.5 Metal oxides & hydroxides as electrode materials

Metal oxides and hydroxides are used as active materials for pseudocapacitors, which have high theoretical capacitances originated from fast faradic reactions and resulted in a much higher energy density than EDLCs. Many metal oxides and hydroxides such as RuO₂, MnO₂, V₂O₅, NiO, Co₃O₄, Fe₂O₃, and FeOOH are some examples of materials, which have been investigated and have shown exceptional results as active materials for ESs. However, majority of these metal oxides and hydroxides suffer from low electrical conductivity, and conductive carbon materials are incorporated to fabricate composite materials.[1], [38]

2.5.1 Positive electrode

2.5.1.1 Ruthenium dioxide (RuO₂)

Ruthenium dioxide is one of the first metal oxide investigated for its application in ESs. Its crystalline and amorphous hydrous forms have the ideal characteristics properties of faradic active materials, such as multiple oxidation states, high electrical and ionic conductivities and good cyclic stabilities[38]. In 1971, Trasatti et al. prepared RuO₂ thin film by thermal decomposition and the film exhibited capacitive behaviour in 1M HClO₄ electrolyte in the voltage range of 0 to 1.45V vs. RHE[39]. In acidic condition, the charge storage mechanism of RuO₂ can be expressed by Eq.2.15.



The pseudocapacitance of RuO₂ thin film was attributed to the successive redox transition from Ru²⁺ to Ru⁴⁺, and the conversion of OH⁻ to O₂⁻ within the structure by transfer of proton[38]. The performance of RuO₂ electrodes is governed by the charge transfer and

diffusion process, such as electron hopping within and between RuO_2 particles, electron transfer from active materials to current collectors and the ion diffusion within RuO_2 [40]. Among the two forms of RuO_2 , the hydrous form of RuO_2 have shown higher capacitance compared to the anhydrous. Sugimoto et al. have investigated the capacitive performance of RuO_2 with different water content, and they have been shown anhydrous RuO_2 has a much lower capacitance (24 F g^{-1}) than the hydrous form (342 F g^{-1}) [41].

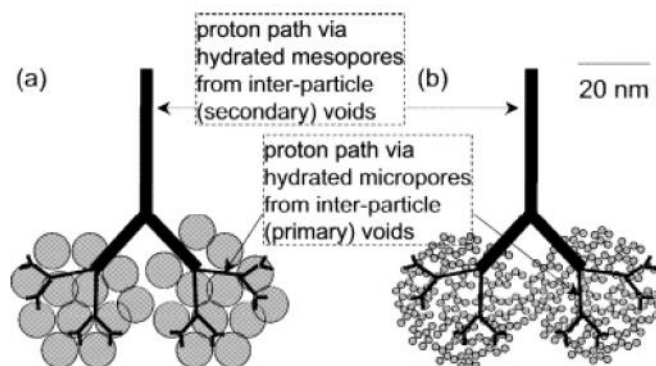


Figure 2.13: Schematic of tree-root model for anhydrous and hydrous RuO_2 . Reprinted with permission from American Chemical Society. [41]

Sugimoto et al. have attempted to explain such phenomena with the tree root model shown in Figure 2.13. For anhydrous RuO_2 , the particles are agglomerated with no available micropores for ion diffusion, and hydrous RuO_2 particles are smaller and hydrated micropores exist between particle allowed good ion transport. Therefore, the water content in RuO_2 plays an important role, which is responsible for fast ionic conduction through porous structure to enhance capacitive performance[41].

Despite having the ideal properties for ESs applications, the high cost of RuO₂ have limited its applications. To address this problem, some research was conducted to fabricate RuO₂ composite with low cost metal oxides or deposition of RuO₂ on conductive substrates[42]. Hu et al. have fabricated hydrous RuO₂ – TiO₂ nanocomposite by hydrothermal process, and such electrode have shown remarkable capacitance of 992 F g⁻¹ at the scan rate of 100 mV s⁻¹ [43]. In another study by Hsieh et al., composite composed of vertically aligned MWCNTs coated with hydrous RuO₂ on a titanium current collector, and a maximum capacitance of 1652 F g⁻¹ was achieved[44].

2.5.1.2 Manganese dioxide (MnO₂)

MnO₂ has been investigated extensively for ESs application due to high theoretical capacitance (1370 F g⁻¹), low cost, low toxicity compared to other metal oxides, and multiple available oxidation states.[8], [42] Similar to RuO₂, the pseudocapitance of MnO₂ is derived from the successive redox transition of Mn³⁺ and Mn⁴⁺[1], and the charge storage mechanism can be expressed by Eq.2.16.



An advantage of MnO₂ compared to RuO₂ is its capability of operating in mild aqueous electrolyte such as Na₂SO₄ and chloride salts (KCl, NaCl)[2], rather than strong acid or base electrolyte used in RuO₂ systems[38].

MnO₂ has various crystal structure, denoted by α , β , γ , δ and λ phases and is a crucial factor of the electrochemical performance of MnO₂.

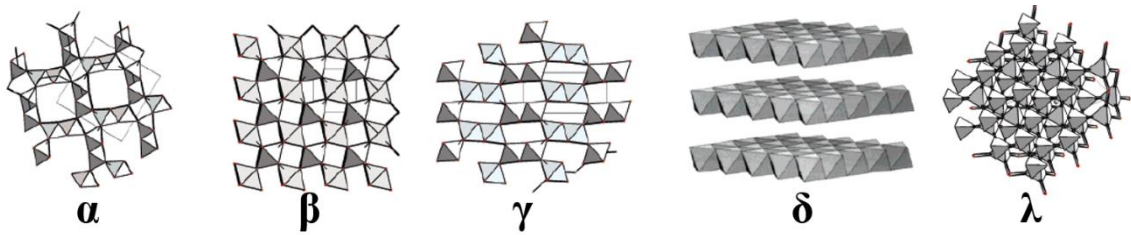


Figure 2.14: Different crystal structure of MnO₂. Reprinted with permission from American Chemical Society. [45]

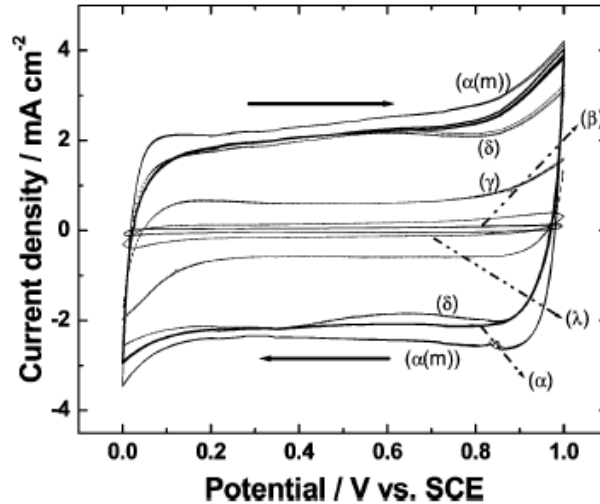


Figure 2.15: Cyclic voltammograms of different phases of MnO₂. Reprinted with permission from American Chemical Society. [45]

Figure 2.14 shows different phases of MnO₂, and for all phases they have tunnel structure for electrolyte access, where the tunnel size varies from 1.89 to 7 Å[45]. Brousse et al. and Devaraj et al. have determined the capacitance of different structure of MnO₂ in a 0.1M K₂SO₄ and 0.1M Na₂SO₄ solution respectively, and both authors suggested that the

capacitance of MnO_2 decrease in the order of $\alpha \cong \delta > \gamma > \lambda > \beta$ as shown in Figure 2.15 [45], [46].

The result have indicated the size of tunnel governed the active surface area for pseudocapacitance, and phases with small tunnel such as the β , λ and γ phase inhibited cations motion whereas large tunnel structure of α and δ allowed fast cations diffusion during charge-discharge.[46] In another study by Ghodbane et al., the Brunauer-Emmett-Teller (BET) surface area of different structures of MnO_2 was investigated to determine the correlation between surface area and capacitance. In EDLCs, increase in surface area typically resulted in improved capacitance, as the amount of charge stored is proportional to the surface area. However, Ghodbane et al. have shown that capacitance of MnO_2 has strong correlation with ionic conductivities, rather than the BET surface area[47]. Brousse et al. have performed a similar investigation for crystalline MnO_2 , and the results were in good agreement with Ghodbane et al[46]. These results have indicated the charge storage mechanism of MnO_2 is not only limited to surface reactions, but also ion intercalation into bulk MnO_2 [46], [47]. Other than the crystal structure, the morphology of MnO_2 is also an important factor in determining the performance as the surface area and aspect ratio can be adjusted to give rise of different degree of pseudocapacitance[8]. Currently, many morphologies of MnO_2 have been fabricated, such as nanowires[48], [49], nanorods[50], hollow spheres[51] and thin films[52].

Despite its high theoretical capacitance and compatibility with aqueous electrolytes, one of the major drawbacks of MnO_2 is the low electrical conductivity.[8], [42] The conductivity of electrode materials has significant impact on the capacitance and rate performance. As

the charge-discharge rate increases low conductivity of electrode materials limits the charge storage process in a confined volume and results in reduced capacitance and poor rate performance. To address this problem, numerous investigations have attempted to improve conductivity by fabrication of MnO₂ composite with metal ions or conductive carbon materials. In one of the investigations, Tang et al. have synthesized Co doped MnO₂ using a light assisted method, and the electrode exhibited specific capacitance of 350 F g⁻¹ and improved rate performance[9]. The doped MnO₂ also had a high cyclic stability and retention 90% of its capacitance after 1000 cycles[9]. As mentioned earlier, conductive carbon material such as MWCNTs has low percolation threshold and a good fit as conductive additive for MnO₂ composite[36], [37]. Li et al. have fabricated MnO₂-MWCNTs with nickel foam current collector, and sodium dodecyl sulfate as dispersant for MWCNTs. It was demonstrated that pure MnO₂ electrode exhibited capacitance below 40 F g⁻¹ between scan rates of 2 to 100 mV s⁻¹, whereas MnO₂-MWCNTs composite electrode with 20 wt.% MWCNTs showed a high capacitance of 150 F g⁻¹ at 2 mV s⁻¹ at high active mass loading of 40 mg cm⁻²[53].

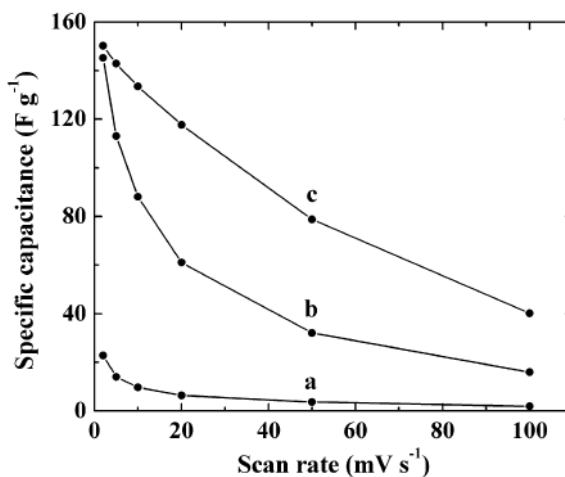


Figure 2.16: Specific capacitance of MnO₂ electrode containing (a) 0 wt.%, (b) 10 wt.% and (c) 20 wt.%. Reprinted with permission from Elsevier. [53]

2.5.1.3 Vanadium pentoxide (V₂O₅)

Other than manganese oxides, V₂O₅ has also shown remarkable performance as active material for batteries and ESs. V₂O₅ possess advantages such as high energy density, low toxicity, low cost, stable layered structure and wide potential window arise from multiple available oxidation states from V²⁺ to V⁵⁺[1], [20], [40], [54]. M. Whittingham first investigated V₂O₅ for rechargeable battery applications in 1976, and he had demonstrated that V₂O₅ were able to form complex ternary oxide with lithium ions upon intercalation with high reversibility[55]. Later in 1999, Lee and Goodenough have fabricated the first amorphous V₂O₅·nH₂O composite electrode by quenching V₂O₅ powder heated at 1223 K for 30 minutes in DI water, and subsequently balled milled with acetylene black and polytetrafluoroethylene (PTFE) then pressed on a Ti substrate[56]. The fabricated electrode showed a close to mirror-image cyclic voltammogram between potential of -0.2 to 0.8 V

vs. SCE in a 2M KCl electrolyte at low pH (pH = 2.32), indicated that amorphous V_2O_5 can give pseudocapacitance in aqueous electrolyte with specific capacitance of 346.4 F g^{-1} [56]. However, they have also found that V_2O_5 composite electrode in 2M KCl in close to neutral electrolyte (pH = 6.67) undergo dissolution at -0.1 V vs. SCE, and such dissolution behavior of V_2O_5 can be reduced by adjusting the pH of electrolyte to more acidic condition. Moreover, V_2O_5 also suffer from low electrical conductivity similar to MnO_2 . Therefore, recent developments of V_2O_5 for ESs application have been focused on two aspects: development of V_2O_5 electrode with unique structure and morphology in an appropriate electrolyte, or development of stable V_2O_5 with conducting polymeric coatings such as polypyrrole[57]. In an approach by Zhu et al., they have fabricated 3D network of V_2O_5 nanosheets by producing 2D nanosheets by hydrothermal synthesis, followed by a freeze-drying procedure. The resulted porous 3D structure allowed high specific capacitance of 451 F g^{-1} in neutral Na_2SO_4 electrolyte, and a remarkable capacitance retention more than 90% over 4000 cycles[58]. Zhu et al. have also compared the 3D network with stacked 2D V_2O_5 nanosheets, and the 3D structure outperformed stacked nanosheets. The improvement can be attributed to the increased surface area and enhanced electrolyte-electrode interactions, as well as the reduction of diffusion path of electrons and ions[58]. In another approach, Qu et al. have attempted to reduce dissolution and improve conductivity using a core-shell structure of polypyrrole (PPy) on V_2O_5 nanoribbon [59]. Figure 2.17 is a TEM image of the core-shell PPy@ V_2O_5 , and it is obvious that PPy was successfully formed on the surface of V_2O_5 with the aid of an anionic surfactant. The electrode coated with V_2O_5 of nanoribbon morphology was tested in a 0.5 M K_2SO_4

electrolyte, and the electrode have shown an exceptionally high specific capacitance of 308 F g⁻¹[59]. The electrode was also subjected to cycling for 10000 cycles, and the capacitance loss was less than 5%, whereas pure V₂O₅ resulted in a 17.5% loss[59]. Overall, the formation of a conducting polymer PPy on V₂O₅ has demonstrated its ability in reduction of dissolution, and also boosted the conductivity of the composite which resulted in high performance V₂O₅ composite electrode.

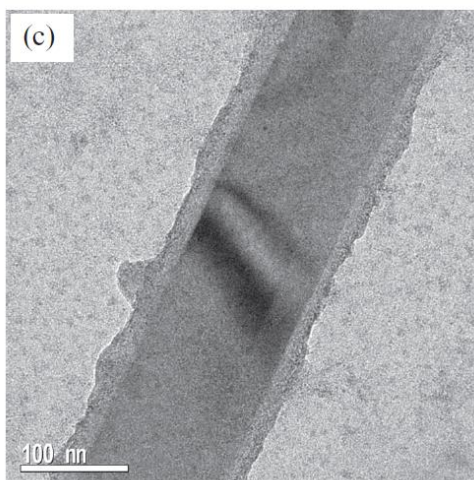


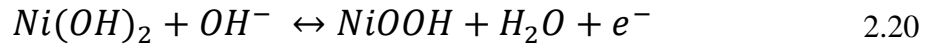
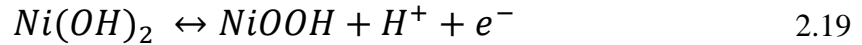
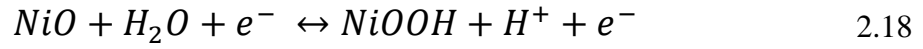
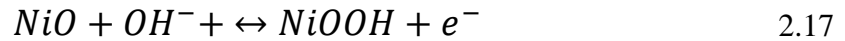
Figure 2.17: TEM image of PPy@V₂O₅ core-shell structure provided by Qu et al.

Reprinted with permission from John Wiley and Sons.[59]

2.5.1.4 Nickel oxide (NiO) & nickel hydroxide (Ni(OH)₂)

NiO is another promising candidate for ESs application, due to its extremely high theoretical capacitance of 2584 F g⁻¹, low cost and low toxicity[60], [61]. NiO is typically synthesized by producing Ni(OH)₂ and subsequently annealed at high temperature to form NiO[40]. The electrolyte for NiO electrode is usually alkaline solutions, however the charge storage mechanism is unclear. There are two theories proposed for the

pseudocapacitance of NiO arise from alkaline solutions, where the first one involves the redox reactions between NiO and nickel oxyhydroxide (NiOOH) (Eq.2.17 & 2.18), and the latter theory involve reactions between Ni(OH)₂ and NiOOH (Eq.2.19 & 2.20)[42]. However, it is commonly believed that Eq.2.17 occurred first to produce NiOOH, followed by the reversible redox reactions between Ni(OH)₂ and NiOOH[61].



It has been shown that there are few issues with NiO, such as significantly lower specific capacitance achievable compared theoretical value, low electrical conductivity and poor cyclic stability[42]. Similar to other metal oxides, efforts have been focusing on fabricating nanostructured NiO or NiO composite with other materials[60], [62]–[65]. Nam et al. have investigated the electrochemical performance of porous NiO film derived from electroplated Ni(OH)₂ film on nickel foil substrate with different deposition current density followed by a heat treatment. The specific capacitance of NiO film increased with deposition rate, and a specific capacitance of 277 F g⁻¹ was achieved in 1M KOH electrolyte for the NiO film with deposition current density of 4 mA cm⁻²[66]. In another investigation by Yuan et al., they have fabricated porous NiO nano and micro spheres to improve rate performance. The approach involved a low temperature precipitation reaction with alkaline solution and nickel salts, and the fabricated electrode exhibited specific capacitance of 525

F g⁻¹ at current density of 4 A g⁻¹[67]. The hierarchical porosity generated by the nano and micro spheres have offered high capacitance retention of 98% after 2000 cycles[67].

Ni(OH)₂ has a hexagonal layered structure with two polymorphs, α-Ni(OH)₂ and β-Ni(OH)₂, and have been demonstrated that the structure has impact on the performance of the electrodes[68]. α-Ni(OH)₂ has intercalated with anions and water within the structure, whereas water is absent in β-Ni(OH)₂[68]. The α-Ni(OH)₂ showed a higher specific capacitance than β-Ni(OH)₂, and the situation can be explained by recalling that hydrous RuO₂ showed higher specific capacitance than anhydrous form due to improved ion transport[41], [69], [70].

2.5.1.5 Cobalt oxide (Co₃O₄) & cobalt hydroxide (Co(OH)₂)

Co₃O₄ is another alternative active material for ESs application, given a high theoretical capacitance of 3560 F g⁻¹, low cost, good corrosion resistance and high electrochemical stability[1], [61]. Co₃O₄ electrodes can be operated in alkaline solutions, and the charge storage mechanism is described by Eq.2.21.



Despite its high theoretical capacitance, the actual capacitance achievable by Co₃O₄ is low, and the poor conductivity is one of the major challenges[71]. Nanostructured Co₃O₄ have been fabricated such as nanotubes[71], nanosheets[72], nanocubes[73] and nanowire arrays[74], and composite with graphene[75] and porous carbon[73] were also investigated. Salunkle et al. have synthesized nanoporous Co₃O₄ using a metal-organic framework. The nanoporous structure has allowed large surface area for charge storage, and the electrode

exhibited specific capacitance of 504 F g^{-1} at scan rate of 5 mV s^{-1} in a 6M KOH electrolyte[73]. In another investigation, Dong et al. have demonstrated the use of graphene- Co_3O_4 for ESs application as well as biosensing applications. They prepared the electrode by first fabricated 3D graphene foam by CVD on Ni foam substrate, and the foam was subsequently immersed in a Co_3O_4 precursor solution and undergo hydrothermal process. The fabricated electrode was tested in a 0.1M NaOH electrolyte and showed specific capacitance of 768 F g^{-1} at current density of 10 A g^{-1} [75]. The cyclic stability of the electrode was also tested, and interestingly the specific capacitance increased to $\sim 1100 \text{ F g}^{-1}$ after 500 cycles and plateau afterward[75]. The authors suggested that the phenomenon was a result of an activation process, where the electrode allowed more complete intercalation and deintercalation during charge-discharge.

Co(OH)_2 has also gained significant interest due to its layered structure with large spacings, and it can facilitate fast ions motions during intercalation and deintercalation[42]. However, in order to retain the structure of hydroxide, the potential window of Co(OH)_2 is limited around 0.5 V [76], [77]. Kong et al. have synthesize asymmetric supercapacitor with $\alpha\text{-Co(OH)}_2$ and AC, and the $\alpha\text{-Co(OH)}_2$ electrode has shown remarkable specific capacitance of 735 F g^{-1} in potential range of 0 to 0.4 V vs. SCE, and the device fabricated has a specific capacitance of 72.4 F g^{-1} within the potential window of $0\text{-}1.6 \text{ V}$ [77]. Jagadale et al. have investigated the electrochemical performance of $\beta\text{-Co(OH)}_2$ thin film deposited on stainless steel substrate potentiodynamically, and the electrode exhibited outstanding specific capacitance of 890 F g^{-1} in 1M KOH electrolyte in the potential window of -0.2 to 0.4 V vs. SCE[78].

2.5.2 Negative Electrodes

2.5.2.1 Iron Oxide (Fe_2O_3) and oxy-hydroxide (FeOOH)

Iron oxides and oxy-hydroxides have gained significant interest for negative electrode in ESs due to their unique properties of low cost, low toxicity and suitable potential window. However, they suffer from drawbacks such as low conductivity, high volume expansion during charge-discharge and poor cyclic stability.[1], [79], [80] Iron oxides has many structures, and hematite ($\alpha\text{-Fe}_2\text{O}_3$) is one of the most stable structure which has good corrosion resistance and exhibits high theoretical capacitance of 3625 F g^{-1} . [1], [79] Similar to other materials, extensive effort has been devoted to development of nanostructured and composite electrodes to address the poor conductivity and stability. Liu et al. have synthesized ultrathin Fe_2O_3 nanoflakes from nanorods by an electrochemically-induced transformation followed by annealing. The nanoflakes morphology allowed for increased surface area and reduced charge transfer resistance, and showed far superior areal capacitance of 145.9 mF cm^{-2} compared to 9.2 mF cm^{-2} for the nanorods structure.[81] In another approach by Wang et al., composite electrode consists of graphene hydrogel and $\alpha\text{-Fe}_2\text{O}_3$ was fabricated by hydrothermal method followed by freeze drying. The graphene hydrogel with high surface area provided high conductivity and fast ions diffusion, and improved the rate capability and cyclic performance of the composite electrode. The composite electrode showed an exceptionally high specific capacitance of 908 F g^{-1} , compared to 272 F g^{-1} for pure graphene hydrogel.[82] The capacitance retention of the

Fe₂O₃ was improved, from 51% after 70 cycles for pure Fe₂O₃ to 75% after 200 cycles for the composite electrode.[82]

For the investigation of iron oxy-hydroxide (FeOOH), Chen et al. have fabricated α -FeOOH-MWCNTs composite electrode by particle extraction through a liquid-liquid interface (PELLI) at a high mass loading of 37 mg cm⁻². The use of PELLI has significantly improved the capacitive performance at high active mass loading, and the electrode displayed high areal capacitance 5.86 F cm⁻². [83] However, Figure 2.18(A) shows that capacitance of FeOOH electrode decreases at more positive potentials (-0.3V vs. SCE) and decreased the overall capacitance. Therefore, Chen et al. and Fan et al. have investigated the feasibility of incorporating PPy with voltage window from -0.5V to +0.4V vs. SCE to enhance capacitance near positive potentials.[84], [85] In both studies, the addition of PPy coated MWCNTs have improved the capacitive performance, especially at more positive potential as shown in Figure 2.18 and Figure 2.19.

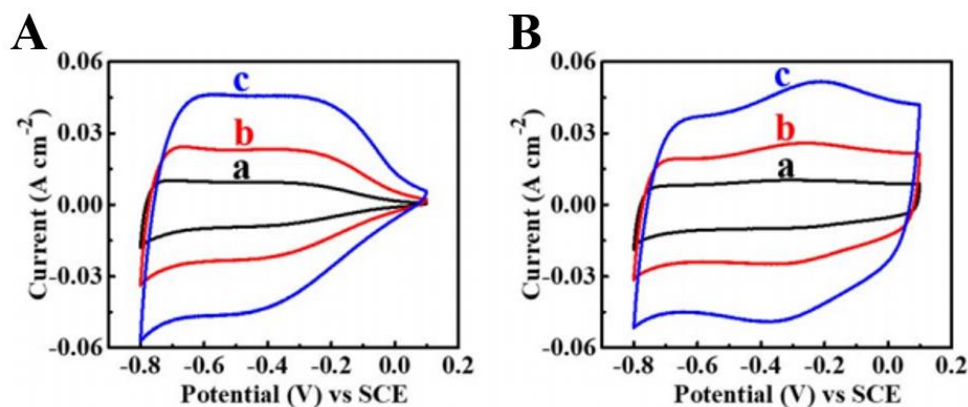


Figure 2.18: CVs for (A) pure α -FeOOH-MWCNTs and (B) α -FeOOH-PPy-MWCNTs composite electrode by Chen et al. Reprinted with permission from Journal of Electrochemical Society. [84]

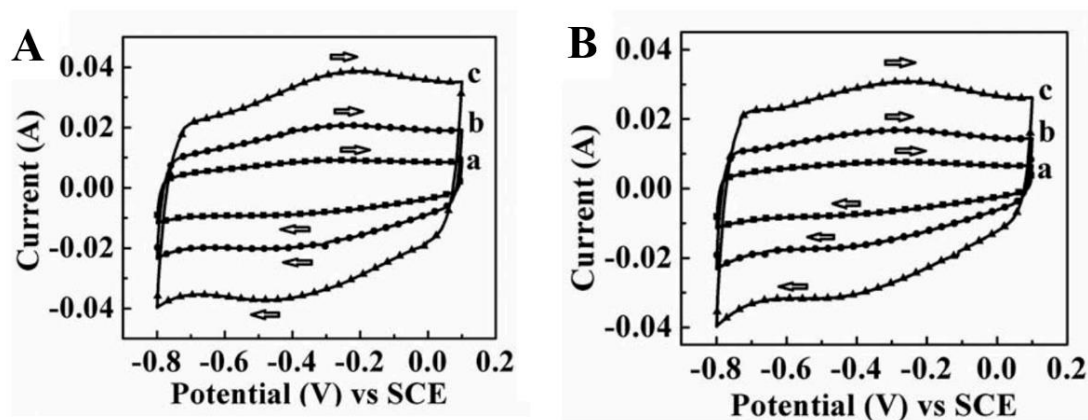
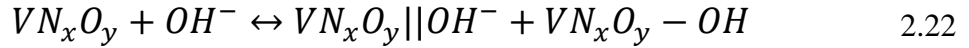


Figure 2.19: CVs of composite consist of 80% PPy-20%MWCNTs with PPy:FeOOH ratio of (A) 7:2 and (B) 7:3 by Fan et al. Reprinted with permission from Taylor & Francis. [85]

2.5.2.2 Vanadium nitride (VN)

Vanadium nitride (VN) is another promising candidate for negative electrode, with suitable voltage window, high theoretical capacitance and high electrical conductivity. However, one of the major drawbacks of VN is the poor cyclic stability in aqueous electrolytes due to irreversible oxidation during operation. Moreover, the synthesis of metal nitride is typically energy intensive, as metal nitrides are synthesized at elevated temperature by annealing in the presence of nitrogen-containing compounds such as nitrogen gas and ammonia.

Choi et al. have fabricated an VN electrode by ammonolysis of VCl_4 in anhydrous chloroform followed by heating treatment. The fabricated VN electrode was tested in 1M KOH, and exhibited high specific capacitance of 1340 F g^{-1} in a voltage window of -1.2 to 0 V vs. Hg/HgO with a mass loading of 0.25 mg cm^{-2} . [86] For VN in alkaline electrolytes, the charge storage mechanism can be expressed by Eq.2.22 [86]:



It was suggested the charge storage mechanism is a combination of both double layer capacitance and pseudocapacitance, where $VN_xO_y||OH^-$ represents OH^- adsorbed on double layer of partially oxidized VN_xO_y and $VN_xO_y - OH$ represents adsorption of OH^- by redox reactions. Choi et al. have also investigated the cyclic stability of VN electrode under different pH and voltage window, and the results are shown in Figure 2.20.

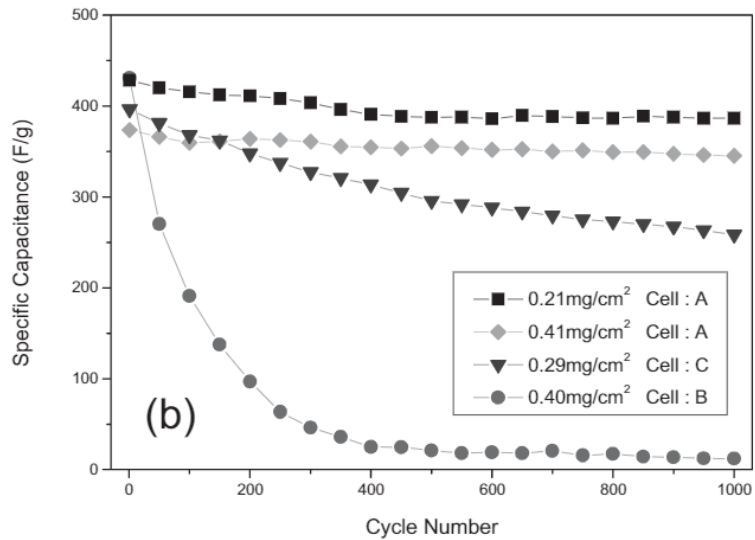


Figure 2.20: Specific capacitance vs. cycle number for VN electrodes under different conditions by Choi et al. Reprinted with permission from John Wiley and Sons. [86]

The investigation was carried out under 3 conditions, denoted cell A, B and C. In cell A, the voltage window is -0.3 to -1.2 V vs. Hg/HgO and electrolyte pH = 12; cell B has voltage window of 0 to -1.2 V vs. Hg/HgO and electrolyte pH = 14, and cell C has voltage window of -0.3 to -1.2 V and electrolyte pH = 14. From Figure 2.20, the result indicated that cyclic stability was improved for electrodes tested in cell A and C compared to cell B. The authors

have suggested an appropriate voltage window and electrolyte pH can reduce the over oxidation of VN, which reduces the dissolution of capacitive V^{5+} species and stabilize the cycling process.[86] In other study, Lu et al. have evaluated the electrochemical performance of flexible asymmetric device using VN and VO_x nanowires as negative and positive electrodes. The VN nanowire electrode has high capacitance of 298.5 F g^{-1} at a scan rate of 10 mV s^{-1} , and high capacitance retention of 71.5% at scan rate of 100 mV s^{-1} . [87] The device showed excellent cyclic stability of 95.3% after 10000 cycles, and maximum power and energy density of 0.85 W cm^{-3} and 0.61 mWh cm^{-3} at current density of 5 and 0.5 mA cm^{-2} respectively.[87] The capacitance of the device under different bending condition remained constant as shown in Figure 2.21, and indicated the potential of this device for flexible ESs.

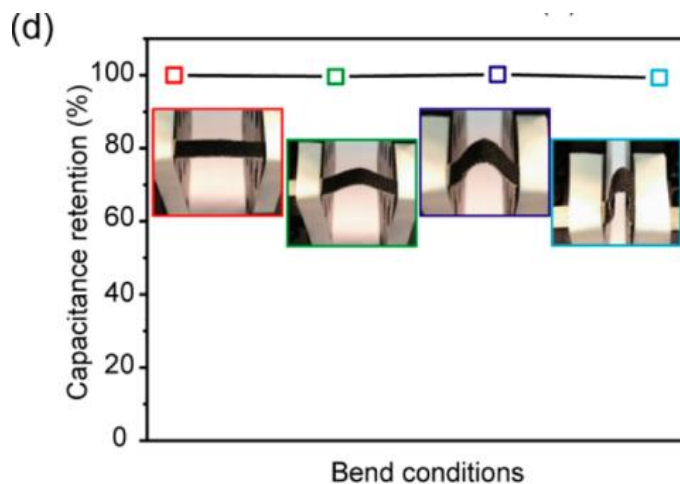


Figure 2.21: Capacitance retention of flexible asymmetric device fabricated using VN and VO_x nanowires. Reprinted with permission from American Chemical Society. [87]

2.6 Configurations and types of ES

EDLCs and pseudocapacitors can be fabricated into device of two configurations: symmetric and asymmetric devices. In both cases, the overall cell capacitance (C_{Cell}) of the device is governed by the capacitance of positive (C_{+ve}) and negative (C_{-ve}) electrode, given by Eq.2.23 as the electrodes are connected in series.

$$\frac{1}{C_{Cell}} = \frac{1}{C_{+ve}} + \frac{1}{C_{-ve}} \quad 2.23$$

The configuration of ESs device is an important consideration when fabrication devices because it affects properties such as voltage window and cyclic stability, which have directly impact on electrochemical performance of the device.

In symmetric devices, the positive and negative electrodes consist of the same active material with same charge storage mechanism. Current commercially available EDLCs are an example of symmetric device, which both electrodes consist of carbon-based materials in an organic electrolyte.[12] The symmetric EDLCs configuration allowed for high power density and long cyclic life, as the charge storage mechanism is based on double layer capacitance.[32] However, the energy density of symmetric EDLCs is low due to the small double layer capacitance. In contrast, symmetric pseudocapacitors offer higher energy density as pseudocapacitance is much larger than double layer capacitance. The pseudocapacitive contribution enhanced the energy density, but the power performance decreases and limited by ions diffusion. For symmetric devices, the cell voltage of the devices is typically bounded by 1 V in aqueous electrolyte due to decomposition of water, and the low cell voltage has hindered the electrochemical performance of the cell.[88]

As the energy and power performance of ESs have strong dependence on the cell voltage, there is a need to widen the voltage window to improve electrochemical performance. To address this problem, asymmetric devices can be fabricated to enlarge the cell voltage. In asymmetric devices, one of the electrodes consist of carbon-based materials (EDLCs type), and the other consist pseudocapacitive or lithium ion materials. The advantage of asymmetric configuration is the extended voltage window over 2 V in aqueous electrolytes due to compensatory overpotential on the positive and negative electrode, which drastically improved the power and energy density of the device given by Eq.2.3 and Eq.2.4.[88]–[90]

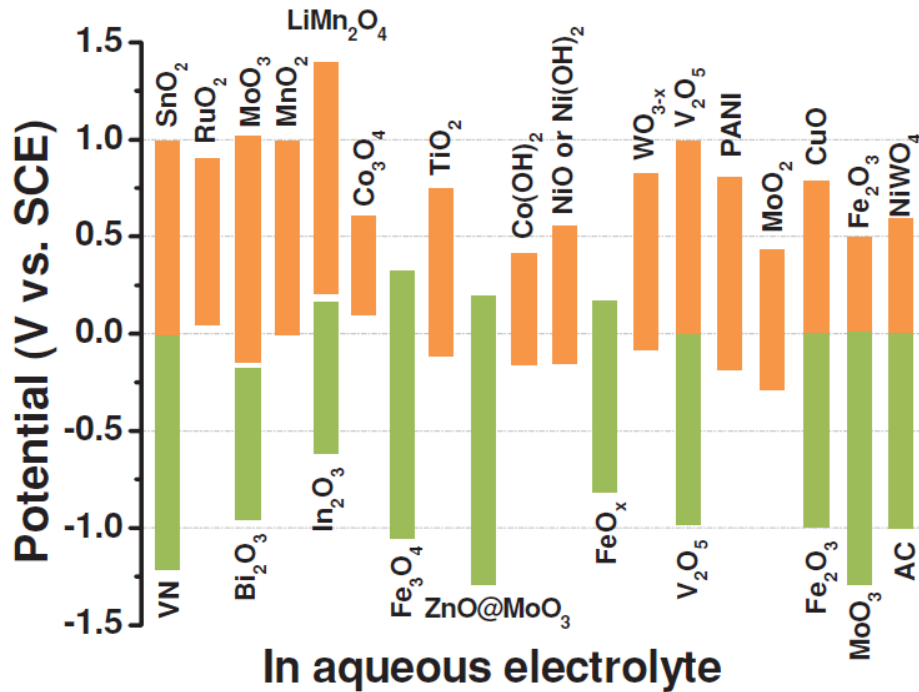


Figure 2.22: Working voltage window of different active materials in aqueous electrolytes. Reprinted with permission from John Wiley and Sons. [88]

However, one of the major problems for asymmetric device is the selection of appropriate active materials and match the capacitance on both electrodes, as different active materials

have different voltage window as shown in Figure 2.22. In the case of asymmetric device, consisting of pseudocapacitive and EDLCs electrode as positive and negative electrode respectively, the areal capacitance arise from pseudocapacitance on the positive electrode is much higher compared to the double layer capacitance on negative electrode. From Eq.2.29, it is important for both positive and negative electrode to have same capacitance to give rise to a high cell capacitance. Therefore, the EDLCs negative electrode must be larger in size than the positive electrode to give comparable areal capacitance. The mismatch of capacitance between electrodes is detrimental for practical application, as the negative electrode must be oversized and coupled with a much smaller positive electrode.[83] There has been an increasing interest in fabricated hybrid asymmetric devices using Li-ion battery-type positive electrode coupled with EDLCs type negative electrode, commonly referred as “Li-ion capacitor”. The benefit of hybrid asymmetric devices is that they have inherited high charge-discharge capability from ESs and high energy density from Li-ion batteries.[32], [38], [88] Li-ion capacitor was first investigated by Amatucci et al. in 2001, where an asymmetric hybrid ES was fabricated using AC and $\text{Li}_4\text{Ti}_5\text{O}_{12}$ (LTO) as a positive and negative electrode respectively, in a lithium tetrafluoroborate in organic acetonitrile electrolyte.[91] The hybrid asymmetric configuration has allowed an enlarged voltage window of 2.25 V compared to 1.5 V for EDLCs in the same electrolyte.[91] It was demonstrated that the cyclic stability of the hybrid asymmetric design was similar to EDLCs, but a much high stability compared conventional Li-ion battery with LiCoO_2 and graphite as electrodes.

2.7 Electrolytes of supercapacitors

The choice of electrolyte for ESs application is an important parameter, as the electrolyte has significant impact on the energy and power density, the internal resistance of the system, the capacitance and the cyclic stability as shown in Figure 2.23.

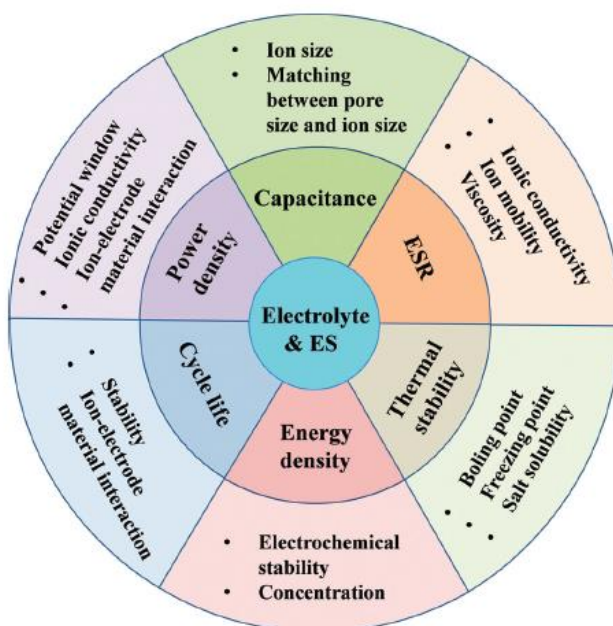


Figure 2.23: Effects of electrolytes on performance of ESs. Reprinted with permission from Royal Society of Chemistry. [92]

For an ideal electrolyte for ESs application, it should have the following characteristics: wide operating potential window, compatible with electrode materials, high ionic conductivity and low electrical resistance, high thermal and electrochemical stability, low flammability and volatility, environmentally friendly and low cost.[92] Zhong et al. are one of the few groups that have compiled a comprehensive review of electrolytes, to discuss the merits and properties of different electrolytes. They have classified electrolytes into

four categories: aqueous electrolytes, organic electrolytes, ionic liquids, and solid/quasi-solid-state electrolytes.

2.7.1 Aqueous Electrolytes

Aqueous electrolytes can be further divided into acid, alkaline and neutral electrolytes, and they exhibit advantages such as higher conductivity, low cost and easily handle compared to other electrolytes.[89], [92] However, the potential window of aqueous electrolytes is limited to 1.23V due to the decomposition of water.[89] The operating temperature of aqueous electrolytes is also limited between the boiling point and freezing point of water. Acidic electrolytes such as H_2SO_4 have been used in EDLC applications, and it has been demonstrated that the specific capacitance is higher in acidic electrolytes than organic electrolyte.[93], [94] Zhong et al. suggested that such increase in capacitance is partially due to higher ionic conductivity and lower resistance, and there is also contribution from increased surface area of carbon materials.[92] Acidic electrolytes are also employed in pseudocapacitors such as RuO_2 system mentioned earlier, as well as surface functionalized carbon materials with heteroatoms such as oxygen and nitrogen, and surface functional groups. Alkaline electrolytes such as KOH are also used for ESs applications, especially for EDLCs and metal hydroxide based pseudocapacitors. Using alkaline electrolytes for EDLCs, the capacitance and energy-power densities are similar to acidic electrolytes, as both electrolytes exhibit high ionic conductivity. The alkaline condition of electrolyte allowed transition metal oxides, hydroxide, sulfides and nitrides to be stable over an appreciable potential window and harness the high theoretical capacitance of these

pseudocapacitive materials.[77], [95], [96] Neutral electrolytes such as Na_2SO_4 have been used for EDLCs and the results were compared with acidic and alkaline electrolytes, and it was demonstrated that the capacitance of EDLCs in neutral electrolytes were lower than acidic or alkaline electrolytes due to lower ionic conductivity.[97] However, EDLCs in neutral electrolytes allowed a larger voltage window compared to acidic or alkaline electrolytes. Demarconnay et al. have fabricated symmetric AC/AC ES in 0.5M Na_2SO_4 , and they have achieved a 93% capacitance retention after 2000 cycles and almost constant up to 10000 cycles with a wide operating voltage window of 1.6 V.[90]

2.7.2 Organic Electrolytes

Organic electrolytes are currently employed in commercial ESs, since the operating voltage window of organic electrolytes are typically between 2.5 to 2.8 V.[38], [88], [92] A larger potential window allowed higher energy and power densities, as they are proportional to voltage square according to Eq.2.3 and Eq.2.4. Organic electrolytes consist of conducting salts dissolved in organic solvents, and an example of organic electrolyte is tetraethylammonium tetrafluoroborate (TEABF_4) dissolved in acetonitrile or propylene carbonate.[92] Despite the high energy and power densities obtained by using organic electrolytes, they suffer from disadvantages such as high cost, low capacitance, low conductivity, flammable and toxic.[38], [88], [92] Another major drawback of organic electrolytes is the need of complicated purification processes and controlled-environment, as organic electrolytes are susceptible contaminations such as moisture and impurities which can lead to performance degradation and self-discharge issues.[88]

2.7.3 Ionic Liquids

Ionic liquids (ILs), also known as low temperature molten salts, typically consist of large cations and organic or inorganic anions. ILs have gained significant interest recently, due to their high stability, low volatility and can be non-flammable.[38], [88], [92] Their properties such as voltage window, working temperature range and conductivity can be altered by using different combinations of cations and anions, and such versatile properties allow ILs to be tailored for different electrode materials. ILs can be categorized into three types based on their composition, and they are aprotic, protic and zwitterionic.[92] For ESs application, aprotic ILs are commonly used, and the cations are typically imidazolium, pyrrolidinium and ammonium, whereas common anions are tetrafluoroborate, hexafluorophosphate and dicyanamide. [92] Obviously, different cations and anions would influence the properties of ILs. It has been shown that imidazolium cations give higher ionic conductivity, and pyrrolidinium cations give wider voltage window.[92] ILs-based ES can have voltage window above 3 V, and their low volatility and flammability make them favorable for high temperature applications compared to organic electrolytes. Unfortunately, ILs have disadvantages such as high viscosity, low ionic conductivity compared to other electrolytes and high cost have limited their applications.[38], [88], [92]

2.7.4 Solid /Quasi-Solid-State Electrolytes

The development of flexible ESs have driven the demand of solid or quasi-solid-state electrolytes, as liquid electrolytes are prone to leakage and consequences are severe, especially for acidic or alkaline electrolytes.[92], [98] Solid-state electrolytes (SSEs)

typically consist of a polymeric matrix with salts within, and quasi-solid or gel polymer electrolytes (GPEs) have aqueous electrolytes within.[92] Due to the presence of solvents in GPEs, their ionic conductivities are the highest among all solid/quasi-solid-state electrolytes. However, the mechanical strength of GPEs are lower compared to SSEs. The disadvantages of SSEs are the limited contact surface area with electrode area, which leads to increase resistance and reduced rate performance.[92], [98] Overall, the ideal characteristics for solid/quasi-solid-state electrolytes are high ionic conductivity, high electrochemical and thermal stability, and high mechanical strength. [92]

2.8 Dispersion of metal oxides and carbon nanotubes for composite fabrication

Earlier in the chapter, it was mentioned that high active surface area is an important factor to achieve high capacitance for metal oxide electrodes. However, in colloidal fabrication of metal oxides nanoparticles, agglomeration of particles becomes one of the major challenges to utilize all surface area. The driving force of agglomeration is minimization of surface energy of particles to be thermodynamically stable.[99] The drying procedure also promotes agglomeration, as the condensation reactions between surface hydroxyl groups on the particles occur.[100], [101] To understand strategies for dispersion of nanoparticles, the relationship between particles and particles-solution interactions should be revisited, by reviewing the development of surface charge and the overall energy balance of the system in Derjaguin-Landau-Verwey-Overbeek (DLVO) theory.

When a solid particle emerges in solution, a surface charge will develop by either adsorption and desorption of ions, or dissociation and substitution of surface charged species.[102] Once the surface charge is developed, electrostatic repulsion will segregate positively and negatively charged species within the vicinity, and at the same time there are also Brownian motion and entropic force to homogenize the species in solution.[102] In aqueous solutions, the surface of oxide particles tends to coordinate with water molecules, and the protons and hydroxyl groups are typically charge determining ions. Depending on the pH of electrolyte, the surface of particles can be positively or negatively charged by adsorption of charge determining ions given by Eq.2.24 and 2.25, and the general surface charge vs. pH plot is shown in Figure 2.24.[103]

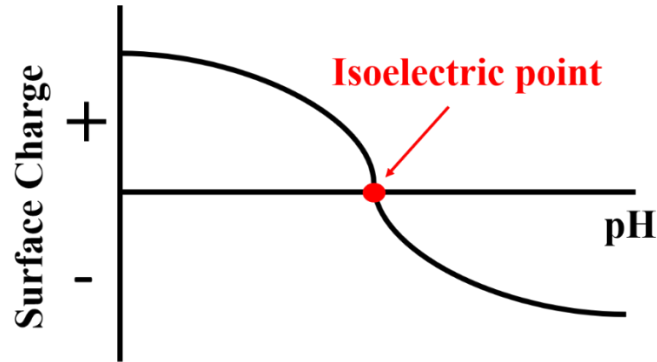
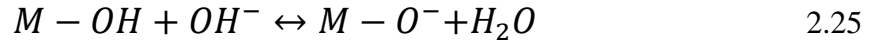
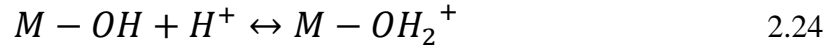


Figure 2.24: Schematic of surface charge of particles as a function of pH.

In Figure 2.24, there exists an isoelectric point (IEP), where the concentration of charge determining ions correspond to a charge neutral surface, and the IEP is different for various materials.[102] At pH below IEP, the reaction in Eq.2.24 dominates and yields positively charged surface, and the surface is negatively charged when pH is above IEP. The surface charge developed by immersing particles in solutions can stabilize the suspension to a certain extent, and it is commonly referred to electrostatic stabilization. However, other than the repulsion between particles, there is also van der Waals attractions between two particles.

To account for attractions between particles, the DLVO theory was developed to understand the relationship between particles in solutions, and the interaction is a combination of electrostatic repulsion and van der Waals attraction.[102], [103] For two identical charged particles, the total potential can be express by Eq.2.26,

$$\Phi_T = \Phi_A + \Phi_R \quad 2.26$$

where Φ_A is the van der Waals attraction potential and Φ_R is the electrostatic repulsion potential. Eq.2.27 is the expression of van da Waals attraction between two particles, where A is the Hamaker constant, r is the radius of spherical particles and S is the separation distance. The equation can be simplified if $S/r \ll 1$ and reduced to Eq.2.28.

$$\Phi_A = -\frac{A}{6} \left\{ \frac{2r^2}{S^2+4rS} + \frac{2r^2}{S^2+4rS+4r^2} + \ln \left(\frac{S^2+4rS}{S^2+4rS+4r^2} \right) \right\} \quad 2.27$$

$$\Phi_A = \frac{-Ar}{12S} \quad 2.28$$

For the electrostatic repulsion potential, the expression is given in Eq.2.29 where ϵ_r is the dielectric constant of solvent, ϵ_0 is the permittivity of vacuum, E is the surface charge density, $\frac{1}{\kappa}$ is the Debye-Huckel screening strength or double layer thickness.

$$\Phi_R = 2\pi\epsilon_r\epsilon_0rE^2\exp(-\kappa S) \quad 2.29$$

The expression for κ is shown is Eq.2.30, where F is the Faraday's constant, C_i and Z_i are the concentration and valence of counter ions of type i, R_g is the gas constant and T is the absolute temperature in Kelvin.

$$\kappa = \left\{ \frac{F^2 \sum_i C_i Z_i^2}{\epsilon \epsilon_0 R_g T} \right\}^{\frac{1}{2}} \quad 2.30$$

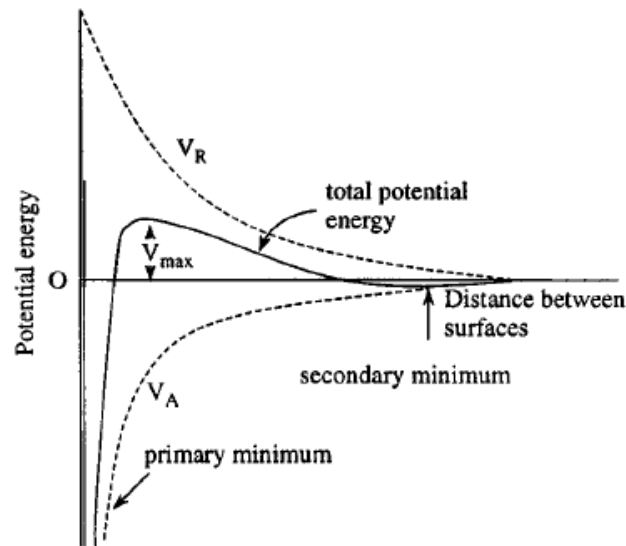


Figure 2.25: Schematic of total potential energy vs. separation distance with contributions from van der Waals attraction and electrostatic repulsion.[102]

By summing the van der Waals and electrostatic repulsion potential energy, a total potential energy vs. separation can be plotted similar to Figure 2.25.

When the distance between surfaces is large, the attraction and repulsion energy reduce to zero, and when the distance is short there is a minimum of potential energy produced by the van der Waals attraction. The maximum potential energy is achieved when a critical separation distance is reached, where contribution from electrostatic repulsion become dominate. This maximum is also known as a repulsive barrier, and if the maximum is greater than $\sim 10kT$ particles agglomeration will not occur.[102] However, if the energy barrier is less than $10kT$, the Brownian motion will overcome the barrier and agglomeration of particles occur. The electrolyte concentration also plays an important role in determining

the electrical double layer thickness, as κ is dependent on concentration and valence of counter ions demonstrated in Eq.2.30.

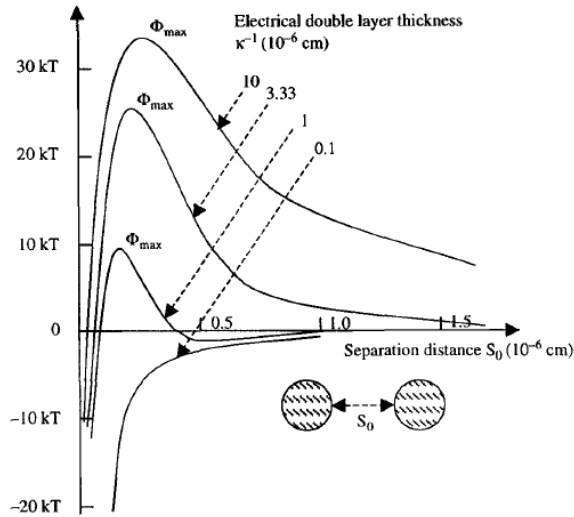


Figure 2.26: Total potential energy vs. separation distance of two spherical particles of different κ^{-1} values.[102]

Figure 2.26 is a plot of total potential energy vs. separation distance for different double layer thickness arise from different electrolyte concentrations. As the electrolyte concentration increases, the double layer thickness decreases, and the maximum potential energy is reduced. Therefore, high concentration and valence of counter ions can promote agglomeration of particles.

In many cases, pure electrostatic repulsion is insufficient to provide good stabilization of colloids. Therefore, other stabilization techniques such as steric stabilization is employed. Steric stabilization typically uses polymers to act as a diffusion barrier for growth species, which can narrow the size distribution of particles as well as dispersion of colloids. There are three types of polymers based on there interactions with particles, anchored polymers,

adsorbing polymers and nonadsorbing polymers.[102] Anchored polymers are polymers that interact with particles irreversibly by one end only; adsorbing polymers adsorb weakly on particles surface at random points of the polymers, and nonadsorbing polymers do not interact with particles surface and do not provide any steric stabilization.[102] Anchored polymers are superior than adsorbing polymers, as adsorbing polymers can adsorb and bridge to other particles. Therefore, strong interactions with particles surface are an ideal property for dispersant of particles.

It has been demonstrated by Wang et al. organic molecules with catechol group can provide strong adsorption to metal oxides particles for electrophoretic deposition (EPD).[104] The investigation involved analysis of carboxylic acids of with different position and amount of hydroxyl groups on the aromatic ring. The acids that were investigated were caffeic acid (CA), *trans*-cinnamic acid (TCA), *p*-coumaric acid (PCA), and 2,4-dihydroxycinnamic acid (DCA), and their chemical structure is shown in Figure 2.27.

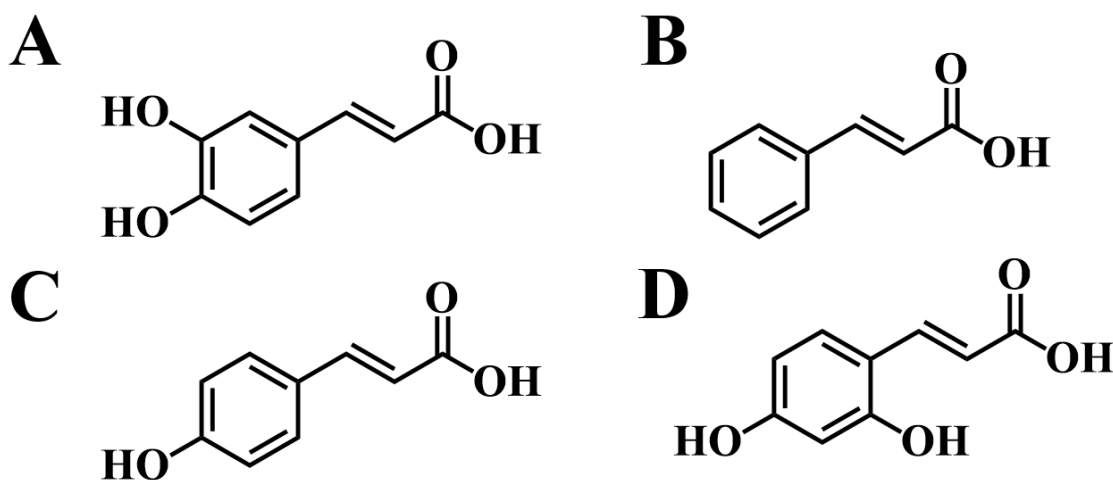


Figure 2.27: Chemical structure of (A) CA, (B) TCA, (C) PCA and (D) DCA.

Among all acids investigated, CA was only acid allowed successful deposition of MnO_2 particles using EPD, while other acids led to decrease in deposition yield.[104] CA belongs to the catechol family, which contains aromatic ring with two adjacent hydroxyl groups. Similar molecules can be found in protein macromolecules of mussels, containing catecholic amino acid L-3,4-dihydroxyphenylalanine (DOPA), adsorbing strongly to different substrates under wet conditions.[105]

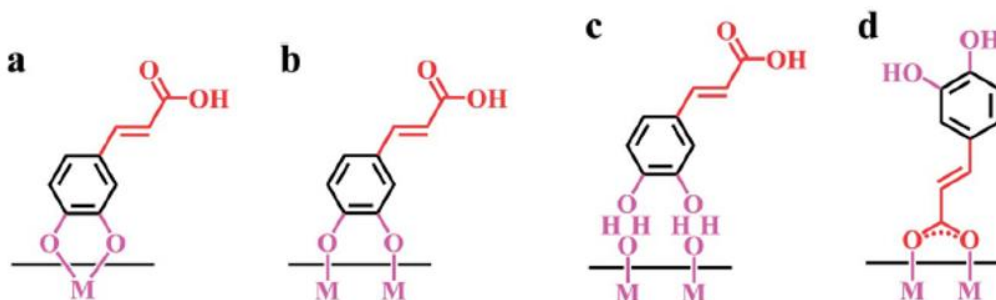


Figure 2.28: Adsorption mechanism of CA suggested by Ata et al., which involved (a) bidentate chelating bonding, (b) inner sphere bidentate bridging bonding, (c) outer sphere bidentate bridging bonding and (d) adsorption by carboxylic group. Reprinted with permission from RSC Publishing. [106]

Ata et al. have suggested a mechanism to describe superior adhesion of CA to metal oxide surface. The strong adsorption to metal oxide particles was attributed to strong chelating and bridging mechanisms, shown in Figure 2.28, to oxide particles surface by adjacent hydroxyl and carboxylic groups.[106] Therefore, the presence of adjacent hydroxyl groups is crucial to strong bonding with metal oxide surface, and for this reason TCA, PCA and DCA were unable to provide strong adhesion.[104], [106]

As mentioned before, CNTs exhibit remarkable properties such as high conductivity and low percolation threshold and used in many applications.[36], [37] However, CNTs tend to form bundle due to high number of van der Waals attractions, and show poor solubility in aqueous and organic solvents.[107]

Dispersion of CNTs is crucial to utilize and retain the excel properties of CNTs. There are many ways to disperse CNTs, and typically involve covalent and non-covalent surface modification.[107] Covalent surface modifications involve surface functionalization of CNTs surface by acid oxidation. Aviles et al. have performed acid oxidation for CNTs using different oxidants and concentrations, such as H_2SO_4 , HNO_3 and H_2O_2 . [108] They have demonstrated that HNO_3 and H_2O_2 were able to oxidize the CNTs surface by introducing oxygen-containing functional groups on the surface. The presence of functional groups led to a reduction of van der Waals attractions between CNTs, and allowed for separation and dispersion of CNTs. However, acid oxidation can reduce CNTs length and damage the surface continuity, which in turn degrade the mechanical and electrical performance of CNTs.[108]

Another approach to disperse CNTs is by non-covalent surface modifications, which avoid the performance degradation caused by surface functionalization. Non-covalent surface modifications typically involve the use of polymers and head-tail surfactants as dispersing agents and to provide stabilization.[107] The driving force of adsorption is the hydrophobic interactions of CNTs surfaces with long hydrocarbons chain in polymers and head-tail surfactants, and the hydrophilic groups give rise to dispersion. However, it is difficult to avoid polymer wrapping of CNTs dispersed using polymers, resulted in insulating

polymeric layer on CNTs.[109] Moreover, it was demonstrated by Vigolo et al. large quantity of head-tail surfactants is required to achieve dispersion using sodium dodecyl sulfate (SDS) as a model head-tail surfactant.[110]

Figure 2.29 is a plot of wt% of SDS vs. wt% of CNTs, where in region C (filled dots) are successful dispersion of CNTs. In region B (downward arrows), the amount of SDS is insufficient to disperse all CNTs and bundles remained after sonication, and in region D (upward arrows) the high concentration of SDS resulted in micelles formation which promoted aggregation of CNTs. Therefore, there is a need for efficient dispersants for CNTs, which do not compromise the structure integrity and properties of CNTs.

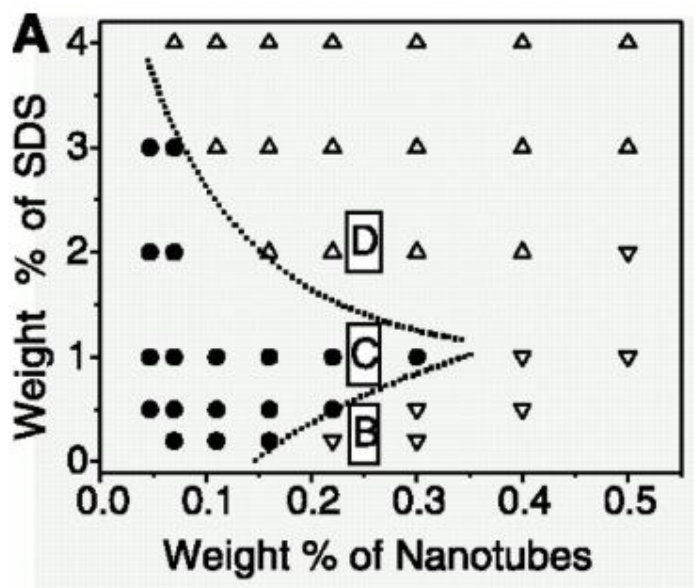


Figure 2.29: Weight % of SDS vs. weight % of CNTs adapted from Vigolo et al. Reprinted with permission from The American Association for the Advancement of Science. [110]

Recently, other types of dispersants are being exploited, specifically from the organic dyes and bile acid families. Bile acid salts (BAS) and organic dyes are small molecules with

different functional groups, and they can penetrate the CNTs bundles from both ends upon sonication and disperse CNTs through an “unzipping” mechanism.[111], [112] Bile acid and their salts are strong anionic biosurfactants, which are capable of solubilizing fatty acids and cholesterol.[113], [114] The high solubility of bile acid salts in aqueous solution have generated significant interest as CNTs dispersant for many applications.

Some chemical structures of BAS are shown in Figure 2.30, and they have a steroid backbone, consists of three six-member and a five-member aromatic rings. BAS have hydrophobic convex and hydrophilic concave surface, and such unique structure allowed strong adsorption of hydrophobic convex surface of BAS to side walls of CNTs and facilitated dispersion.[113] The steroid structure also allowed BAS to wrap around CNTs surface with the hydrophobic surface inward, and it has been confirmed the coverage of BAS on CNTs surface is higher than conventional head-tail surfactants.[115]

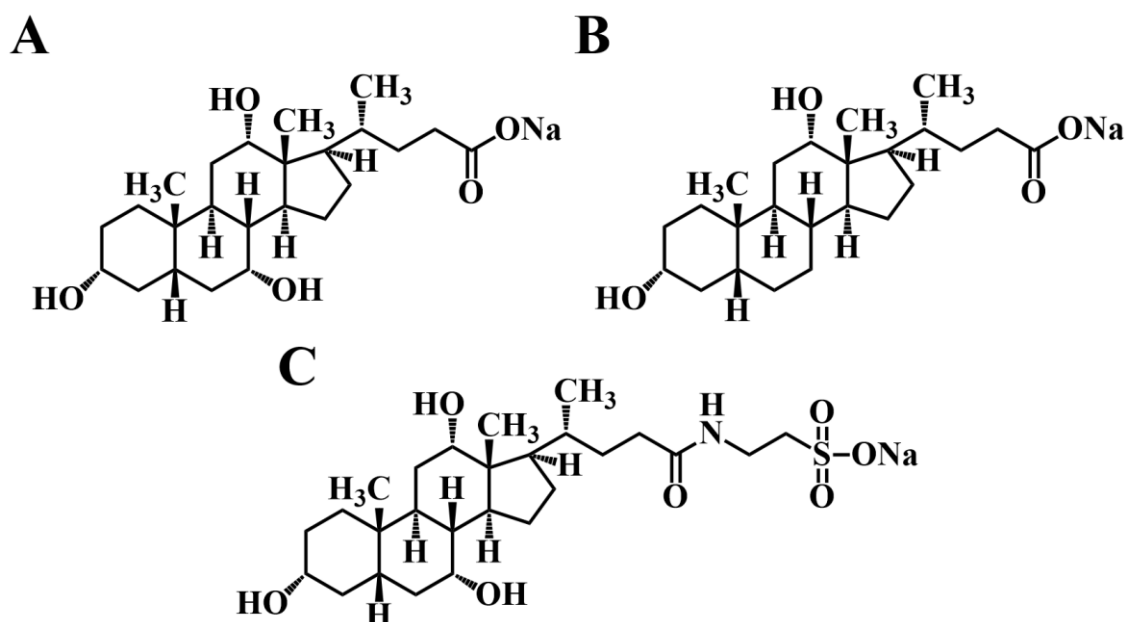


Figure 2.30: Chemical structures of some BAS, including (A) cholic acid sodium salts (CAS), (B) deoxycholic acid sodium salts (DCAS) and (C) taurocholic acid sodium salts (TCAS).

CAS, DCAS and TCAS were used as dispersing agent for fabrication of MnO_2 and PPy-MWCNTs composite electrodes, and the electrodes showed enhanced capacitive behaviour.[116], [117]

Organic dyes with aromatic rings are known to interact with the sidewalls of CNT by π - π interactions, and it was demonstrated such interaction has insignificant impact on properties of CNTs .[118], [119] The adsorption of organic dyes on CNT can be improved by increasing the number of aromatic rings and hydroxyl groups to enhance π - π interactions .[120]. Other factors such as concentration, pH and temperature are also important for good adsorption. The π - π interactions between organic dyes and CNT resulted in surface modifications, and cationic or anionic dyes can achieve dispersion via electrostatic

repulsion, without sacrificing the superior properties of CNT unlike covalent surface modifications. Various dyes such as triarylmethane, azo, perylene and anthraquinone dyes have shown excellent adsorption on CNTs and facilitated CNTs dispersion for many applications.[121] Using charged organic dyes for CNT dispersion, Mn_3O_4 -MWCNTs composite electrodes was fabricated by an electrostatic heterocoagulation technique by Ata et al.. The electrostatic heterocoagulation technique used cationic dyes ethyl violet (EV) and pyronin Y (PY) as MWCNTs dispersants, while Mn_3O_4 nanoparticles were dispersed by catechol-containing anionic polymer poly(4-styrenesulfonic acid-co-maleic acid) sodium salts (P(SSA-MA)).[122] The fabricated electrodes showed excellent electrochemical performance, which can be attributed to superior dispersion of organic dyes and improved mixing between Mn_3O_4 and MWCNTs. The electrode fabricated with PY showed higher capacitance of 2.8 F cm^{-2} , and the electrode fabricated with EV showed better capacitance retention of 88% for scan rate range 2-100 mV s^{-1} . [122] In another study, Chen et al. have fabricated PPy-coated MWCNTs composite electrodes using anionic dyes as dopants and dispersants, and investigated the effect of anionic dyes with different charge to mass ratios. The anionic dyes of interest were sodium benzene-1,3-disulfonate(BDS), 1,3,(6,7)-naphthalenetrisulfonic acid (NTS), potassium indigotrisulfonate (ITR) and potassium indigotetrasulfonate (ITT), and their structures are shown in Figure 2.31.

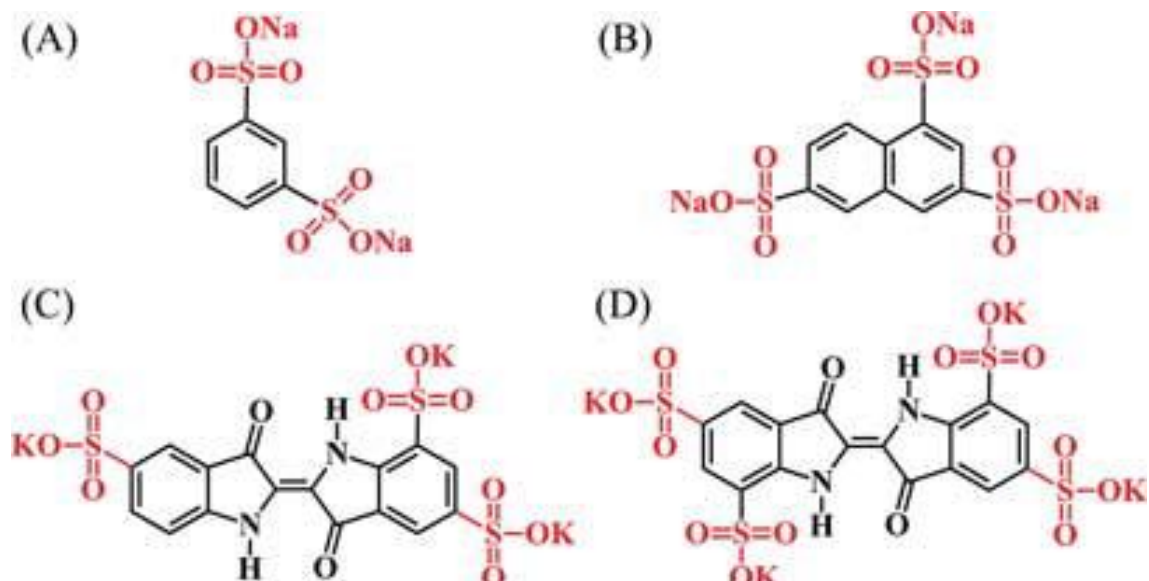


Figure 2.31: Chemical structure of (A) BDS, (B) NTS, (C) ITR and (D) ITT. Reprinted with permission from Taylor & Francis. [123]

It was demonstrated that anionic dyes with higher charge to mass ratio such as ITR and ITT can reduce particle size of PPy, as larger molecules with higher charge can provide stronger repulsion to inhibit growth of particles.[123] Furthermore, PPy-MWCNTs composite fabricated using BDS and NTS consisted of agglomerated PPy and MWCNTs, whereas composite fabricated using ITR and ITT resulted in unique PPy-coated MWCNTs. Authors suggested the coating mechanism involved ITR and ITT adsorption on MWCNTs, followed by polymerization of pyrrole on the MWCNTs surface.[123] Among all dopants, composite electrode fabricated using ITT resulted in the best performance. The electrode exhibited a high areal capacitance of 3.99 and 2.67 F cm⁻² at scan rate of 2 and 100 mV s⁻¹ respectively, and exceptional cyclic stability of 98.7% over 1000 cycles.[123]

2.9 References

- [1] G. Wang, L. Zhang, and J. Zhang, "A review of electrode materials for electrochemical supercapacitors," *Chem Soc Rev*, vol. 41, no. 2, pp. 797–828, 2012.
- [2] W. Wei, X. Cui, W. Chen, and D. G. Ivey, "Manganese oxide-based materials as electrochemical supercapacitor electrodes," *Chem Soc Rev*, vol. 40, no. 3, pp. 1697–1721, 2011.
- [3] N. Omar, J. Van Mierlo, F. Van Mulders, and P. Van den Bossche, "Assessment of Behaviour of Super Capacitor-battery System in Heavy Hybrid Lift Truck Vehicles," *J. Asian Electr. Veh.*, vol. 7, no. 2, pp. 1277–1282, 2009.
- [4] N. Omar *et al.*, "Assessment of lithium-ion capacitor for using in battery electric vehicle and hybrid electric vehicle applications," *Electrochimica Acta*, vol. 86, pp. 305–315, Dec. 2012.
- [5] S. Lu, K. A. Corzine, and M. Ferdowsi, "A New Battery/Ultracapacitor Energy Storage System Design and Its Motor Drive Integration for Hybrid Electric Vehicles," *IEEE Trans. Veh. Technol.*, vol. 56, no. 4, pp. 1516–1523, Jul. 2007.
- [6] I.-H. Kim and K.-B. Kim, "Ruthenium Oxide Thin Film Electrodes for Supercapacitors," *Electrochem. Solid-State Lett.*, vol. 4, no. 5, p. A62, 2001.
- [7] H. Y. Lee and J. B. Goodenough, "Supercapacitor Behavior with KCl Electrolyte," *J. Solid State Chem.*, vol. 144, no. 1, pp. 220–223, Apr. 1999.
- [8] M. Huang, F. Li, F. Dong, Y. X. Zhang, and L. L. Zhang, "MnO₂-based nanostructures for high-performance supercapacitors," *J. Mater. Chem. A*, vol. 3, no. 43, pp. 21380–21423, 2015.
- [9] C.-L. Tang *et al.*, "Cobalt-Doped MnO₂ Hierarchical Yolk–Shell Spheres with Improved Supercapacitive Performance," *J. Phys. Chem. C*, vol. 119, no. 16, pp. 8465–8471, Apr. 2015.
- [10] A. M. Hashem, H. M. Abuzeid, N. Narayanan, H. Ehrenberg, and C. M. Julien, "Synthesis, structure, magnetic, electrical and electrochemical properties of Al, Cu and Mg doped MnO₂," *Mater. Chem. Phys.*, vol. 130, no. 1–2, pp. 33–38, Oct. 2011.
- [11] W. D. Callister, *Materials Science and Engineering: An Introduction*, 8th ed. John Wiley & Sons Inc.
- [12] P. Sharma and T. S. Bhatti, "A review on electrochemical double-layer capacitors," *Energy Convers. Manag.*, vol. 51, no. 12, pp. 2901–2912, Dec. 2010.
- [13] B. E. Conway, *Electrochemical Supercapacitors: Scientific Fundamentals and Technological Applications*. Boston, MA: Springer US, 1999.
- [14] H. Zhang, W. Zhang, J. Cheng, G. Cao, and Y. Yang, "Acetylene black agglomeration in activated carbon based electrochemical double layer capacitor electrodes," *Solid State Ion.*, vol. 179, no. 33–34, pp. 1946–1950, Oct. 2008.
- [15] B. E. Conway, V. Birss, and J. Wojtowicz, "The role and utilization of pseudocapacitance for energy storage by supercapacitors," *J. Power Sources*, vol. 66, no. 1–2, pp. 1–14, May 1997.

- [16] H. Nakagawa, A. Shudo, and K. Miura, “High-Capacity Electric Double-Layer Capacitor with High-Density-Activated Carbon Fiber Electrodes,” *J. Electrochem. Soc.*, vol. 147, no. 1, p. 38, 2000.
- [17] H. Tamai, M. Kunihiro, M. Morita, and H. Yasuda, “Mesoporous activated carbon as electrode for electric double layer capacitor,” *J. Mater. Sci.*, vol. 40, no. 14, pp. 3703–3707, Jul. 2005.
- [18] V. V. N. Obreja, “On the performance of supercapacitors with electrodes based on carbon nanotubes and carbon activated material—A review,” *Phys. E Low-Dimens. Syst. Nanostructures*, vol. 40, no. 7, pp. 2596–2605, May 2008.
- [19] B. E. Conway, “Transition from ‘Supercapacitor to Battery’ Behavior in Electrochemical Energy Storage,” p. 9.
- [20] V. Augustyn, P. Simon, and B. Dunn, “Pseudocapacitive oxide materials for high-rate electrochemical energy storage,” *Energy Environ. Sci.*, vol. 7, no. 5, p. 1597, 2014.
- [21] M. Toupin, T. Brousse, and D. Bélanger, “Charge Storage Mechanism of MnO₂ Electrode Used in Aqueous Electrochemical Capacitor,” *Chem. Mater.*, vol. 16, no. 16, pp. 3184–3190, Aug. 2004.
- [22] A. G. Pandolfo and A. F. Hollenkamp, “Carbon properties and their role in supercapacitors,” *J. Power Sources*, vol. 157, no. 1, pp. 11–27, Jun. 2006.
- [23] L. Borchardt, M. Oschatz, and S. Kaskel, “Tailoring porosity in carbon materials for supercapacitor applications,” *Mater Horiz*, vol. 1, no. 2, pp. 157–168, 2014.
- [24] P. Simon and A. Burke, “Nanostructured Carbons: Double-Layer Capacitance and More,” *Electrochem. Soc. Interface*, p. 6, 2008.
- [25] L. L. Zhang and X. S. Zhao, “Carbon-based materials as supercapacitor electrodes,” *Chem. Soc. Rev.*, vol. 38, no. 9, p. 2520, 2009.
- [26] T. Chen and L. Dai, “Carbon nanomaterials for high-performance supercapacitors,” *Mater. Today*, vol. 16, no. 7–8, pp. 272–280, Jul. 2013.
- [27] Y. Wang *et al.*, “Supercapacitor Devices Based on Graphene Materials,” *J. Phys. Chem. C*, vol. 113, no. 30, pp. 13103–13107, Jul. 2009.
- [28] S. Bose, T. Kuila, A. K. Mishra, R. Rajasekar, N. H. Kim, and J. H. Lee, “Carbon-based nanostructured materials and their composites as supercapacitor electrodes,” *J Mater Chem*, vol. 22, no. 3, pp. 767–784, 2012.
- [29] Y. Shao *et al.*, “Graphene-based materials for flexible supercapacitors,” *Chem. Soc. Rev.*, vol. 44, no. 11, pp. 3639–3665, 2015.
- [30] W. K. Chee, H. N. Lim, Z. Zainal, N. M. Huang, I. Harrison, and Y. Andou, “Flexible Graphene-Based Supercapacitors: A Review,” *J. Phys. Chem. C*, vol. 120, no. 8, pp. 4153–4172, Mar. 2016.
- [31] H. Pan, J. Li, and Y. P. Feng, “Carbon Nanotubes for Supercapacitor,” *Nanoscale Res. Lett.*, vol. 5, no. 3, pp. 654–668, Mar. 2010.
- [32] Z. S. Iro, “A Brief Review on Electrode Materials for Supercapacitor,” *Int. J. Electrochem. Sci.*, pp. 10628–10643, Dec. 2016.
- [33] P. R. Bandaru, “Electrical Properties and Applications of Carbon Nanotube Structures,” *J. Nanosci. Nanotechnol.*, vol. 7, no. 4, pp. 1239–1267, Apr. 2007.

- [34] C. Niu, E. K. Sichel, R. Hoch, D. Moy, and H. Tennent, "High power electrochemical capacitors based on carbon nanotube electrodes," *Appl. Phys. Lett.*, vol. 70, no. 11, pp. 1480–1482, Mar. 1997.
- [35] K. H. An *et al.*, "Supercapacitors Using Single-Walled Carbon Nanotube Electrodes," *Adv. Mater.*, vol. 13, no. 7, pp. 497–500, Apr. 2001.
- [36] J. K. W. Sandler, J. E. Kirk, I. A. Kinloch, M. S. P. Shaffer, and A. H. Windle, "Ultra-low electrical percolation threshold in carbon-nanotube-epoxy composites," *Polymer*, vol. 44, no. 19, pp. 5893–5899, Sep. 2003.
- [37] A. Battisti, A. A. Skordos, and I. K. Partridge, "Percolation threshold of carbon nanotubes filled unsaturated polyesters," *Compos. Sci. Technol.*, vol. 70, no. 4, pp. 633–637, Apr. 2010.
- [38] M. Y. Ho, P. S. Khiew, D. Isa, T. K. Tan, W. S. Chiu, and C. H. Chia, "A review of metal oxide composite electrode materials for electrochemical capacitors," *Nano*, vol. 09, no. 06, p. 1430002, Aug. 2014.
- [39] S. Trasatti and G. Buzzanca, "Ruthenium dioxide: A new interesting electrode material. Solid state structure and electrochemical behaviour," *J. Electroanal. Chem. Interfacial Electrochem.*, vol. 29, no. 2, pp. A1–A5, Feb. 1971.
- [40] C. D. Lokhande, D. P. Dubal, and O.-S. Joo, "Metal oxide thin film based supercapacitors," *Curr. Appl. Phys.*, vol. 11, no. 3, pp. 255–270, May 2011.
- [41] W. Sugimoto, H. Iwata, K. Yokoshima, Y. Murakami, and Y. Takasu, "Proton and Electron Conductivity in Hydrous Ruthenium Oxides Evaluated by Electrochemical Impedance Spectroscopy: The Origin of Large Capacitance," *J. Phys. Chem. B*, vol. 109, no. 15, pp. 7330–7338, Apr. 2005.
- [42] F. Shi, L. Li, X. Wang, C. Gu, and J. Tu, "Metal oxide/hydroxide-based materials for supercapacitors," *RSC Adv*, vol. 4, no. 79, pp. 41910–41921, Aug. 2014.
- [43] C.-C. Hu, Y.-L. Yang, and T.-C. Lee, "Microwave-Assisted Hydrothermal Synthesis of RuO₂·xH₂O–TiO₂ Nanocomposites for High Power Supercapacitors," *Electrochem. Solid-State Lett.*, vol. 13, no. 12, p. A173, 2010.
- [44] T.-F. Hsieh, C.-C. Chuang, W.-J. Chen, J.-H. Huang, W.-T. Chen, and C.-M. Shu, "Hydrous ruthenium dioxide/multi-walled carbon-nanotube/titanium electrodes for supercapacitors," *Carbon*, vol. 50, no. 5, pp. 1740–1747, Apr. 2012.
- [45] S. Devaraj and N. Munichandraiah, "Effect of Crystallographic Structure of MnO₂ on Its Electrochemical Capacitance Properties," *J. Phys. Chem. C*, vol. 112, no. 11, pp. 4406–4417, Mar. 2008.
- [46] T. Brousse, M. Toupin, R. Dugas, L. Athouël, O. Crosnier, and D. Bélanger, "Crystalline MnO₂ as Possible Alternatives to Amorphous Compounds in Electrochemical Supercapacitors," *J. Electrochem. Soc.*, vol. 153, no. 12, p. A2171, 2006.
- [47] O. Ghodbane, J.-L. Pascal, and F. Favier, "Microstructural Effects on Charge-Storage Properties in MnO₂-Based Electrochemical Supercapacitors," *ACS Appl. Mater. Interfaces*, vol. 1, no. 5, pp. 1130–1139, May 2009.

- [48] P. Yang *et al.*, “Low-Cost High-Performance Solid-State Asymmetric Supercapacitors Based on MnO₂ Nanowires and Fe₂O₃ Nanotubes,” *Nano Lett.*, vol. 14, no. 2, pp. 731–736, Feb. 2014.
- [49] X. Chen, X. Li, Y. Jiang, C. Shi, and X. Li, “Rational synthesis of α -MnO₂ and γ -Mn₂O₃ nanowires with the electrochemical characterization of α -MnO₂ nanowires for supercapacitor,” *Solid State Commun.*, vol. 136, no. 2, pp. 94–96, Oct. 2005.
- [50] Q. Qu *et al.*, “Electrochemical Performance of MnO₂ Nanorods in Neutral Aqueous Electrolytes as a Cathode for Asymmetric Supercapacitors,” *J. Phys. Chem. C*, vol. 113, no. 31, pp. 14020–14027, Aug. 2009.
- [51] M. Xu, L. Kong, W. Zhou, and H. Li, “Hydrothermal Synthesis and Pseudocapacitance Properties of α -MnO₂ Hollow Spheres and Hollow Urchins,” *J. Phys. Chem. C*, vol. 111, no. 51, pp. 19141–19147, Dec. 2007.
- [52] N. R. Chodankar, D. P. Dubal, G. S. Gund, and C. D. Lokhande, “Flexible all-solid-state MnO₂ thin films based symmetric supercapacitors,” *Electrochimica Acta*, vol. 165, pp. 338–347, May 2015.
- [53] J. Li, Q. M. Yang, and I. Zhitomirsky, “Nickel foam-based manganese dioxide–carbon nanotube composite electrodes for electrochemical supercapacitors,” *J. Power Sources*, vol. 185, no. 2, pp. 1569–1574, Dec. 2008.
- [54] B. Saravanakumar, K. K. Purushothaman, and G. Muralidharan, “Interconnected V₂O₅ Nanoporous Network for High-Performance Supercapacitors,” *ACS Appl. Mater. Interfaces*, vol. 4, no. 9, pp. 4484–4490, Sep. 2012.
- [55] M. S. Whittingham, “The Role of Ternary Phases in Cathode Reactions,” *J. Electrochem. Soc.*, vol. 123, no. 3, p. 315, 1976.
- [56] H. Y. Lee and J. B. Goodenough, “Ideal Supercapacitor Behavior of Amorphous V₂O₅·nH₂O in Potassium Chloride (KCl) Aqueous Solution,” *J. Solid State Chem.*, vol. 148, no. 1, pp. 81–84, Nov. 1999.
- [57] J. Yang, T. Lan, J. Liu, Y. Song, and M. Wei, “Supercapacitor electrode of hollow spherical V₂O₅ with a high pseudocapacitance in aqueous solution,” *Electrochimica Acta*, vol. 105, pp. 489–495, Aug. 2013.
- [58] J. Zhu *et al.*, “Building 3D Structures of Vanadium Pentoxide Nanosheets and Application as Electrodes in Supercapacitors,” *Nano Lett.*, vol. 13, no. 11, pp. 5408–5413, Nov. 2013.
- [59] Q. Qu, Y. Zhu, X. Gao, and Y. Wu, “Core-Shell Structure of Polypyrrole Grown on V₂O₅ Nanoribbon as High Performance Anode Material for Supercapacitors,” *Adv. Energy Mater.*, vol. 2, no. 8, pp. 950–955, Aug. 2012.
- [60] J. W. Lee, T. Ahn, J. H. Kim, J. M. Ko, and J.-D. Kim, “Nanosheets based mesoporous NiO microspherical structures via facile and template-free method for high performance supercapacitors,” *Electrochimica Acta*, vol. 56, no. 13, pp. 4849–4857, May 2011.
- [61] Y. Wang, J. Guo, T. Wang, J. Shao, D. Wang, and Y.-W. Yang, “Mesoporous Transition Metal Oxides for Supercapacitors,” *Nanomaterials*, vol. 5, no. 4, pp. 1667–1689, Oct. 2015.

- [62] S.-I. Kim, J.-S. Lee, H.-J. Ahn, H.-K. Song, and J.-H. Jang, "Facile Route to an Efficient NiO Supercapacitor with a Three-Dimensional Nanonetwork Morphology," *ACS Appl. Mater. Interfaces*, vol. 5, no. 5, pp. 1596–1603, Mar. 2013.
- [63] C.-Y. Cao, W. Guo, Z.-M. Cui, W.-G. Song, and W. Cai, "Microwave-assisted gas/liquid interfacial synthesis of flowerlike NiO hollow nanosphere precursors and their application as supercapacitor electrodes," *J. Mater. Chem.*, vol. 21, no. 9, p. 3204, 2011.
- [64] K.-C. Liu and M. A. Anderson, "Porous Nickel Oxide/Nickel Films for Electrochemical Capacitors," *J Electrochem Soc*, vol. 143, no. 1, p. 7, 1996.
- [65] X. Zhang *et al.*, "Synthesis of porous NiO nanocrystals with controllable surface area and their application as supercapacitor electrodes," *Nano Res.*, vol. 3, no. 9, pp. 643–652, Sep. 2010.
- [66] K.-W. Nam and K.-B. Kim, "A Study of the Preparation of NiO_x Electrode via Electrochemical Route for Supercapacitor Applications and Their Charge Storage Mechanism," *J. Electrochem. Soc.*, vol. 149, no. 3, p. A346, 2002.
- [67] C. Yuan, X. Zhang, L. Su, B. Gao, and L. Shen, "Facile synthesis and self-assembly of hierarchical porous NiO nano/micro spherical superstructures for high performance supercapacitors," *J. Mater. Chem.*, vol. 19, no. 32, p. 5772, 2009.
- [68] Y. Ren and L. Gao, "From Three-Dimensional Flower-Like α -Ni(OH)₂ Nanostructures to Hierarchical Porous NiO Nanoflowers: Microwave-Assisted Fabrication and Supercapacitor Properties: Rapid Communications of the American Ceramic Society," *J. Am. Ceram. Soc.*, vol. 93, no. 11, pp. 3560–3564, Nov. 2010.
- [69] H. Du, L. Jiao, K. Cao, Y. Wang, and H. Yuan, "Polyol-Mediated Synthesis of Mesoporous α -Ni(OH)₂ with Enhanced Supercapacitance," *ACS Appl. Mater. Interfaces*, vol. 5, no. 14, pp. 6643–6648, Jul. 2013.
- [70] M. C. Bernard, P. Bernard, M. Keddad, S. Senyarich, and H. Takenouti, "Characterisation of new nickel hydroxides during the transformation of α Ni(OH)₂ to β Ni(OH)₂ by ageing," *Electrochimica Acta*, vol. 41, no. 1, pp. 91–93, 1996.
- [71] J. Xu, L. Gao, J. Cao, W. Wang, and Z. Chen, "Preparation and electrochemical capacitance of cobalt oxide (Co₃O₄) nanotubes as supercapacitor material," *Electrochimica Acta*, vol. 56, no. 2, pp. 732–736, Dec. 2010.
- [72] S. Xiong, C. Yuan, X. Zhang, B. Xi, and Y. Qian, "Controllable Synthesis of Mesoporous Co₃O₄ Nanostructures with Tunable Morphology for Application in Supercapacitors," *Chem. - Eur. J.*, vol. 15, no. 21, pp. 5320–5326, May 2009.
- [73] R. R. Salunkhe, J. Tang, Y. Kamachi, T. Nakato, J. H. Kim, and Y. Yamauchi, "Asymmetric Supercapacitors Using 3D Nanoporous Carbon and Cobalt Oxide Electrodes Synthesized from a Single Metal–Organic Framework," *ACS Nano*, vol. 9, no. 6, pp. 6288–6296, Jun. 2015.
- [74] X. Xia, J. Tu, Y. Mai, X. Wang, C. Gu, and X. Zhao, "Self-supported hydrothermal synthesized hollow Co₃O₄ nanowire arrays with high supercapacitor capacitance," *J. Mater. Chem.*, vol. 21, no. 25, p. 9319, 2011.

- [75] X.-C. Dong *et al.*, “3D Graphene–Cobalt Oxide Electrode for High-Performance Supercapacitor and Enzymeless Glucose Detection,” *ACS Nano*, vol. 6, no. 4, pp. 3206–3213, Apr. 2012.
- [76] T. Zhao, H. Jiang, and J. Ma, “Surfactant-assisted electrochemical deposition of α -cobalt hydroxide for supercapacitors,” *J. Power Sources*, vol. 196, no. 2, pp. 860–864, Jan. 2011.
- [77] L.-B. Kong, M. Liu, J.-W. Lang, Y.-C. Luo, and L. Kang, “Asymmetric Supercapacitor Based on Loose-Packed Cobalt Hydroxide Nanoflake Materials and Activated Carbon,” *J. Electrochem. Soc.*, vol. 156, no. 12, p. A1000, 2009.
- [78] A. D. Jagadale, V. S. Jamadade, S. N. Pusawale, and C. D. Lokhande, “Effect of scan rate on the morphology of potentiodynamically deposited β -Co(OH)₂ and corresponding supercapacitive performance,” *Electrochimica Acta*, vol. 78, pp. 92–97, Sep. 2012.
- [79] V. D. Nithya and N. S. Arul, “Review on α -Fe₂O₃ based negative electrode for high performance supercapacitors,” *J. Power Sources*, vol. 327, pp. 297–318, Sep. 2016.
- [80] X. Lu, G. Li, and Y. Tong, “A review of negative electrode materials for electrochemical supercapacitors,” *Sci. China Technol. Sci.*, vol. 58, no. 11, pp. 1799–1808, Nov. 2015.
- [81] T. Liu *et al.*, “Investigation of hematite nanorod–nanoflake morphological transformation and the application of ultrathin nanoflakes for electrochemical devices,” *Nano Energy*, vol. 12, pp. 169–177, Mar. 2015.
- [82] H. Wang, Z. Xu, H. Yi, H. Wei, Z. Guo, and X. Wang, “One-step preparation of single-crystalline Fe₂O₃ particles/graphene composite hydrogels as high performance anode materials for supercapacitors,” *Nano Energy*, vol. 7, pp. 86–96, Jul. 2014.
- [83] R. Chen, I. K. Puri, and I. Zhitomirsky, “High areal capacitance of FeOOH-carbon nanotube negative electrodes for asymmetric supercapacitors,” *Ceram. Int.*, vol. 44, no. 15, pp. 18007–18015, Oct. 2018.
- [84] R. Chen, I. K. Puri, and I. Zhitomirsky, “Polypyrrole-Carbon Nanotube-FeOOH Composites for Negative Electrodes of Asymmetric Supercapacitors,” *J. Electrochem. Soc.*, vol. 166, no. 6, pp. A935–A940, 2019.
- [85] H. Fan, R. Chen, and I. Zhitomirsky, “Manufacturing of polypyrrole-FeOOH supercapacitors,” *Mater. Manuf. Process.*, vol. 34, no. 9, pp. 1068–1071, Jul. 2019.
- [86] D. Choi, G. E. Blomgren, and P. N. Kumta, “Fast and Reversible Surface Redox Reaction in Nanocrystalline Vanadium Nitride Supercapacitors,” *Adv. Mater.*, vol. 18, no. 9, pp. 1178–1182, May 2006.
- [87] X. Lu *et al.*, “High Energy Density Asymmetric Quasi-Solid-State Supercapacitor Based on Porous Vanadium Nitride Nanowire Anode,” *Nano Lett.*, vol. 13, no. 6, pp. 2628–2633, Jun. 2013.
- [88] J. Yan, Q. Wang, T. Wei, and Z. Fan, “Recent Advances in Design and Fabrication of Electrochemical Supercapacitors with High Energy Densities,” *Adv. Energy Mater.*, vol. 4, no. 4, p. 1300816, Mar. 2014.

- [89] L. Demarconnay, E. Raymundo-Piñero, and F. Béguin, “Adjustment of electrodes potential window in an asymmetric carbon/MnO₂ supercapacitor,” *J. Power Sources*, vol. 196, no. 1, pp. 580–586, Jan. 2011.
- [90] L. Demarconnay, E. Raymundo-Piñero, and F. Béguin, “A symmetric carbon/carbon supercapacitor operating at 1.6V by using a neutral aqueous solution,” *Electrochem. Commun.*, vol. 12, no. 10, pp. 1275–1278, Oct. 2010.
- [91] G. G. Amatucci, F. Badway, A. Du Pasquier, and T. Zheng, “An Asymmetric Hybrid Nonaqueous Energy Storage Cell,” *J. Electrochem. Soc.*, vol. 148, no. 8, p. A930, 2001.
- [92] C. Zhong, Y. Deng, W. Hu, J. Qiao, L. Zhang, and J. Zhang, “A review of electrolyte materials and compositions for electrochemical supercapacitors,” *Chem. Soc. Rev.*, vol. 44, no. 21, pp. 7484–7539, 2015.
- [93] D. Jiménez-Cordero, F. Heras, M. A. Gilarranz, and E. Raymundo-Piñero, “Grape seed carbons for studying the influence of texture on supercapacitor behaviour in aqueous electrolytes,” *Carbon*, vol. 71, pp. 127–138, May 2014.
- [94] K.-W. Nam, C.-W. Lee, X.-Q. Yang, B. W. Cho, W.-S. Yoon, and K.-B. Kim, “Electrodeposited manganese oxides on three-dimensional carbon nanotube substrate: Supercapacitive behaviour in aqueous and organic electrolytes,” *J. Power Sources*, vol. 188, no. 1, pp. 323–331, Mar. 2009.
- [95] C. Long, T. Wei, J. Yan, L. Jiang, and Z. Fan, “Supercapacitors Based on Graphene-Supported Iron Nanosheets as Negative Electrode Materials,” *ACS Nano*, vol. 7, no. 12, pp. 11325–11332, Dec. 2013.
- [96] C.-S. Dai *et al.*, “Hierarchically Structured Ni₃S₂/Carbon Nanotube Composites as High Performance Cathode Materials for Asymmetric Supercapacitors,” *ACS Appl. Mater. Interfaces*, vol. 5, no. 22, pp. 12168–12174, Nov. 2013.
- [97] X. Zhang, X. Wang, L. Jiang, H. Wu, C. Wu, and J. Su, “Effect of aqueous electrolytes on the electrochemical behaviors of supercapacitors based on hierarchically porous carbons,” *J. Power Sources*, vol. 216, pp. 290–296, Oct. 2012.
- [98] H. Gao and K. Lian, “Proton-conducting polymer electrolytes and their applications in solid supercapacitors: a review,” *RSC Adv*, vol. 4, no. 62, pp. 33091–33113, 2014.
- [99] L. Vayssieres, “On the thermodynamic stability of metal oxide nanoparticles in aqueous solutions,” *Int. J. Nanotechnol.*, vol. 2, no. 4, p. 411, 2005.
- [100] R. Chen, M. S. Ata, X. Zhao, A. Clifford, I. Puri, and I. Zhitomirsky, “Strategies for liquid-liquid extraction of oxide particles for applications in supercapacitor electrodes and thin films,” *J. Colloid Interface Sci.*, vol. 499, pp. 1–8, Aug. 2017.
- [101] C. Wallar, T. Zhang, K. Shi, and I. Zhitomirsky, “Synthesis of metal and metal oxide nanoparticles, liquid-liquid extraction and application in supercapacitors,” *Colloids Surf. Physicochem. Eng. Asp.*, vol. 500, pp. 195–202, Jul. 2016.
- [102] G. Cao and Y. Wang, *Nanostructures and nanomaterials: synthesis, properties, and applications*, 2. ed. Hackensack, NJ: World Scientific, 2011.
- [103] I. Zhitomirsky, “Cathodic electrodeposition of ceramic and organoceramic materials. Fundamental aspects,” *Adv. Colloid Interface Sci.*, vol. 97, no. 1–3, pp. 279–317, Mar. 2002.

- [104] Y. Wang and I. Zhitomirsky, "Bio-inspired catechol chemistry for electrophoretic nanotechnology of oxide films," *J. Colloid Interface Sci.*, vol. 380, no. 1, pp. 8–15, Aug. 2012.
- [105] H. Lee, S. M. Dellatore, W. M. Miller, and P. B. Messersmith, "Mussel-Inspired Surface Chemistry for Multifunctional Coatings," *Science*, vol. 318, no. 5849, pp. 426–430, Oct. 2007.
- [106] M. S. Ata, Y. Liu, and I. Zhitomirsky, "A review of new methods of surface chemical modification, dispersion and electrophoretic deposition of metal oxide particles," *RSC Adv.*, vol. 4, no. 43, p. 22716, 2014.
- [107] O. V. Kharissova, B. I. Kharisov, and E. G. de Casas Ortiz, "Dispersion of carbon nanotubes in water and non-aqueous solvents," *RSC Adv.*, vol. 3, no. 47, p. 24812, 2013.
- [108] F. Avilés, J. V. Cauich-Rodríguez, L. Moo-Tah, A. May-Pat, and R. Vargas-Coronado, "Evaluation of mild acid oxidation treatments for MWCNT functionalization," *Carbon*, vol. 47, no. 13, pp. 2970–2975, Nov. 2009.
- [109] W. Khan, R. Sharma, and P. Saini, "Carbon Nanotube-Based Polymer Composites: Synthesis, Properties and Applications," in *Carbon Nanotubes - Current Progress of their Polymer Composites*, M. R. Berber and I. H. Hafez, Eds. InTech, 2016.
- [110] B. Vigolo, "Macroscopic Fibers and Ribbons of Oriented Carbon Nanotubes," *Science*, vol. 290, no. 5495, pp. 1331–1334, Nov. 2000.
- [111] M. Gubitosi *et al.*, "Characterization of Carbon Nanotube Dispersions in Solutions of Bile Salts and Derivatives Containing Aromatic Substituents," *J. Phys. Chem. B*, vol. 118, no. 4, pp. 1012–1021, Jan. 2014.
- [112] M. S. Strano *et al.*, "The Role of Surfactant Adsorption during Ultrasonication in the Dispersion of Single-Walled Carbon Nanotubes," *J. Nanosci. Nanotechnol.*, vol. 3, no. 1, pp. 81–86, Feb. 2003.
- [113] S. Mukhopadhyay and U. Maitra, "Chemistry and biology of bile acids," *Curr. Sci.*, vol. 87, no. 12, p. 18, 2004.
- [114] L. Galantini *et al.*, "Bile salts and derivatives: Rigid unconventional amphiphiles as dispersants, carriers and superstructure building blocks," *Curr. Opin. Colloid Interface Sci.*, vol. 20, no. 3, pp. 170–182, Jun. 2015.
- [115] W. Wenseleers, I. I. Vlasov, E. Goovaerts, E. D. Obraztsova, A. S. Lobach, and A. Bouwen, "Efficient Isolation and Solubilization of Pristine Single-Walled Nanotubes in Bile Salt Micelles," *Adv. Funct. Mater.*, vol. 14, no. 11, pp. 1105–1112, Nov. 2004.
- [116] M. S. Ata and I. Zhitomirsky, "Colloidal methods for the fabrication of carbon nanotube–manganese dioxide and carbon nanotube–polypyrrole composites using bile acids," *J. Colloid Interface Sci.*, vol. 454, pp. 27–34, Sep. 2015.
- [117] M. S. Ata and I. Zhitomirsky, "Electrochemical Deposition of Composites Using Deoxycholic Acid Dispersant," *Mater. Manuf. Process.*, vol. 31, no. 1, pp. 67–73, Jan. 2016.

- [118] F. Tournus, S. Latil, M. I. Heggie, and J.-C. Charlier, “ π -stacking interaction between carbon nanotubes and organic molecules,” *Phys. Rev. B*, vol. 72, no. 7, Aug. 2005.
- [119] L. M. Woods, Ş. C. Bădescu, and T. L. Reinecke, “Adsorption of simple benzene derivatives on carbon nanotubes,” *Phys. Rev. B*, vol. 75, no. 15, Apr. 2007.
- [120] D. Lin and B. Xing, “Adsorption of Phenolic Compounds by Carbon Nanotubes: Role of Aromaticity and Substitution of Hydroxyl Groups,” *Environ. Sci. Technol.*, vol. 42, no. 19, pp. 7254–7259, Oct. 2008.
- [121] M. S. Ata, R. Poon, A. M. Syed, J. Milne, and I. Zhitomirsky, “New developments in non-covalent surface modification, dispersion and electrophoretic deposition of carbon nanotubes,” *Carbon*, vol. 130, pp. 584–598, Apr. 2018.
- [122] M. S. Ata, J. Milne, and I. Zhitomirsky, “Fabrication of Mn₃O₄–carbon nanotube composites with high areal capacitance using cationic and anionic dispersants,” *J. Colloid Interface Sci.*, vol. 512, pp. 758–766, Feb. 2018.
- [123] S. Chen and I. Zhitomirsky, “Strategies to Optimize the Capacitive Behavior of Polypyrrole Electrodes,” *Mater. Manuf. Process.*, vol. 31, no. 15, pp. 2017–2022, Nov. 2016.

Chapter 3 Objectives

As mentioned in the literature review, many attempts have been made to improve the performance of pseudocapacitors by improved mixing with conductive additives. These attempts have demonstrated some improvements and achieved high capacitance comparable to theoretical capacitance. However, these approaches suffer from drawbacks such as low active mass loadings and complex fabrication techniques, which have limited their potential for practical applications. To address these problems, the objective of this investigation was the development and fabrication of high performance advanced nanocomposite electrodes at high active mass loadings for ES applications.

This was achieved by:

- Investigation of advanced dispersants for metal oxides and MWCNTs
- Development of scalable processing techniques for fabrication advanced nanocomposites
- Development of advanced colloidal processing techniques for fabrication of non-agglomerated particles
- Investigation of alternative metal oxides for ES applications
- Fabrication and electrochemical testing of advanced nanocomposite electrodes at high active mass loadings.

Chapter 4 Supercapacitor electrodes with high active mass loading

R Poon* and I. Zhitomirsky*^a

*Department of Materials Science and Engineering, McMaster University,
Hamilton, Ontario, L8S 4L7, Canada

^aCorresponding Author: zhitom@mcmaster.ca; 905-525-9140 ext. 23914

Submitted on 25th April 2018. Revised and Accepted on 6th August 2018.

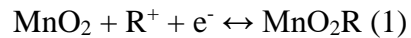
Copyright 2018, reproduced with permission from Cambridge University Press.

4.1 Abstract

We report the fabrication and testing of MnO₂–carbon nanotube (NT) electrodes for supercapacitors (SCap) with high active mass (AM). Cetylpyridinium chloride surfactant was used as a capping agent for synthesis and a phase transfer agent for the liquid–liquid extraction. Water immiscible solvent, n-butanol, was used as a receiving and reducing medium for the synthesis of MnO₂ from cetylpyridinium permanganate. Improved co-dispersion and nanoscale mixing of MnO₂ and NT enabled the fabrication of advanced electrodes with mass loading of 42–61 mg cm⁻², ratio of AM to current collector mass of 0.63–0.91, which showed the highest capacitance of 8.95 F cm⁻².

4.2 Introduction

MnO₂ has gained significant interest as a supercapacitor (SCap) material due to its high gravimetric capacitance (C_g , F g⁻¹), large and stable voltage window in Na₂SO₄ aqueous electrolyte, low toxicity, and low cost.[1–6] The charging process is described by the below equation:



Small size of MnO₂ particles and porous electrode microstructure enable good ion access ($\text{R}^+ = \text{H}^+$, Na^+ , and K^+) to the particle surface.[7] Carbon nanotube (NT) additives allow for improved electronic conductivity of MnO₂–NT composites.[8–10] Despite the impressive progress[4,8,11–14] achieved in the design of MnO₂-based composites, there is a need for the manufacturing of advanced SCap electrodes with high active mass (AM) for practical applications. It is known that C_g decreases significantly with increasing AM.[15]

Moreover,[15] limited electrolyte access to AM can result in reduction of areal capacitance (C_s , $F\text{ cm}^{-2}$) with increasing AM. In this scenario, the bulk material exhibits low capacitance whereas surface region is highly capacitive, and the overall capacitance is reduced since total capacitance is governed by the capacitor with lower capacitance. A high C_s must be achieved at low electrode resistance. Another important characteristic of the SCap electrodes is the ratio (δm) of AM to current collector mass. It should be noted that δm values are often about 0.5–2% for films with AM of 0.5–1.0 mg cm^{-2} on metal foils. Substantially higher δm values are required for advanced lightweight SCap.

The objective of this study was the development of MnO_2 – NT electrodes with high AM and enhanced performance. Our conceptually novel manufacturing method is based on the synthesis of surfactant– MnO_4 complex compound for the MnO_2 fabrication. The surfactant inhibited MnO_2 particle growth, enabled liquid–liquid extraction of MnO_2 , and formation of composites with improved morphology. This method eliminated the problems related to the MnO_2 particle agglomeration during filtration and drying and their re-dispersion in the electrode processing medium. Moreover, the method facilitated improved co-dispersion and nanoscale mixing of non-agglomerated MnO_2 and NT, which enabled enhanced performance of the composite electrodes at high AM. We fabricated electrodes with AM of 42–61 mg cm^{-2} and δm values of 0.63–0.91. The C_s of 8.95 $F\text{ cm}^{-2}$ was achieved.

4.3 Experimental Procedure

Commercial cetylpyridinium chloride (CPC), KMnO_4 , Na_2SO_4 , poly(vinyl butyral) (PVB), n-butanol, multiwalled NTs (ID of 4 nm, OD of 13 nm, length in the range of 1–2 μm , Bayer Company, Germany), and Ni foam (porosity of 95%, Vale, Canada) were used.

Solutions of 3.45 mM CPC in 150 mL of deionized (DI) water and 3.45 mM KMnO_4 in 50 mL of DI water were prepared and stirred for 15 min. Mixing of the solutions resulted in the synthesis of cetylpyridinium permanganate precipitate. The addition of 50 mL of n-butanol as a reducing agent and stirring for 1 h allowed for the synthesis of MnO_2 particles. The particles were spontaneously transferred to the n-butanol phase, whereas the aqueous phase became clear. The suspension of MnO_2 particles was filtered, then washed and dried particles were studied by X-ray diffraction (XRD). The results of XRD studies presented below confirmed the formation of MnO_2 . The drying of the particles resulted in their agglomeration.

NT were added to water and ultrasonicated. It was found that the addition of n-butanol resulted in the transfer of NT to the n-butanol phase, whereas the aqueous phase became clear (Supplementary Materials Figure 4.5). This observation paved the way for the phase transfer of the as-prepared MnO_2 and NT from water to the n-butanol phase. Therefore, the procedure for the synthesis of MnO_2 was modified by adding NT to the synthesis medium. In the modified procedure, NTs were dispersed in water in the presence of CPC surfactant, which facilitated NT dispersion. Then, KMnO_4 solution was added to form cetylpyridinium permanganate. The addition of n-butanol to the mixture, containing cetylpyridinium

permanganate and NTs, resulted in the MnO₂ synthesis and co-dispersion of MnO₂ and NT in the n-butanol phase (Supplementary Materials Figure 4.6). The mass ratio of MnO₂ and NT was 4:1. The slurry, containing MnO₂ and NT in a solvent, containing dissolved PVB binder, was used for the impregnation of Ni foam current collectors. The AM loading of MnO₂ and NT of the electrodes was in the range of 42–61 mg cm⁻². The mass of the PVB binder was in the range of 0.5–1% of the total AM. The electrodes were dried at 60 °C for 48 h.

XRD analysis was performed using a powder diffractometer equipped with a Bruker SMART6000 CCD area detector and a Rigaku Cu K α rotating anode. Scanning electron microscopy (SEM) and electrochemical characterization methods were described in Ref.

15.

4.4 Results and Discussion

Previous investigations showed that interactions of cationic surfactants and other long chain organic cations with permanganates resulted in the formation of complex compounds, such as cetyltrimethylammonium permanganate,[16] triphenylphosphonium permanganate,[17] tetrabutylammonium permanganate,[18] and other compounds,[19,20] which were used as oxidants for many applications.[19] In this investigation, we prepared cetylpyridinium permanganate by reaction of CPC and KMnO_4 in water. The addition of n-butanol allowed synthesis of MnO_2 in the n-butanol phase. The synthesis of MnO_2 was confirmed by the XRD analysis (Figure 4.1). The XRD pattern showed reflections of the birnessite phase. However, the mechanism of MnO_2 formation is not well understood. Previous investigations[21] showed that the reduction of Mn^{7+} species at the interface of aqueous KMnO_4 solutions and n-butanol resulted in the precipitation of MnO_2 in water. In contrast, in this investigation we prepared cetylpyridinium permanganate in water and the addition of n-butanol led to the formation of MnO_2 in the n-butanol phase. The analysis of the literature indicated that cationic surfactants facilitate [22] phase transfer of MnO_4^- species from water to an organic phase. The organic phase, containing transferred MnO_4^- species has been separated and the addition of a reducing agent to the organic phase allowed the fabrication of MnO_2 particles[22].

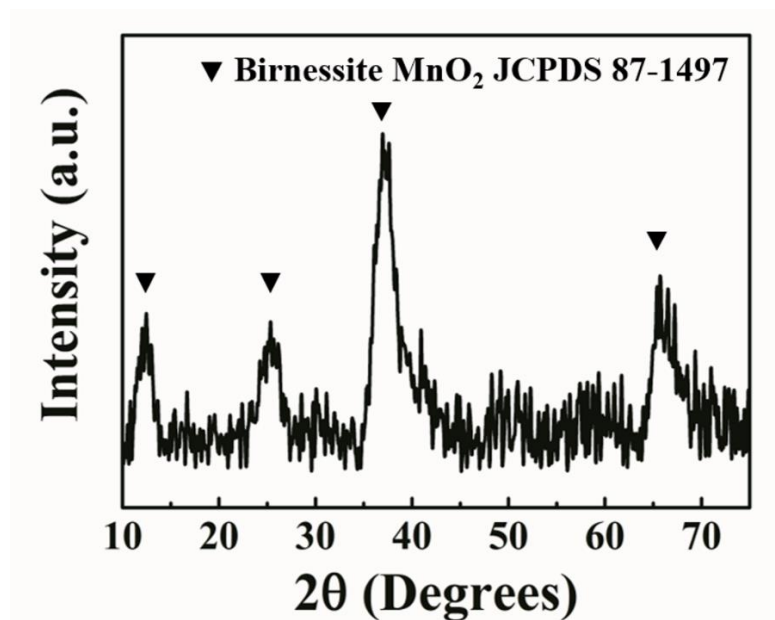


Figure 4.1: XRD pattern of MnO₂ powder.

We suggested that stirring of the mixture, containing cetylpyridinium permanganate and n-butanol, resulted in the phase transfer of cetylpyridinium permanganate from water to n-butanol and its dissociation in the n-butanol phase. The redox reaction of MnO₄⁻ species with n-butanol resulted in the precipitation of MnO₂, which remained in the n-butanol phase. We suggested that surfactant was adsorbed on the MnO₂ particles during synthesis and surfactant modified particles were dispersed in n-butanol. In the previous studies performed without surfactant [21], the MnO₂ prepared by the reduction of MnO₄⁻ species with n-butanol, precipitated in an aqueous phase.

The ability to synthesize and disperse MnO₂ particles in the organic phase offers benefits for SCap applications. In previous investigations [23], MnO₂ particles were synthesized from aqueous KMnO₄ solutions, then dried and dispersed again in an organic phase, containing water-insoluble binder for the fabrication of SCap electrodes. However, the

drying procedure resulted in particle agglomeration, which hindered their mixing with NT. The major reasons of the agglomeration are the reduction of surface energy of MnO_2 nanoparticles and surface condensation reactions. In contrast, in this investigation we found that drying and re-dispersion steps can be avoided and MnO_2 particles can be prepared and mixed with NT in the n-butanol phase.

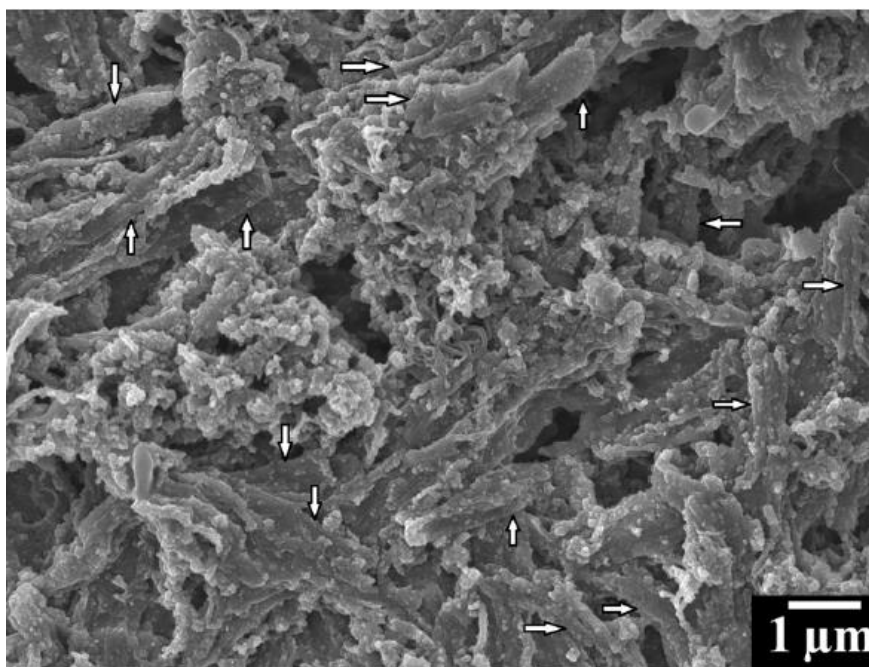


Figure 4.2: SEM image of MnO_2 -NT composite; arrows show examples of elongated particles.

As mentioned above, NTs can be transferred from water to n-butanol spontaneously without the use of a surfactant. However, the use of CPC facilitated dispersion of NTs and their transfer to n-butanol.

The addition of n-butanol to the aqueous phase, containing cetylpyridinium permanganate and NT led to the formation of a suspension of MnO_2 and NT (Supplementary Materials

Figure 4.6). We suggest that CPC facilitated co-dispersion MnO_2 and NT as well as their mixing. Moreover, we found that good dispersion facilitated the impregnation of Ni foam current collectors and allowed the fabrication of electrodes with high AM.

Figure 4.2 shows an SEM image of a MnO_2 -NT composite formed by filtering and drying of the suspension of MnO_2 and NT in n-butanol. The SEM studies indicated that phase segregation of MnO_2 and NT was avoided. The microstructure showed many elongated particles, the formation of such particles is probably governed by the shape of NT encapsulated in the MnO_2 matrix. The SEM images at higher magnifications and transmission electron microscopy images revealed many MnO_2 coated NTs (Supplementary Materials Figure 4.7 and Figure 4.8). The analysis of the electron microscopy data showed improved mixing of MnO_2 and NT. As a result, we achieved improved electrode performance at high AM.

The capacitive performance of the electrodes was analyzed by different methods (Figure 4.3 and Figure 4.4, Supplementary Materials Figure 4.9 to Figure 4.11, Table 4.1). Figure 4.3(a) and (b), 9(a) show cyclic voltammetry (CVs) for MnO_2 -NT composites with AM loadings in the range of 42–61 mg cm^{-2} . The nearly ideal box shape CVs represent good capacitive behavior, which was achieved at high AM. The capacitances of 6.03, 7.22, and 8.95 F cm^{-2} were achieved for mass loadings of 42, 51, and 61 mg cm^{-2} , respectively, at a scan rate of 2 mV s^{-1} .

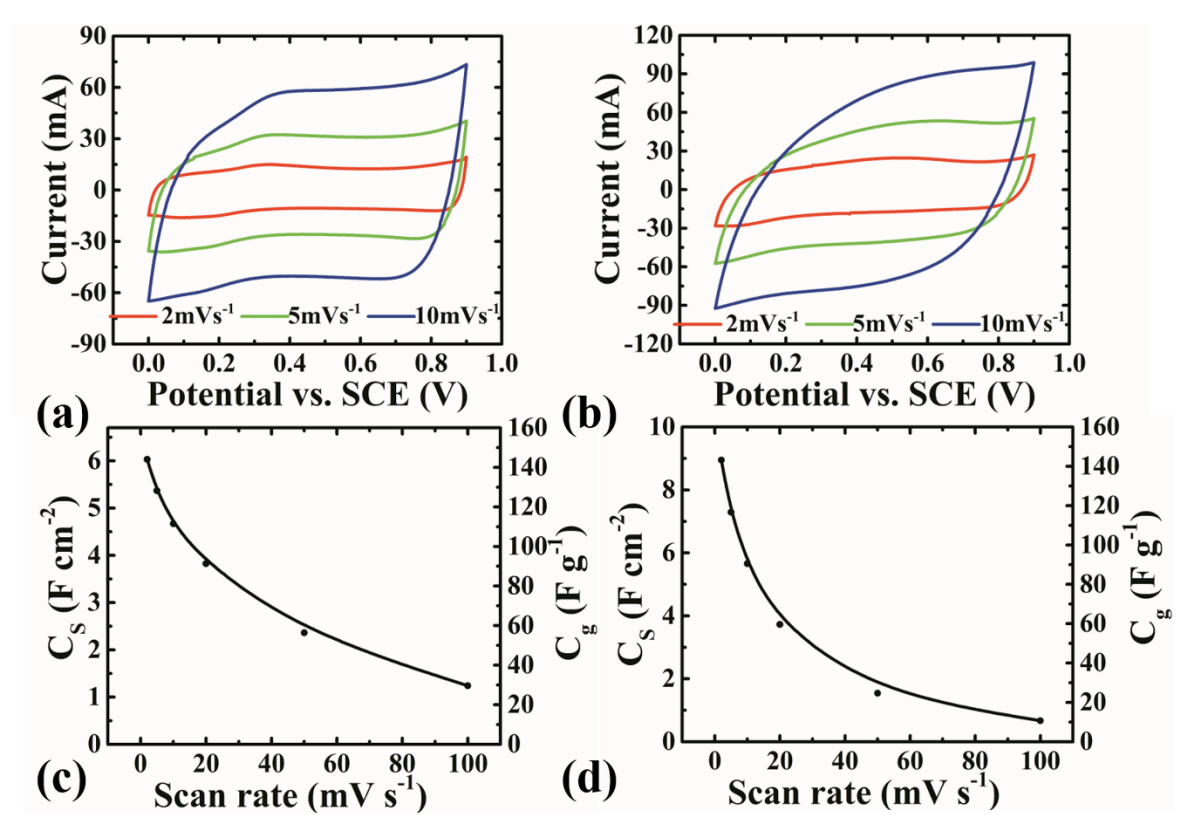


Figure 4.3: (a, b) CVs at different scan rates and (c, d) C_g and C_S versus scan rate for MnO_2 -NT electrodes with AM of (a, c) 42 mg cm^{-2} and (b, d) 61 mg cm^{-2} .

However, C_S decreased with scan rate increase due to limited diffusion of electrolyte in pores [Figure 4.3(c) and 3(d), 9(b)]. The δm values were in the range of 0.63–0.91 for AM of 42–61 mg cm^{-2} . The relatively high δm values offer benefits for the fabrication of devices with reduced mass. The high capacitance was achieved at relatively low electrode resistance. Figure 4.4(a) and 9(c) show complex impedance data in the Nyquist diagram. For the electrode with AM of 42 mg cm^{-2} the slope of the graph was close to 90° , indicating good capacitive properties. The electrode with AM of 61 mg cm^{-2} showed slightly higher resistance and reduced Nyquist diagram slope. The equivalent series resistance value

increased from .97 to 1.27 Ohms with AM increase in the range of 42–61 mg cm^{-2} . The complex capacitance, derived from the AC impedance data [Figure 4.4(b) and 4(c), 9(d)] showed a frequency dispersion of the relaxation type,[24,25] due to the decrease of the real part (C_s') with frequency increase and relaxation maxima in the imaginary part(C_s''). The frequency of the relaxation maximum decreased with increasing AM due to limited diffusion in pores. The constant current charge–discharge graphs (Figure 4.11) were of nearly ideal symmetric triangular shape, which indicated good capacitive properties.

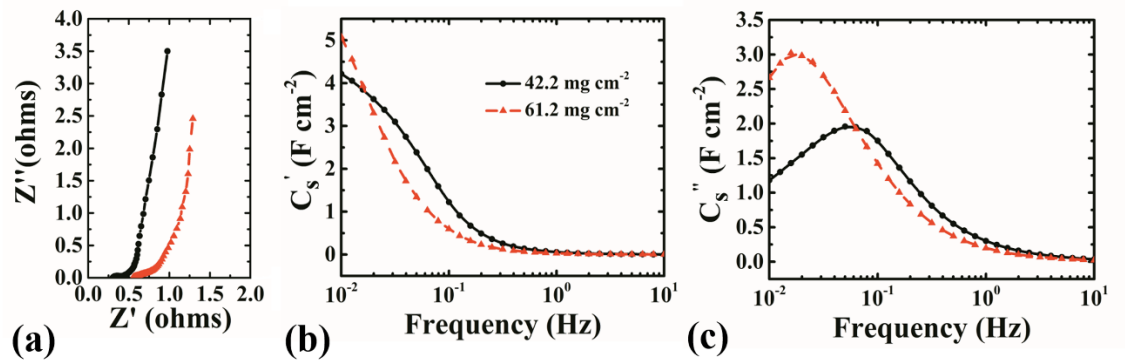


Figure 4.4: (a) Nyquist plot of complex impedance and (b, c) frequency dependences of components of complex capacitance for MnO_2 -NT electrodes with AM of 42 and 61 mg cm^{-2} .

4.5 Conclusions

A conceptually new method has been developed for the manufacturing of MnO_2 -NT electrodes for SCaps. CPC was used as a complexing and capping agent for synthesis and a phase transfer agent for liquid-liquid particle extraction. We suggested a mechanism of synthesis, which involved the formation of cetylpyridinium permanganate in an aqueous phase, phase transfer to n-butanol phase and reduction of MnO_4^- species by n-butanol. In this method, the problem of particle agglomeration in the drying process was eliminated. The co-dispersion of MnO_2 and NT in n-butanol facilitated their improved mixing, which allowed the fabrication of advanced electrodes with high AM. We demonstrated the formation of SCap electrodes with AM loading in the range of 42–61 mg cm^{-2} . The high AM loading allowed for high δ_m , which was beneficial for the fabrication of SCap with reduced total mass. The electrodes showed enhanced capacitive behavior and low resistance. The highest C_s of 8.95 F cm^{-2} was obtained.

4.6 Acknowledgements

This investigation was supported by NSERC Canada.

4.7 Supplementary Materials



Figure 4.5: Extraction of MWCNT from the aqueous phase (bottom) to the 1-butanol phase (top).

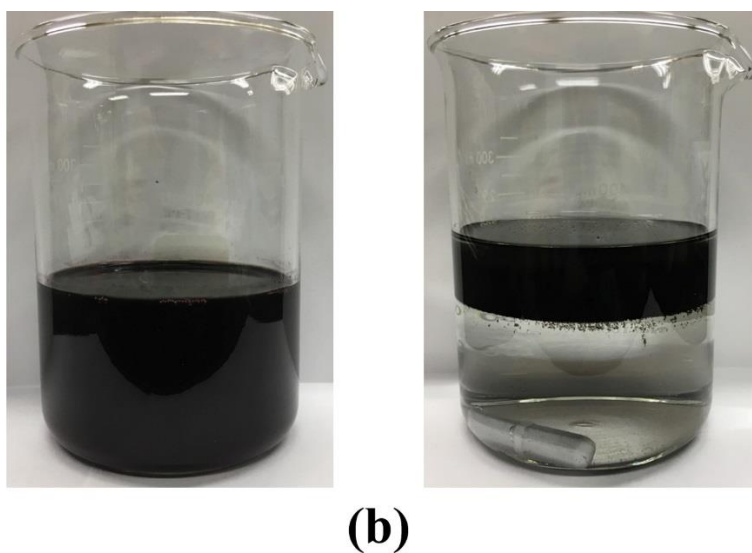


Figure 4.6: (a) Aqueous mixture of cetylpyridinium permanganate and MWCNT, (b) phase transfer and formation of mixed suspension of MnO_2 and MWCNT in the 1-butanol phase.

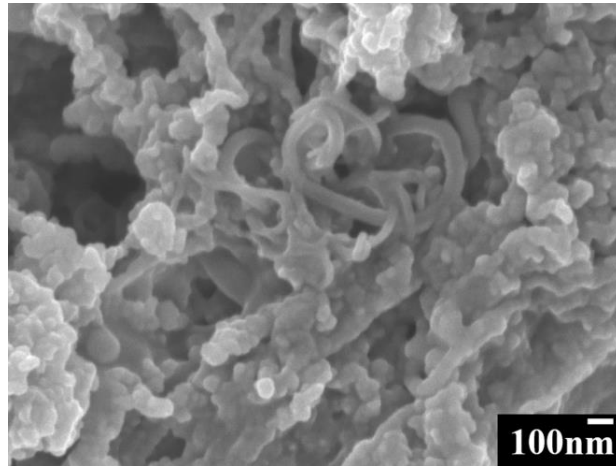


Figure 4.7: High magnification SEM image of the MnO_2 -MWCNT composite material. The diameter of the MWCNT in the middle of the picture is significantly larger, compared to the diameter of original MWCNT (13 nm).

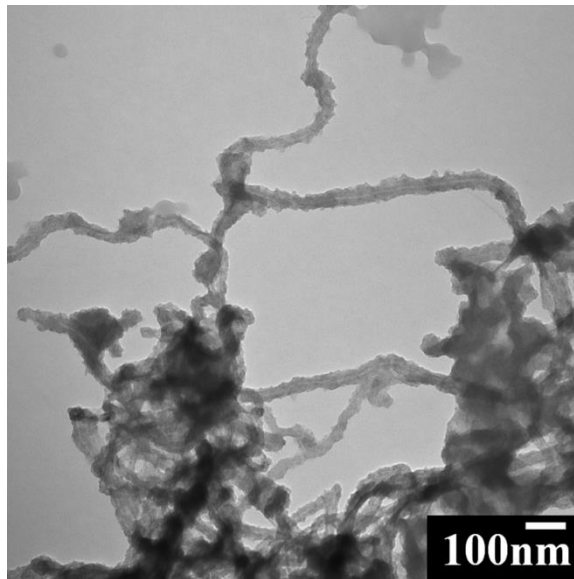


Figure 4.8: Transmission electron microscopy (TEM) (JEOL, JEM 1200 EX TEMSCAN) image of MnO_2 -MWCNT composite.

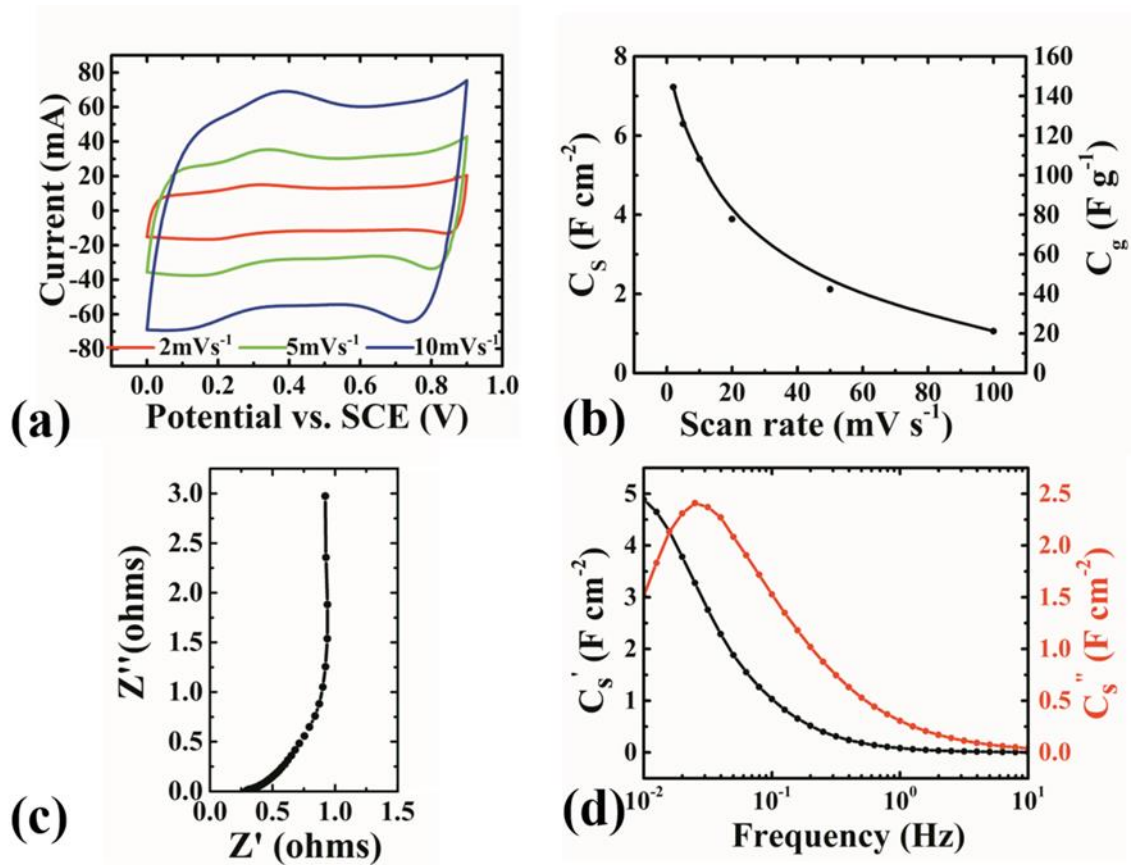


Figure 4.9: (a) CVs at different scan rates, (b) specific capacitance, calculated from the CV data versus scan rate, (c) Nyquist plot of complex impedance and (d) frequency dependencies of the components of complex capacitance, calculated from the impedance data for MnO₂-MWCNT electrodes with mass loading of 51 mg cm⁻².

Table 4.1: Capacitances calculated from the CV data versus scan rates for MnO₂-MWCNT electrodes with different mass loadings.

Scan Rate (mV s ⁻¹)	Mass loadings (mg cm ⁻²)					
	42		51		61	
	C _s (F cm ⁻²)	C _g (F g ⁻¹)	C _s (F cm ⁻²)	C _g (F g ⁻¹)	C _s (F cm ⁻²)	C _g (F g ⁻¹)
2	6.03	142.9	7.22	141.1	8.95	146.2
5	5.67	127.2	6.29	122.9	7.29	119.2
10	4.67	110.7	5.41	105.6	5.66	92.4
20	3.82	90.6	3.89	76.0	3.73	60.9
50	2.36	55.9	2.12	41.4	1.54	25.2
100	1.24	29.4	1.05	20.7	0.67	10.9

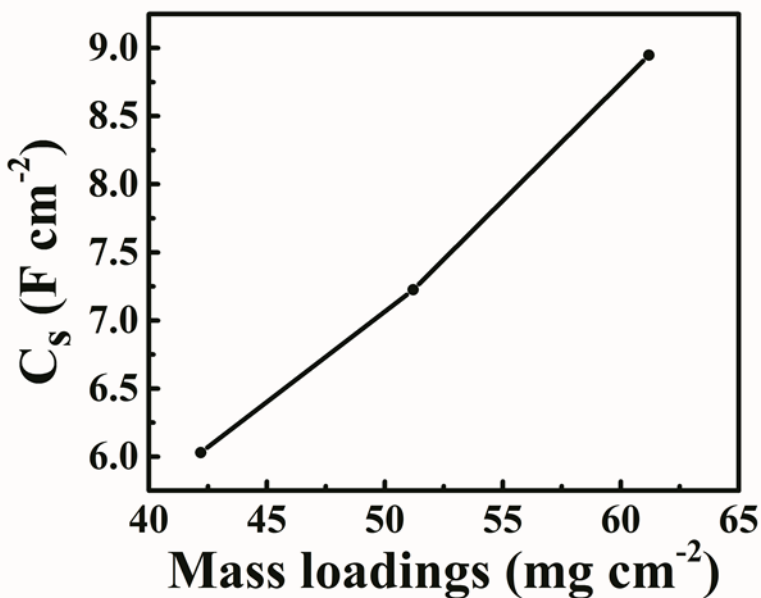


Figure 4.10: Specific capacitance, calculated from CV data at 2 mV s⁻¹ versus mass loading for MnO₂-MWCNT electrodes.

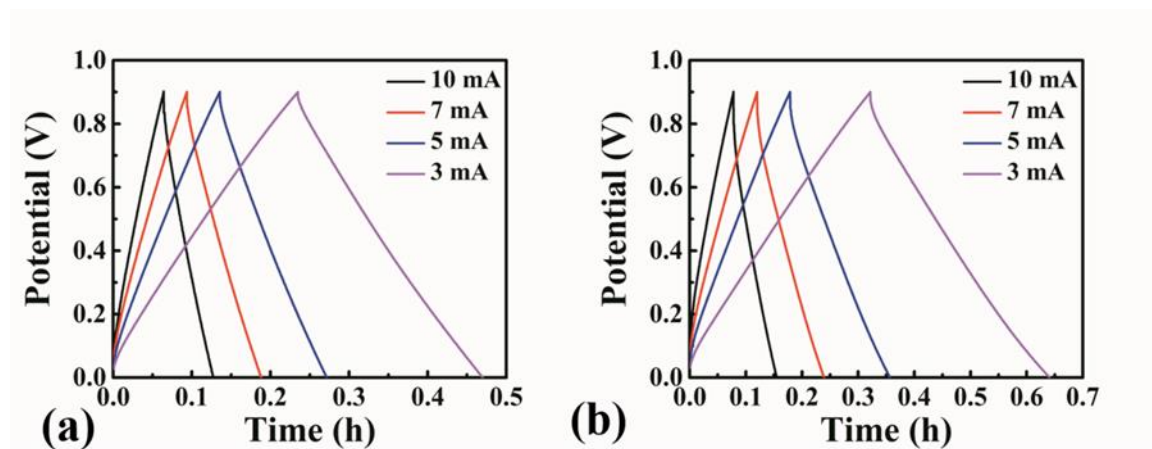


Figure 4.11: Galvanostatic charge-discharge behavior at different current densities for MnO₂-MWCNT electrodes with mass loadings of (a) 42 and (b) 61 mg cm⁻².

4.8 References

- [1] S. Devaraj and N. Munichandraiah, "High Capacitance of Electrodeposited MnO₂ by the Effect of a Surface-Active Agent", *Electrochemical and Solid-State Letters*, vol. 8, no. 7, p. A373, 2005.
- [2] T. Brousse et al., "Long-term cycling behavior of asymmetric activated carbon/ MnO₂ aqueous electrochemical supercapacitor", *Journal of Power Sources*, vol. 173, no. 1, pp. 633-641, 2007.
- [3] Y.U. Jeong and A. Manthiram, "Nanocrystalline manganese oxides for electrochemical capacitors with neutral electrolytes", *J. Electrochem. Soc.*, vol. 149, pp. A1419–A1422, 2002.
- [4] N.R. Chodankar, D.P. Dubal, G.S. Gund, and C.D. Lokhande, "Bendable all-solid-state asymmetric supercapacitors based on MnO₂ and Fe₂O₃ thin films", *Energy Technol.* 3, 625–631, 2015.
- [5] C.A. Beasley, M.B. Sassin, and J.W. Long, "Extending electrochemical quartz crystal microbalance techniques to macroscale electrodes: insights on pseudocapacitance mechanisms in MnO_x-coated carbon nanofoams", *J. Electrochem. Soc.*, vol. 162, A5060–A5064, 2015.
- [6] L. Athouël, P. Arcidiacono, C. Ramirez-Castro, O. Crosnier, C. Hamel, Y. Dandeville, P. Gillemet, Y. Scudeller, D. Guay, D. Belanger, and T. Brousse, "Investigation of cavity microelectrode technique for electrochemical study with manganese dioxides", *Electrochim. Acta*, vol. 86, pp. 268–276, 2012.
- [7] L. Coustan, A. Le Comte, T. Brousse, and F. Favier, "MnO₂ as ink material for the fabrication of supercapacitor electrodes", *Electrochim. Acta*, vol. 152, pp. 520–529, 2015.
- [8] L. Demarconnay, E. Raymundo-Pinero, and F. Béguin, "Adjustment of electrodes potential window in an asymmetric carbon/ MnO₂ supercapacitor", *J. Power Sources*, vol. 196, pp. 580–586, 2011.
- [9] Y. Lei, B. Daffos, P.L. Taberna, P. Simon, and F. Favier, "MnO₂-coated Ni nanorods: enhanced high rate behavior in pseudo-capacitive supercapacitor", *Electrochim. Acta*, vol. 55, pp. 7454–7459, 2010.
- [10] F. Grote, R.S. Kühnel, A. Balducci, and Y. Lei, "Template assisted fabrication of free-standing MnO₂ nanotube and nanowire arrays and their application in supercapacitors", *Appl. Phys. Lett.*, vol. 104, pp. 053904, 2014.
- [11] N. Goubard-Bretesché, O. Crosnier, G. Buvat, F. Favier, and T. Brousse, "Electrochemical study of aqueous asymmetric FeWO₄/ MnO₂ supercapacitor", *J. Power Sources*, vol. 326, pp. 695–701, 2016.

- [12] H. Xia and C. Huo, "Electrochemical properties of MnO₂/CNT nanocomposite in neutral aqueous electrolyte as cathode material for asymmetric supercapacitors", *Int. J. Smart Nano Mater.*, vol. 2, pp. 283–291, 2011.
- [13] M. Borysiewicz, M. Wzorek, M. Ekielski, J. Kaczmarek, and T. Wojciechowski, "Controlling the nanoscale morphology and structure of the ZnO/ MnO₂ system for efficient transparent supercapacitors", *MRS Commun*, vol. 7, pp. 173–178, 2017.
- [14] G.S. Gund, D.P. Dubal, N.R. Chodankar, J.Y. Cho, P. Gomez-Romero, C. Park, and C.D. Lokhande, "Low-cost flexible supercapacitors with high energy density based on nanostructured MnO₂ and Fe₂O₃ thin films directly fabricated onto stainless steel", *Sci. Rep*, vol. 5, pp. 12454, 2015.
- [15] R. Chen, R. Poon, R.P. Sahu, I.K. Puri, and I. Zhitomirsky, "MnO₂-carbon nanotube electrodes for supercapacitors with high active mass loadings", *J. Electrochem. Soc*, vol. 164, A1673–A1678, 2017.
- [16] S. Dash and B.K. Mishra, "Mn(VII) oxidation using cetyltrimethylammonium permanganate: self-oxidation of CTAP and oxidation of benzyl alcohol", *Int. J. Chem. Kinet*, vol. 27, pp. 627–635, 1995.
- [17] S. Uppugalla, R. Boddula, and P. Srinivasan, "Methyl triphenylphosphonium permanganate as a novel oxidant for aniline to polyanilinemanganese(II, IV) oxide: material for high performance pseudocapacitor", *J. Solid State Electrochem*, vol. 22, pp. 407–415, 2018.
- [18] S. Ching, E.J. Welch, S.M. Hughes, A.B. Bahadoor, and S.L. Suib, "Nonaqueous sol-gel syntheses of microporous manganese oxides", *Chem. Mater.*, vol. 14, pp. 1292–1299, 2002.
- [19] S. Dash, S. Patel, and B.K. Mishra, "Oxidation by permanganate: synthetic and mechanistic aspects", *Tetrahedron*, vol.65, pp. 707–739, 2009.
- [20] H. Karaman, R.J. Barton, B.E. Robertson, and D.G. Lee, "Preparation and properties of quaternary ammonium and phosphonium permanganates", *J. Org. Chem*, vol. 49, pp. 4509–4516, 1984.
- [21] C. Wallar, T. Zhang, K. Shi, and I. Zhitomirsky, "Synthesis of metal and metal oxide nanoparticles, liquid–liquid extraction and application in supercapacitors", *Colloids Surf.*, vol. A 500, pp. 195–202, 2016.
- [22] M.A. Malik and Z. Khan, "Permanganate transfer and reduction by D-glucose in benzene-cetyltrimethylammoniumbromide aqueous solution: a kinetic study", *Int. J. Chem. Kinet*, vol. 40, pp. 496–503, 2008.
- [23] Y. Wang, Y. Liu, and I. Zhitomirsky, "Surface modification of MnO₂ and carbon nanotubes using organic dyes for nanotechnology of electrochemical supercapacitors", *J. Mater. Chem.*, vol. A 1, pp. 12519–12526, 2013.

[24] K. Shi and I. Zhitomirsky, “Influence of current collector on capacitive behavior and cycling stability of Tiron doped polypyrrole electrodes”, *J. Power Sources*, vol. 240, pp. 42–49, 2013.

[25] Y. Su and I. Zhitomirsky, “Asymmetric electrochemical supercapacitor, based on polypyrrole coated carbon nanotube electrodes”, *Appl. Energy*, vol. 153, pp. 48–55, 2015.

Chapter 5 **Zn-doped FeOOH-polypyrrole electrodes for supercapacitors**

W. Liang^{*=}, R. Poon^{*=} and I. Zhitomirsky^{* α}

*Department of Materials Science and Engineering, McMaster University,
Hamilton, Ontario, L8S 4L7, Canada

^{α} Corresponding Author: zhitom@mcmaster.ca; 905-525-9140 ext. 23914

Submitted on 9th April 2019. Accepted on 14th August 2019.

Copyright 2019, reprinted with permission from Elsevier.

Author's Contributions:

- Development of new scalable synthesis of procedure for MC electrode
 - Synthesis of positive MC electrode
 - Electrochemical testing of MC electrode and devices
 - Manuscript preparation

⁼The authors contributed equally to this work

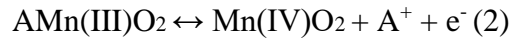
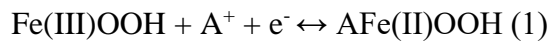
5.1 Abstract

The problem of poor cyclic stability of FeOOH anodes for supercapacitors was addressed by Zn-doping. Zn-doped FeOOH materials exhibited significant improvement in capacitance retention during cycling. Further improvement in capacitance retention and capacitive properties at low absolute values of negative potentials was achieved in composites containing Zn-doped FeOOH and polypyrrole-coated carbon nanotubes. Another important finding was a simple procedure for the fabrication of MnO₂ cathodes, which avoided particle agglomeration during the drying stage and facilitated enhanced mixing of MnO₂ and conductive carbon nanotube additives. Enhanced capacitive properties of cathodes and anodes at high active mass loadings allowed good capacitive behavior of the asymmetric devices, which showed promising charge-storage properties for practical applications.

Key words: supercapacitor; iron; polypyrrole; zinc; dopant; nanotube

5.2 Introduction

FeOOH is a promising material for anodes of aqueous supercapacitors[1, 2]. Of particular interest are asymmetric supercapacitor cells with enlarged voltage windows, which contain FeOOH anodes and MnO₂ cathodes in mild A₂SO₄ (A=Li, Na, K) electrolytes[1, 3]. The charging mechanisms of FeOOH and MnO₂ are described by the following reactions:



The interest in FeOOH anodes is attributed to relatively high specific capacitance of FeOOH, which is comparable with specific capacitance of MnO₂ materials for cathodes. The ability to match the capacitance of FeOOH anodes with high capacitance of MnO₂ cathodes is important for the development of cells with high total capacitance. However, from the previous investigations it appears that FeOOH based electrodes showed relatively high resistance and poor cyclic stability[4]. The poor capacitance retention of FeOOH is attributed to relatively high solubility of Fe(II) species formed during electrode cycling in A₂SO₄ electrolyte solutions[5]. Another difficulty is related to the deviation of the shape of cyclic voltammograms (CV) of FeOOH from the ideal box shape, especially at low negative potentials[4]. In contrast, MnO₂ electrodes showed nearly ideal box shape CV even at high electrode mass[6]. This introduces problems for the fabrication of asymmetric devices. Previous investigations[7] highlighted the need in the development of efficient FeOOH electrodes with enhanced performance at high active mass loadings in order to

achieve high areal capacitance and low relative mass of current collector and other passive components.

The goal of this investigation was the development of advanced anodes with enhanced cyclic stability and improved charge-discharge behavior for application in the asymmetric devices. The testing results presented below indicated that Zn doping of FeOOH resulted in enhanced cyclic stability. Further improvement in cyclic stability and charge-discharge behavior of the anodes as well as asymmetric devices was achieved by the fabrication of composites of Zn-doped FeOOH and polypyrrole coated multiwalled carbon nanotubes (MWCNT). Moreover, we report a new procedure for the fabrication of composite MnO₂-MWCNT cathodes, which offers benefits of simplicity and low cost for the mass scale production of the composites with reduced particle agglomeration and enhanced mixing of the individual components. The procedure facilitated the fabrication of electrodes and devices with high active mass loadings, which showed good electrochemical performance.

5.3 Experimental Procedure

Synthesis of FeOOH and Zn-doped FeOOH was based on the method, described in ref[8]. Pure FeOOH, 8%Zn-FeOOH and 12%Zn-FeOOH were mixed with MWCNT (Bayer) to form composites FC, 8ZFC and 12ZFC, respectively. Polypyrrole coated MWCNT were prepared by the method, described in ref[9] and mixed with 12ZFC to form 12ZFCPC composite, containing 50% 12ZFC. The composite slurries in ethanol were impregnated in Ni foam current collectors. The composites contained 30% MWCNT and 3 % polyvinyl butyral (PVB) binder.

For the synthesis of MnO₂-MWCNT composite, 0.5 mL of 40% NaMnO₄ solution was added to a mixture of 1.5 mL water and 5 mL of ethanol. In this procedure, ethanol was used as a reducing agent. The by-product of this reaction contained Na ions. However, the washing procedure was avoided, because Na ions were involved in charging of the active material in the Na₂SO₄ solutions. In this procedure we also avoided drying of MnO₂, which usually results in agglomeration and generates problems with re-dispersion in the device processing medium and mixing with MWCNT. Therefore, MWCNT were added directly to the obtained MnO₂ suspension in a mass ratio of MWCNT:MnO₂=1:4. PVB solution in ethanol was added to the suspension. The mass of the PVB was 3% of the total mass of MWCNT and MnO₂. The suspension was impregnated into the Ni foam current collector to form MnO₂-MWCNT (MC) cathodes. The mass loadings of cathodes and anodes was 40 mg cm⁻².

The electrodes and devices were tested in 0.5 M Na₂SO₄ electrolyte solutions using equipment described in ref.[9]. The individual electrodes were tested in a three-electrode system and device was tested in a two-electrode system.

5.4 Results and Discussion

Figure 5.1(A-D) shows cyclic voltammetry (CV) data at different scan rates for FC, 8ZFC, 12ZFC, 12ZFCPC in the potential range -0.8-0.0 V. The CVs for FC, 8ZFC, 12ZFC show good capacitive behavior at potentials below -0.2 V, as indicated by high currents and large CV areas. However, reduced currents were recorded at lower absolute values of the negative potentials. In contrast, the 12ZFCPC electrodes showed enhanced performance at

potentials -0.2 - 0.0 V (Figure 5.1D) and -0.2 - +0.1 V(Supplementary materials, Figure 5.5). It will be shown below that improved charge storage properties of 12ZFCPC offer benefits for the fabrication of asymmetric devices.

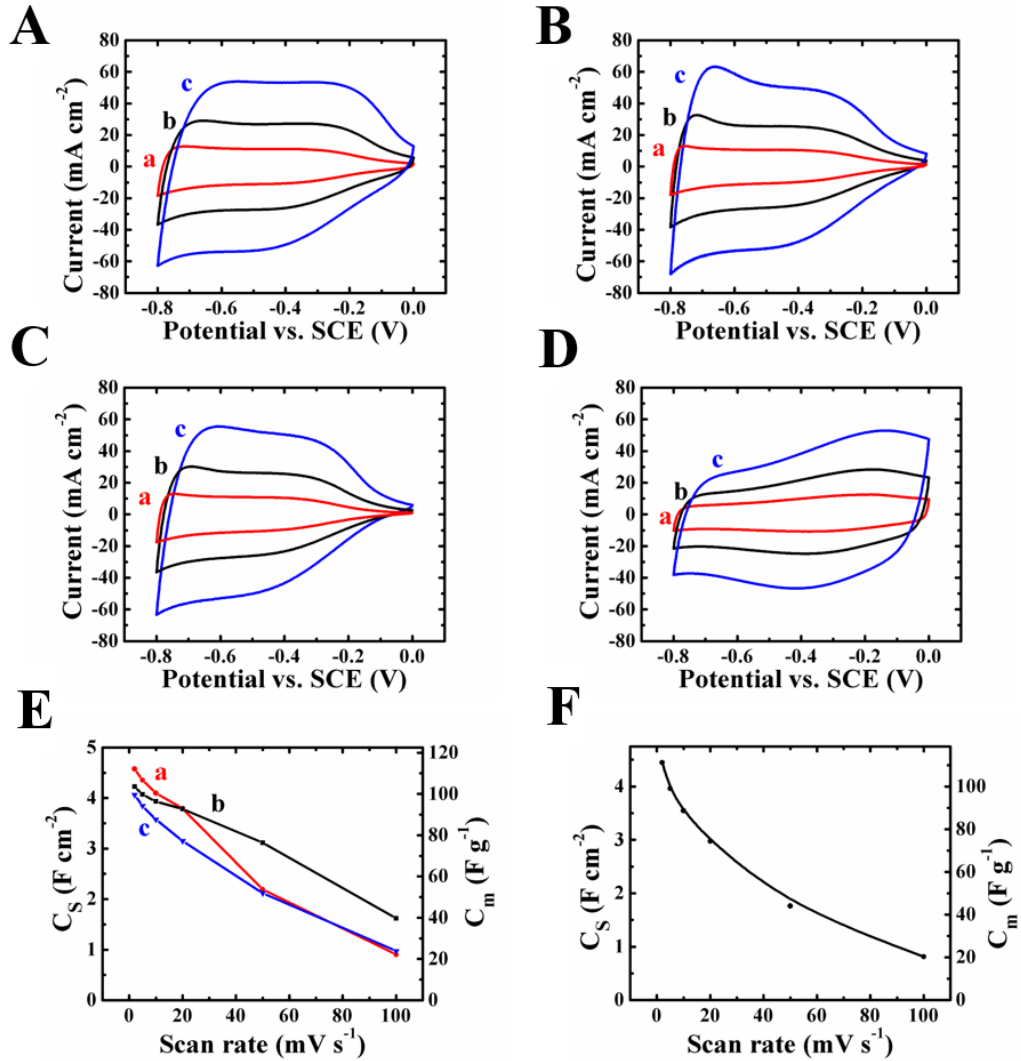


Figure 5.1: (A–D) CVs at scan rates of (a) 2, (b) 5 and (c) 10 mV s⁻¹ and (E,F) C_s and C_m versus scan rate for (A, E(a)) FC, (B, E(b)) 8ZFC, (C, E(c)) 12ZFC, (D,F) 12ZFCPC.

Figure 5.1(E,F) shows capacitances of the composites versus scan rate. The FC, 8ZFC, 12ZFC and 12ZFCPC electrodes showed capacitances of 4.5, 4.2, 4.0 and 4.4 F cm⁻²,

respectively, at a scan rate of 2 mV s^{-1} . The capacitance, normalized by the FeOOH mass was 112.1, 111.7 and 111.7 F g^{-1} for FC, 8ZFC and 12ZFC, respectively. The capacitance decreased with increasing scan rate due to electrolyte diffusion limitations in pores of the electrode materials. The electrodes showed relatively low impedance and relaxation type dispersion of complex AC capacitance, derived from the impedance data (Figure 5.6, Figure 5.7).

FC, 8ZFC, 12ZFC electrodes exhibited maxima in the capacitance retention (Figure 5.2A). The capacitance increase at the beginning of the cycling can result from the changes in the electrode microstructure. We suggested that partial dissolution of the Fe(II) species can result in increased porosity and improved electrolyte access to the bulk of the active materials.

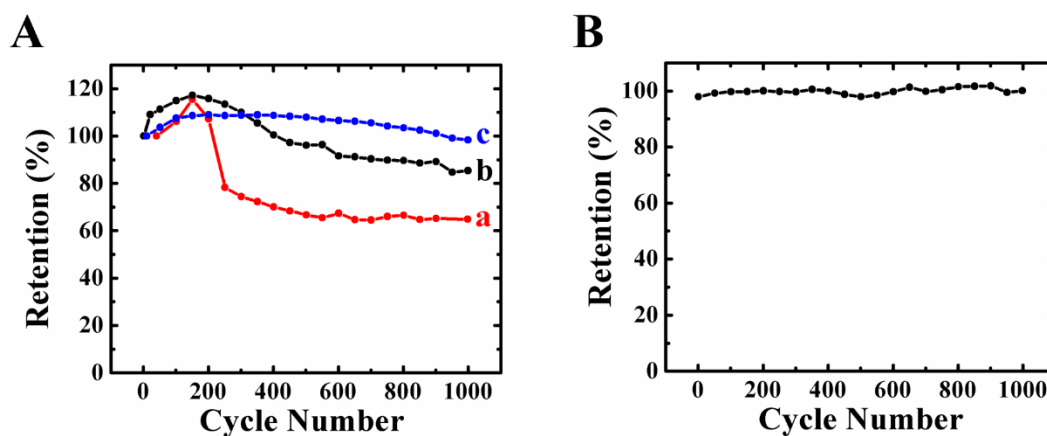


Figure 5.2: Capacitance retention versus cycle number for (A)(a) FC (b) 8ZFC (c) 12ZFC (B) 12ZFCPC.

However, FC showed significant reduction of the capacitance after first 150 cycles and capacitance retention of 64% was obtained after 1000 cycles. In order to reduce electrode

degradation during cycling, we modified FeOOH with Zn. 8ZFC and 12ZFC showed capacitance retention of 85 and 98%, respectively after 1000 cycles. It is known that Zn compounds promote iron hydroxide precipitation [10]. Therefore, more electrochemically negative Zn species prevent release of the Fe(II) ions from the electrodes during cycling. 12ZFCPC showed 98% cyclic stability and reduced capacitance variations during 1000 cycles (Figure 5.2B).

MC electrodes, prepared by a modified method showed (Figure 5.3) nearly box-shape CVs in the potential range of 0.0 - +0.9V and relatively high capacitance of 5.3 F cm⁻² at 2 mV s⁻¹, which was achieved at low electrode impedance (Figure 5.8).

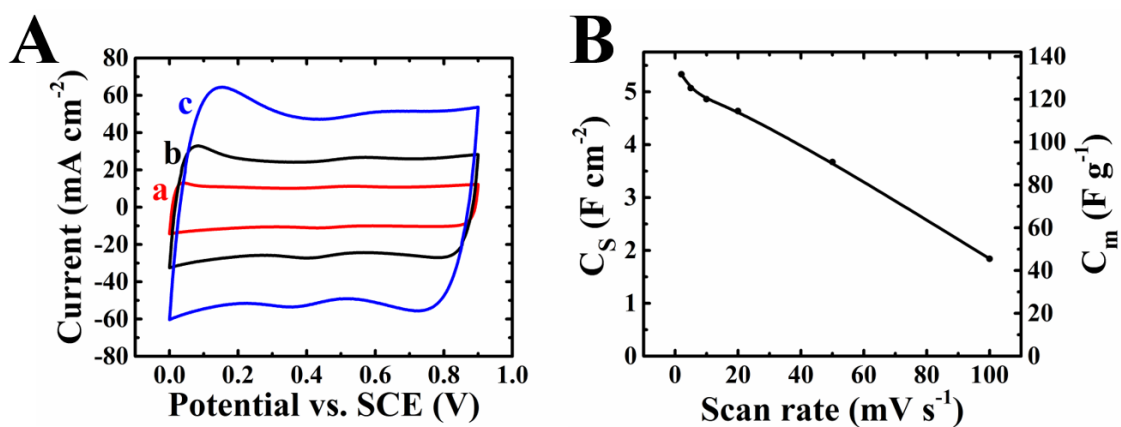


Figure 5.3: (A) CVs at scan rates of (a) 2, (b) 5 and (c) 10 mV s⁻¹, and (B) C_s and C_m versus scan rate for MC.

Therefore, the procedure, developed in this investigation is promising for the practical application. It offers benefits of simplicity, reduced agglomeration and improved mixing of MnO₂ and MWCNT.

12ZFC and 12ZFCPC were combined with MC for the fabrication of the asymmetric devices. The capacitance of the asymmetric devices is given by formula $1/C=1/C_C+1/C_A$, where C_C and C_A are the capacitances of cathode and anode, respectively. The relatively poor capacitive properties of 12ZFC at low absolute values of the negative potential resulted in the poor capacitive properties of the 12ZFCMC device at voltages below 0.2 V, as indicated by the low CV areas in this range (Figure 5.4). However, nearly box-shape CVs were obtained for the 12ZFCPC-MC devices, which showed higher capacitance and low impedance (Figure 5.9). The galvanostatic charge-discharge curves were of nearly triangular shape (Figure 5.10). The highest capacitance of 2.2 F cm^{-2} was obtained at 2 mV s^{-1} . The 12ZFCPC-MC devices were capable of powering a blue LED display (Figure 5.4D, inset).

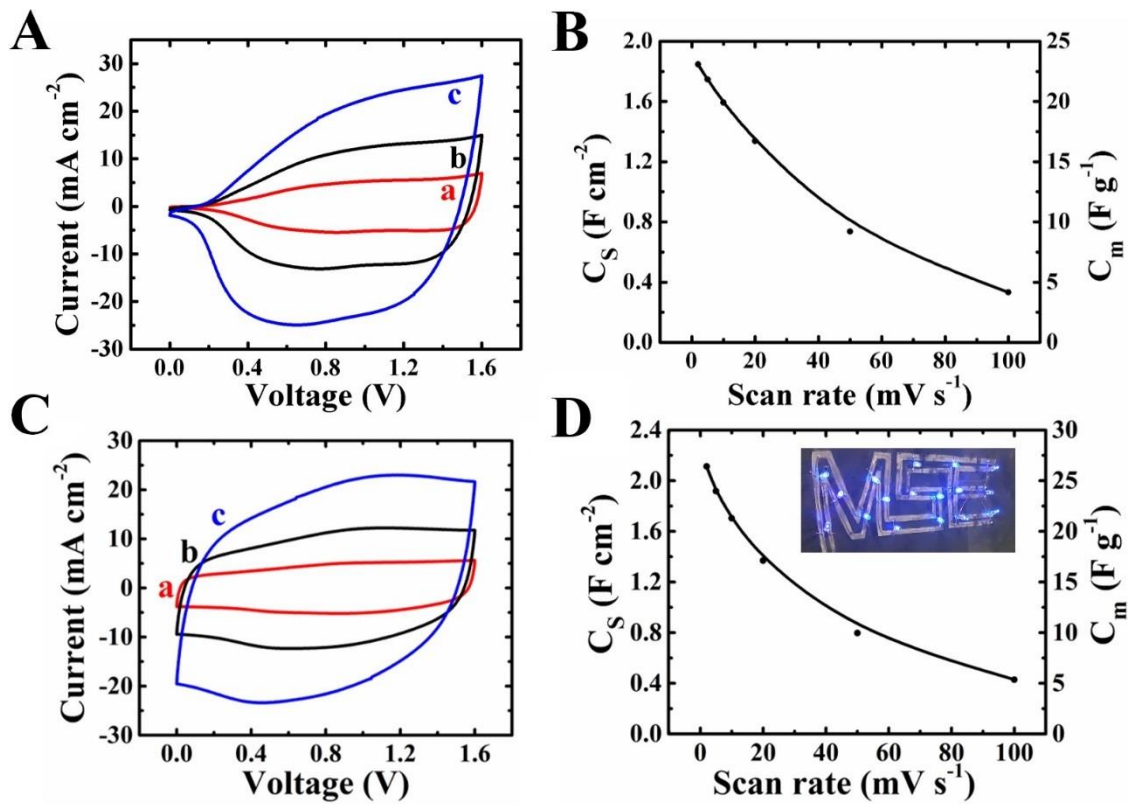


Figure 5.4: Testing data for (A,B) 12ZFC-MC and (C,D) 12ZFCPC-MC cells: (A,C) CVs at scan rates of (a)2, (b) 5 and (c) 10 mV s⁻¹, and (B,D) Cs and Cm, inset shows LEDs powered by a supercapacitor module.

5.5 Conclusions

The problem of poor cyclic stability of FeOOH anodes was addressed by Zn-doping. Testing results showed that 8ZFC, 12ZFC exhibit significant improvement in capacitance retention during cycling. Further improvement in capacitance retention and capacitive properties at low absolute values of negative potentials was achieved in 12ZFCPC composites. Another important finding was a simple procedure for the fabrication of MC anodes, which avoided particle agglomeration during the drying stage and facilitated enhanced mixing of the individual components. Enhanced capacitive properties of cathodes and anodes allowed good capacitive behavior of the 12ZFCPC – MC devices, which showed promising capacitive properties for practical applications.

5.6 Acknowledgements

The authors gratefully acknowledge the Natural Sciences and Engineering Research Council of Canada for the financial support.

5.7 Supplementary Materials

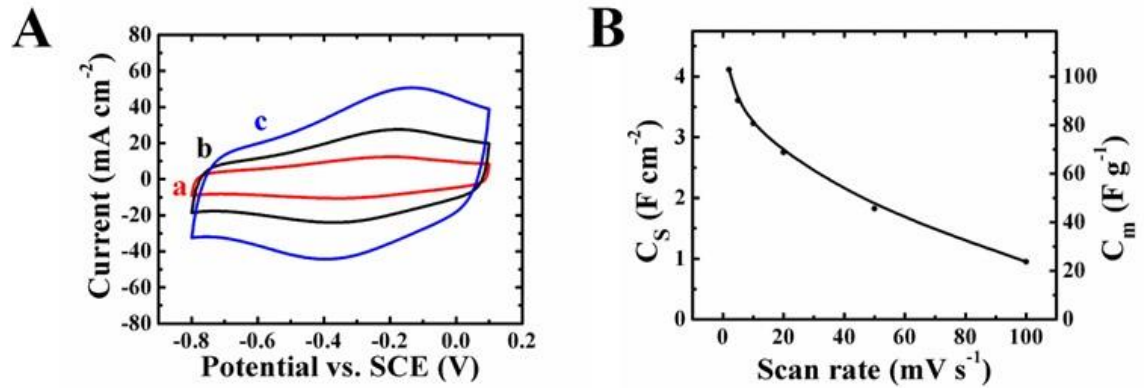


Figure 5.5: (A) CVs at scan rates of (a) 2, (b) 5 and (c) 10 mV s⁻¹ and (B) C_S and C_m versus scan rate for 12ZFCPC.

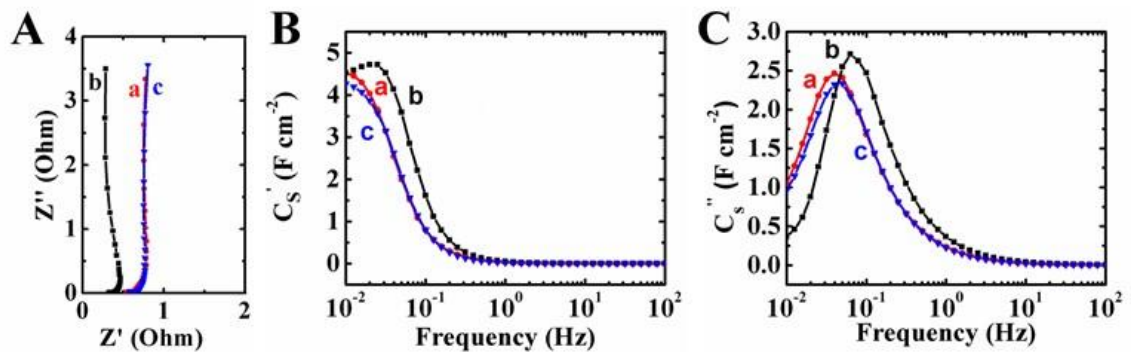


Figure 5.6: (A) Nyquist plot of complex impedance, and frequency dependences of (B) C_S' and (C) C_S'' for (a) FC, (b) 8ZFC, (c) 12ZFC.

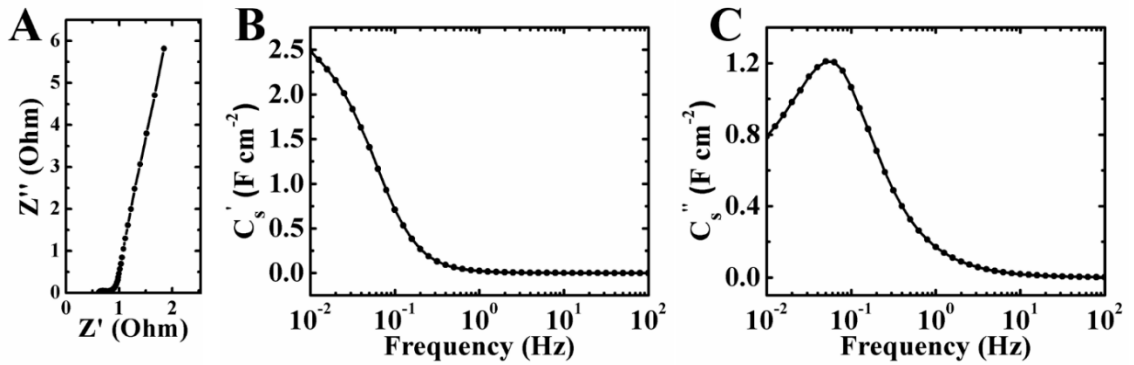


Figure 5.7: (A) Nyquist plot of complex impedance, and frequency dependence of (B) C_s' and (C) C_s'' for 12ZFCPC.

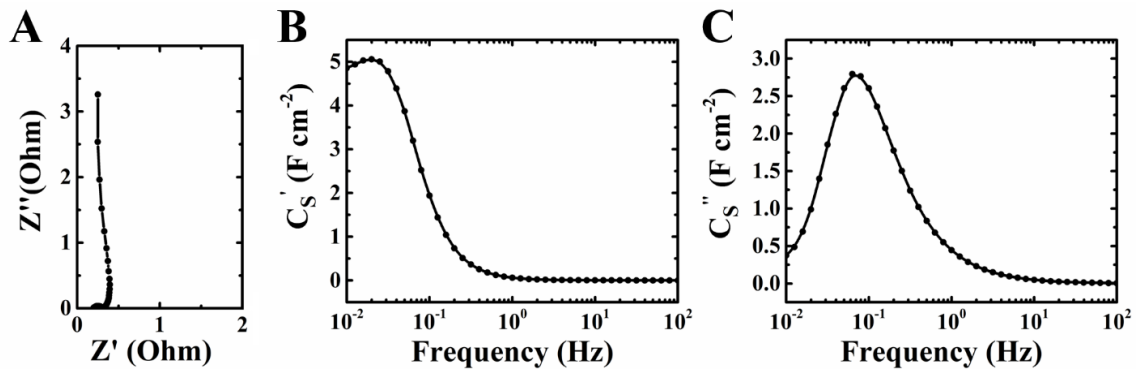


Figure 5.8: (A) Nyquist plot of complex impedance, and frequency dependence of complex capacitance (B) C_s' and (C) C_s'' for MC.

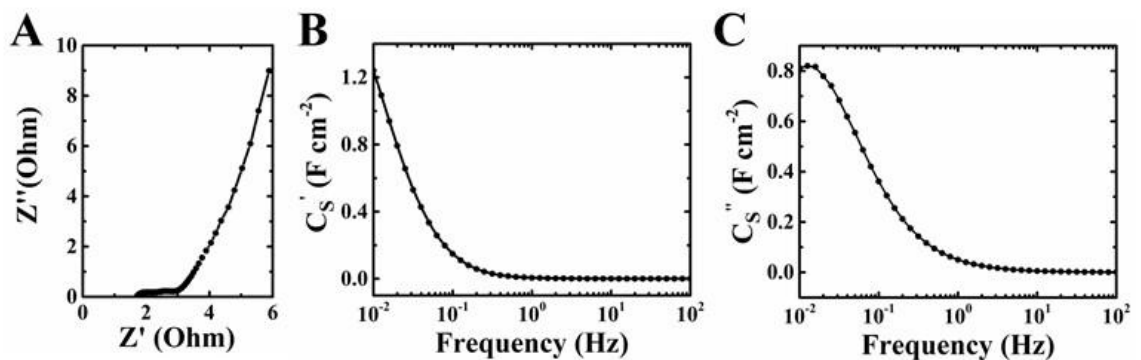


Figure 5.9: Nyquist plot of complex impedance, and frequency dependence of complex capacitance (B) C_s' and (C) C_s'' for asymmetric 12ZFCPC-MC device.

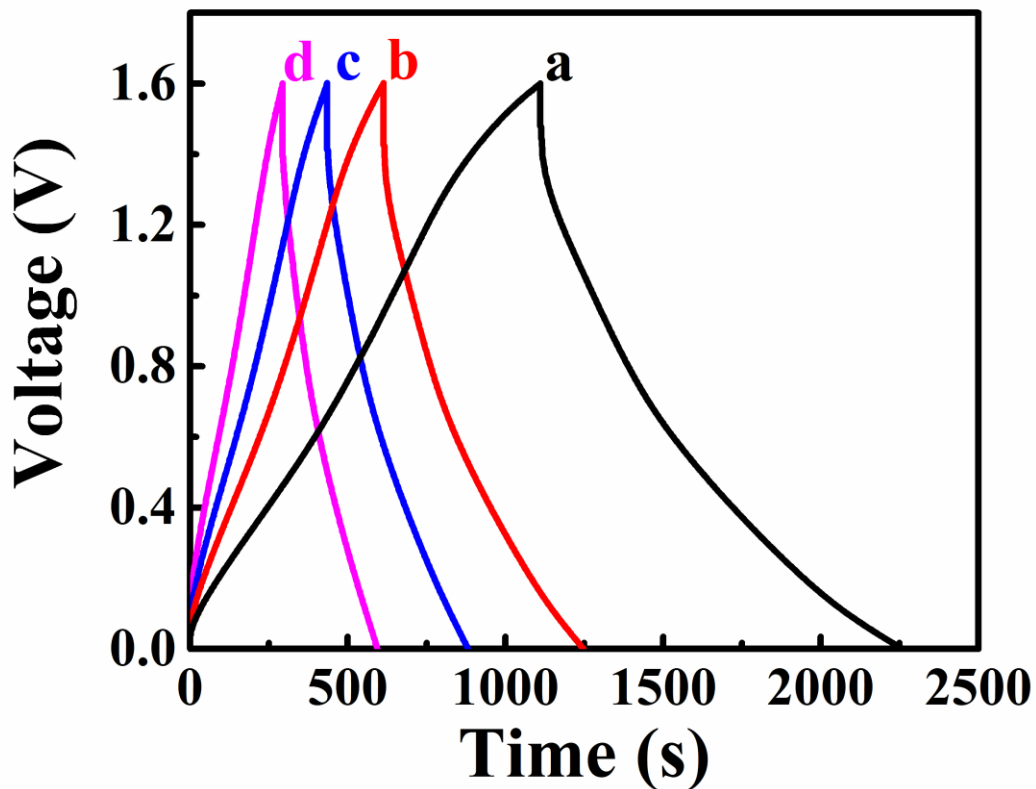


Figure 5.10: Galvanostatic charge-discharge for asymmetric 12ZFCPC-MC device at current densities of (a) 3, (b) 5, (c) 7 and (d) 10 mA cm⁻².

5.8 References

- [1] Y.C. Chen, Y.G. Lin, Y.K. Hsu, S.C. Yen, K.H. Chen, L.C.J.S. Chen, Novel iron oxyhydroxide lepidocrocite nanosheet as ultrahigh power density anode material for asymmetric supercapacitors, *Small* 10 (2014) 3803-3810.
- [2] X. Gong, S. Li, P.S. Lee, A fiber asymmetric supercapacitor based on FeOOH/PPy on carbon fibers as an anode electrode with high volumetric energy density for wearable applications, *Nanoscale* 9 (2017) 10794-10801.
- [3] R. Barik, B.K. Jena, A. Dash, M. Mohapatra, In situ synthesis of flowery-shaped α -FeOOH/Fe₂O₃ nanoparticles and their phase dependent supercapacitive behaviour, *RSC Advances* 4 (2014) 18827-18834.
- [4] Q. Shou, J. Cheng, L. Zhang, B.J. Nelson, X. Zhang, Synthesis and characterization of a nanocomposite of goethite nanorods and reduced graphene oxide for electrochemical capacitors, *Journal of Solid State Chemistry* 185 (2012) 191-197.
- [5] K.K. Lee, R.W.Y. Ng, K.K. She, W.S. Chin, C.H. Sow, Vertically aligned iron (III) oxyhydroxide/oxide nanosheets grown on iron substrates for electrochemical charge storage, *Materials Letters* 118 (2014) 150-153.
- [6] Y. Su, I. Zhitomirsky, Hybrid MnO₂/carbon nanotube-VN/carbon nanotube supercapacitors, *Journal of Power Sources* 267 (2014) 235-242.
- [7] R. Chen, I.K. Puri, I. Zhitomirsky, High areal capacitance of FeOOH-carbon nanotube negative electrodes for asymmetric supercapacitors, *Ceramics International* 44 (2018) 18007-18015.
- [8] S. Krehula, S. Musić, Ž. Skoko, S. Popović, The influence of Zn-dopant on the precipitation of α -FeOOH in highly alkaline media, *Journal of Alloys and Compounds* 420 (2006) 260-268.
- [9] Y. Su, I. Zhitomirsky, Asymmetric electrochemical supercapacitor, based on polypyrrole coated carbon nanotube electrodes, *Applied Energy* 153 (2015) 48-55.
- [10] M.R.C. Ismael, J.M.R. Carvalho, Iron recovery from sulphate leach liquors in zinc hydrometallurgy, *Minerals Engineering* 16 (2003) 31-39.

Chapter 6 Phase transfer of oxide particles for application in thin films and supercapacitors

R. Poon*, X. Zhao*, M.S. Ata*, A. Clifford*, I. Zhitomirsky*^α

*Department of Materials Science and Engineering, McMaster University,
Hamilton, Ontario, L8S 4L7, Canada

^αCorresponding Author: zhitom@mcmaster.ca; 905-525-9140 ext. 23914

Submitted on 22nd February 2017. Accepted on 21st March 2017.

Copyright 2017, reproduced with permission from Elsevier.

Author's Contributions:

- Synthesis of Mn₃O₄-MWCNT electrode materials
- Electrochemical testing of Mn₃O₄-MWCNT electrode
- Characterization of composite with XRD and FTIR
 - Manuscript preparation

6.1 Abstract

This paper reports efficient liquid-liquid extraction strategies for concentrated suspensions of oxide particles and demonstrates the benefits of using such strategies for thin film applications and the fabrication of supercapacitor electrodes. We performed materials synthesis in an aqueous phase and achieved efficient materials transfer to an organic phase, avoiding agglomeration during the drying stage. The metal oxides, suspended in an organic solvent were used directly for the deposition of polymer-titania composite films and fabrication of Mn₃O₄-carbon nanotube composite electrodes for supercapacitors. Strategy E1 involved the modification of particles in-situ during synthesis and a Schiff base reaction with an extractor at the liquid-liquid interface. In the one-step E2 procedure the interface reactions were used for the extraction. We discuss advantages of the E1 and E2 strategies. Both strategies featured a biomimetic approach for the surface modification of the particles, which allowed for strong adsorption of the extractors. The ability to perform efficient extraction using concentrated suspensions allowed for the fabrication of Mn₃O₄-carbon nanotube electrodes with high active mass loading. The electrodes showed a capacitance of 2.63 F cm⁻², good capacitance retention at high charge-discharge rates and low impedance. The results of this investigation pave the way for the agglomerate free processing of various functional materials for applications in advanced films, coatings and devices.

Key words: supercapacitor, manganese oxide, titania, carbon nanotube, energy storage, particles

6.2 Introduction

The creation of advanced materials for electronic, electrochemical, magnetic and optical applications can be accomplished by the development of advanced techniques for the synthesis and processing of functional metal oxide particles. In many fabrication procedures [1–3], the use of organic solvents is critical for the development of moisture stable ceramic films, coatings and devices. In such procedures, the particles must be dispersed in organic solvents, containing dissolved functional organic molecules or macromolecules, binders and film forming agents, which are insoluble in water. Organic solvents are used in many film fabrication techniques, such as electrophoretic deposition [4,5], spray deposition [6], spin-casting [7] and dip coating [8]. The use of organic solvents is of particular importance for tape casting of multilayer solid-state capacitors and fuel cells, due to the superior properties of polymer binders that are soluble in organic solvents, compared to water soluble binders [9]. Non-aqueous processing is critical for the development of electrodes of aqueous supercapacitors and batteries, biomedical implants and other composites containing water insoluble polymers as functional components or film forming agents [10,11].

It is important to note that many important techniques for inorganic particle synthesis are based on aqueous processing. The synthesized particles are usually dried and then re-dispersed in organic solvents for the fabrication of films, coatings and devices. However, drying the particles results in their agglomeration. The reduction of particle surface energy

and condensation of surface OH groups are major driving forces for the formation of hard agglomerates. This problem can be addressed by using liquid-liquid extraction to transfer the synthesized particles from an aqueous phase to an organic phase, avoiding the particle agglomeration during the drying stage.

Recent investigations showed that particles of metals and quantum dots can be extracted from water to different organic solvents. Various strategies have been developed for the extraction of gold [12–14] and silver [15] nanoparticles. Size-dependent transfer of gold particles allowed obtaining suspensions with narrow particle size distribution [16]. Luminescent CdTe and HgTe quantum dots, synthesized in an aqueous media were transferred to non-polar organic solvents for the fabrication of photovoltaic and optoelectronic devices [17]. Liquid-liquid extraction has been utilized for the separation of rare earth fluorescent powders [18]. It was found that magnetite particles [19] can be transferred from an aqueous to an organic phase for applications in magnetic devices.

Considerable attention has been given to the development extractor molecules [16,18,20–22] and analysis of the extraction mechanisms [23]. The extraction efficiency was enhanced in the presence of cosolvents, such as sub-oil phase [22] or acetone [17] and by changes of temperature [24]. In many cases the investigations were focused on the use of very dilute suspensions of metal nanoparticles. The important task is the development of efficient extractors for the particles of functional oxides in concentrated suspensions. However, the major difficulty in particle extraction is poor adsorption of the extractor molecules on the oxide particle surface at the liquid-liquid interface.

The goal of this investigation was the development of advanced methods for the extraction of oxide particles, synthesized in an aqueous phase to an organic phase. Mn_3O_4 and titania were selected as model materials, which have a variety of advanced functional properties. Two strategies, described below, were based on strong adsorption of molecules from the catechol and gallic acid families on the oxide particles. One strategy involved the in-situ modification of particles in an aqueous phase during synthesis and then at the liquid-liquid interface using a Schiff base reaction with extractor molecules. Another strategy involved modifications only at the liquid-liquid interface. Both techniques allowed for the use of concentrated suspensions. The advantages of the methods were demonstrated by the fabrication and testing of Mn_3O_4 -carbon nanotube electrodes for supercapacitors, which showed high capacitance at high active mass loading. Moreover, we showed advantages of the liquid-liquid extraction for the fabrication of composite polymer-titania films, containing well dispersed titania particles.

6.3 Experimental Procedure

3,4-dihydroxybenzaldehyde, 1-hexadecylamine, lauryl gallate, TiOSO_4 , $\text{Mn}(\text{NO}_3)_2$, NaOH , 1-butanol, poly(vinyl butyral-co-vinyl alcohol-co-vinyl acetate) (PVB, average $M_w=50,000-80,000$) (Aldrich), multiwalled carbon nanotubes (MWCNT, ID 4 nm, OD 13 nm, length 1–2 μm , Bayer, Germany) were used. Ni foams with 95% porosity were provided by Vale Limited Company.

The synthesis of colloidal titania [25] was performed using aqueous TiOSO_4 solutions. The pH of the solutions was adjusted to $\text{pH} = 6$ by NaOH . The synthesis of Mn_3O_4 particles [26]

was performed using $\text{Mn}(\text{NO}_3)_2$ solutions. The pH of the solutions was adjusted to pH = 10 by NaOH.

The precipitates were washed with water, dried in air and then used for X-ray diffraction and electron microscopy analysis.

The extraction procedures E1 and E2 were based on the use of water immiscible 1-butanol as the receiving organic liquid, containing 1-hexadecylamine or lauryl gallate as extractors. The concentration of titania and Mn_3O_4 in the 1-butanol phase after extraction was varied in the range of 5–15 g L⁻¹. The mass ratio of extractor/oxide was 0.2–0.3.

In the extraction procedure E1, 3,4-dihydroxybenzaldehyde was added to TiOSO_4 or $\text{Mn}(\text{NO}_3)_2$ solutions before synthesis. After the pH adjustment and precipitation, the 1-hexadecylamine solution in 1-butanol was added. The particles were extracted to 1-butanol using 1-hexadecylamine as an extractor, which reacted with 3,4-dihydroxybenzaldehyde, adsorbed on the particle surface. It is important to note that 1-hexadecylamine did not allow extraction without surface modification of the particles with 3,4-dihydroxybenzaldehyde. In the extraction procedure E2, titania and Mn_3O_4 synthesized without 3,4-dihydroxybenzaldehyde additive, were extracted to 1-butanol phase using lauryl gallate as an extractor. In both procedures the ultrasonic agitation and stirring facilitated the extraction of the precipitated materials to the 1-butanol phase.

The suspension of titania, prepared by the procedure E1, was mixed with PVB solution in ethanol and used for the deposition of composite films on stainless steel substrates by spray coating. The mass ratio of titania to PVB was 1:1.

The suspension of Mn_3O_4 , prepared by the procedure E2, was mixed with MWCNT suspension in 1-butanol, containing lauryl gallate as a dispersant and dissolved PVB as a binder. The mass ratio of Mn_3O_4 :MWCNT:PVB was 80:20:3. The obtained slurry was used for the impregnation of Ni foam current collectors for the fabrication of supercapacitor electrodes. The mass loading of the impregnated material after drying was 30.4 mg cm^{-2} . Electron microscopy investigations were performed using a JEOL JSM-7000F scanning electron microscope (SEM). X-ray diffraction (XRD) studies were performed using a powder diffractometer (Nicolet I2, monochromatized $\text{CuK}\alpha$ radiation). FTIR studies were performed on Bruker Vertex 70 spectrometer. Dynamic light scattering (DLS, DelsaMax Pro: Beckman Coulter) was used for the particle size distribution analysis. The suspensions of particles in 1-butanol, separated from the aqueous phase, were diluted with ethanol for the particle distribution analysis.

Cyclic voltammetry and impedance spectroscopy investigations were performed using a potentiostat (PARSTAT 2273, Princeton Applied Research, USA). Capacitive behavior of the electrodes was studied in three-electrode cells using 0.5 M Na_2SO_4 aqueous solutions. The area of the working electrode was 1 cm^2 . The counter electrode was a platinum gauze, and the reference electrode was a standard calomel electrode (SCE). Cyclic voltammetry (CV) studies were performed at scan rates of 2–100 mV s^{-1} . The integral capacitances $C_S=Q/\Delta V_S$ and $C_m=Q/\Delta V_m$ were calculated using half the integrated area of the CV curve to obtain the charge Q , and subsequently dividing the charge Q by the width of the potential window ΔV and electrode area S or active mass m . The alternating current measurements of complex impedance $Z^* = Z' - iZ''$ were performed in the frequency range of 10 mHz –

100 kHz at the amplitude of the signal of 5 mV. The complex differential capacitance $C_S^* = C_S' - iC_S''$ was calculated [27] from the impedance data as $C_S' = Z''/\omega|Z|^2S$ and $C_S'' = Z'/\omega|Z|^2S$, where $\omega = 2\pi f$ (f -frequency).

6.4 Results and Discussion

Figure 6.1 shows X-ray diffraction patterns of the synthesized and dried materials. The titania particles were amorphous. The XRD pattern for Mn_3O_4 shows diffraction peaks, corresponding to the JCPDS file 024-0734. Figure 6.2 shows SEM images of Mn_3O_4 and titania particles after drying. The dried powders of both materials contained large agglomerates, which are detrimental for many applications.

The liquid-liquid extraction procedures E1 and E2 were developed in order to avoid the drying process and reduce particle agglomeration. The approach was based on the use of 1-butanol as an organic solvent, immiscible with water. In the E1 procedure the particles were modified with 3,4-dihydroxybenzaldehyde (R' -CHO). Figure 6.3(A) shows a chemical structure of this molecule, which includes a catechol group and an aldehyde group. The unique property of catecholates is their strong adsorption on various inorganic surfaces. The catechol chemistry allows high bonding strength under wet conditions. The interest in catecholate adhesives resulted from the fundamental investigations [28–30] of mechanisms of strong mussel adhesion to different surfaces in seawater, which involved protein macromolecules, containing catecholic amino acid, L-3,4-dihydroxyphenylalanine. Further investigations of catecholates resulted in the development of advanced capping and dispersing agents for the synthesis and dispersion of inorganic nanoparticles [5,31].

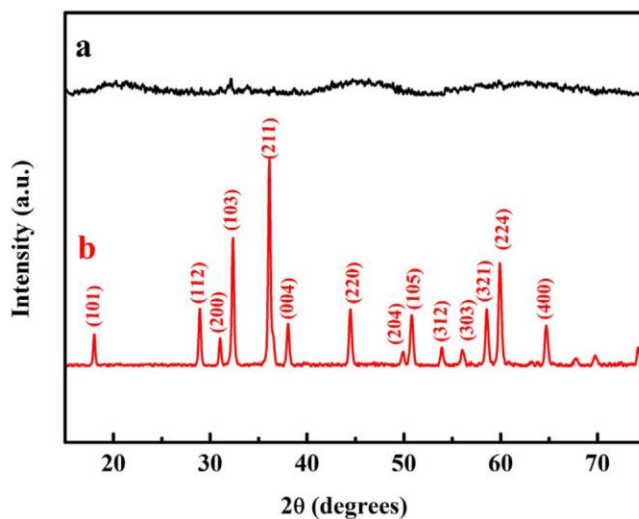


Figure 6.1: X-ray diffraction patterns of (a) titania and (b) Mn₃O₄, prepared by chemical precipitation.

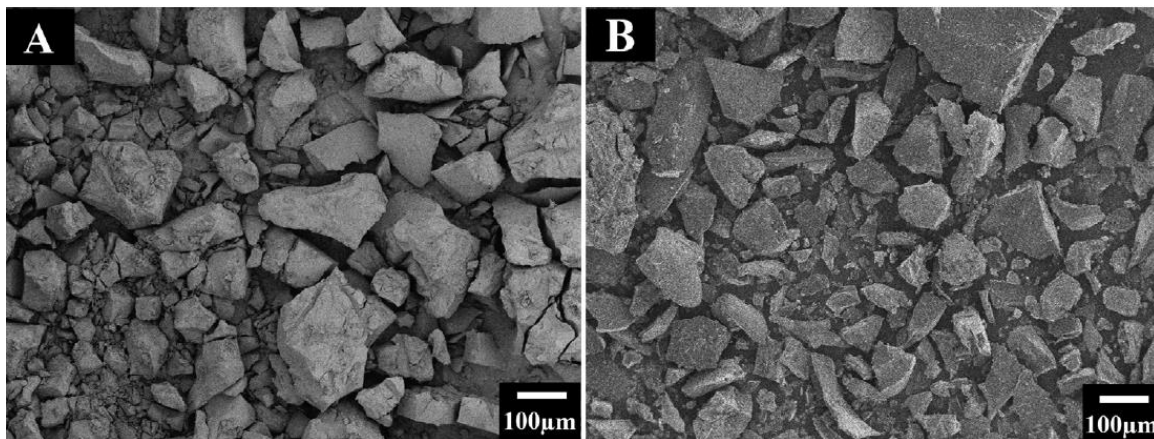


Figure 6.2: SEM images of (a) Mn₃O₄ and (b) titania powders.

We found that the particles, modified with R'-CHO in water can be extracted to the 1-butanol phase using 1-hexadecylamine (NH₂R'') as an extractor. It is important to note that we did not observe extraction of unmodified particles due to the poor adsorption of NH₂R'' on the particles. Figure 6.3(B) shows a chemical structure of NH₂R''. This molecule is a typical head-tail surfactant, insoluble in water.

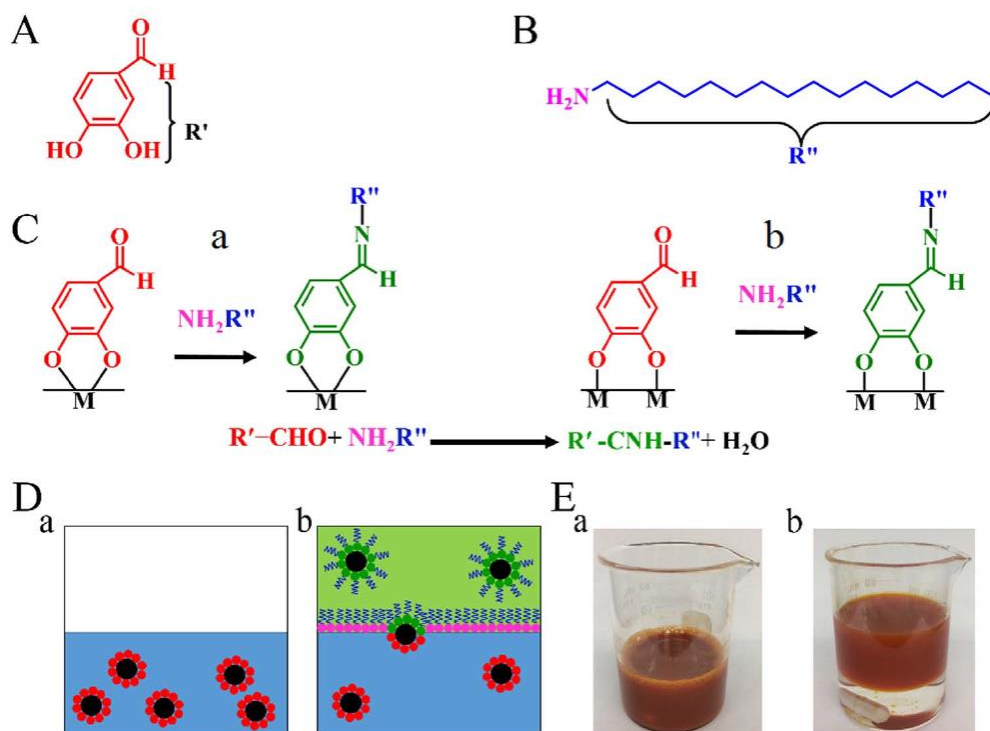


Figure 6.3: (A) Chemical structure of $R'-CHO$, (B) chemical structure of H_2NR'' , (C) Schiff base reactions between H_2NR'' and $R'-CHO$, adsorbed by (a) chelation or (b) bridging of metal atoms (M) on the particle surface, (D) schematic of extraction, involving (a) modification of particles with $R'-CHO$ during synthesis and (b) extraction by Schiff base formation, (E) (a) synthesized titania, modified with $R'-CHO$, (b) extracted titania.

The extraction mechanism involved the Schiff base reaction of the aldehyde groups of $R'-CHO$ and amino groups of NH_2R'' . Figure 6.3(C) shows adsorption of $R'-CHO$ on particles by (a) chelating bonding [5] and (b) bridging bonding [5] of metal atoms on particle surfaces and the Schiff base reaction with NH_2R'' . The synthesis and extraction steps are illustrated in Figure 6.3D(a), (b).

The particles prepared without $R'-CHO$ showed relatively fast sedimentation. In contrast, the adsorption of $R'-CHO$ on particles resulted in improved colloidal stability in the

aqueous phase. This is not surprising, because various catecholates molecules with a similar structure were found to be efficient dispersants for inorganic particles [5]. It was found that R'-CHO adsorption on colloidal titania particles resulted in color change from white to red (Figure 6.3E(a)). A similar color change was observed for colloidal titania particles, modified with other catecholates molecules [25]. The modification of oxide particles with catecholates is of significant scientific interest, because it resulted in advanced optical, photovoltaic, magnetic, charge transfer and other functional properties [5,25]. The red color of the particles remained after their transfer to the organic phase (Figure 6.3E(b)). The aqueous phase was clear and colorless (Figure 6.3E(b)) after the transfer, indicating efficient extraction, which was achieved at relatively high suspension concentrations. Similar to other head-tail surfactants, NH₂R'' was accumulated at the liquid-liquid interface with hydrophilic -NH₂ groups exposed to water and hydrophobic hydrocarbon groups extended out of the water phase into the organic phase. The Schiff base reaction resulted in the modification of the particles at the liquid-liquid interface and allowed particle transfer to the organic phase (Figure 6.3D(b)). The liquid-liquid interface provided unique conditions for surface modification, because the accumulation of NH₂R'' molecules and their orientation at the interface facilitated the Schiff base reaction.

The results of the FTIR analysis supported the proposed extraction mechanism. Figure 6.4 compared the FTIR spectra of as-received NH₂R'', R'-CHO, extracted titania and Mn₃O₄ particles. The peaks at 2848 and 2920 cm⁻¹ in the spectrum of NH₂R'' are attributed to stretching vibrations [32,33] of CH₂ and CH₃ groups. The absorption at 1488 cm⁻¹ resulted from the deformation C-H vibrations [32]. The absorptions at 1651 and 1589 cm⁻¹ in the

spectrum of R'-CHO resulted from aromatic C—C vibrations and the absorption at 1294 cm^{-1} was attributed to C—O stretching vibrations [34]. Similar absorptions, observed in the spectra of the extracted particles (Figure 6.4(c),(d)), indicated that $\text{NH}_2\text{R}''$ and R'-CHO adsorbed on the particles and formed a Schiff base.

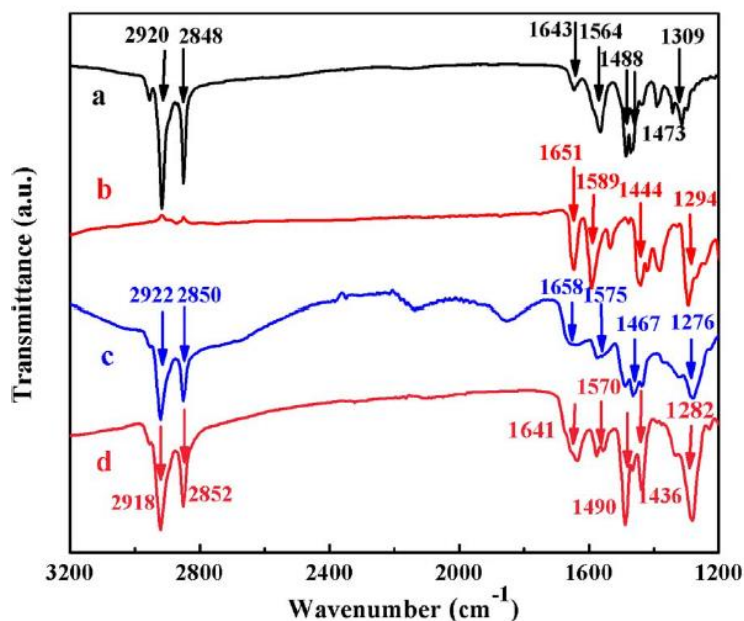


Figure 6.4: FTIR spectra of (a) $\text{H}_2\text{NR}''$, (b) R'-CHO, (c) titania, extracted by Schiff base formation, (d) Mn_3O_4 , extracted by Schiff base formation.

The extraction of the synthesized particles from water to the organic phase resulted in the reduced particle agglomeration. The investigation of extracted particles by dynamic light scattering method (Figure 6.5) showed that the average radius of titania and Mn_3O_4 particles was 63 and 69 nm, respectively. The extracted titania particles were used for the fabrication of TiO_2 -PVB films by spray coating. The SEM image (Figure 6.6) showed relatively smooth and continuous film. The comparison of such morphology with SEM

image of the dried powder (Figure 6.2) indicated that the formation of large agglomerates was avoided by eliminating the drying stage.

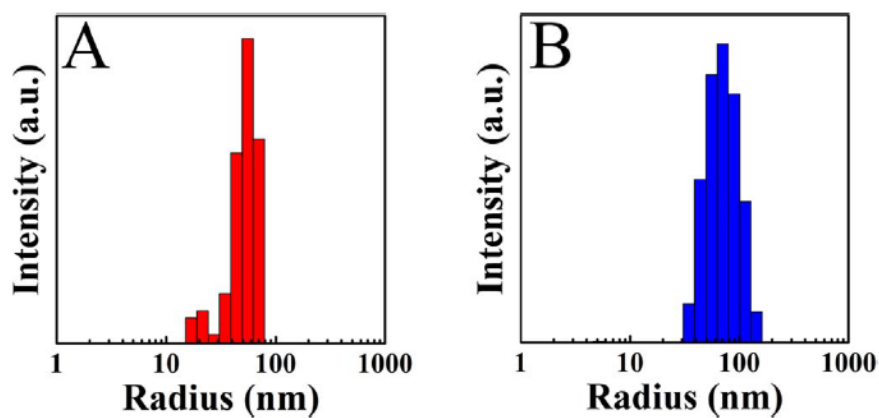


Figure 6.5: Particle size distribution for (a) titania and (b) Mn₃O₄, extracted by Schiff base formation method.

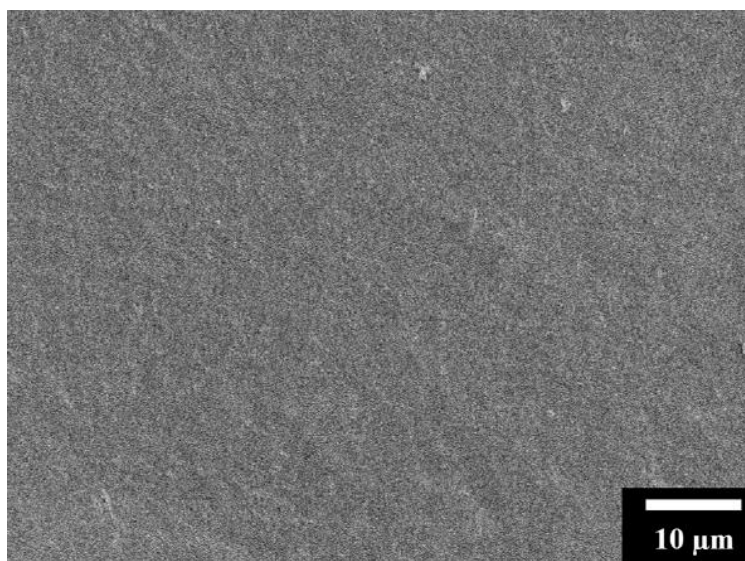


Figure 6.6: SEM image of a titania-PVB film.

The interest in TiO₂-PVB composite is attributed to their advanced antibacterial properties and biocompatibility [35], corrosion protection [36,37], mechanical, selective permeability and other functional properties [38–40].

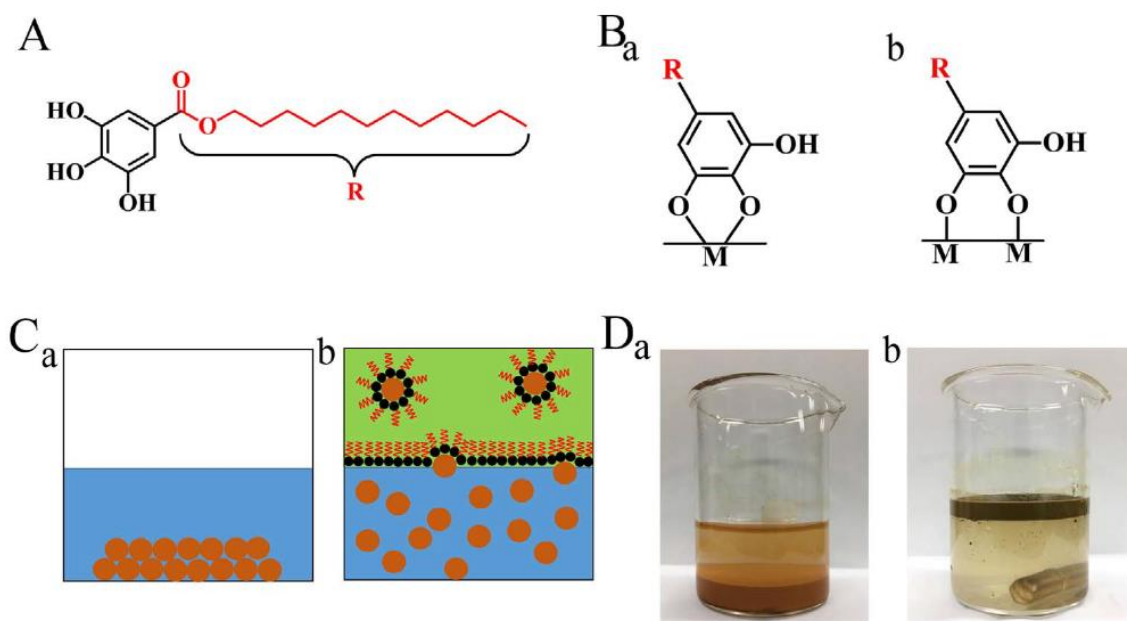


Figure 6.7: (A) Chemical structure of GR, (B) GR adsorption on a particle surface by (a) chelation and (b) bridging of metal atoms (M) on a particle surface, (C) schematic of extraction, involving (a) synthesis and precipitation of particles and (b) extraction using GR adsorption at the liquid-liquid interface, (D) (a) precipitated Mn₃O₄ and (b) Mn₃O₄ extraction by adsorbed GR.

In the extraction procedure E2 we used lauryl gallate (GR) molecules as extractors. The chemical structure (Figure 6.7A) of GR includes the hydrophilic galloyl group and a hydrophobic hydrocarbon group. The galloyl group contains three phenolic OH groups, bonded to the adjacent carbon atoms of the aromatic ring. Similar to catechol, the galloyl group shows remarkably strong adsorption on particles by chelating (Figure 6.7B(a)) or bridging (Figure 6.7B(b)) mechanisms. It is important to note that GR is insoluble in water.

Similar to other head-tail surfactants, the GR molecules accumulated at the liquid-liquid interface with hydrophilic galloyl groups exposed to water and hydrophobic hydrocarbon tails extended out of the water phase into the organic phase. Such accumulation and orientation of the GR molecules facilitated GR adsorption on the particles at the liquid-liquid interface and particle extraction. Figure 6.7(C) shows a schematic of extraction, which was also illustrated by the images of Mn_3O_4 suspension before and after extraction (Figure 6.7D(a),(b)).

The adsorption of GR on particles was confirmed by the results of the FTIR studies. The FTIR spectrum (Figure 6.8(a)) of as-received GR shows absorptions at 2916 and 2848 cm^{-1} , related to stretching vibrations [32,33] of CH_2 and CH_3 groups. The spectra of extracted materials (Figure 6.8(b),(c)) showed similar peaks, indicating that GR was adsorbed on the particle surfaces. The peaks in the range of 1400–1600 cm^{-1} , related to stretching C–C vibrations [41] of the aromatic ring of GR (Figure 6.8(a)) were also observed in the spectra of the extracted materials (Figure 6.8(b),(c)).

Figure 6.9 shows particle size distribution for the extracted materials. The average radius for titania and Mn_3O_4 particles was 71 and 152 nm, respectively. The particle size was significantly lower than the size of agglomerates, observed in the SEM images of the dried powders (Figure 6.2). The particle size for the powders, extracted in the E2 method was larger than that in the E1 method. It is suggested that R'-CHO adsorption on particles during synthesis limited the particle growth. However, E2 method offers advantages of a simple one-step procedure.

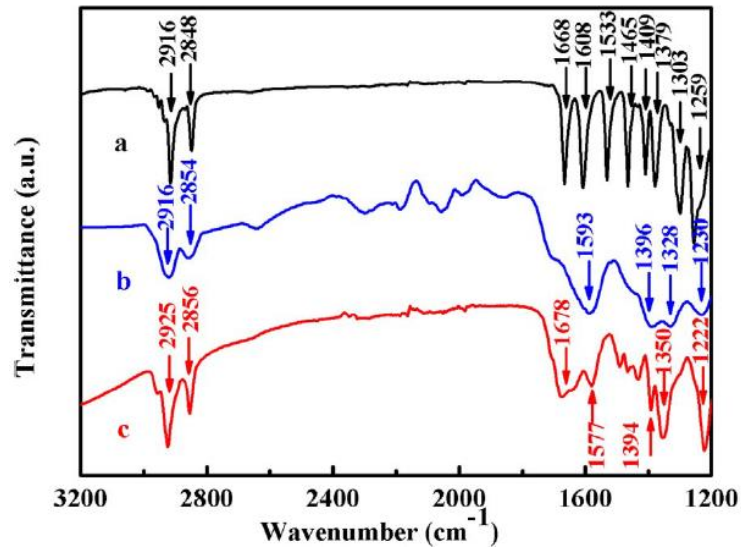


Figure 6.8: FTIR spectra of (a) GR, (b) titania, extracted using GR and (c) Mn₃O₄ extracted using GR.

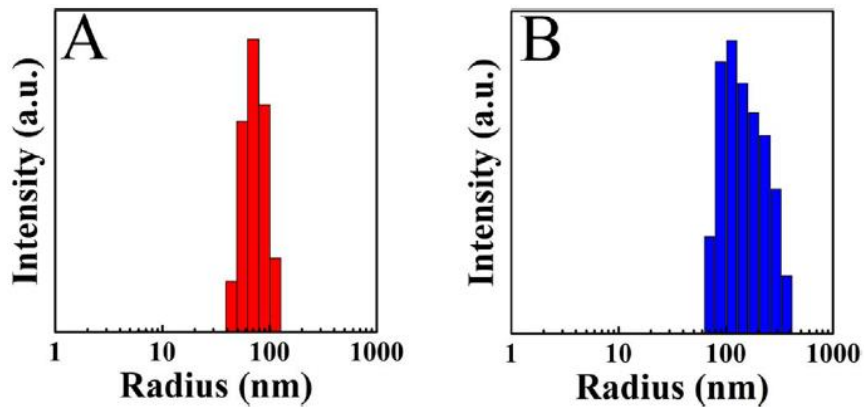


Figure 6.9: Particle size distribution for (a) titania and (b) Mn₃O₄, extracted by adsorbed GR.

Both methods allowed the use of relatively concentrated suspensions. The benefits of the E2 method were demonstrated by the fabrication of Mn₃O₄-MWCNT electrodes for supercapacitors. It was found that GR allows for improved dispersion of MWCNT in 1-

butanol. The suspensions of Mn_3O_4 and MWCNT were mixed and used for the fabrication of composite electrode with Mn_3O_4 :MWCNT mass ratio of 4:1.

Previous investigations [42–45] showed that specific capacitance of supercapacitor electrodes does not correlate with BET surface area, because very small pores are not accessible by the electrolyte. However, the reduction in particle agglomeration can result in improved electrolyte access to the particle surface and enhanced capacitance. We targeted the fabrication of electrodes with high active mass loading, which must be above 10 mg cm^{-2} for practical applications [46]. The gravimetric capacitance decreases drastically with increasing active mass loading, especially at high charge-discharge rates; therefore the true electrochemical performance [46] at high mass loadings must also be presented as an areal capacitance. It was found that at high charge-discharge rates the increase in active mass loading can result in the reduction of areal capacitance [47]. It was shown that diffusion limitations of electrolyte at high charge-discharge rates resulted in poor electrolyte access to the bulk of thick films. [47] In this case the bulk electrode material behaved as a capacitor with low capacitance, connected in series with capacitive surface layer and reduced the total capacitance of the film.

The Mn_3O_4 and composite electrodes were fabricated and tested in several investigations [48–53]. The areal capacitance at low charge-discharge rates [48–53] was in the range of $0.12\text{--}0.60 \text{ F cm}^{-2}$ for mass loadings of $0.4\text{--}2 \text{ mg cm}^{-2}$. The capacitance decreased drastically with increased charge-discharge rates. In our investigation we tested electrodes with significantly higher active mass loading of 30.4 mg cm^{-2} . We observed good capacitive behavior (Figure 6.10A), as it was indicated by nearly box shape CVs. The capacitance,

calculated from the CV data (Figure 6.10B) at a scan rate of 2 mV s^{-1} was 2.63 F cm^{-2} . The capacitance, measured at 100 mV s^{-1} was 0.95 F cm^{-2} .

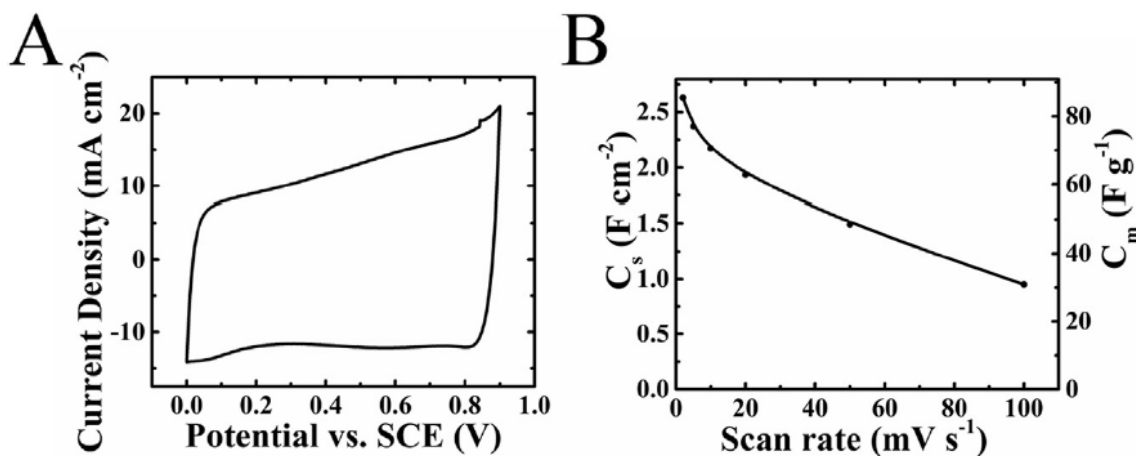


Figure 6.10: CV at a scan rate of 10 mV s^{-1} , C_s and C_m versus scan rate for the composite Mn_3O_4 –MWCNT electrode.

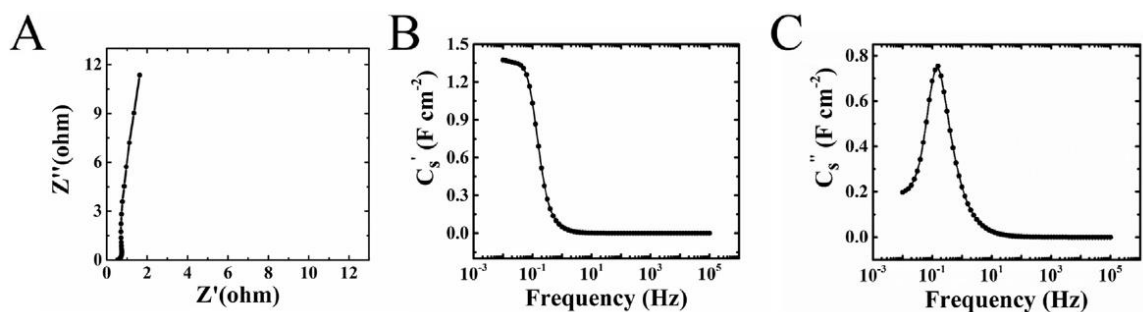


Figure 6.11: (A) Nyquist plot of complex impedance, (B) C_s' and (C) C_s'' versus frequency for the composite Mn_3O_4 –MWCNT electrode.

The obtained capacitances exceed significantly the areal capacitance data reported in the literature for Mn_3O_4 electrodes. Moreover, the real part of impedance Z' (Figure 6.11A) for mass loading of 30.4 mg cm^{-2} was significantly lower, compared to the literature data for electrodes with low mass loading [50–52].

The differential capacitance (Figure 6.11B,C) showed a relaxation type dispersion, as indicated by the decrease of real part with frequency and a relaxation maximum in the frequency dependence of the imaginary part. The relatively high relaxation frequency of 15 Hz indicates good capacitive behavior. The results indicate that liquid-liquid extraction is a promising technique for the fabrication of advanced materials and can be used for other applications.

6.5 Conclusions

The use of liquid-liquid strategies E1 and E2 offers advantages of reduced particle agglomeration and process simplicity, because the particle drying stage can be avoided. Practically important is the ability to achieve efficient extraction using relatively concentrated suspensions. Strong adsorption of catechol and galloyl groups on particle surfaces is a key for the efficient extraction.

Another important factor is the concentration and orientation of the extractor molecules at the liquid-liquid interface, which facilitates the extractor adsorption in Schiff base reactions in the E1 method and bonding of the galloyl groups in the E2 method. The ability to modify the particles during synthesis and limit particle growth can potentially reduce the particle size in the E1 method. However, the one-step E2 method offers the advantages of process simplicity.

Building on the processing advantages offered by our approach, we have demonstrated the fabrication of polymer-titania films, containing non-agglomerated particles by a spray deposition method. A similar approach can be used for other inorganic materials and deposition techniques. Excellent capacitive performance of Mn_3O_4 -MWCNT supercapacitor electrodes was achieved at high active mass loading. The capacitances of 2.63 F cm^{-2} at 2 mV s^{-1} and 0.95 F cm^{-2} at 100 mV s^{-1} are significantly higher than the literature data for Mn_3O_4 based electrodes. In addition to exceptionally high capacitance we achieved significantly lower impedance, which is beneficial for supercapacitor

applications. The results of this investigation pave the way for the agglomerate free processing of various materials and fabrication of advanced films, coatings and devices.

6.6 Acknowledgements

The authors gratefully acknowledge the Natural Sciences and Engineering Research Council of Canada for the financial support and Vale Canada for the donation of Ni foam.

6.7 References

- [1] S. Yamada, Z. Wang, E. Mouri and K. Yoshinaga, "Crystallization of titania ultra-fine particles from peroxotitanic acid in aqueous solution in the present of polymer and incorporation into poly(methyl methacrylate) via dispersion in organic solvent," *Colloid Polym. Sci.*, vol. 287, no.2, pp. 139-146, 2009.
- [2] W. Chen, C. Takai, H.R. Khosroshahi, M. Fuji and T. Shirai, "A modified sol-gel method using acetone-ethanol mixed solvent for fast constructing nanometric TiO₂ shells," *Ceram. Int.*, vol. 42, pp. 559-568, 2016.
- [3] Y. Zhang, J. Wang, L. Yu, L. Wang, P. Wan, H. Wei, L. Lin and S. Hussain, "Ni@NiCo₂O₄ core/shells composite as electrode material for supercapacitor," *Ceram. Int.*, vol. 43, pp.2057-2062, 2017.
- [4] O.O. Van der Biest and L.J. Vandeperre, "Electrophoretic deposition of materials," *Ann. Rev. Mater. Sci.*, vol. 29, pp. 327-352, 1999.
- [5] M. Ata, Y. Liu and I. Zhitomirsky, "A review of new methods of surface chemical modification, dispersion and electrophoretic deposition of metal oxide particles," *RSC Adv.*, vol. 4, pp. 22716-22732, 2014.
- [6] X. Zhao, C. Hincliffe, C. Johnston, P.J. Dobson and P.S. Grant, "Spray deposition of polymer nanocomposite films for dielectric applications," *Mater. Sci. Eng. B*, vol. 151, pp. 140-145, 2008.
- [7] T. Wang and J.L. Keddie, "Design and fabrication of colloidal polymer nanocomposites," *Adv. Colloid Interface Sci.*, vol. 147-148, pp. 319-332, 2009.
- [8] F. Mauvy, P. Lenormand, C. Lalanne, F. Ansart, J.M. Bassat and J.C. Grenier, "Electrochemical characterization of YSZ thick films deposited by dip-coating process," *J. Power Sources*, vol. 171, pp. 783-788, 2007.
- [9] M. Jabbari, R. Bulatova, A.I.Y. Tok, C.R.H. Bahl, E. Mitsoulis and J.H. Hattel, "Ceramic tape casting: a review of current methods and trends with emphasis on rheological behaviour and flow analysis," *Mater. Sci. Eng. B*, vol. 212, pp. 39-61, 2016.
- [10] M. Ata, S. Ghosh and I. Zhitomirsky, "Electrostatic assembly of composite supercapacitor electrodes, triggered by charged dispersants," *J. Mater. Chem. A*, vol. 4, pp. 17857-17865, 2016.
- [11] K. Rezwani, Q.Z. Chen, J.J. Blaker and A.R. Boccaccini, "Biodegradable and bioactive porous polymer/inorganic composite scaffolds for bone tissue engineering," *Biomaterials*, vol. 27, pp. 3413-3431, 2006.
- [12] M. Karg, N. Schelero, C. Opperl, M. Gradzielski, T. Hellweg and R. von Klitzing, "Versatile phase transfer of gold nanoparticles from aqueous media to different organic media," *Chem. A Eur. J.*, vol. 17, pp.4648-4654, 2011.

- [13] A. Kumar, P. Mukherjee, A. Guha, S. Adyantaya, A. Mandale, R. Kumar and M. Sastry, "Amphoterization of colloidal gold particles by capping with valine molecules and their phase transfer from water to toluene by electrostatic coordination with fatty amine molecules," *Langmuir*, vol. 16, pp. 9775-9783, 2000.
- [14] K.S. Mayya and F. Caruso, "Phase transfer of surface-modified gold nanoparticles by hydrophobization with alkylamines," *Langmuir*, vol. 19, pp. 6987-6993, 2003.
- [15] A. Kumar, H. Joshi, R. Pasricha, A. Mandale and M. Sastry, "Phase transfer of silver nanoparticles from aqueous to organic solutions using fatty amine molecules," *J. Colloid Interface Sci.*, vol. 264, pp.396-401, 2003.
- [16] W. Cheng and E. Wang, "Size-dependent phase transfer of gold nanoparticles from water into toluene by tetraoctylammonium cations: a wholly electrostatic interaction," *J. Phys. Chem. B*, vol. 108, pp. 24-26, 2004.
- [17] N. Gaponik, D.V. Talapin, A.L. Rogach, A. Eychmuller and H. Weller, "Efficient phase transfer of luminescent thiol-capped nanocrystals: from water to nonpolar organic solvents," *Nano Lett.*, vol. 2, pp. 803-806, 2002.
- [18] A. Otsuki, G. Dodbiba, A. Shibayama, J. Sadaki, G. Mei and T. Fujita, "Separation of rare earth fluorescent powders by two-liquid flotation using organic solvents," *Jpn. J. Appl. Phys.*, vol. 47, pp. 5093, 2008.
- [19] J. Erler, S. Machunsky, P. Grimm, H.-J. Schmid and U.A. Peuker, "Liquid-liquid phase transfer of magnetite nanoparticles-evaluation of surfactants," *Powder Technol.*, vol. 247, pp. 265-269, 2013.
- [20] G. Zambrana, R. Medina, G. Gutierrez and R. Vargas, "Recovery of minus ten micron cassiterite by liquid-liquid extraction," *Int. J. Miner. Process.*, vol. 1, pp. 335-345, 1974.
- [21] L.P. Wang, Y. Kanemitsu, G. Dodbiba, T. Fujita, Y. Oya and H. Yokoyama, "Separation of ultrafine particles of alumina and zircon by liquid-liquid extraction using kerosene as the organic phase and sodium dodecylsulfate (SDS) as the surfactant collector for abrasive manufacturing waste recycling," *Sep. Purif. Technol.*, vol. 108, pp. 133-138, 2013.
- [22] B. Hu, Y. Nakahiro and T. Wakamatsu, "The effect of organic solvents on the recovery of fine mineral particles by liquid-liquid extraction," *Miner. Eng.*, vol. 6, pp. 731-742, 1993.
- [23] S. Underwood and P. Mulvaney, "Effect of the solution refractive index on the color of gold colloids," *Langmuir*, vol. 10, pp. 3427-3430, 1994.
- [24] X. Feng, H. Ma, S. Huang, W. Pan, X. Zhang, F. Tian, C. Gao, Y. Cheng and J. Luo, "Aqueous-organic phase-transfer of highly stable gold, silver, and platinum nanoparticles and new route for fabrication of gold nanofilms at the oil/water interface and on solid supports," *J. Phys. Chem. B*, vol. 110, pp. 12311-12317, 2006.

- [25] I.A. Jankovic, Z.V. Saponjic, M.I. Comor and J.M. Nedeljkovic, "Surface modification of colloidal TiO₂ nanoparticles with bidentate benzene derivatives," *J. Phys. Chem. C*, vol. 113, pp. 12645-12652, 2009.
- [26] F. Giovannelli, Cc Autret-Lambert, C. Mathieu, T. Chartier, F. Delorme and A. Seron, "Synthesis of manganese spinel nanoparticles at room temperature by coprecipitation," *J. Solid State Chem.*, vol. 192, pp. 109-112, 2012.
- [27] P. Taberna, P. Simon and J.F. Fauvarque, "Electrochemical characteristics and impedance spectroscopy studies of carbon-carbon supercapacitors," *J. Electrochem. Soc.*, vol. 150, pp. A292-A300, 2003.
- [28] B.P. Lee, P.B. Messersmith, J.N. Israelachvili and J.H. Waite, "Mussel-inspired adhesives and coatings," *Ann. Rev. Mater. Res.*, vol. 41, pp. 99-132, 2011.
- [29] H. Lee, S.M. Dellatore, W.M. Miller and P.B. Messersmith, "Mussel-inspired surface chemistry for multifunctional coatings," *Science*, vol. 318, pp. 426-430, 2007.
- [30] H. Lee, B.P. Lee and P.B. Messersmith, "A reversible wet/dry adhesive inspired by mussels and geckos," *Nature*, vol. 448, pp. 338-341, 2007.
- [31] T. Zhang, P. Wojtal, O. Rubel and I. Zhitomirsky, "Density functional theory and experimental studies of caffeic acid adsorption on zinc oxide and titanium dioxide nanoparticles," *RSC Adv.*, vol. 5, pp. 106877-106885, 2015.
- [32] M. Giza, P. Thissen and G. Grundmeier, "Adsorption kinetics of organophosphonic acids on plasma-modified oxide-covered aluminum surfaces", *Langmuir*, vol. 24, pp. 8688-8694, 2008.
- [33] E.S. Dzunuzovic, J.V. Dzunuzovic, A.D. Marinkovic, M.T. Marinovic-Cincovic, K.B. Jeremic and J.M. Nedeljkovic, "Influence of surface modified TiO₂ nanoparticles by gallates on the properties of PMMA/TiO₂ nanocomposites," *Eur. Polym. J.*, vol. 48, pp. 1385-1393, 2012.
- [34] D. Luo, T. Zhang and I. Zhitomirsky, "Electrophoretic deposition of tannic acid polypyrrolidone films and composites," *J. Colloid Interface Sci.*, vol. 469, pp. 177-183, 2016.
- [35] F. Yalcinkaya and D. Lubasova, "Quantitative evaluation of antibacterial activities of nanoparticles (ZnO, TiO₂, ZnO/TiO₂, SnO₂, CuO, ZrO₂, and AgNO₃) incorporated into polyvinyl butyral nanofibers," *Polym. Adv. Technol.*, vol. 28, pp. 137-140, 2017.
- [36] F. Yu and R. Akid, "Corrosion protection of AA2024-T3 alloy by modified hybrid titania containing sol-gel coatings," *Prog. Org. Coat.*, vol. 102, pp. 120-129, 2017.
- [37] M. Mahmoudian, Y. Alias, W. Basirun and M. Ebadi, "Effects of different polypyrrole/TiO₂ nanocomposite morphologies in polyvinyl butyral coatings for preventing the corrosion of mild steel," *Appl. Surf. Sci.*, vol. 268, pp. 302-311, 2013.

- [38] X. Fu, H. Matsuyama and H. Nagai, "Structure control of asymmetric poly (vinyl butyral)-TiO₂ composite membrane prepared by nonsolvent induced phase separation," *J. Appl. Polym. Sci.*, vol. 108, pp. 713-723, 2008.
- [39] K. Nakane, J. Ohashi and F. Suzuki, "Preparation and properties of a composite of poly (vinyl butyral) and titania," *J. Appl. Polym. Sci.*, vol. 71, pp. 185-188, 1999.
- [40] K. Nakane, T. Kurita, T. Ogihara and N. Ogata, "Properties of poly (vinyl butyral)/TiO₂ nanocomposites formed by sol-gel process," *Composites B*, vol. 35, pp. 219-222, 2004.
- [41] K. Shi and I. Zhitomirsky, "Polypyrrole nanofiber-carbon nanotube electrodes for supercapacitors with high mass loading obtained using an organic dye as a co-dispersant," *J. Mater. Chem. A*, vol. 1, pp. 11614-11622, 2013.
- [42] W. Dong, D.R. Rolison and B. Dunn, "Electrochemical properties of high surface area vanadium oxide aerogels," *Electrochem. Solid-State Lett.*, vol. 3, pp. 457-459, 2000.
- [43] W. Dong, J.S. Sakamoto and B. Dunn, "Electrochemical properties of vanadium oxide aerogels," *Sci. Technol. Adv. Mater.*, vol. 4, pp. 3-11, 2003.
- [44] Y.U. Jeong and A. Manthiram, "Nanocrystalline manganese oxides for electrochemical capacitors with neutral electrolytes," *J. Electrochem. Soc.*, vol. 149, pp. A1419-A1422, 2002.
- [45] R.N. Reddy and R.G. Reddy, "Sol-gel MnO₂ as an electrode material for electrochemical capacitors," *J. Power Sources*, vol. 124, pp. 330-337, 2003.
- [46] Y. Gogotsi and P. Simon, "True performance metrics in electrochemical energy storage," *Science*, vol. 334, pp. 917-918, 2011.
- [47] K. Shi and I. Zhitomirsky, "Influence of current collector on capacitive behavior and cycling stability of Tiron doped polypyrrole electrodes," *J. Power Sources*, vol. 240, pp.42-49, 2013.
- [48] D. Dubal, D. Dhawale, R. Salunkhe, V. Fulari and C. Lokhande, "Chemical synthesis and characterization of Mn₃O₄ thin films for supercapacitor application," *J. Alloy. Compd.*, vol. 497, pp. 166-170, 2010.
- [49] Y. Qiao, Q. Sun, J. Xi, H. Cui, Y. Tang and X. Wang, "A modified solvothermal synthesis of porous Mn₃O₄ for supercapacitor with excellent rate capability and long cycle life," *J. Alloy. Compd.*, vol. 660, pp. 416-422, 2016.
- [50] A.A. Yadav, "Influence of electrode mass-loading on the properties of spray deposited Mn₃O₄ thin films for electrochemical supercapacitors," *Thin Solid Films*, vol. 608, pp. 88-96, 2016.
- [51] X.J. Li, Z.w. Song, Y. Zhao, Y. Wang, X.C. Zhao, M. Liang, W.G. Chu, P. Jiang and Y. Liu, "Vertically porous nickel thin film supported Mn₃O₄ for enhanced energy storage performance," *J. Colloid Interface Sci.*, vol. 483, pp. 17-25, 2016.

[52] A. Radhamani and R. Rao, "Tunable supercapacitance of electrospun Mn_3O_4 beaded chains via charge-discharge cycling and control parameters," *Appl. Surf. Sci.*, vol. 403, pp. 601-611, 2017.

[53] Y. Hu, C. Guan, G. Feng, Q. Ke, X. Huang and J. Wang, "Flexible asymmetric supercapacitor based on structure-optimized Mn_3O_4 /reduced graphene oxide nanohybrid paper with high energy and power density," *Adv. Funct. Mater.*, vol. 25, pp. 7291-7299, 2015.

Chapter 7 High areal capacitance of Mn₃O₄-carbon nanotube electrodes

R Poon* and I. Zhitomirsky*^α

*Department of Materials Science and Engineering, McMaster University,
Hamilton, Ontario, L8S 4L7, Canada

^αCorresponding Author: zhitom@mcmaster.ca; 905-525-9140 ext. 23914

Submitted on 25th July 2017. Accepted on 10th December 2017.

Copyright 2017, reproduced with permission from Elsevier.

7.1 Abstract

This paper reports the fabrication of Mn_3O_4 -multiwalled carbon nanotube (MWCNT) electrodes for supercapacitors with a high active mass loading of 35 mg cm^{-2} , which showed high capacitance of 3.5 F cm^{-2} , good capacitance retention at high charge-discharge rates and low impedance. Good electro-chemical performance was achieved using non-covalent modification of MWCNT with an anionic steroid dispersant, which allowed excellent MWCNT dispersion and facilitated the fabrication of Mn_3O_4 -MWCNT nanocomposites with uniform distributions of individual components. The electrodes showed activation behavior, related to capacitance increase, impedance reduction and enrichment of the Mn^{3+} and Mn^{4+} oxidation states.

Key words: carbon nanotubes, nanoparticles, supercapacitor, manganese oxide, composite, electrode

7.2 Introduction

Mn_3O_4 is a promising material for energy storage in electrochemical supercapacitors [1]. Advanced Mn_3O_4 based composites have been developed [2,3], containing various conductive additives. Investigations showed good capacitive performance of Mn_3O_4 electrodes with active mass loading below 2 mg cm^{-2} . The typical areal capacitances (C_s) reported in the literature [4–8] for Mn_3O_4 based electrodes were in the range of $0.02\text{--}0.6 \text{ F cm}^{-2}$. An important parameter is the ratio (R_m) of active material mass to current collector mass. The R_m values for electrodes with active mass loadings of $0.1\text{--}2 \text{ mg cm}^{-2}$ and metal foil collectors are typically below 1–3%. However, practical applications of supercapacitors require electrodes with significantly higher C_s and R_m .

Despite the impressive progress achieved in the materials synthesis and microstructure design [1–8], further investigations are necessary for the preparation of Mn_3O_4 based composites for advanced supercapacitor electrodes with higher C_s and R_m , which can potentially be achieved at higher active mass loadings. However, the capacitive performance of Mn_3O_4 usually decreases with increasing active mass due to poor electrolyte access to the active material and low electronic conductivity. Therefore, new strategies must be used for the development of advanced electrode microstructures.

The goal of this investigation was the fabrication of advanced $\text{Mn}_3\text{O}_4\text{--MWCNT}$ composites for electrodes of electrochemical supercapacitors with high active mass loading, low impedance, high C_s and R_m .

7.3 Experimental Procedure

Sodium taurodeoxycholate (TD), $\text{Mn}(\text{NO}_3)_2$, NaOH, poly(vinyl butyral-co-vinyl alcohol-co-vinyl acetate) (PVB, average $M_w = 50,000\text{--}80,000$) (Aldrich), MWCNT (ID 4 nm, OD 13 nm, length 1–2 μm , Bayer) were used. Ni foams with 95% porosity were provided by Vale Ltd.

The synthesis of Mn_3O_4 particles was performed using aqueous 0.5 M $\text{Mn}(\text{NO}_3)_2$ solution. The pH of the solution was adjusted to pH = 10 by NaOH addition. The obtained precipitate was washed with water and dried in air. The suspension of 4 g L^{-1} Mn_3O_4 , was mixed with 1 g L^{-1} MWCNT suspension, containing 0.5 g L^{-1} TD. The obtained mixture was filtrated, washed and dried in air. The PVB solution in ethanol was added to the mixture. The PVB content in the slurry was 3% of the total mass of Mn_3O_4 and MWCNT. The obtained slurry was used for the impregnation of Ni foam current collectors. The active mass loading was 35 mg cm^{-2} .

Scanning electron microscopy (SEM) investigations were performed using JEOL JSM-7000F microscope. X-ray diffraction (XRD) studies were carried out using a powder diffractometer (Nicolet I2, $\text{CuK}\alpha$ radiation). XPS analysis was performed using Quantera II Scanning XPS instrument and PHI MultiPak Version 9.4.0.7 software (Physical Electronics Inc.). Cyclic voltammetry (CV) and electrochemical impedance spectroscopy (EIS) investigations were carried out using a potentiostat (PARSTAT 2273, Princeton Applied Research). The capacitive behavior of the electrodes was studied in a three-electrode cell using 0.5 M Na_2SO_4 aqueous solutions. The area of the working electrode

was 1 cm^2 . The counter electrode was a platinum gauze, and the reference electrode was a standard calomel electrode (SCE). The areal capacitance $C_s = Q/\Delta VS$ and gravimetric capacitance $C_m = Q/\Delta Vm$ were calculated using half the integrated area of the CV curve to calculate the charge (Q), and subsequently dividing the charge Q by the width of the potential window (ΔV) and electrode area (S) or active mass (m). The measurements of complex impedance $Z^* = Z' - iZ''$ were performed in the frequency range of 10 mHz –100 kHz at the amplitude of the signal of 5 mV. The complex capacitance $C_s^* = C_s' - iC_s''$ was calculated from the EIS data as $C_s' = Z''/\omega|Z|^2S$ and $C_s'' = Z'/\omega|Z|^2S$, where $\omega = 2\pi f$ (f -frequency). A testing procedures (TP) involved 2, 3, 5, 10, 10, 10 cycles at scan rates of 2, 5, 10, 20, 50, 100 mV s^{-1} , respectively. The capacitance was calculated from the CV data for the last cycle at each scan rate.

7.4 Results and Discussion

XRD pattern (Figure 7.1A) of as-precipitated material, dried at room temperature showed diffraction peaks of Mn_3O_4 (JCPDS file 024- 0734). MWCNT were well dispersed in water using TD (Supplementary Materials, Figure 7.6) as a dispersant. Sedimentation tests showed excellent suspension stability. The 1 g L^{-1} MWCNT suspensions, containing 1 g L^{-1} TD were stable for 12 months. TD (Figure 7.5) is an anionic molecule, which belong to the bile acid family. The adsorption and dispersion properties of bile acids and salts are related to their steroid structure with concave hydrophilic and convex hydrophobic surface [9]. The analysis of adsorption of sodium cholate molecules on single walled carbon nanotubes (SWCNT) showed that such molecules wrap around SWCNT with hydrophobic

face pointing inward to form a ring [9]. The hydrophobic interactions of the bile salt with SWCNT resulted in strong adsorption [9].

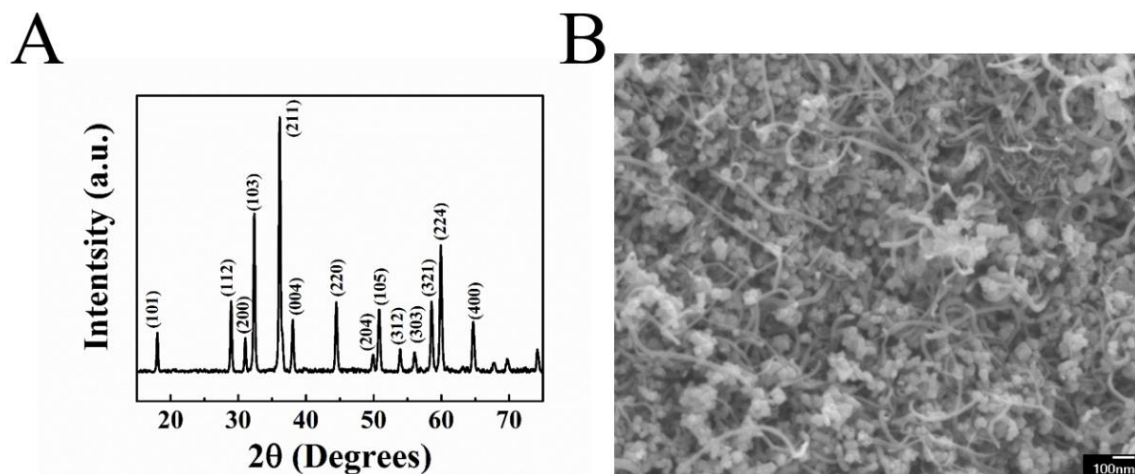


Figure 7.1: (A) X-ray diffraction pattern of as-prepared Mn₃O₄, (B) SEM image of Mn₃O₄-MWCNT electrode material.

A similar adsorption mechanism can be suggested for TD adsorption on MWCNT. The adsorbed TD provided electrostatic dispersion of MWCNT. The good dispersion of MWCNT facilitated the fabrication of composites with good mixing of Mn₃O₄ and MWCNT. Figure 7.1B shows an SEM image of a composite electrode, containing well mixed MWCNT and Mn₃O₄ nanoparticles.

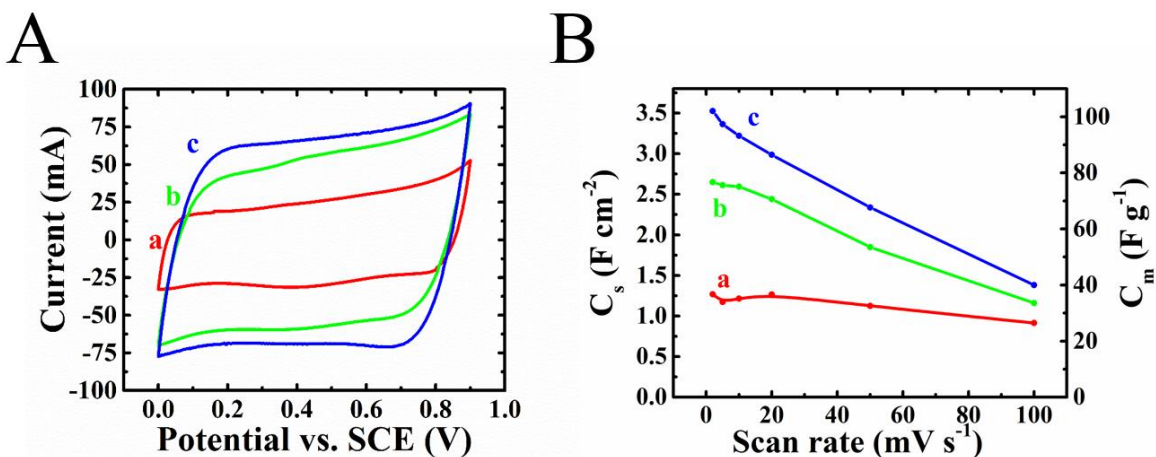


Figure 7.2: (A) CVs at a scan rate of 20 mV s^{-1} and (B) capacitance versus scan rate dependences for (a) 1st, (b) 3rd and (c) 5th TP for Mn_3O_4 -MWCNT electrode.

Electrochemical testing showed significant increase in the CV area (Figure 7.2A) and capacitance, calculated from the CV (Figure 7.2B) during the first five TPs. Relatively small changes were observed during the following TPs. The remarkably high capacitance of $C_s = 3.52 \text{ F cm}^{-2}$ ($C_m = 101 \text{ F g}^{-1}$) was obtained at a scan rate of 2 mV s^{-1} for the 5th TP. The capacitance decreased with increasing scan rate. The capacitance of $C_s = 1.38 \text{ F cm}^{-2}$ was obtained at 100 mV s^{-1} . The obtained capacitance exceeded significantly the capacitance values of $0.02\text{--}0.6 \text{ F cm}^{-2}$, reported in the literature [4–8]. In contrast to other investigations, we have achieved good electrochemical performance for relatively high $R_m = 38\%$, which is beneficial for the fabrication of practical devices with reduced mass.

Figure 7.3A shows EIS data, presented in the Nyquist plot. The Mn_3O_4 -MWCNT electrodes showed relatively low resistance $R=Z'$, which decreased during the first 5 TPs. The slope of the graphs increased during the first 5 TPs and the Nyquist plot for 5th cycle was a nearly vertical line, which indicated good capacitive behavior. The decrease of Z''

during the first 5 TPs indicated capacitance increase. Indeed, the low frequency capacitance, calculated from the impedance data increased drastically during TPs (Figure 7.3B) in agreement with the CV data. The frequency dependences of the AC capacitance showed a relaxation type dispersion, as indicated by reduction of C_s' with frequency and corresponding relaxation maxima (Figure 7.3C) in the frequency dependences of C_s'' . The EIS characteristics showed very small variations after the 5th TP.

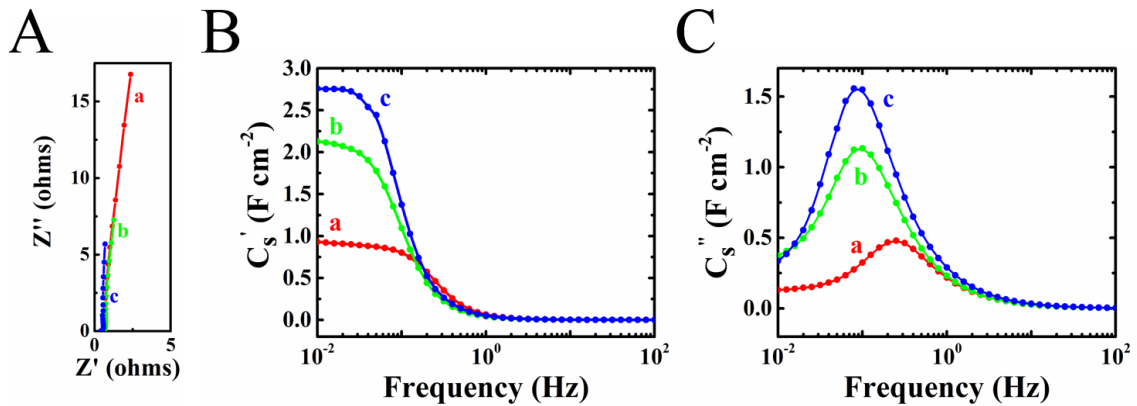


Figure 7.3: Nyquist plot of complex impedance and frequency dependences of (B) C_s' and (C) C_s'' after (a) 1st, (b) 3rd and (c) 5th TP for Mn_3O_4 -MWCNT composite electrode.

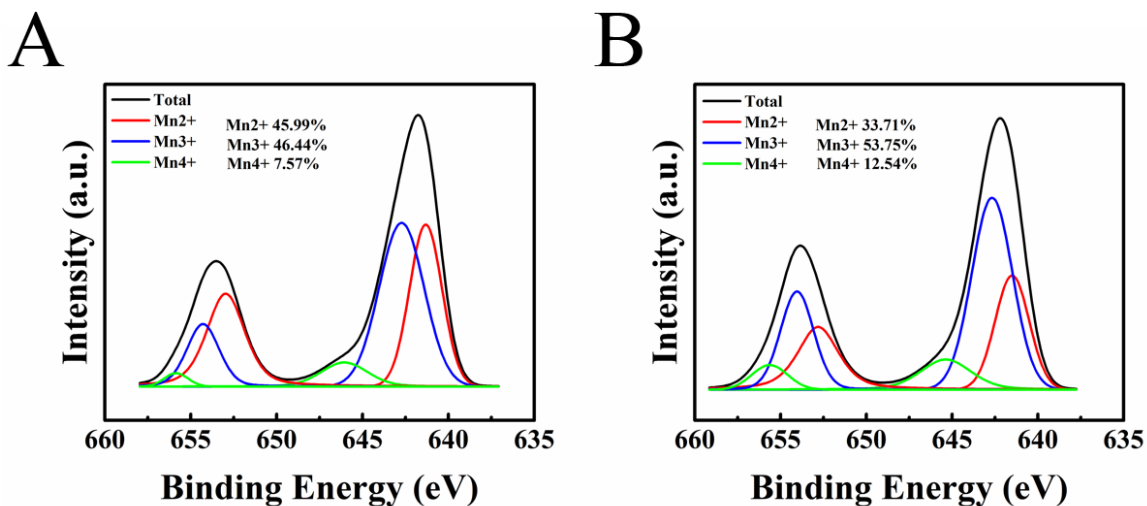


Figure 7.4: XPS spectra of Mn₃O₄-MWCNT composite (A) as-prepared and (B) after 5th TP.

XPS data for the as-prepared electrode material (Figure 7.4A) showed high content of Mn²⁺ and Mn³⁺ originated from the mixed valence nature of Mn₃O₄, and the presence of Mn⁴⁺ could be a result of surface oxidation or vacancies in the lattice. The XPS data after the 5th TP (Figure 7.4B) showed enrichment of the Mn³⁺ and Mn⁴⁺ oxidation states which resulted in capacitance increase due to increased pseudocapacitive contribution from the Mn³⁺/Mn⁴⁺ redox couple. It is important to note that literature data [10] on electrochemical cycling of thin film Mn₃O₄ electrodes revealed microstructure changes, which resulted in increased porosity. A similar microstructure changes can be expected in the bulk of the electrodes, studied in this work. The microstructure changes can also contribute to the capacitance increase and result in decrease of resistance. The Mn₃O₄-MWCNT composites are promising for practical applications in supercapacitor electrodes due to high capacitance and low impedance, achieved at high active mass loadings.

7.5 Conclusions

The non-covalent modification of MWCNT with a steroid TD dispersant allowed excellent suspension stability and facilitated the fabrication of advanced electrode microstructures with uniform distribution of individual components. Good electrochemical performance was achieved at high active mass loading (35 mg cm^{-2}) and high R_m (38%), which allowed the fabrication of electrodes with C_S of 3.52 and 1.38 F cm^{-2} at 2 and 100 mV s^{-1} , respectively. Compared to the literature, we achieved significantly higher C_S at a lower impedance. The electrodes showed activation behavior, related to enrichment of the Mn^{3+} and Mn^{4+} oxidation states. The Mn_3O_4 -MWCNT composites are promising for practical applications in supercapacitors.

7.6 Acknowledgements

Authors acknowledge the Natural Sciences and Engineering Research Council of Canada for the financial support.

7.7 Supplementary Materials

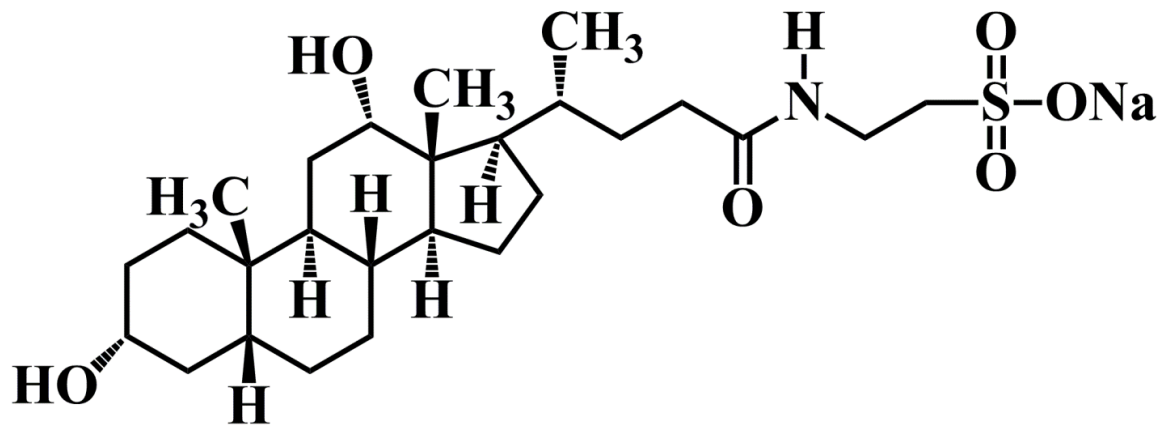


Figure 7.5: Chemical structure of TD.

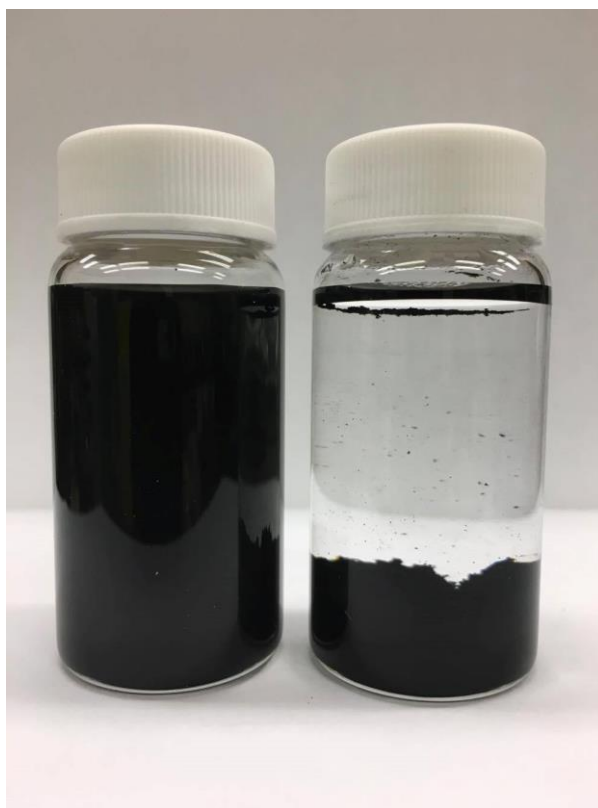


Figure 7.6: 1 g L⁻¹ MWCNT suspensions, containing 1 g L⁻¹ TD (left) and without TD (right).

7.8 References

- [1] Y. Luo, T. Yang, Z. Li, B. Xiao and M. Zhang, “High performance of Mn_3O_4 cubes for supercapacitor applications”, *Materials Letters*, vol. 178, pp. 171-174, 2016.
- [2] L. Wang, Y. Li, Z. Han, L. Chen, B. Qian, X. Jiang, J.O. Pinto and G. Yang, “Composite structure and properties of Mn_3O_4 /graphene oxide and Mn_3O_4 /graphene”, *Journal of Materials Chemistry A*, 1,no. 29, 8385–8397, 2013.
- [3] J. Cao, Y. Wang, Y. Zhou, D. Jia, J.-H. Ouyang and L. Guo, “Performances of highvoltage electrochemical capacitor using ball-milled graphite/ Mn_3O_4 composite electrodes”, *Journal of Electroanalytical Chemistry*, vol 682, pp. 23-28, 2012.
- [4] D. Dubal, D. Dhawale, R. Salunkhe, V. Fulari and C. Lokhande, “Chemical synthesis and characterization of Mn_3O_4 thin films for supercapacitor application”, *Journal of Alloys and Compounds*, vol. 497, pp. 166-170, 2010.
- [5] A.A. Yadav, “Influence of electrode mass-loading on the properties of spray deposited Mn_3O_4 thin films for electrochemical supercapacitors”, *Thin Solid Films*, vol. 608, pp. 88-96, 2016.
- [6] X.-J. Li, Z.-W. Song, Y. Zhao, Y. Wang, X.-C. Zhao, M. Liang, W.-G. Chu, P. Jiang and Y. Liu, “Vertically porous nickel thin film supported Mn_3O_4 for enhanced energy storage performance”, *Journal of Colloid Interface Science*, vol. 483, pp. 17-25, 2016.
- [7] A. Radhamani and R. Rao, “Tunable supercapacitance of electrospun Mn_3O_4 beaded chains via charge-discharge cycling and control parameters”, *Applied Surface Science*, vol. 403, pp.601-611, 2017.
- [8] Y. Hu, C. Guan, G. Feng, Q. Ke, X. Huang and J. Wang, “Flexible asymmetric supercapacitor based on structure-optimized Mn_3O_4 /reduced graphene oxide nanohybrid paper with high energy and power density”, *Advance Functional Material*, vol. 25, pp. 7291-7299, 2015.
- [9] S. Lin and D. Blankschtein, “Role of the bile salt surfactant sodium cholate in enhancing the aqueous dispersion stability of single-walled carbon nanotubes: a molecular dynamics simulation study”, *The Journal of Physical Chemistry B*, vol. 114, pp.15616-15625, 2010.
- [10] N. Nagarajan, M. Cheong and I. Zhitomirsky, “Electrochemical capacitance of MnO_x films”, *Materials Chemistry and Physics*, vol 103, no.1, pp. 47-53, 2007.

Chapter 8 Mn_3O_4 and $(\text{ZnFe})\text{OOH}$ composites for supercapacitors with high active mass

R. Poon^{*=}, W. Liang^{*=} and I. Zhitomirsky^{* α}

^{*}Department of Materials Science and Engineering, McMaster University,
Hamilton, Ontario, L8S 4L7, Canada

^{α} Corresponding Author: zhitom@mcmaster.ca; 905-525-9140 ext. 23914

Submitted on 15th August, 2019. Accepted on 12th November, 2019.

Author's Contributions:

- Synthesis and fabrication of Mn_3O_4 -CNT composite electrode
- Electrochemical testing of Mn_3O_4 -CNT electrode and devices
- Characterization of Mn_3O_4 -CNT composite with XRD, SEM
- XPS sample preparation and fabrication of LED display
 - Literature review
 - Manuscript preparation

⁼The authors contributed equally to this work

8.1 Abstract

A new colloidal method has been developed for the fabrication of Mn₃O₄-carbon nanotube (CNT) composites for positive electrodes of supercapacitors and areal capacitance of 5.04 F cm⁻² has been achieved. In this method, chemical precipitation of Mn₃O₄ was performed in the presence of carbon nanotubes, dispersed using a toloum chloride dye. An electrostatic heterocoagulation mechanism has been developed, which allowed for enhanced mixing of Mn₃O₄ and CNT, and resulted in enhanced electrochemical performance at high active mass of 36 mg cm⁻². Testing results revealed changes in microstructure and oxidation state of Mn during cycling, which allowed for enhanced capacitance. In order to utilize the high capacitance of the positive Mn₃O₄-CNT electrodes in supercapacitor devices, advanced negative electrodes have been developed. (ZnFe)OOH – polypyrrole coated CNT electrodes with enhanced areal capacitance in a negative potential window have been fabricated. Asymmetric devices showed promising performance in a voltage window of 1.6 V.

Key words: manganese oxide, iron hydroxide, polypyrrole, carbon nanotubes, supercapacitor, composite

8.2 Introduction

Mn₃O₄ is a promising ceramic cathode materials for supercapacitors due to its high capacitance and low cost^{1,2}. However, the specific capacitance of Mn₃O₄ decreased significantly with increasing electrode mass due to poor electrolyte access to the active material and low electronic conductivity. It is challenging to achieve good electrode performance at practically important active mass above 10 mg cm⁻². Therefore, research efforts were focused on the synthesis of nanoparticles with high surface area and design of advanced composites.

It is important to note that Mn₃O₄ is a member of a large group of advanced materials with a spinel crystalline structure. Therefore, the advantage of Mn₃O₄, compared to other pseudocapacitive ceramic materials, is the ability to form solid solutions with various spinel compounds. The rich chemistry of spinel offers possibilities³ for the modification of composition, conductivity and capacitive properties of Mn₃O₄.

Many investigations focused on pure Mn₃O₄ films⁴⁻⁸ and reported capacitances at low active mass loadings in the range of 0.16 -1.2 mg cm⁻². High specific capacitances of 568⁷ and 597⁸ F g⁻¹ were reported at mass loadings of 0.16 and 0.64 mg cm⁻², respectively. Good electrochemical performance at higher mass loadings in the range of 2-9.5 mg cm⁻² was achieved in composites, containing various conductive additives, such as graphite⁹, carbon black¹⁰, acetylene black¹¹⁻¹³ and other materials¹⁴. High gravimetric capacitance of 222.4 F g⁻¹ was achieved at a mass loading of 9.5 mg cm⁻² and resulted¹³ in areal capacitance of 2.11 F cm⁻². Mn₃O₄ was combined with capacitive carbon materials such as graphene^{15,16} and

activated carbon¹⁷ for the fabrication of composites. Of particular interest are Mn₃O₄-graphene oxide composites, which showed capacitances of 538 F g⁻¹ (2.69 F cm⁻²)¹⁸ and 258.6 F g⁻¹ (2.33 F cm⁻²)¹⁹ at mass loadings of 5 and 9 mg cm⁻², respectively. Recent studies showed that good capacitive behavior can be achieved at higher mass loadings using advanced colloidal techniques²⁰. Mn₃O₄-carbon nanotube electrodes showed areal capacitances of 2.8²⁰ and 4.2²¹ F cm⁻² at active mass loadings of 28.4 and 33 mg cm⁻². Mn₃O₄ cathodes were combined with various anodes, such as graphene²², activated carbon²³, lithium titanate²⁴ and polypyrrole²⁵ for the fabrication of asymmetric devices with large voltage windows. However, the progress in the development of Mn₃O₄ cathodes introduces problems related to the use of various anodes, which have lower capacitances. Therefore, there is a need in the development of advanced ceramic anodes, which match capacitive properties of the Mn₃O₄ cathodes.

The goal of this investigation was the development of advanced Mn₃O₄ electrodes and asymmetric supercapacitor devices. The approach was based on the synthesis of Mn₃O₄ nanoparticles and electrostatic heterocoagulation with dispersed carbon nanotubes. The results presented below indicated that this approach allowed enhanced mixing of the individual components and enhanced capacitive behavior was achieved at mass loading of 36 mg cm⁻². Good material utilization resulted in high areal capacitance of 5.04 F cm⁻² and good rate capability, which were achieved at low electrode resistance. In order to match high capacitance of Mn₃O₄ cathodes, we developed advanced negative electrodes, containing (Fe,Zn)OOH and polypyrrole coated carbon nanotubes (PNT). The use of

composites allowed for improved capacitive behavior and enhanced cyclic stability. The asymmetric device showed promising capacitive properties.

8.3 Experimental Procedure

Tolonium chloride (TL), $\text{Mn}(\text{NO}_3)_2 \cdot 4\text{H}_2\text{O}$, $\text{FeCl}_3 \cdot 6\text{H}_2\text{O}$, ZnCl_2 , NaOH, Na_2SO_4 , polyvinyl butyral (PVB) (Aldrich), carbon nanotubes (CNT, multiwalled, Bayer), and Ni foams (Vale) were used.

For the synthesis of Mn_3O_4 -CNT composite, 1 g L^{-1} CNT and 0.5 g L^{-1} of TL were added to 100mL DI water and ultrasonicated. $\text{Mn}(\text{NO}_3)_2$ was added to the CNT suspension, and the pH of the suspension was adjusted to $\text{pH} = 10$ by NaOH to synthesize Mn_3O_4 . The mass ratio of CNT: Mn_3O_4 in the suspension was 1:4. The composite was filtrated, washed and dried at 60°C . The obtained material was mixed with PVB (3 wt%) to produce a slurry in ethanol and impregnated into the Ni foam.

The synthesis of pure FeOOH and (Fe,Zn)OOH ($[\text{Zn}]/([\text{Zn}]+[\text{Fe}]) = 0.1$) was based on the method, described in the literature²⁶. CNT were added to (Fe,Zn)OOH suspensions at $\text{pH} = 7$ in order to obtain (Fe,Zn)OOH-CNT suspensions.

The procedure for the formation of polypyrrole coated CNT (PNT) was described in a previous investigation²⁷. The suspensions of (Fe,Zn)OOH-CNT and PNT were mixed, ultrasonicated, filtrated and dried at 60°C . The mass ratio of (Fe,Zn)OOH-CNT:PNT was 1:1. The obtained composite materials were mixed with PVB (2.5 wt%) in ethanol and the slurries were impregnated into the Ni foam current collectors. The mass loading of all the electrodes was 36 mg cm^{-2} .

XPS analysis was performed using Quantera II Scanning instrument (Physical Electronics Inc.). JEOL JSM-7000F microscope was used for SEM investigations. XRD studies were performed using a Bruker D8 diffractometer. Cyclic voltammetry (CV) and impedance spectroscopy (EIS) were performed using equipment, described in refs.^{28,29}

8.4 Results and Discussion

The formation of Mn_3O_4 was confirmed by XRD studies (Figure 8.1), which showed peaks, corresponding to JCPDS file 024-0734.

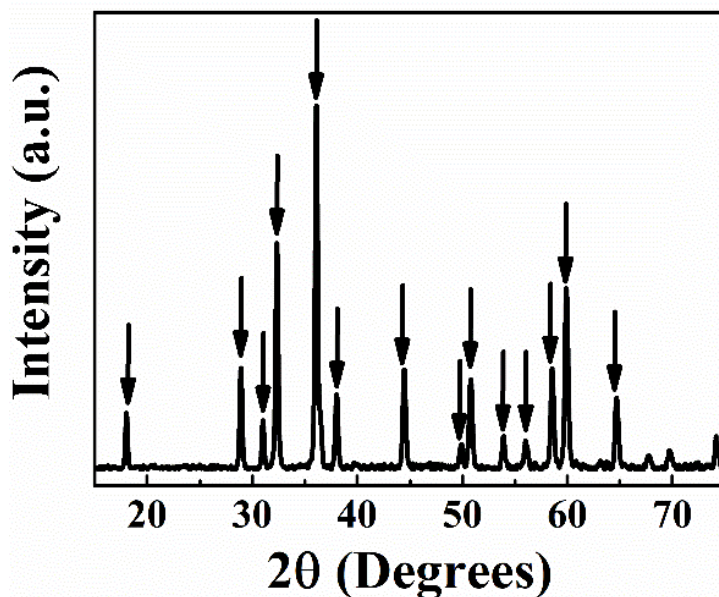


Figure 8.1: XRD pattern of as-precipitated powder, arrows show peaks, corresponding to JCPDS file 024-0734.

Figure 8.2A shows CVs for the Mn_3O_4 -CNT electrode. The nearly box shapes of the CVs indicated good capacitive behavior. The areal capacitance (C_s) of 5.04 F cm^{-2} was obtained at a sweep rate of 2 mV s^{-1} . The capacitance decreased with sweep rate (Figure 8.2B) to the value of 1.78 F cm^{-2} at 100 mV s^{-1} . The C_s of obtained Mn_3O_4 -CNT electrode was higher,

compared to the literature data for various Mn_3O_4 composites, described in the Introduction section.

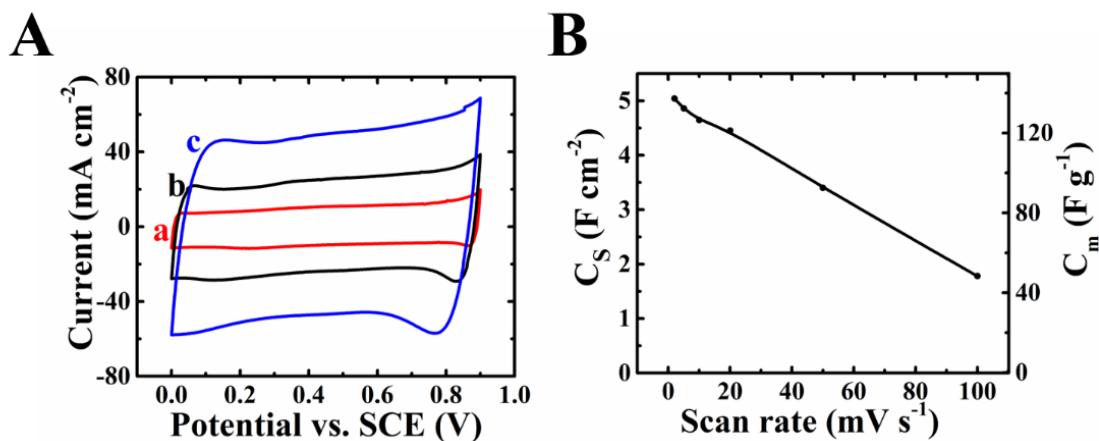


Figure 8.2: (A) CVs at scan rates of (a) 2, (b) 5 and (c) 10 mV s^{-1} and (B) C_s and C_m for Mn_3O_4 -CNT electrode.

The enhanced capacitance resulted from improved mixing of Mn_3O_4 and CNT. It was found that cationic TL adsorbed on CNT and provided good dispersion of CNT in water. The adsorption mechanism involved π - π interactions of the polyaromatic TL with CNT. The adsorbed cationic TL molecules imparted a positive charge to CNT and provided electrostatic dispersion of CNT. The TL adsorption on CNT resulted in good colloidal stability of 1 g L^{-1} CNT suspensions, containing 0.5 - 1 g L^{-1} TL.

Literature data indicates that the isoelectric point of Mn_3O_4 is in the range of 3.7-5.7³⁰. Therefore, the Mn_3O_4 particles formed at $\text{pH} = 10$ were negatively charged. It is suggested that electrostatic attraction of the negatively charged Mn_3O_4 and well-dispersed positively charged CNT facilitated their enhanced mixing.

The low impedance of the Mn₃O₄-CNT composites provided additional evidence of good dispersion of CNT and enhanced mixing of Mn₃O₄ and CNT. Figure 8.3A shows a Nyquist plot of the impedance spectroscopy data. The low real part of the complex impedance indicated a low resistance, whereas the low imaginary part resulted from high capacitance. The components of complex capacitance derived from the impedance data (Figure 8.3B,C) showed a frequency dispersion of the relaxation type. The relaxation frequency, corresponding to the maximum of the imaginary part of the complex capacitance was about 0.08 Hz.

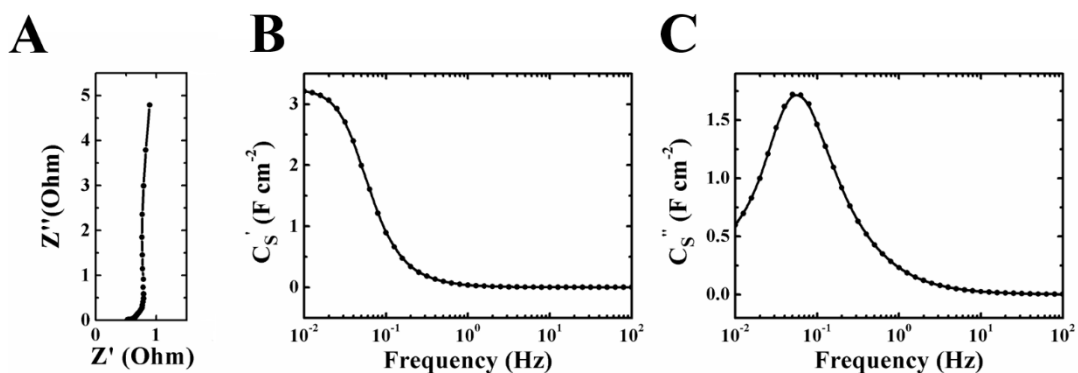


Figure 8.3: (A) Nyquist plot of complex impedance, and frequency dependence of complex capacitances (B) C_S' and (C) C_S'' for Mn₃O₄-CNT electrode.

SEM studies showed that as-prepared electrodes contained nanoparticles of Mn₃O₄ (Figure 8.4A) with a typical size of 30-50 nm. Cycling resulted in significant changes of the electrode microstructure. The SEM image of the electrode after cycling showed a porous microstructure, containing flakes of a manganese oxide (Figure 8.4B). Such microstructure is beneficial for the electrolyte access to the active material. XPS studies of the electrodes

before and after cycling showed changes in the oxidation state of Mn. It was found that cycling resulted in the reduction of the Mn^{2+} content and increasing content of Mn^{3+} and Mn^{4+} (Figure 8.4C,D) in the electrode material.

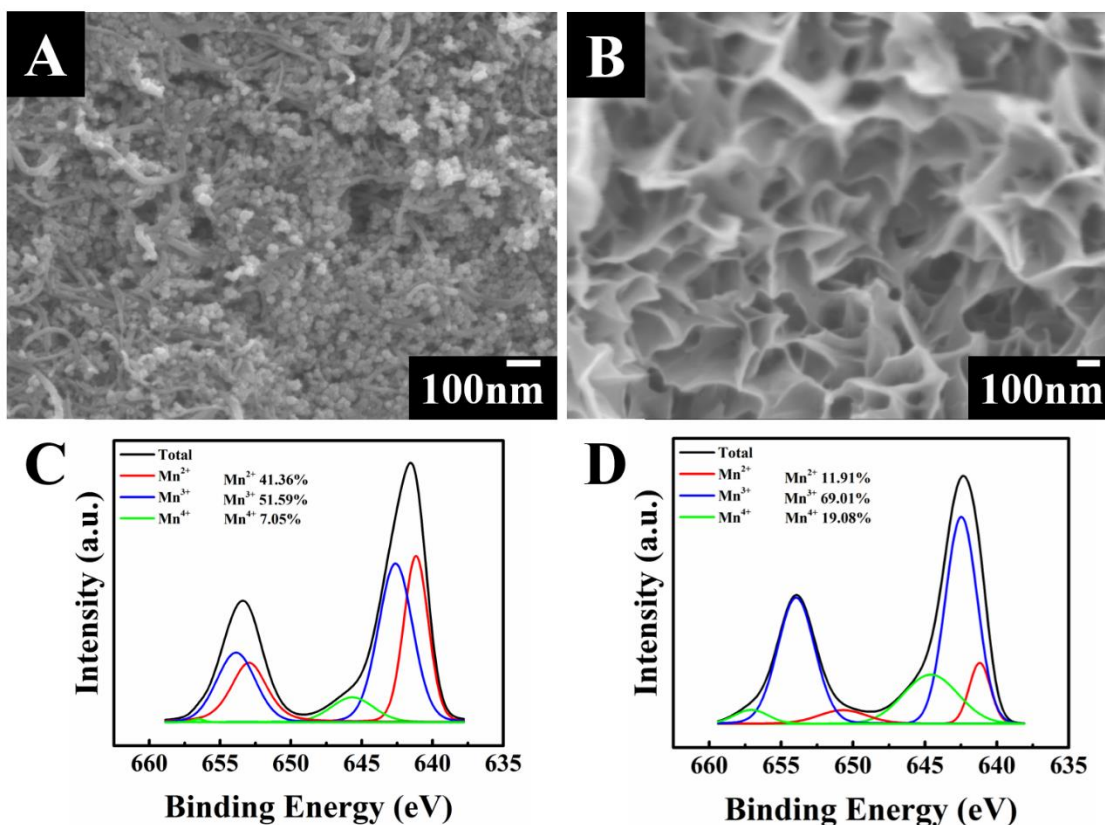


Figure 8.4: (A,B) SEM images and (C,D) XPS spectra for Mn_3O_4 -CNT electrode: (A,C) as prepared and (B,D) after testing.

Cycling of the Mn_3O_4 -CNT electrodes (Figure 8.5) showed initial increase in capacitance during the first 200 cycles and then capacitance reduction. The capacitance was relatively stable between 400th and 1000th cycles. The initial capacitance increase resulted from the increased porosity (Figure 8.4B), which facilitated electrolyte access to the active material.

The high capacitance of Mn₃O₄-CNT positive electrodes, obtained in this investigation, can be utilized for the fabrication of asymmetric supercapacitor devices. The development of asymmetric devices requires comparable capacitances of individual electrodes in partially overlapping potential ranges^{31,32}.

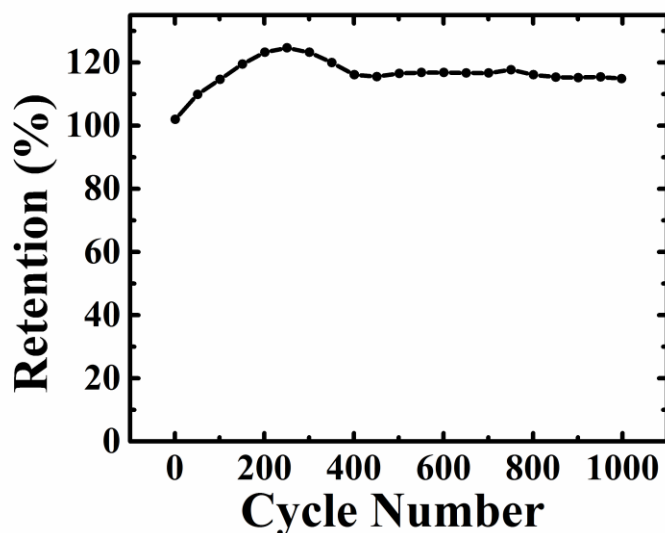


Figure 8.5: Capacitance retention of Mn₃O₄-MWCNT electrode during cycling.

FeOOH-CNT electrodes were tested in the potential range of -0.8 - +0.1 V in 0.5M Na₂SO₄ electrolyte. Figure 8.6A shows CV for the FeOOH-CNT electrodes at different scan rates. The CVs deviated significantly from the ideal box shape. The low currents in the range of -0.2 - +0.1 V indicated poor capacitive properties in this potential range. The integral areal capacitance (Figure 8.6D(a)) in the voltage window of -0.8 - +0.1 V was 3.0 F cm⁻² at a scan rate of 2 mV s⁻¹. The capacitance retention at 100 mV s⁻¹ was found to be 31%. The capacitance of the FeOOH-CNT electrodes was significantly lower, compared to that of Mn₃O₄-MWCNT electrodes. The FeOOH-CNT electrodes showed poor cyclic stability.

The capacitance calculated from the CV for the 1000th cycle was 60% of the capacitance calculated from the CV for the 1st cycle (Figure 8.7a). (Fe,Zn)OOH-CNT showed improved capacitive performance, as indicated by the larger CV areas at the same scan rates (Figure 8.6B). However, the currents remained low in the potential range of -0.2 - +0.1 V. The capacitance decreased (Figure 8.6D(b)) from 3.6 F cm⁻² to 1.4 F cm⁻² with increasing sweep rate from 2 to 100 mV s⁻¹.

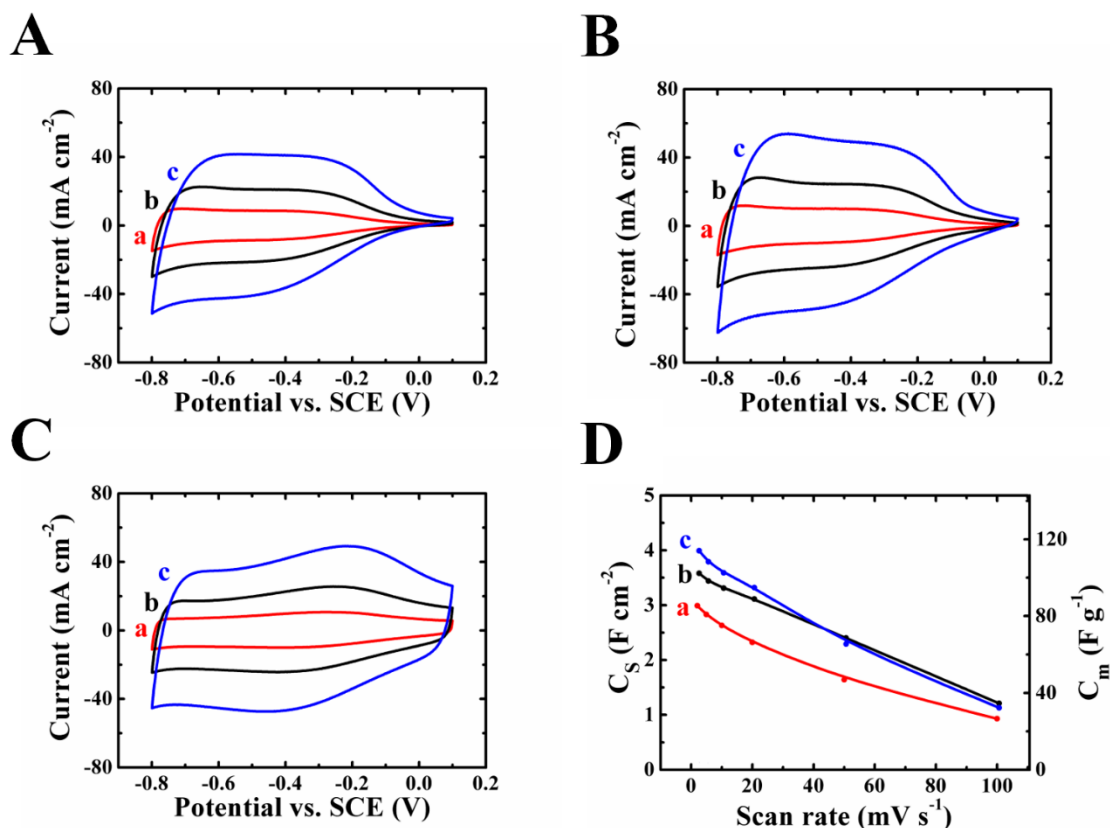


Figure 8.6: (A,B,C) CVs at scan rates of (a) 2, (b) 5 and (c) 10 mV s⁻¹ and (D) C_s and C_m for (A,D(a)) FeOOH-CNT, (B,D(b)) (Fe,Zn)OOH-CNT and (C,D(c)) (Fe,Zn)OOH-CNT-PNT electrodes.

(Fe,Zn)OOH-CNT showed enhanced cyclic stability, compared to FeOOH-CNT. The capacitance retention was 80% after 1000 cycles (Figure 8.7b). The enhanced cyclic

stability is related to reduced dissolution of the capacitive Fe component of the solid solution. It is suggested that more electrochemically negative Zn species prevent release of Fe^{2+} ions from the electrodes and promote the precipitation of iron hydroxide³³.

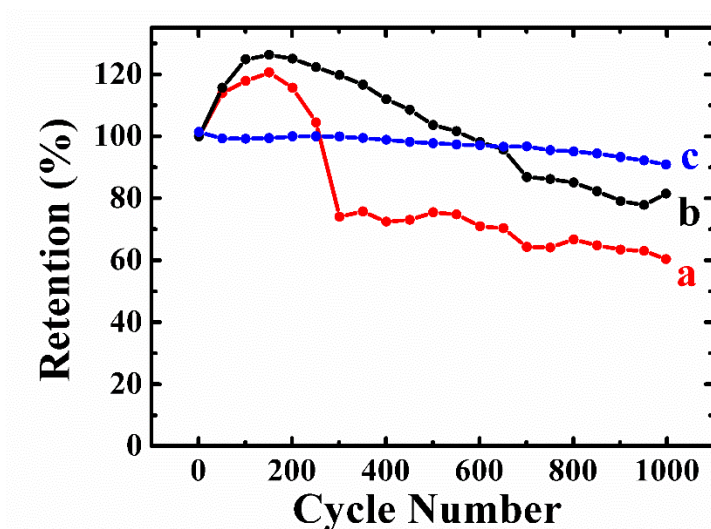


Figure 8.7: Capacitance retention during cycling for (a) FeOOH-CNT (b) (Fe,Zn)OOH-CNT (c) (Fe,Zn)OOH-CNT-PNT electrode.

Further improvement of the capacitive performance of the negative electrodes was achieved using (Fe,Zn)OOH-CNT-PNT composites. The CV data for such composites (Figure 8.6C) showed significant increase in currents in the potential range of $-0.2 - +0.1$ V. The capacitance (Figure 8.6D(c)) of 4 F cm^{-2} was obtained at a sweep rate of 2 mV s^{-1} . The capacitance retention was 91% after 1000 cycles (Figure 8.7c). The improved capacitive behavior of (Fe,Zn)OOH-CNT-PNT compared with (Fe,Zn)OOH-CNT was confirmed by impedance spectroscopy analysis, which was performed at different electrode potentials.

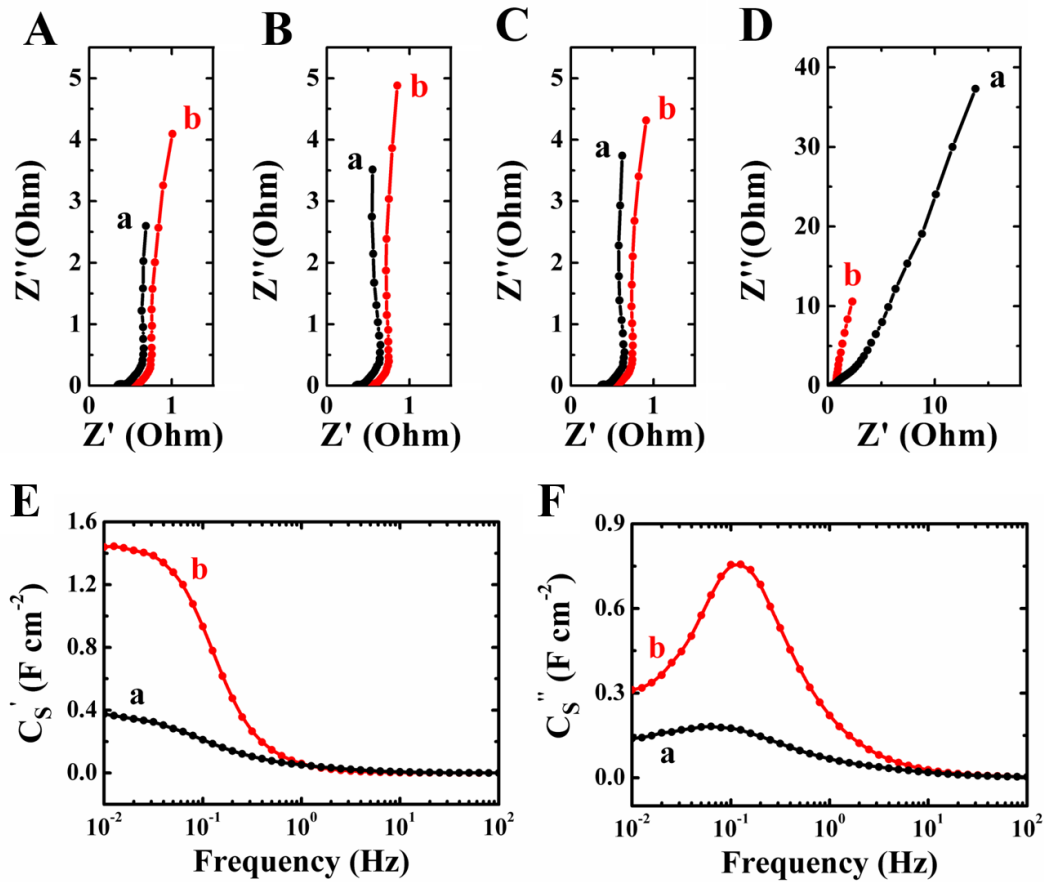


Figure 8.8: (A-D) Nyquist plot of complex impedances at (A)-0.8, (B)-0.5, (C)-0.3 V, and (D)+0.1 V vs. SCE for (a) (Fe,Zn)OOH-CNT (b) (Fe,Zn)OOH-CNT-PNT electrodes; (E,F) frequency dependence of complex capacitances (E) C_s' and (F) C_s'' for (a) (Fe,Zn)OOH-CNT (b) (Fe,Zn)OOH-CNT-PNT electrode at fixed potential of +0.1 V vs. SCE.

Figure 8.8(A-C) shows Nyquist plot of impedance data at electrode potentials of -0.8, -0.5, and -0.3 V. The Nyquist plots show relatively low impedances for (Fe,Zn)OOH-CNT-PNT and (Fe,Zn)OOH-CNT electrodes. (Fe,Zn)OOH-CNT electrodes showed slightly lower impedance at potentials -0.8, -0.5 and -0.3 V. In contrast, (Fe,Zn)OOH-CNT showed (Figure 8.8D) significantly higher impedance at +0.1 V. The high real component of

complex impedance of (Fe,Zn)OOH-CNT indicated high resistance, whereas high imaginary part resulted from low capacitance. The (Fe,Zn)OOH-CNT-PNT electrode showed significantly lower impedance, indicating low resistance and higher capacitance (Figure 8.8D). The real and imaginary components of capacitance were calculated from the impedance data and presented in Figure 8.8(E,F). (Fe,Zn)OOH-CNT-PNT electrodes showed significantly higher capacitances C_s' at low frequencies, compared to (Fe,Zn)OOH-CNT (Figure 8.8E). Both electrodes showed a relaxation type frequency dispersion of capacitance. The C_s'' maximum for (Fe,Zn)OOH-CNT-PNT was observed at a higher frequency and indicated better rate performance (Figure 8.8F).

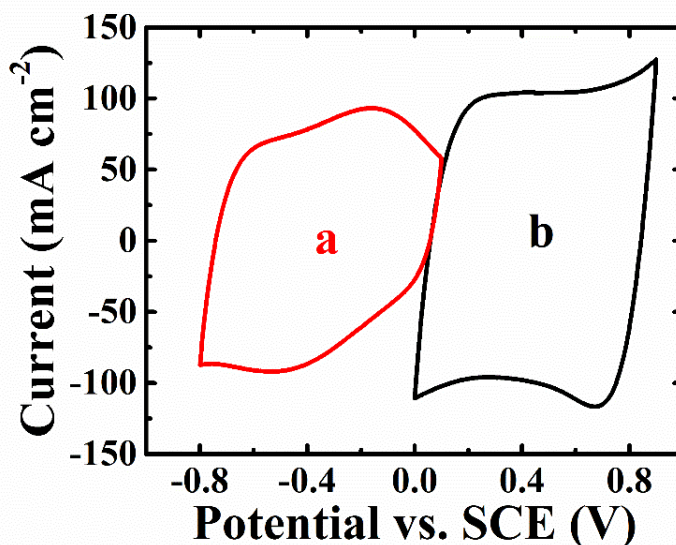


Figure 8.9: CVs at a scan rate of 20 mVs⁻¹ for (a) (Fe,Zn)OOH-CNT-PNT electrode and (b) Mn₃O₄-CNT electrode.

Figure 8.9 shows CVs for (Fe,Zn)OOH-CNT-PNT electrode in a negative potential range and for Mn₃O₄-CNT electrode in a positive potential range in 0.5 M Na₂SO₄ electrolyte at a sweep rate of 20 mV s⁻¹. The CVs have comparable areas in partially overlapped voltage

windows. The electrodes were used for the fabrication of an asymmetric capacitor device, which was tested in a voltage window of 1.6V. Figure 8.10 indicates that nearly box shape CVs were obtained at different sweep rates. The device showed a capacitance of 1.87 F cm^{-2} at 2 mV s^{-1} . The capacitance retention at 100 mV s^{-1} was 24%. The analysis of the cyclic stability showed that capacitance retention after 1000 cycles was 84% (Figure 8.11). Two devices connected in series were used for powering of 20 mA LED bulbs (Figure 8.11 inset).

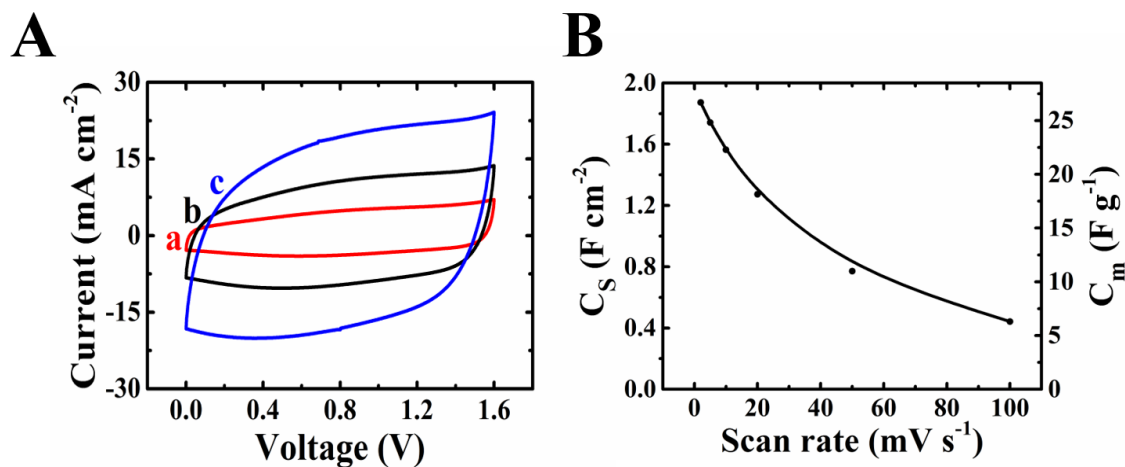


Figure 8.10: (A) CVs at scan rate of (a) 2, (b) 5 and (c) 10 mV s^{-1} and (B) C_s and C_m for device, fabricated using $\text{Mn}_3\text{O}_4\text{-CNT}$ and $(\text{Fe,Zn})\text{OOH-CNT-PNT}$ as positive and negative electrodes, respectively.

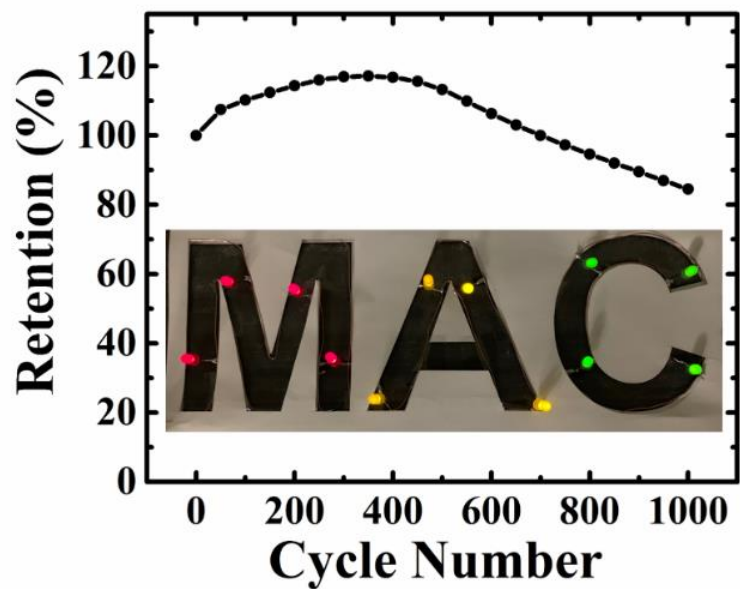


Figure 8.11: Capacitance retention during cycling of the device fabricated using Mn_3O_4 -CNT and (Fe,Zn)OOH-CNT-PNT as positive and negative electrodes, respectively and (inset) LED bulbs powered by two devices connected in series.

8.5 Conclusions

Composite Mn₃O₄-CNT material has been prepared by chemical precipitation of Mn₃O₄ and electrostatic heterocoagulation. The areal capacitance of Mn₃O₄-CNT electrodes was higher than the capacitances of Mn₃O₄ composites, reported in the literature. Good capacitive behavior has been achieved at high active mass loading of 36 mg cm⁻² due to enhanced mixing of Mn₃O₄ and CNT, which resulted from several factors, such as good dispersion of CNT using cationic TL, synthesis of nanostructured Mn₃O₄ particles in the presence of well dispersed CNT and electrostatic heterocoagulation of Mn₃O₄ and CNT. Cycling of the electrodes resulted in changes in microstructure and oxidation state of Mn. The problem of low capacitance of negative electrodes has been addressed by the development of (ZnFe)OOH-PNT electrodes. These studies revealed beneficial effect of Zn and polypyrrole on charge-discharge behavior and impedance at different electrode potentials, enhanced capacitance and cyclic stability of the electrodes. Asymmetric devices have been fabricated and tested, which showed promising performance in a voltage window of 1.6 V.

8.6 Acknowledgements

The authors gratefully acknowledge the Natural Sciences and Engineering Research Council of Canada for the financial support.

8.7 References

1. W. Wei, X. Cui, W. Chen, and D. G. Ivey, 'Manganese oxide-based materials as electrochemical supercapacitor electrodes' *Chem. Soc. Rev.*, 2011, **40**(3), 1697-1721.
2. S. Zhang and G. Z. Chen, 'Manganese oxide based materials for supercapacitors' *Energy Mater.*, 2008, **3**(3), 186-200.
3. R. Dong, Q. Ye, L. Kuang, X. Lu, Y. Zhang, X. Zhang, G. Tan, Y. Wen, and F. Wang, 'Enhanced Supercapacitor Performance of Mn_3O_4 Nanocrystals by Doping Transition-Metal Ions' *ACS Appl. Mater. Interfaces*, 2013, **5**(19), 9508-9516.
4. D. Dubal, D. Dhawale, R. Salunkhe, S. Pawar, V. Fulari, and C. Lokhande, 'A novel chemical synthesis of interlocked cubes of hausmannite Mn_3O_4 thin films for supercapacitor application' *J. Alloys Compounds*, 2009, **484**(1-2), 218-221.
5. Y.F. Lee, K.H. Chang, C.C. Hu, and Y.H. Chu, 'Designing tunable microstructures of Mn_3O_4 nanoparticles by using surfactant-assisted dispersion' *J. Power Sources*, 2012, **206**, 469-475.
6. Z. Qi, A. Younis, D. Chu, and S. Li, 'A facile and template-free one-pot synthesis of Mn_3O_4 nanostructures as electrochemical supercapacitors' *Nano-micro Letters*, 2016, **8**(2), 165-173.
7. D. P. Shaik, P. Rosaiah, K. S. Ganesh, Y. Qiu, and O. Hussain, 'Improved electrochemical performance of Mn_3O_4 thin film electrodes for supercapacitors' *Mater. Sci. Semiconductor Processing*, 2018, **84**, 83-90.
8. A. A. Yadav, 'Influence of electrode mass-loading on the properties of spray deposited Mn_3O_4 thin films for electrochemical supercapacitors' *Thin Solid Films*, 2016, **608**, 88-96.
9. J. Cao, Y. Wang, Y. Zhou, D. Jia, J.-H. Ouyang, and L. Guo, 'Performances of high voltage electrochemical capacitor using ball-milled graphite/ Mn_3O_4 composite electrodes' *J. Electroanal. Chem.*, 2012, **682**, 23-28.
10. S. Li, L.-L. Yu, R.-B. Li, J. Fan, and J.-T. Zhao, 'Template-free and room-temperature synthesis of 3D sponge-like mesoporous Mn_3O_4 with high capacitive performance' *Energy Storage Mater.*, 2018, **11**, 176-183.
11. Y. Qiao, Q. Sun, J. Xi, H. Cui, Y. Tang, and X. Wang, 'A modified solvothermal synthesis of porous Mn_3O_4 for supercapacitor with excellent rate capability and long cycle life' *Journal Alloys Compounds*, 2016, **660**, 416-422.
12. Y. Qiao, Q. Sun, O. Sha, X. Zhang, Y. Tang, T. Shen, L. Kong, and W. Gao, 'Synthesis of Mn_3O_4 nano-materials via CTAB/SDS vesicle templating for high performance supercapacitors' *Mater. Lett.*, 2018, **210**, 128-132.
13. D. Yan, Y. Li, Y. Liu, R. Zhuo, Z. Wu, B. Geng, J. Wang, P. Ren, P. Yan, and Z. Geng, 'Hydrothermal synthesis and electrochemical properties of hexagonal

- hydrohausmannite plates as supercapacitor electrode material' *Mater. Lett.*, 2014, **117**, 62-65.
14. Z. Gao, H. Wang, Z. Cao, T. Zhou, C. An, and Y. Zhao,'Silver Nanowires@ Mn₃O₄ Core-Shell Nanocables as Advanced Electrode Materials for Aqueous Asymmetric Supercapacitors' *Energy Technol.*, 2017, **5**(12), 2275-2282.
15. L. Liu, L. Su, J. Lang, B. Hu, S. Xu, and X. Yan,'Controllable synthesis of Mn₃O₄ nanodots@nitrogen-doped graphene and its application for high energy density supercapacitors' *J. Mater. Chem. A*, 2017, **5**(11), 5523-5531.
16. K. Subramani, D. Jeyakumar, and M. Sathish,'Manganese hexacyanoferrate derived Mn₃O₄ nanocubes-reduced graphene oxide nanocomposites and their charge storage characteristics in supercapacitors' *Phys.Chem. Chem. Phys.*, 2014, **16**(10), 4952-4961.
17. X. Xiao, Y. Wang, G. Chen, L. Wang, and Y. Wang,' Mn₃O₄/activated carbon composites with enhanced electrochemical performances for electrochemical capacitors' *J. Alloys Compounds*, 2017, **703**, 163-173.
18. J. Yao, S. Yao, F. Gao, L. Duan, M. Niu, and J. Liu,'Reduced graphene oxide/Mn₃O₄ nanohybrid for high-rate pseudocapacitive electrodes' *J. Colloid Interface Sci.*, 2018, **511**, 434-439.
19. J. Xu, X. Fan, Q. Xia, Z. Shao, B. Pei, Z. Yang, Z. Chen, and W. Zhang,'A highly atom-efficient strategy to synthesize reduced graphene oxide-Mn₃O₄ nanoparticles composites for supercapacitors' *J. Alloys Compounds*, 2016, **685**, 949-956.
20. M. S. Ata, J. Milne, and I. Zhitomirsky,'Fabrication of Mn₃O₄-carbon nanotube composites with high areal capacitance using cationic and anionic dispersants' *J. Colloid Interface Sci.*, 2018, **512**, 758-766.
21. J. Milne and I. Zhitomirsky,'Application of octanohydroxamic acid for liquid-liquid extraction of manganese oxides and fabrication of supercapacitor electrodes' *J. Colloid Interface Sci.*, 2018, **515**, 50-57.
22. Y. Zhou, L. Guo, W. Shi, X. Zou, B. Xiang, and S. Xing,'Rapid Production of Mn₃O₄/rGO as an Efficient Electrode Material for Supercapacitor by Flame Plasma' *Materials*, 2018, **11**(6), 881.
23. Y. Xiao, Y. Cao, Y. Gong, A. Zhang, J. Zhao, S. Fang, D. Jia, and F. Li,'Electrolyte and composition effects on the performances of asymmetric supercapacitors constructed with Mn₃O₄ nanoparticles-graphene nanocomposites' *J.Power Sources*, 2014, **246**, 926-933.
24. C. Liu, H. Song, C. Zhang, Y. Liu, C. Zhang, X. Nan, and G. Cao,'Coherent Mn₃O₄-carbon nanocomposites with enhanced energy-storage capacitance' *Nano Research*, 2015, **8**(10), 3372- 3383.

25. N. S. Arul, J. I. Han, and P. C. Chen, 'Solid State Supercapacitor Based on Manganese Oxide@Reduced Graphene Oxide and Polypyrrole Electrodes' *ChemElectroChem*, 2018, **5**(19), 2747-2757.
26. S. Krehula, S. Musić, Ž. Skoko, and S. Popović, 'The influence of Zn-dopant on the precipitation of α -FeOOH in highly alkaline media' *J Alloys Compounds*, 2006, **420**(1), 260-268.
27. Y. Zhu, K. Shi, and I. Zhitomirsky, 'Anionic dopant–dispersants for synthesis of polypyrrole coated carbon nanotubes and fabrication of supercapacitor electrodes with high active mass loading' *J. Mater. Chem. A*, 2014, **2**(35), 14666-14673.
28. C. Shi and I. Zhitomirsky, 'Electrodeposition and Capacitive Behavior of Films for Electrodes of Electrochemical Supercapacitors' *Nanoscale Res. Lett.*, 2010, **5**(3), 518.
29. Y. Su and I. Zhitomirsky, 'Hybrid MnO₂/carbon nanotube-VN/carbon nanotube supercapacitors' *J. Power Sources*, 2014, **267**, 235-242.
30. M. Kosmulski, 'Isoelectric points and points of zero charge of metal (hydr)oxides: 50 years after Parks' review' *Adv. Colloid and Interface Sci.*, 2016, **238**, 1-61.
31. R. Attias, D. Sharon, A. Borenstein, D. Malka, O. Hana, S. Luski, and D. Aurbach, 'Asymmetric supercapacitors using chemically prepared MnO₂ as positive electrode materials' *J. Electrochem. Soc.*, 2017, **164**(9), A2231-A2237.
32. Z. Zhang, K. Chi, F. Xiao, and S. Wang, 'Advanced solid-state asymmetric supercapacitors based on 3D graphene/MnO₂ and graphene/polypyrrole hybrid architectures' *J. Mater. Chem. A*, 2015, **3**(24), 12828-12835.
33. M. R. C. Ismael and J. M. R. Carvalho, 'Iron recovery from sulphate leach liquors in zinc hydrometallurgy' *Minerals Eng.*, 2003, **16**(1), 31-39.

Chapter 9 Fabrication of high areal capacitance Mn₃O₄-Carbon nanotube composite electrode by Schiff base formation

R. Poon* and I. Zhitomirsky*^α

*Department of Materials Science and Engineering, McMaster University,
Hamilton, Ontario, L8S 4L7, Canada

^αCorresponding Author: zhitom@mcmaster.ca; 905-525-9140 ext. 23914

Unpublished.

9.1 Abstract

A novel colloidal method has been developed for the fabrication of Mn₃O₄-multi walled carbon nanotubes (MWCNTs) composites as cathode materials for electrochemical supercapacitors. In this technique, 3,4-dihydroxybenzaldehyde (DHB) and tolonium chloride dye (TL) were used as advanced dispersants for Mn₃O₄ and MWCNTs. Schiff base formation between DHB and TL allowed for improved mixing of Mn₃O₄ and MWCNTs, and enhanced electrochemical performance at high active mass loadings. The fabricated electrode showed high areal capacitance of 5.16 F cm⁻² at a mass loading of 38 mg cm⁻², good capacitance retention at high scan rates and low impedance. The results of this investigation have demonstrated benefits of the conceptually new colloidal method, and offer new insights for colloidal fabrication of advanced composites.

9.2 Introduction

Mn_3O_4 is an advanced cathode material for electrochemical supercapacitors due to its high specific capacitance and low cost [1-3]. It belongs to a large group of advanced materials with a spinel crystalline structure, and is capable of forming solid solutions with various spinel compounds. The rich chemistry of spinel offers possibilities [4] for tailoring of composition, conductivity and capacitive properties of Mn_3O_4 for different applications. The ability to synthesize Mn_3O_4 nanoparticles from Mn^{2+} salt solutions offers many technological advantages, which make this material very promising for the future development of the supercapacitor technology.

Good capacitive performance of the pseudocapacitive materials at practical active mass loadings is vital for the development of the next generation of supercapacitor devices. However, electrochemical performance at practical active mass loading above 10 mg cm^{-2} are typically inferior, as the gravimetric capacitance decreased significantly with increasing electrode mass due to poor electrolyte access to the active material and low electronic conductivity [1]. Therefore, research efforts were devoted to the synthesis of nanoparticles with high surface area, and the design and fabrication of advanced composites. Various conductive additives were combined with Mn_3O_4 to fabricate composites in order to enhance electronic conductivity and facilitate charge-discharge redox reactions [5].

The capacitances of Mn_3O_4 and composite electrodes, prepared by different techniques, were compared in the literature [6,7]. Numerous investigations focused on pure Mn_3O_4 thin films [8-12] and reported high specific capacitances of 568 F g^{-1} [11] and 597 F g^{-1} [12] at mass

loadings of 0.16 and 0.64 mg cm⁻², respectively. Despite the high specific capacitances, the low active mass loading of thin film electrodes resulted in low areal capacitances, which is detrimental for practical application. The use of Mn²⁺ salts for Mn₃O₄ synthesis facilitated the application of conductive additives and dispersing agents [13,14]. Mn₃O₄ composites containing graphite [15], carbon black [16], acetylene black [13,14,17] and other conductive additives [18] showed enhanced electrochemical performance at higher mass loadings in the range of 2-9.5 mg cm⁻². High gravimetric capacitance of 222.4 F g⁻¹ was achieved at mass loading of 9.5 mg cm⁻² and resulted in areal capacitance of 2.11 F cm⁻² for Mn₃O₄-acetylene black composite electrode[17]. Mn₃O₄ composites were also fabricated with capacitive carbon materials such as graphene [19,20] and activated carbon [21]. High specific capacitances of 538 F g⁻¹ (2.69 F cm⁻²) [22] and 258.6 F g⁻¹ (2.33 F cm⁻²) [23] were achieved at mass loadings of 5 and 9 mg cm⁻², respectively, for Mn₃O₄-graphene oxide composites.

It has been demonstrated that the capacitive behavior of Mn₃O₄ composites can be enhanced at high mass loadings using advanced colloidal techniques [24]. Mn₃O₄-carbon nanotube electrodes fabricated using advanced colloidal techniques showed superior areal capacitances of 2.8 [24] and 4.2 [25] F cm⁻² at high active mass loadings of 28.4 and 33 mg cm⁻². Using Mn₃O₄ as cathodes, asymmetric devices with large voltage windows were fabricated with various anodes such as graphene [26], activated carbon [27], lithium titanate [28] and polypyrrole [29], and have shown excellent electrochemical performance.

The goal of this investigation was the development of advanced Mn₃O₄ – multiwalled carbon nanotube (MWCNT) electrodes. A conceptually new colloidal strategy has been

designed for the fabrication of Mn_3O_4 -MWCNT composites, which showed good capacitive behavior at high active mass loading of 38 mg cm^{-2} . The high areal capacitance of 5.16 F cm^{-2} was achieved at a low electrode resistance. The approach was based on the synthesis of Mn_3O_4 nanoparticles from a Mn^{2+} solution and their surface modification with 3,4-dihydroxybenzaldehyde (DHB). The important feature of our approach was the surface modification and dispersion of MWCNT with tolonium chloride (TL), and the Schiff base formation between of DHB and TL. The Schiff base formation facilitated enhanced mixing between Mn_3O_4 particles and MWCNT, and allowed the electrode to achieve high areal capacitance of 5.16 F cm^{-2} . The approach developed in this investigation can be used for the fabrication of other composites with advanced functionality.

9.3 Experimental Procedure

DHB, TL, $\text{Mn}(\text{NO}_3)_2 \cdot 4\text{H}_2\text{O}$, NaOH, Na_2SO_4 , and poly(vinyl butyral-co-vinyl-alcohol-co-vinyl acetate) (PVB, average $M_w=50,000-80,000$) were purchased from Sigma Aldrich and used without further purification. MWCNT (ID 4nm, OD 13nm, length 1~2 μm) were purchased from Bayer Material Science, Germany, and Ni foams with 95% porosity were provided by Vale Ltd..

The synthesis of Mn_3O_4 was performed using a 0.5 M aqueous solution of $\text{Mn}(\text{NO}_3)_2$. The pH of solution was increased to pH = 10 by dropwise addition of 2 M NaOH under ultrasonication. DHB was added to the $\text{Mn}(\text{NO}_3)_2$ solutions before the synthesis or to the Mn_3O_4 suspension after synthesis, the mass ratio of DHB: Mn_3O_4 was 1:2. 1g L^{-1} MWCNT suspension in water was prepared using 0.5 g L^{-1} TL as a dispersant. The suspensions of

Mn₃O₄, modified with DHB, and MWCNT, modified with TL were mixed to achieve mass ratio Mn₃O₄: MWCNT=4:1.

The final composite suspension was filtrated, the obtained material was washed and dried at 60 °C. The composite was mixed with PVB in ethanol to fabricate a slurry for the impregnation of the Ni foam current collector. The PVB content in the slurry was 3% of the mass of the composite. The active mass loading of the obtained electrodes was 38 mg cm⁻².

XRD investigation was performed using a powder diffractometer equipped with a Rigaku RU200 Cu K α rotating anode and a Bruker Smart6000 CCD area detector. FTIR measurements were carried out on a Bruker Vertex 70 spectrometer in the wavenumber range of 400 - 4000 cm⁻¹. Cyclic voltammetry (CV) and electrochemical impedance spectroscopy (EIS) were performed using a potentiostat (PARStat 2273, Princeton Applied Research). The electrochemical measurements were carried out in a three-electrode setup with 0.5 M Na₂SO₄ electrolyte. The area of working electrode was 1 cm². Pt gauze was used as counter electrode and saturated calomel electrode (SCE) was used as reference electrode. CV studies were performed at scan rates of 2, 5, 10, 20, 50 and 100 mV s⁻¹, and the gravimetric capacitance ($C_m = Q/2\Delta Vm$) and areal capacitance ($C_s = Q/2\Delta VA$) were calculated by integrating the CV curve area to obtain charge Q, and subsequently divided by the voltage window (ΔV) and active mass (m) or area (A). EIS measurements were carried out in the frequency range of 10 mHz – 100 kHz with a sinusoidal signal of 5 mV. The components of complex capacitance (C_s' and C_s'') were calculated from EIS data as $C_s' = Z'/\omega|Z|^2A$ and $C_s'' = Z''/\omega|Z|^2A$, where $\omega=2\pi f$ and f is frequency. An activation

procedure consisted of 2, 3, 5, 10, 10, 10 cycles at scan rates of 2, 5, 10, 20 50, 100 mV s⁻¹.

9.4 Results and Discussion

Figure 9.1 shows the XRD pattern of Mn₃O₄ with DHB addition after synthesis. The pattern corresponds to crystalline Mn₃O₄ in JDCPS file 024-0734, and indicated that the addition of DHB after synthesis of Mn₃O₄ did not change the phase content of the material.

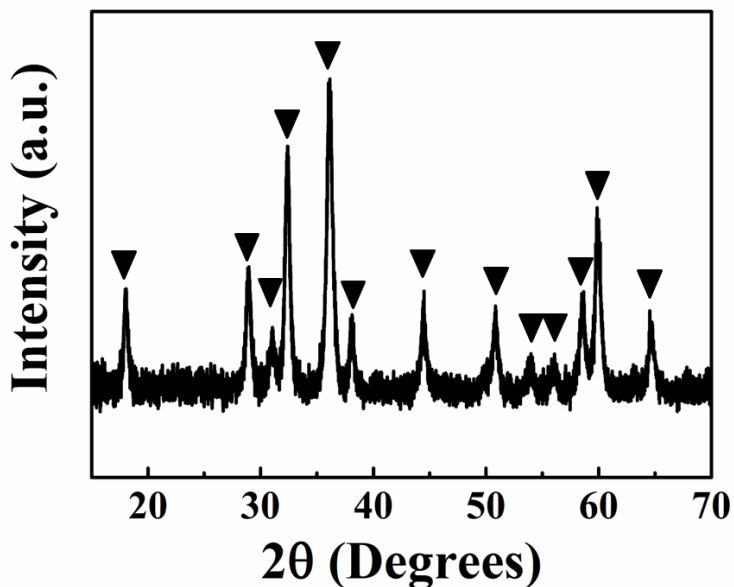


Figure 9.1: XRD pattern of Mn₃O₄ with addition of DHB after synthesis.

The adsorption of DHB onto Mn₃O₄ is mainly driven by the presence of catechol group, which has shown remarkable adsorption to metal and metal oxides in literature[30]. The adsorption mechanism is illustrated in Figure 9.2, where catechol group adsorbs on a metal atom by bridging or chelating mechanisms.

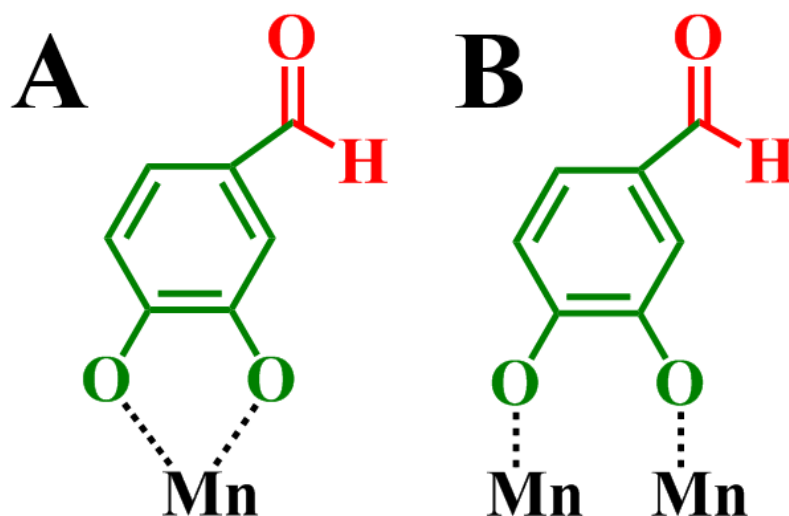


Figure 9.2: Adsorption of DHB on Mn atom by (A) chelating and (B) bridging mechanisms.

To confirm the adsorption of DHB on Mn_3O_4 , FTIR studies were performed on DHB modified Mn_3O_4 and compared with pure materials. Figure 9.3 shows the FTIR spectra for pure Mn_3O_4 , as-received DHB and Mn_3O_4 particles with addition of DHB after synthesis. The FTIR spectrum of DHB modified Mn_3O_4 shows peaks at 1580 and 1484 cm^{-1} , which can be attributed to aromatic C=C stretching of DHB. The peaks at 1436 and 1264 cm^{-1} are attributed to C–O stretching, and peak at 1113 cm^{-1} resulted from in-plane C–H bending of DHB. Based on the FTIR results, absorption peaks of DHB were observed on modified Mn_3O_4 and it can be concluded that DHB is adsorbed onto Mn_3O_4 surface.

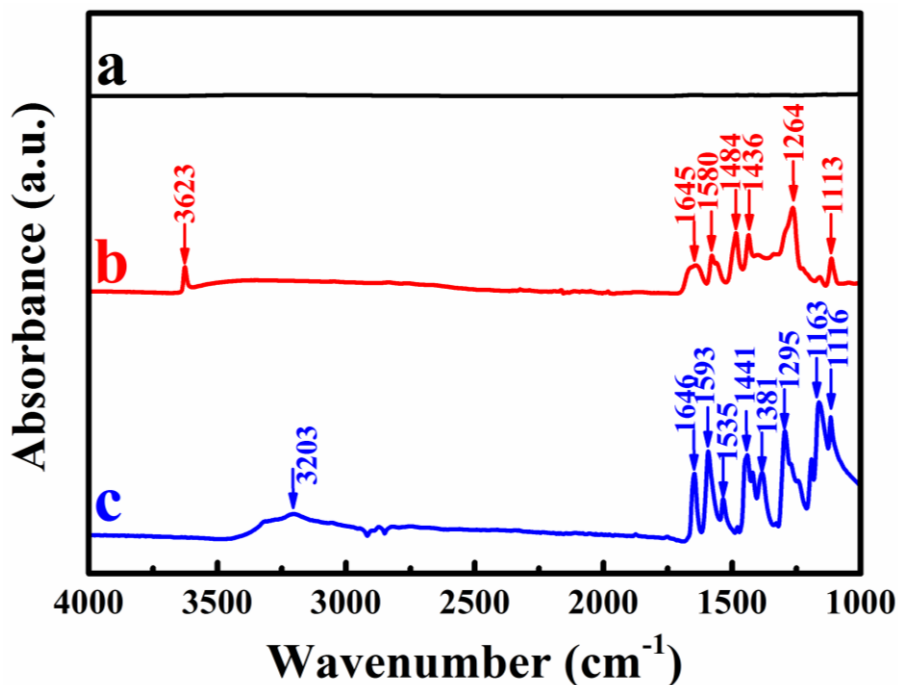


Figure 9.3: FTIR spectra of (a) pure Mn₃O₄, (b) Mn₃O₄-DHB, and (c) pure DHB.

Catechol group of DHB have shown remarkable adsorption to Mn₃O₄ particles, and the aldehyde group of DHB can react with amine to form a chemical Schiff base linkage. Figure 9.4(A) and (B) show the chemical structure of DHB, and a small amine-containing aromatic dye, TL. Small aromatic molecules offer advantages for dispersion of MWCNTs and have shown superior dispersion compared to traditional surfactants [31-33]. It was suggested that small molecules can disperse MWCNTs by an “unzipping” mechanism. Small molecules are able to penetrate MWCNTs bundles from the ends and adsorb onto individual MWCNT to facilitate dispersion [34-36]. Using DHB and TL as dispersants for Mn₃O₄ and MWCNT, respectively, the mixing is enhanced by Schiff base formation shown in Figure 9.4C. Such heterocoagulation procedure facilitated the formation of advanced composite.

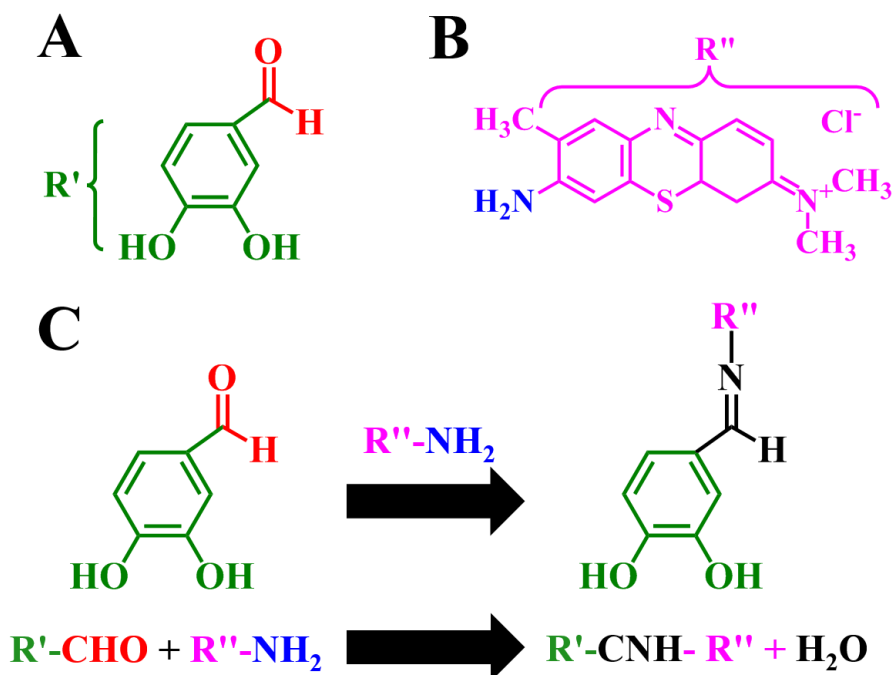


Figure 9.4: Chemical structure of (A) DHB and (B) TL, and (C) Schiff base formation between R'-CHO and R''-NH₂.

The fabricated electrode was tested for 4 iterations of activation procedure, and such activation procedure was reported by our group previously [32,37]. The goal of the activation procedure is to promote the formation of electrochemically active MnO₂ surface layer to enhance capacitive performance [38]. Figure 9.5 shows the CVs of the composite electrode after 4 iterations of the activation procedure. The CVs after activation procedure are nearly box shape, indicating good capacitive behaviour. The highest capacitance achieved was C_S = 5.16 F cm⁻² and C_m = 134.8 F g⁻¹ at a scan rate of 2 mV s⁻¹, then decreased to C_S = 1.84 F cm⁻² and C_m = 48.1 F g⁻¹ at a scan rate of 100 mV s⁻¹ with a capacitance retention of 36%. The areal capacitances of the composite electrode are far superior than other Mn₃O₄ electrodes reported in literatures at practical mass loadings. Figure 9.6(A)

shows the EIS results of the composite electrode presented in Nyquist plot, and the electrode exhibited very low resistance ($Z' = R$) and good capacitive performance indicated by the vertical segment at low frequencies. The complex capacitances shown in Figure 9.6(B) and (C) are in good agreement with capacitance calculated from CVs, and the C_s'' shows relaxation type frequency dispersion with relaxation frequency of $f = 0.09$ Hz indicating good rate capability of electrode.

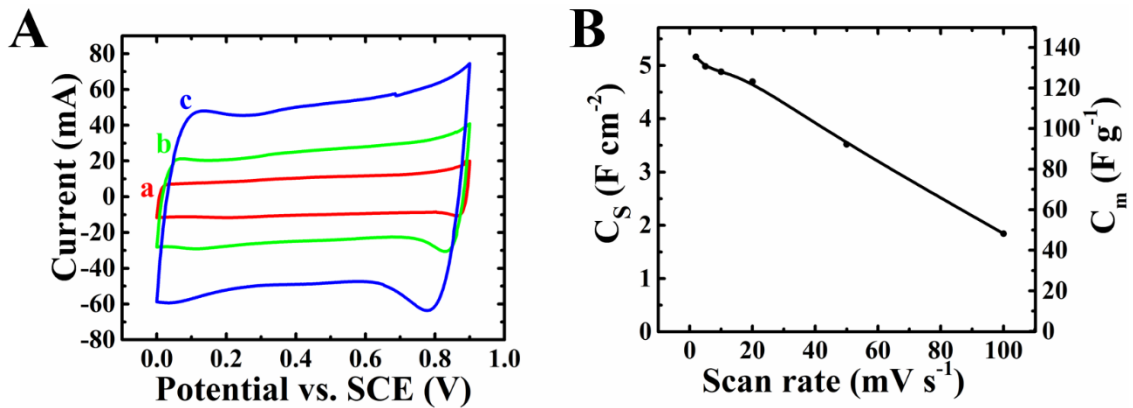


Figure 9.5: (A) CVs at scan rate of (a) 2, (b) 5 and (c) 10 mV s⁻¹, and (B) C_s and C_m versus scan rates for Mn₃O₄-MWCNT composite electrode after the 4th activation procedure.

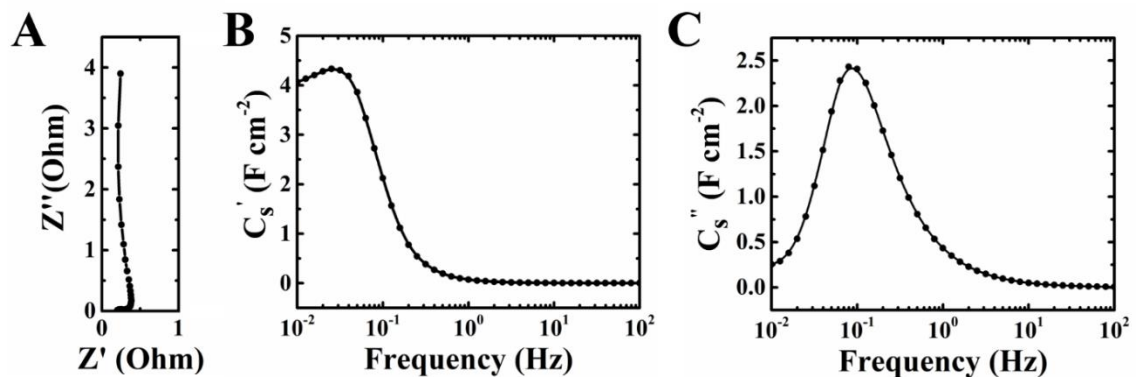


Figure 9.6: (A) Nyquist plot of complex impedance and frequency dependences of (B) C_s' and (C) C_s'' of Mn₃O₄-MWCNT composite electrode after the 4th activation procedure.

To investigate the effect of addition of DHB during synthesis of Mn_3O_4 nanoparticles, an electrode with similar mass loading was fabricated with the presence of DHB during Mn_3O_4 synthesis. The electrode underwent the same activation procedure presented earlier, and the highest capacitance achieved was $C_S = 2.96 \text{ F cm}^{-2}$ and $C_m = 77.7 \text{ F g}^{-1}$ at a scan rate of 2 mV s^{-1} , then decreased to $C_S = 1.94 \text{ F cm}^{-2}$ and $C_m = 50.9 \text{ F g}^{-1}$ at a scan rate of 100 mV s^{-1} (Figure 9.7B). The electrode exhibited a higher relaxation frequency of $f = 0.18 \text{ Hz}$ as shown in Figure 9.8C, indicating high rate capability of the electrode. The electrode showed lower capacitance at low scan rates, yet better capacitance retention and rate performance compared to the electrode fabricated with DHB addition after Mn_3O_4 synthesis. We suggested that DHB can adsorb onto Mn_3O_4 nanoparticles during synthesis and reduced the particle size. However, small nanoparticles can form more compacted structure which inhibit electrolyte access and are more susceptible to dissolution during electrochemical cycling due to the high surface energy. Moreover, the smaller particle size and dissolution of Mn_3O_4 has generated higher active surface area, which enhanced the capacitive and rate performance especially at higher scan rates.

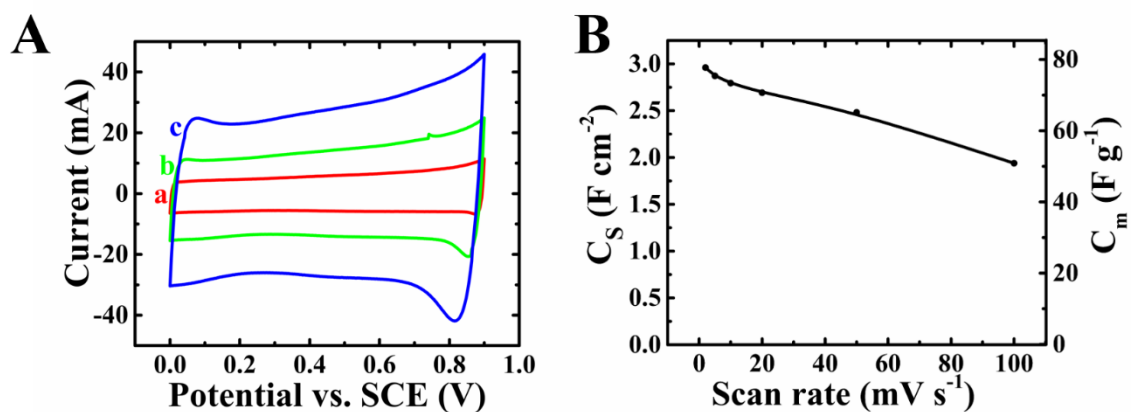


Figure 9.7: (A) CVs at scan rate of (a) 2, (b) 5 and (c) 10 mV s⁻¹, and (B) C_S and C_m versus scan rates for Mn₃O₄-MWCNT composite electrode fabricated with DHB during synthesis.

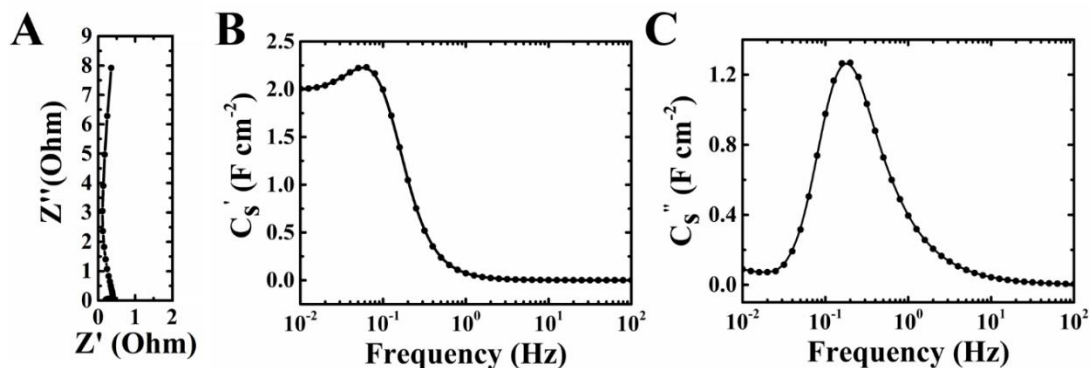


Figure 9.8: (A) Nyquist plot of complex impedance and frequency dependences of (B) C_S' and (C) C_S'' of Mn₃O₄-MWCNT composite electrode fabricated with DHB during synthesis.

Despite the low conductivity of Mn₃O₄, using new Schiff base formation and an activation procedure has allowed the composite electrode to achieve good capacitances at high active mass loadings. Compared to literatures, the electrode exhibited excellent electrochemical performance at high active mass to current collector mass ratio of 0.59, which is advantageous for fabrication of electrodes for practical applications.

9.5 Conclusions

Mn₃O₄-MWCNT composite electrodes were fabricated using advanced dispersants DHB and TL, and the Schiff base formation allowed for enhanced mixing of the individual components. The catechol group of DHB allowed for strong adsorption on Mn atoms on the particle surface, while the polyaromatic structure of TL allowed for surface modification of MWCNT by strong π - π interactions and facilitated the dispersion even at low dispersant concentration. The Schiff base formation between DHB and TL facilitated improved mixing of Mn₃O₄ and MWCNT, and the electrochemical testing results showed remarkable performance at high active mass loading of 38 mg cm⁻². The highest capacitance achieved was 5.16 F cm⁻² at a scan rate of 2 mV s⁻¹ for the electrode with DHB addition after synthesis, and the electrode fabricated with DHB addition during synthesis resulted in improved capacitance retention and rate performance.

9.6 References

- [1] W. Wei, X. Cui, W. Chen, D.G. Ivey, Manganese oxide-based materials as electrochemical supercapacitor electrodes, *Chemical society reviews* 40(3) (2011) 1697-1721.
- [2] S. Zhang, G.Z. Chen, Manganese oxide based materials for supercapacitors, *Energy Materials* 3(3) (2008) 186-200.
- [3] C. Zhao, W. Zheng, A review for aqueous electrochemical supercapacitors, *Frontiers in Energy Research* 3 (2015) 23.
- [4] R. Dong, Q. Ye, L. Kuang, X. Lu, Y. Zhang, X. Zhang, G. Tan, Y. Wen, F. Wang, Enhanced Supercapacitor Performance of Mn_3O_4 Nanocrystals by Doping Transition-Metal Ions, *ACS Applied Materials & Interfaces* 5(19) (2013) 9508-9516.
- [5] W. Yuan, L. Cheng, B. Zhang, H. Wu, 2D- Ti_3C_2 as hard, conductive substrates to enhance the electrochemical performance of MnO_2 for supercapacitor applications, *Ceramics International* 44(14) (2018) 17539-17543.
- [6] B. Li, X. Zhang, J. Dou, C. Hu, Facile synthesis of pseudocapacitive Mn_3O_4 nanoparticles for high-performance supercapacitor, *Ceramics International* in press (2019).
- [7] D.P.M.D. Shaik, R. Pitcheri, Y. Qiu, O.M. Hussain, Hydrothermally synthesized porous Mn_3O_4 nanoparticles with enhanced electrochemical performance for supercapacitors, *Ceramics International* 45(2, Part A) (2019) 2226-2233.
- [8] D. Dubal, D. Dhawale, R. Salunkhe, S. Pawar, V. Fulari, C. Lokhande, A novel chemical synthesis of interlocked cubes of hausmannite Mn_3O_4 thin films for supercapacitor application, *Journal of Alloys and Compounds* 484(1-2) (2009) 218-221.
- [9] Y.F. Lee, K.H. Chang, C.C. Hu, Y.H. Chu, Designing tunable microstructures of Mn_3O_4 nanoparticles by using surfactant-assisted dispersion, *Journal of Power Sources* 206 (2012) 469-475.
- [10] Z. Qi, A. Younis, D. Chu, S. Li, A facile and template-free one-pot synthesis of Mn_3O_4 nanostructures as electrochemical supercapacitors, *Nano-micro letters* 8(2) (2016) 165-173.
- [11] D.P. Shaik, P. Rosaiah, K.S. Ganesh, Y. Qiu, O. Hussain, Improved electrochemical performance of Mn_3O_4 thin film electrodes for supercapacitors, *Materials Science in Semiconductor Processing* 84 (2018) 83-90.
- [12] A.A. Yadav, Influence of electrode mass-loading on the properties of spray deposited Mn_3O_4 thin films for electrochemical supercapacitors, *Thin Solid Films* 608 (2016) 88-96.
- [13] Y. Qiao, Q. Sun, J. Xi, H. Cui, Y. Tang, X. Wang, A modified solvothermal synthesis of porous Mn_3O_4 for supercapacitor with excellent rate capability and long cycle life, *Journal of alloys and compounds* 660 (2016) 416-422.

- [14] Y. Qiao, Q. Sun, O. Sha, X. Zhang, Y. Tang, T. Shen, L. Kong, W. Gao, Synthesis of Mn_3O_4 nano-materials via CTAB/SDS vesicle templating for high performance supercapacitors, *Materials Letters* 210 (2018) 128-132.
- [15] J. Cao, Y. Wang, Y. Zhou, D. Jia, J.-H. Ouyang, L. Guo, Performances of high voltage electrochemical capacitor using ball-milled graphite/ Mn_3O_4 composite electrodes, *Journal of Electroanalytical Chemistry* 682 (2012) 23-28.
- [16] S. Li, L.L. Yu, R.B. Li, J. Fan, J.T. Zhao, Template-free and room-temperature synthesis of 3D sponge-like mesoporous Mn_3O_4 with high capacitive performance, *Energy Storage Materials* 11 (2018) 176-183.
- [17] D. Yan, Y. Li, Y. Liu, R. Zhuo, Z. Wu, B. Geng, J. Wang, P. Ren, P. Yan, Z. Geng, Hydrothermal synthesis and electrochemical properties of hexagonal hydrohausmannite plates as supercapacitor electrode material, *Materials Letters* 117 (2014) 62-65.
- [18] Z. Gao, H. Wang, Z. Cao, T. Zhou, C. An, Y. Zhao, Silver Nanowires@ Mn_3O_4 Core-Shell Nanocables as Advanced Electrode Materials for Aqueous Asymmetric Supercapacitors, *Energy Technology* 5(12) (2017) 2275-2282.
- [19] L. Liu, L. Su, J. Lang, B. Hu, S. Xu, X. Yan, Controllable synthesis of Mn_3O_4 nanodots@ nitrogen-doped graphene and its application for high energy density supercapacitors, *Journal of Materials Chemistry A* 5(11) (2017) 5523-5531.
- [20] K. Subramani, D. Jeyakumar, M. Sathish, Manganese hexacyanoferrate derived Mn_3O_4 nanocubes-reduced graphene oxide nanocomposites and their charge storage characteristics in supercapacitors, *Physical Chemistry Chemical Physics* 16(10) (2014) 4952-4961.
- [21] X. Xiao, Y. Wang, G. Chen, L. Wang, Y. Wang, Mn_3O_4 /activated carbon composites with enhanced electrochemical performances for electrochemical capacitors, *Journal of Alloys and Compounds* 703 (2017) 163-173.
- [22] J. Yao, S. Yao, F. Gao, L. Duan, M. Niu, J. Liu, Reduced graphene oxide/ Mn_3O_4 nanohybrid for high-rate pseudocapacitive electrodes, *Journal of Colloid and Interface Science* 511 (2018) 434-439.
- [23] J. Xu, X. Fan, Q. Xia, Z. Shao, B. Pei, Z. Yang, Z. Chen, W. Zhang, A highly atom-efficient strategy to synthesize reduced graphene oxide- Mn_3O_4 nanoparticles composites for supercapacitors, *Journal of Alloys and Compounds* 685 (2016) 949-956.
- [24] M.S. Ata, J. Milne, I. Zhitomirsky, Fabrication of Mn_3O_4 -carbon nanotube composites with high areal capacitance using cationic and anionic dispersants, *Journal of Colloid and Interface Science* 512 (2018) 758-766.
- [25] J. Milne, I. Zhitomirsky, Application of octanohydroxamic acid for liquid-liquid extraction of manganese oxides and fabrication of supercapacitor electrodes, *Journal of Colloid and Interface Science* 515 (2018) 50-57.

- [26] Y. Zhou, L. Guo, W. Shi, X. Zou, B. Xiang, S. Xing, Rapid Production of $\text{Mn}_3\text{O}_4/\text{rGO}$ as an Efficient Electrode Material for Supercapacitor by Flame Plasma, *Materials* 11(6) (2018) 881.
- [27] Y. Xiao, Y. Cao, Y. Gong, A. Zhang, J. Zhao, S. Fang, D. Jia, F. Li, Electrolyte and composition effects on the performances of asymmetric supercapacitors constructed with Mn_3O_4 nanoparticles–graphene nanocomposites, *Journal of Power Sources* 246 (2014) 926-933.
- [28] C. Liu, H. Song, C. Zhang, Y. Liu, C. Zhang, X. Nan, G. Cao, Coherent Mn_3O_4 -carbon nanocomposites with enhanced energy-storage capacitance, *Nano Research* 8(10) (2015) 3372-3383.
- [29] N.S. Arul, J.I. Han, P.C. Chen, Solid State Supercapacitor Based on Manganese Oxide@Reduced Graphene Oxide and Polypyrrole Electrodes, *ChemElectroChem* 5(19) (2018) 2747-2757.
- [30] C. Wallar, T. Zhang, K. Shi, I. Zhitomirsky, Synthesis of metal and metal oxide nanoparticles, liquid–liquid extraction and application in supercapacitors, *Colloids and Surfaces A: Physicochemical and Engineering Aspects* 500 (2016) 195–202.
- [31] M.S. Ata, S. Ghosh, I. Zhitomirsky, Electrostatic assembly of composite supercapacitor electrodes, triggered by charged dispersants, *Journal of Materials Chemistry A* 4 (45) (2016) 17857-17865.
- [32] M.S. Ata, J. Milne, I. Zhitomirsky, Fabrication of Mn_3O_4 –carbon nanotube composites with high areal capacitance using cationic and anionic dispersants, *Journal of Colloid and Interface Science* 512 (2018) 758-766.
- [33] M.S. Ata, R. Poon, A. Syed, J. Milne and I. Zhitomirsky, New developments in non-covalent surface modification, dispersion and electrophoretic deposition of carbon nanotubes, *Carbon* 130 (2018) 584-598.
- [34] M. Gubitosi, J.V. Trillo, A.A. Vargas, N.V. Pavel, D. Gazzoli, S. Sennato, A. Jover, F. Mejjide, L. Galantini, Characterization of Carbon Nanotube Dispersions in Solutions of Bile Salts and Derivatives Containing Aromatic Substituents, *Journal of Physical Chemistry B* 118 (4) (2014) 1012–1021.
- [35] M.S. Strano, V.C. Moore, M.K. Miller, M.J. Allen, E.H. Haroz, C. Kittrell, R.H. Hauge, R.E. Smalley, The Role of Surfactant Adsorption during Ultrasonication in the Dispersion of Single-Walled Carbon Nanotubes, *Journal of Nanoscience and Nanotechnology* 3 (1) (2003) 81–86.
- [36] F. Tournus, S. Latil, M.I. Heggie, J.C. Charlier, π -stacking interaction between carbon nanotubes and organic molecules, *Physical Review B* 72 (7) (2005) 075431.
- [37] R. Poon and I. Zhitomirsky, High areal capacitance of Mn_3O_4 -carbon nanotube electrodes, *Materials Letters* (215) (2018) 4–7.

[38] D.P. Dubal, D.S. Dhawale, R.R. Salunkhe, and C.D. Lokhande, Conversion of Chemically Prepared Interlocked Cubelike Mn_3O_4 to Birnessite MnO_2 Using Electrochemical Cycling, *Journal of Electrochemical Society* 157(7) (2010) A812.

Chapter 10 High areal capacitance of V₂O₃-carbon nanotube electrodes

C.J. Wallar^{*=}, R Poon^{*=} and I. Zhitomirsky^{*α}

^{*}Department of Materials Science and Engineering, McMaster University,
Hamilton, Ontario, L8S 4L7, Canada

^αCorresponding Author: zhitom@mcmaster.ca; 905-525-9140 ext. 23914

Submitted on 14th August 2017. Published on 29th November 2017.

Reprinted with permission from *J. Electrochem. Soc.*, 164, A3620-A3627 (2017).

Copyright 2017, reproduced with permission from The Electrochemical Society.

Author's Contributions:

- Processing and fabrication of V₂O₃(m) and V₂O₃(r)-MWCNT composite electrode
 - Electrochemical testing of V₂O₃(m) and V₂O₃(r)-MWCNT electrodes
- Characterization of V₂O₃(m)-MWCNT composite with SEM, XRD and XPS
 - Manuscript preparation

⁼The authors contributed equally to this work

10.1 Abstract

V_2O_3 -multiwalled carbon nanotube (MWCNT) electrodes with active mass loading of 30 mg cm^{-2} and ratio of active material mass to current collector mass of 33% have been developed for charge storage in electrochemical supercapacitors. Good electrochemical performance at high active mass loading allowed for an electrode areal capacitance as high as 4.4 F cm^{-2} and low electrode resistance. This high performance was, in part, achieved using an advanced colloidal processing method, which involved the use of lauryl gallate (LG) as a dispersant. It was demonstrated that LG allowed for good dispersion of both V_2O_3 and MWCNT and facilitated their mixing. An electrode activation procedure (AP) was also developed, and contributed to the high capacitance and low resistance at high active mass loadings. To further understand the AP, as received and ball milled V_2O_3 electrodes were investigated using cyclic voltammetry and impedance spectroscopy before and after activation, as well as with cycling stability. This, coupled with XRD, XPS and SEM data provided an insight into the composition and morphology changes of the active material. The influence of particle size on electrode capacitance, cyclic stability and capacitance retention at high charge-discharge rates has been analyzed. The results of this investigation showed that V_2O_3 -MWCNT composites are promising for practical applications in electrochemical supercapacitors.

Key words: carbon nanotube, supercapacitor, vanadium oxide

10.2 Introduction

Electrochemical supercapacitors are under intensive investigation for advanced energy-storage applications [1–6]. Major research focus areas include the development of advanced electrode materials and electrolytes, improvement in performance of electrodes and device design [7–11]. Particularly important for future progress in this area was the recent development of a guideline [12] for reporting performance metrics of individual electrodes and devices. These studies highlighted the importance of high active mass loadings of supercapacitor electrodes. For practical applications, high gravimetric capacitance must be achieved at high mass loadings. The important parameter for the characterization of supercapacitor electrodes with high active mass loadings is areal capacitance. It is known that gravimetric capacitance decreases with increasing active mass loadings due to limited electrolyte access to active material and increased resistance. Moreover, the increase in electrode mass can result in reduction of areal capacitance, especially at high charge-discharge rates [13].

Vanadium oxides, prized for their multiple vanadium valence states and metal-insulator phase transitions [14], have generated great interest for charge storage in supercapacitors [15–18]. It was found [18,19] that V_2O_5 is a promising material for the positive electrodes of aqueous supercapacitors. The multiple valence states of vanadium (III-V) can potentially provide significantly higher charge storage capability for vanadium oxide electrode materials, compared to other inexpensive metal oxides [15].

Numerous investigations have been conducted to date to analyze the charge-discharge mechanism and develop advanced electrodes with enhanced electrochemical performance [20–22]. Advanced film deposition techniques have been utilized for the fabrication of V_2O_5 electrodes [23,24]. Also of great interest are investigations focused on the development of nanocomposites [21,25]. New processing techniques have been explored for the fabrication of flexible electrodes and devices [26,27]. The development of advanced microstructures, which allow good electrolyte access to the active material, has received particular attention in the literature [21,28–30]. Various strategies have been developed for the synthesis of vanadium oxide particles with small size and high surface area, which allowed for high performance supercapacitor electrodes [31–34]. Device performance was enhanced by adjusting and optimizing the initial electrode potential [35]. Advanced templates and impregnation techniques have been developed [36] for the fabrication of porous microstructures.

Impressive progress has been achieved in the fabrication of V_2O_5 and other vanadium oxide electrodes with active mass loading of $0.04\text{--}3.1\text{ mg cm}^{-2}$, which showed high mass normalized capacitance (C_g) [37–45]. However, recent studies [46] showed that for many practical applications the active mass loading must be at least $10\text{--}20\text{ mg cm}^{-2}$ and high areal capacitance (C_s) must be achieved. Moreover, the ratio of active material mass to current collector mass (R_m) must be significantly increased. The key to achieving high C_s and R_m is the development of efficient electrodes with high C_g and low resistance at high active mass loadings. The low resistance can be achieved using metallic current collectors. However, for active mass loadings around 1 mg cm^{-2} on metallic current collectors, the R_m

values are typically below 1–2%. Significantly higher active mass loadings and R_m are necessary for practical applications.

The increase in active mass loading of V_2O_5 introduces problems related to drastic reduction in C_g due to low conductivity of this electrode material [15]. The C_S values of electrodes reported in the literature [47,48] were typically below 400 mF cm^{-2} . Another problem is poor cyclic stability [15,20] of V_2O_5 . Attempts have been made to address this issue through the development of advanced electrolytes [49]. In another investigation it was demonstrated that VO_x electrodes [50], prepared by anodic oxidation of V_2O_3 , exhibited remarkable cyclic stability during 100 000 cycles and C_S of 356.8 mF cm^{-2} was achieved at a mass loading of 1.48 mg cm^{-2} . It was found [50] that high electronic conductivity of V_2O_3 was beneficial for the fabrication of electrodes with high capacitance. Carbon coated V_2O_3 core-shell composites [51] were also developed for supercapacitor applications.

The goal of this investigation was the fabrication of efficient V_2O_3 -multiwalled carbon nanotube (MWCNT) composite electrodes with high active mass loading for energy storage in electrochemical supercapacitors. Previous investigations of other active materials showed that high active mass loading and high R_m can be achieved using Ni foam current collectors[52,53]. Therefore, commercial Ni foam current collectors were impregnated with V_2O_3 and MWCNT in order to achieve active mass loading of $\sim 30 \text{ mg cm}^{-2}$. A biomimetic strategy has been developed for the dispersion of V_2O_3 , which facilitated efficient mixing of V_2O_3 and MWCNT. This study revealed significant increase of capacitance during initial electrochemical cycling and an activation procedure has been developed in order to optimize the electrode capacitance. Surprisingly, the electrode

resistance decreased drastically during the activation process. A remarkably high $C_S = 4.4 \text{ F cm}^{-2}$ and low electrode resistance were achieved after activation. Testing results showed strong evidence that activation process resulted in V_2O_3 surface oxidation to form electrochemically active V_2O_5 surface. We analyzed the influence of particle morphology on the electrode performance. The experimental data, presented below indicated that V_2O_3 -MWCNT electrodes with high active mass loading can be used for practical applications in supercapacitor devices.

10.3 Experimental Procedure

Lauryl gallate (LG), V_2O_3 , Na_2SO_4 , poly(vinyl butyral-co-vinyl alcohol-co-vinyl acetate) (PVB, average $M_w = 50,000\text{--}80,000$) (Aldrich), multiwalled carbon nanotubes (MWCNT, ID 4 nm, OD 13 nm, length 1–2 μm , Bayer, Germany) were used. Figure 10.1 shows SEM images of as-received MWCNT, which formed large agglomerates. LG was used as a dispersant for MWCNT. As received ($\text{V}_2\text{O}_3(\text{r})$) and ball milled ($\text{V}_2\text{O}_3(\text{m})$) materials were used. Ni foams with 95% porosity were provided by Vale Limited Company.

Two suspensions were prepared in a water-ethanol (50 vol% ethanol) solvent. Suspension A contained 0.16 g $\text{V}_2\text{O}_3(\text{r})$ or $\text{V}_2\text{O}_3(\text{m})$ and 0.08 g LG in 80 mL of the solvent. Suspension B contained 0.04 g MWCNT and 0.04 g LG in 40 mL of the solvent. Both suspensions were ultrasonicated for 15 min, then mixed together and ultrasonicated again for 10 min. The mixture was filtrated, washed with ethanol, dried in air at 50°C and stored in a desiccator.

For the fabrication of electrodes, the mixture was suspended in ethanol and then 3 wt% of PVB binder was added. The obtained slurry was used for impregnation of Ni foam current collectors. The active mass loading was 30 mg cm^{-2} ($\pm 5\%$).

XPS analysis was performed using Quantera II Scanning XPS instrument (Physical Electronics Inc.). Scanning electron microscopy (SEM) investigations were performed using JEOL JSM-7000F microscope. X-ray diffraction (XRD) studies were performed using a powder diffractometer (Nicolet I2, monochromatized $\text{CuK}\alpha$ radiation). Cyclic voltammetry (CV) and electrochemical impedance spectroscopy (EIS) investigations were performed using a potentiostat (PARSTAT 2273, Princeton Applied Research, USA). The capacitive behavior of the electrodes was studied in three-electrode cells using 0.5M Na_2SO_4 aqueous solutions. The pH of the solution was adjusted to 3.6 using H_2SO_4 . The area of the working electrode was 1 cm^2 . The counter electrode used was a platinum gauze, and the reference electrode was a standard calomel electrode (SCE). CV studies were performed at scan rates of 2–100 mV s^{-1} . The areal capacitance $C_s = Q/\Delta V S$ and gravimetric capacitance $C_g = Q/\Delta V m$ were calculated using half the integrated area of the CV curve divided by the scan rate to obtain the charge Q , and subsequently dividing the charge Q by the width of the potential window ΔV , and electrode area S or active mass m . The alternating current measurements of complex impedance $Z^* = Z' - iZ''$ were performed in the frequency range of 10 mHz – 100 kHz at the amplitude of the signal of 5 mV. The complex differential capacitance $C_s^* = C_s' - iC_s''$ was calculated from the EIS data as $C_s' = Z''/\omega|Z|^2 S$ and $C_s'' = Z'/\omega|Z|^2 S$, where $\omega = 2\pi f$ (f -frequency).

We observed a significant capacitance increase and impedance reduction for the V_2O_5 -MWCNT electrodes during initial cycling. An activation procedure (AP) was thus developed, which included consecutive cycling at scan rates of 50 mV s^{-1} (100 cycles), 100 mV s^{-1} (50 cycles), 5 mV s^{-1} (8 cycles) and 2 mV s^{-1} (8 cycles). The voltage window was 0–0.7 V vs SCE for the AP and electrochemical testing after AP. This voltage window was selected after consideration of the paper by Lee & Goodenough [19].

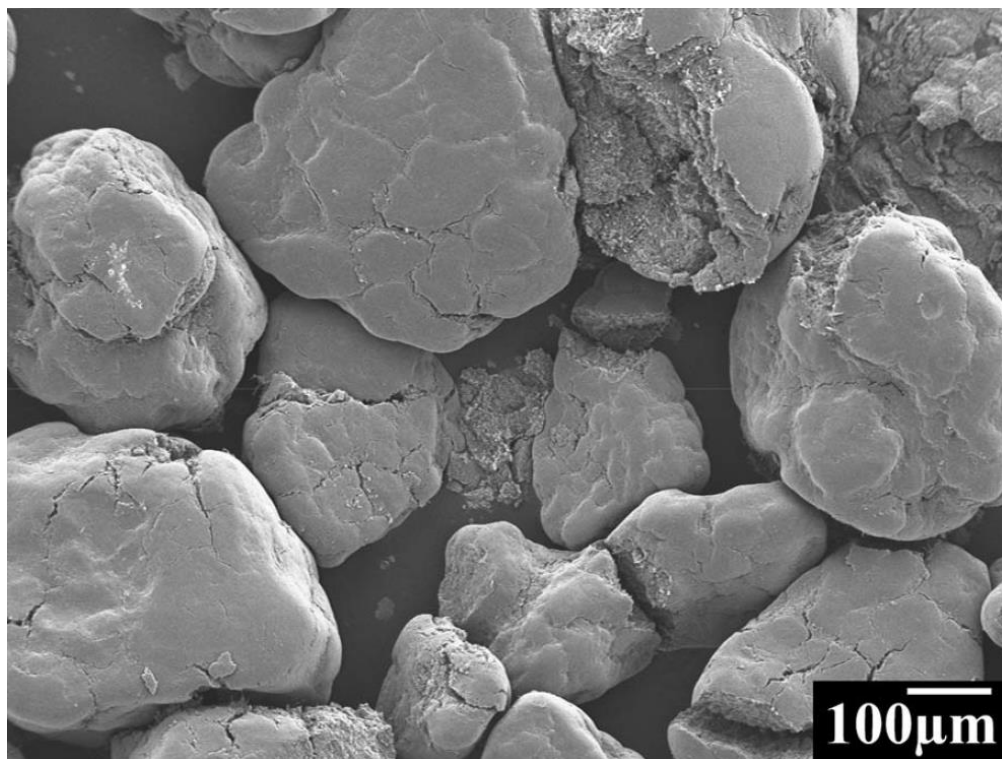


Figure 10.1: SEM images of as-received MWCNT.

10.4 Results and Discussion

Figure 10.2A shows an SEM image of $V_2O_3(r)$. The powder contained particles of irregular shape with a typical size of 2–10 μm . Ball milling of $V_2O_3(r)$ resulted in significant reduction of the particle size. Figure 10.2B indicates that the typical size of $V_2O_3(m)$ was 0.5–1 μm , however larger particles or agglomerates with size of 1–2 μm were also observed. $V_2O_3(r)$ and $V_2O_3(m)$ were used for the fabrication of composite V_2O_3 -MWCNT electrodes through a slurry impregnation method. The choice of a dispersant was an important step in producing the slurries for the impregnation of current collectors and electrode fabrication. In this investigation LG was used as a dispersant, which facilitated improved dispersion and mixing of V_2O_3 and MWCNT.

LG belongs to the family of organic molecules that contain galloyl groups, which are highly reactive and adsorb on oxide surfaces through complexation or bridging bonding of surface metal atoms. The adsorption of LG and other gallates [54] is based on bidentate catecholate type bonding (Figure 10.3A), which involves two adjacent phenolic OH groups. The interest in catecholate type bonding for the colloidal processing of materials was generated by investigations of the mechanism sea mussels use to adhere to various surfaces. Fundamental studies showed that strong mussel adhesion involves protein macromolecules, containing the catecholic amino acid, L-3,4-dihydroxyphenylalanine (DOPA) [55,56]. It was found that the phenolic OH groups of DOPA provided strong chelating or bridging bonding to the metal atoms on the material's surface. The analysis of mussel adhesion has

driven the development of biomimetic strategies for the surface modification, dispersion and deposition of materials [54].

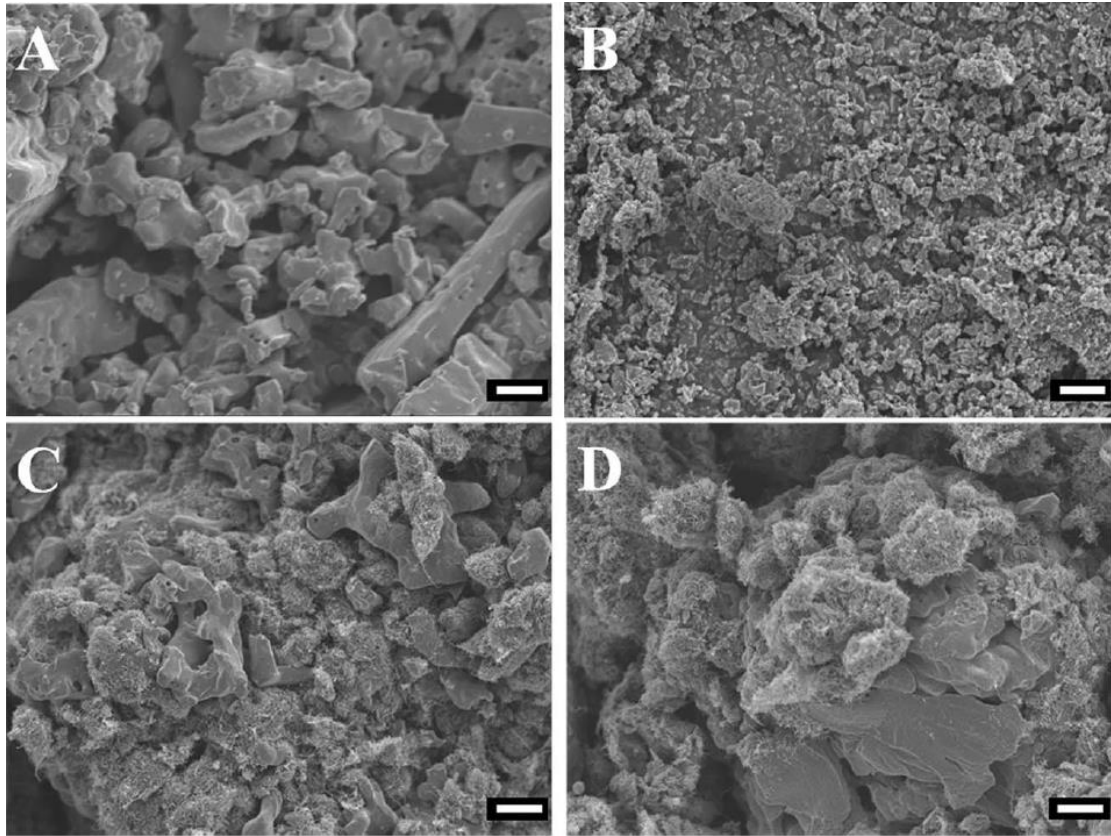


Figure 10.2: SEM images of (A) $V_2O_3(r)$, (B) $V_2O_3(m)$, (C) $V_2O_3(r)$ -MWCNT composite before testing, (D) $V_2O_3(r)$ -MWCNT composite after testing (scale bar = 2 μm).

The addition of LG to the V_2O_3 suspensions resulted in improved suspension stability (Figure 10.3B). Moreover, LG allowed for improved stability of MWCNT suspensions (Figure 10.3C). It is suggested that similar to other head-tail surfactants [57,58], the adsorption of LG on MWCNT involved hydrophobic interactions of long hydrocarbon chains (Figure 10.3A). Our approach is different from the molecular bridging method, based on the diazonium chemistry [59]. The LG molecule has two different functional ends,

which allow bridging of different components only. Therefore, LG allows improved mixing of different components, such as MnO_2 and MWCNT. Moreover, the bidentate catecholate type bonding of LG allows strong adsorption on MnO_2 .

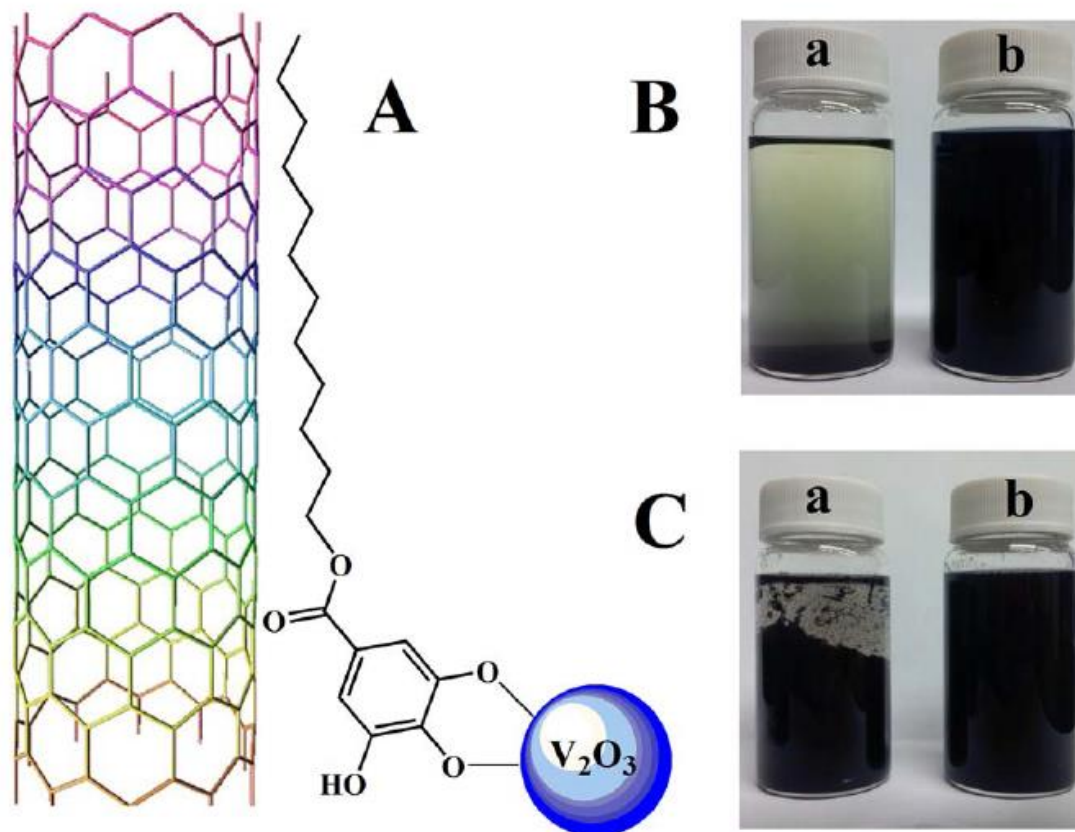


Figure 10.3: (A) Schematic of LG adsorption on $\text{V}_2\text{O}_3(\text{r})$ and MWCNT, (B,C) sedimentation tests for (B) $1 \text{ g L}^{-1} \text{ V}_2\text{O}_3$, (C) $1 \text{ g L}^{-1} \text{ MWCNT}$ in a water-ethanol solvent (50 vol.% ethanol) (a) without LG and (b) in the presence of $0.5 \text{ g L}^{-1} \text{ LG}$.

The two different adsorption mechanisms of LG can potentially improve mixing by enhancing individual suspension dispersion and stability while also creating LG bridges between V_2O_3 and MWCNT after suspension mixing (Figure 10.3A). The bridging of V_2O_3 and MWCNT by LG can explain some noteworthy observations from Figure 10.2C and D.

The SEM images of composites before and after electrochemical testing show many V_2O_3 particles covered by MWCNT. Later discussion will show that AP resulted in surface oxidation of V_2O_3 particles to form electrochemically active surface V_2O_5 . However, the capacitive V_2O_5 phase has a low conductivity. Therefore, the improved mixing of vanadium oxide particles and conductive MWCNT can enhance the electrode's electrochemical performance, especially at high active mass loadings.

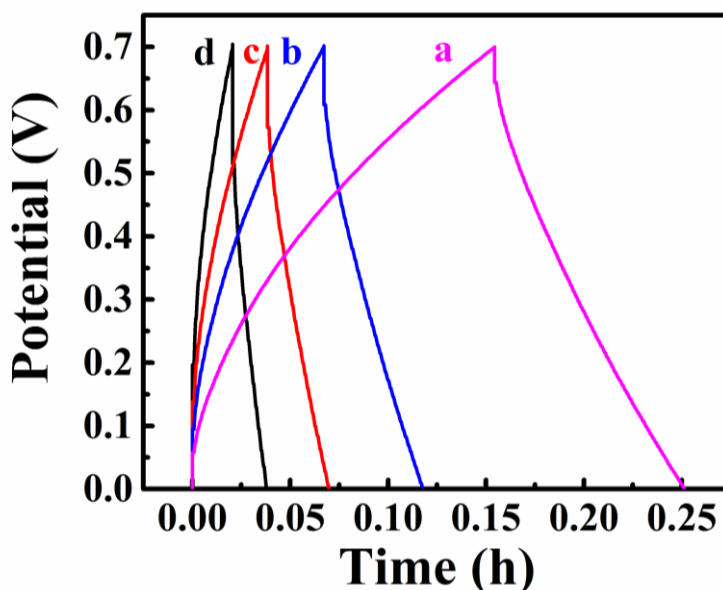


Figure 10.4: Charge-discharge behavior of $V_2O_3(r)$ -MWCNT composites, prepared using LG, at current densities of (a) 3, (b) 5, (c) 7 and (d) 10 mA cm^{-2} .

The galvanostatic charge-discharge behavior of the $V_2O_3(r)$ -MWCNT composites is shown in Figure 10.4. The charge-discharge curves were of nearly triangular shape. However, the electrodes showed significant changes in electrochemical behavior during initial cycling. The variation in the capacitive behavior of the electrodes during initial cycling was investigated using cyclic voltammetry.

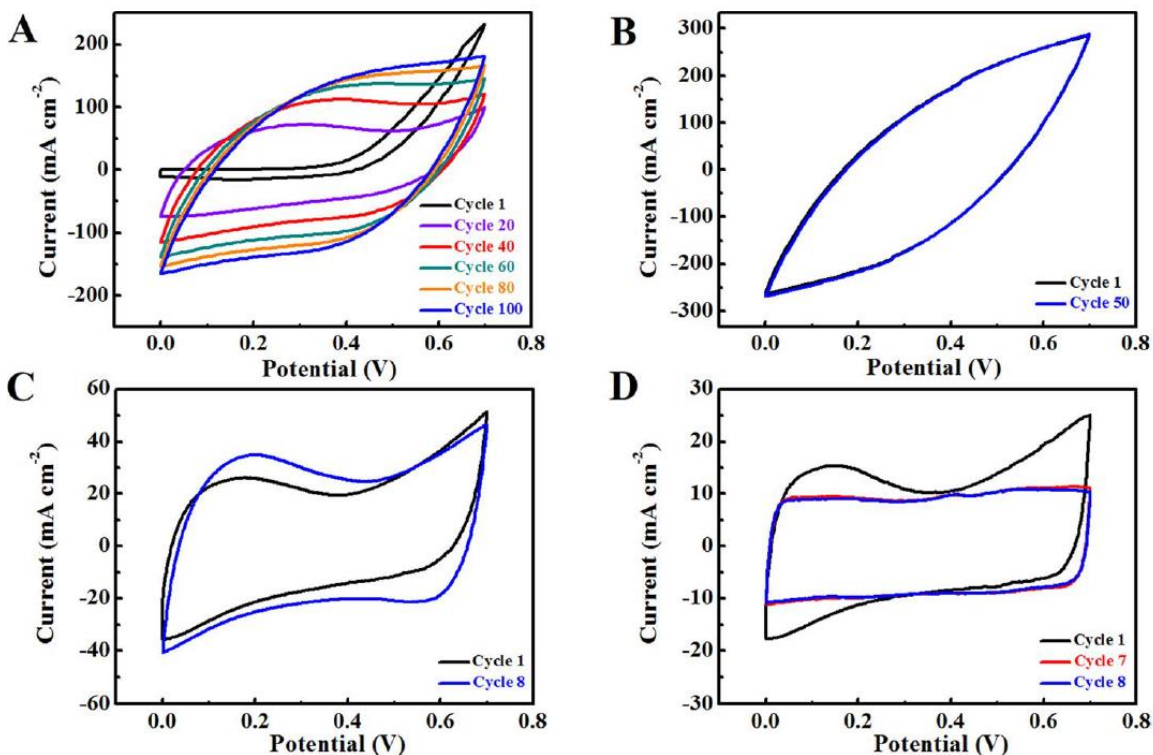


Figure 10.5: CVs for consecutive cycling at (A) 50, (B) 100, (C) 5 and (D) 2 mV s⁻¹ for V₂O₃(r)-MWCNT composites, prepared using LG.

Figure 10.5 shows CVs for as-prepared V₂O₃(r)-MWCNT composites. The first cycle at 50 mV s⁻¹ revealed a small current response at potentials 0–0.4V and a current increase in the range of 0.4–0.7V (Figure 10.5A). The characteristic “box-shape” CV curve, indicative of capacitive behavior, began to take form after just a few cycles at this scan rate. The analysis of CVs showed that the CV shape improved and the current response increased with every cycle, especially during the first 60 cycles. After 100 cycles at 50 mV s⁻¹, the cycling was continued at different scan rates in order to see if the kinetics of the observed activation was dependent on the scan rate. It was found that 50 cycles at 100 mV s⁻¹, after already cycling at 50mV s⁻¹, resulted in limited change in the CV’s shape and current density

(Figure 10.5B). However, 8 cycles at 5 mV s^{-1} resulted in significant increase in CV area, which indicated an increase in capacitance (Figure 10.5C). Further cycling at 2 mVs^{-1} resulted in drastic changes in the CV, becoming the box-like shape of an ideal capacitor (Figure 10.5D). Cycling at the lowest scan rate of 2 mV s^{-1} was terminated when it was observed that there was little change between the 7th and 8th cycle, as can be seen in Figure 10.5D.

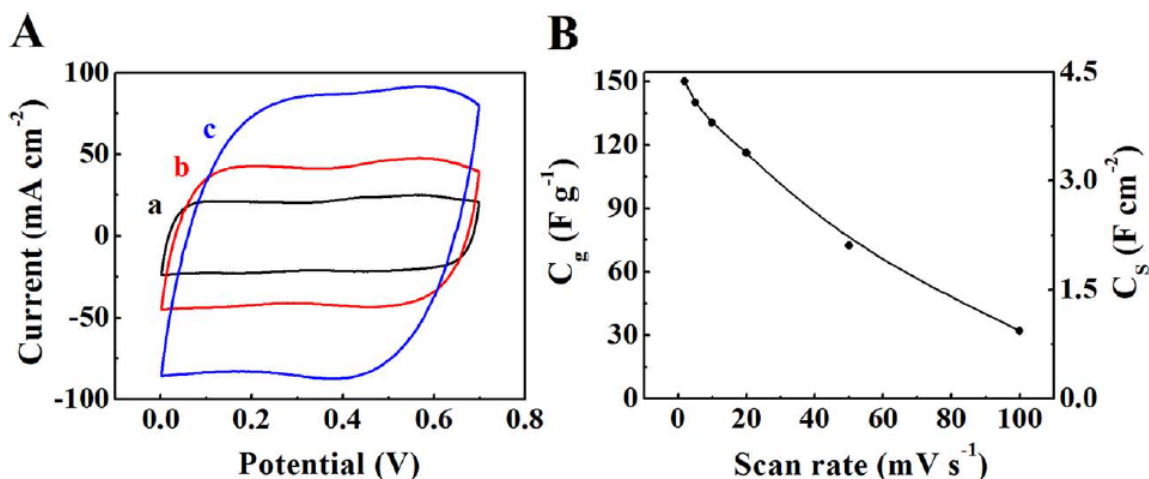


Figure 10.6: (A) CVs at scan rates of (a) 5, (b) 10 and (c) 20 mV s^{-1} and (B) C_g and C_s versus scan rate for $\text{V}_2\text{O}_3(\text{r})$ -MWCNT composites, prepared using LG, after AP.

The electrochemical testing was performed after the AP. Figure 10.6A shows CVs at different scan rates. The box shapes of the CVs indicated good capacitive behavior. A remarkably high areal capacitance $C_s = 4.4 \text{ F cm}^{-2}$ (capacity 102.7 C g^{-1}) was observed at a scan rate of 2 mV s^{-1} . The obtained C_s is significantly higher compared to the literature data for other vanadium oxides, which reported C_s values [47,48,50] below 400 mF cm^{-2} . The capacitance decreased with increasing scan rate (Figure 10.6B), due to the limitation

of electrolyte diffusion in the bulk of the electrode material. The capacitance retention at 100 mV s^{-1} was found to be 21%. The high C_s at low scan rates indicated good material utilization at high active mass loadings. As pointed out above, one of the major problems in the development of supercapacitor electrodes is reduction of gravimetric capacitance with increasing electrode mass. This is usually attributed to poor mixing of active materials and conductive additives or poor electrolyte access to the active material. The bulk of the electrode can be considered as a capacitor with low capacitance, connected in series with the highly capacitive surface layer. As a result of low capacitance of the bulk material, the increase in electrode mass does not necessarily result in increase of areal capacitance. In this investigation we achieved good capacitive behavior at relatively high active mass loading of 30 mg cm^{-2} . We increased areal capacitance by factor of 11, compared to the literature data for vanadium oxide electrodes. Another important parameter for practical application is R_m , which was increased to the level of 33% due to high active mass loading. The results of this investigation indicated that V_2O_3 is a potential material of choice for practical applications in electrodes of electrochemical supercapacitors. The capacitance of $\text{V}_2\text{O}_3(\text{r})$ -MWCNT was comparable with capacitance of MnO_2 -MWCNT electrodes at high active mass loadings. For example, MnO_2 -MWCNT electrodes [60] with active mass loading of 40 mg cm^{-2} showed C_s of 5.9 F cm^{-2} . The C_g values reported for MnO_2 -MWCNT electrodes [60] at scan rates $2\text{--}100 \text{ mV s}^{-1}$ were very close to the C_g of $\text{V}_2\text{O}_3(\text{r})$ -MWCNT (Figure 10.6B).

In order to analyze the influence of MWCNT, as a conductive additive, on the electrode properties we investigated pure $\text{V}_2\text{O}_3(\text{r})$ electrodes. Moreover, the testing of $\text{V}_2\text{O}_3(\text{r})$ -

MWCNT electrodes, prepared without LG, provided an insight into the influence of the improved dispersion and mixing of MWCNT and V_2O_3 , achieved using LG, on the properties of $V_2O_3(r)$ -MWCNT composites. $V_2O_3(r)$ and $V_2O_3(r)$ -MWCNT, prepared without LG, with mass loading of 30 mg cm^{-2} were activated using the AP, described above.

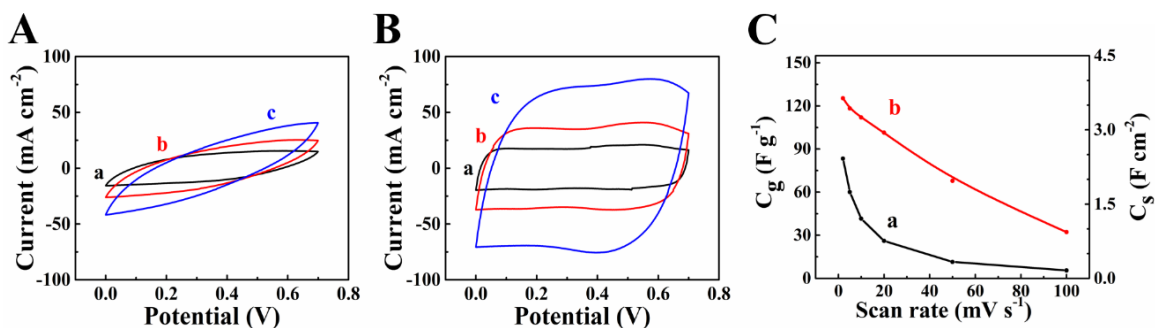


Figure 10.7: (A,B) CVs at scan rates of (a) 5, (b) 10 and (c) 20 mV s^{-1} for (A) $V_2O_3(r)$ and (B) $V_2O_3(r)$ -MWCNT composite, prepared without LG, (C) C_g and C_s versus scan rate for (a) $V_2O_3(r)$ and (b) $V_2O_3(r)$ -MWCNT composite, prepared without LG after AP.

Testing results (Figure 10.7A) showed poor electrochemical performance of pure V_2O_3 electrodes, as indicated by the tilted CVs with low area. The addition of MWCNT resulted in nearly box shape CVs, which had larger areas (Figure 10.7B). The capacitance decreased from 2.5 to 0.16 F cm^{-2} and from 3.67 to 0.94 F cm^{-2} for $V_2O_3(r)$ and $V_2O_3(r)$ -MWCNT, respectively, with increasing scan rate from 2 to 100 mV s^{-1} . The comparison of the experimental data, presented in Figure 10.7A–C, showed a beneficial effect of MWCNT. The capacitance of $V_2O_3(r)$ -MWCNT, prepared without LG (Figure 10.7), was significantly lower compared to the capacitance of $V_2O_3(r)$ -MWCNT electrodes, prepared using LG (Figure 10.6). Therefore, the improved dispersion and mixing of $V_2O_3(r)$ -MWCNT, achieved using LG, was beneficial for electrode fabrication.

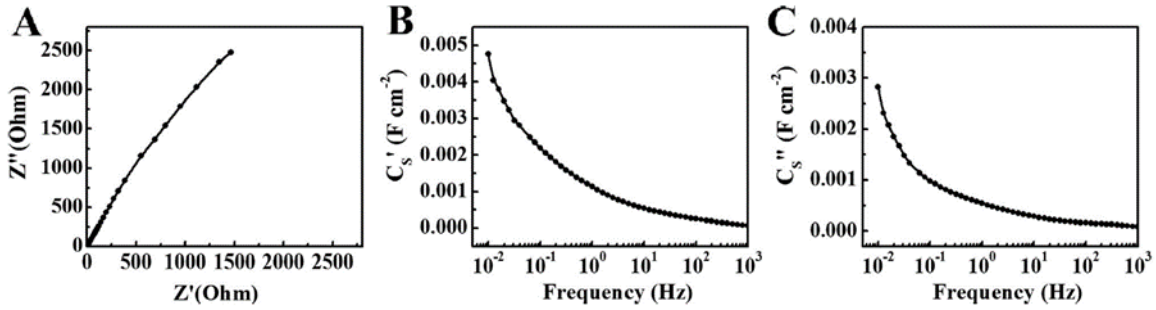


Figure 10.8: (A) Nyquist plot of complex impedance, (B,C) frequency dependences of components of complex capacitance (B) C_s' and (C) C_s'' , calculated from the EIS data for $V_2O_3(r)$ -MWCNT composites, prepared using LG, before AP.

The analysis of the impedance data provided additional information about the activation process and capacitive performance of the $V_2O_3(r)$ -MWCNT electrodes. The Nyquist plot for $V_2O_3(r)$ -MWCNT before the AP (Figure 10.8A) shows relatively high electrode resistance $R = Z'$, which is detrimental for supercapacitor applications. Moreover, relatively high Z'' indicated low capacitance. Indeed, the calculations of C_s' from the impedance data showed that C_s' was extremely low (Figure 10.8B) and decreased drastically with frequency at relatively low frequencies.

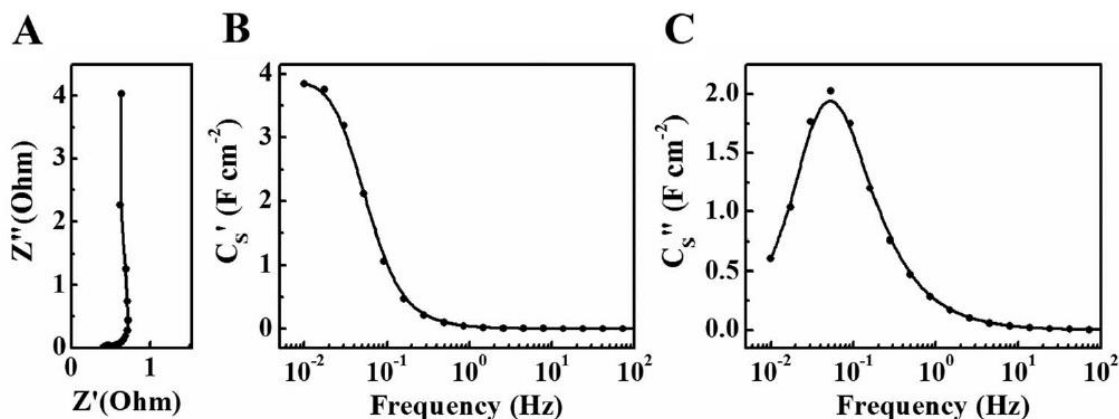


Figure 10.9: (A) Nyquist plot of complex impedance, (B,C) frequency dependences of components of complex capacitance (B) C_s' and (C) C_s'' , calculated from the EIS data for $V_2O_3(r)$ -MWCNT composites, prepared using LG, after AP.

After the AP, the Nyquist plot (Figure 10.9A) displayed a low frequency vertical segment, a characteristic impedance response for a capacitor. The analysis of the impedance after AP (Figure 10.9A) showed significantly lower $R = Z'$, which was below 1 Ohm. The reduction of Z'' indicates that capacitance increase after the AP, which agrees with the CV data. The C_s' , calculated from the impedance data (Figure 10.9B) also showed significant increase after the AP. The low frequency C_s' was comparable with C_s , calculated from the CV data at low scan rates. The frequency dependence of the complex capacitance showed a relaxation type dispersion [52], as indicated by the C_s' decrease with frequency (Figure 10.9B) and a relaxation maximum in the frequency dependence of C_s'' (Figure 10.9C). The comparison of the capacitance data before (Figure 10.8B, 8C) and after (Figure 10.9B, 9C) the AP showed that the relaxation maximum shifted to higher frequencies after the AP. Such a shift indicates better capacitive performance at higher charge discharge frequencies.

The analysis of cyclic behavior after the AP showed relatively stable performance (Figure 10.10). The capacitance increase after 1000 cycles was about 7%.

The testing results presented above indicated that the AP was critical to achieve good electrochemical performance. Therefore, the electrode material was analyzed using XRD and XPS before and after the AP to obtain additional information on changes in the material, resulting from the AP. The XRD pattern of the as-received material (Figure 10.11A) showed well defined peaks of V_2O_3 . Small peaks of MWCNT were also observed (Figure 10.11B) in the diffraction pattern of V_2O_3 (r)- MWCNT before AP in addition to the peaks of V_2O_3 .

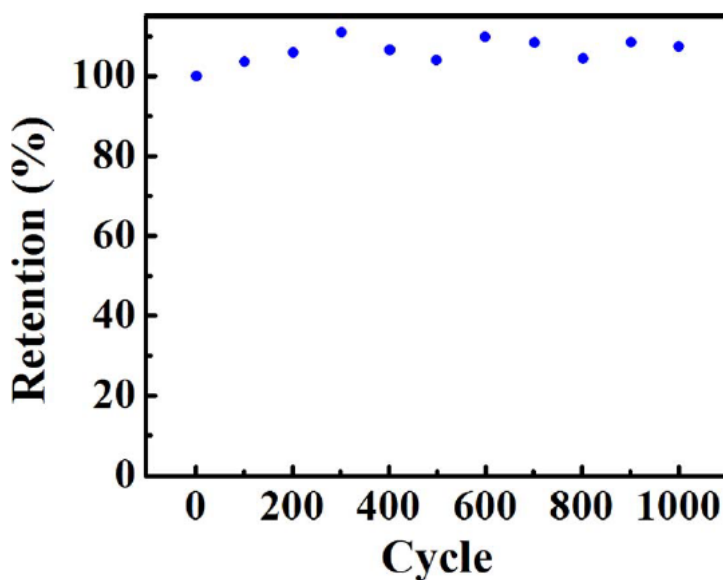


Figure 10.10: Capacitance retention versus cycle number for V_2O_3 (r)-MWCNT composites, prepared using LG, after AP.

The relative intensity of the V_2O_3 peaks decreased after the AP (Figure 10.11C). This can result from partial surface oxidation [50] of V_2O_3 to form an amorphous surface, containing

V^{4+} and V^{5+} oxides. Previous investigations [50] showed that stable capacitive performance and good cycling stability were observed when a proper content of V^{3+} , V^{4+} and V^{5+} species was achieved. The charge-discharge process [50] resulted from the redox reactions.

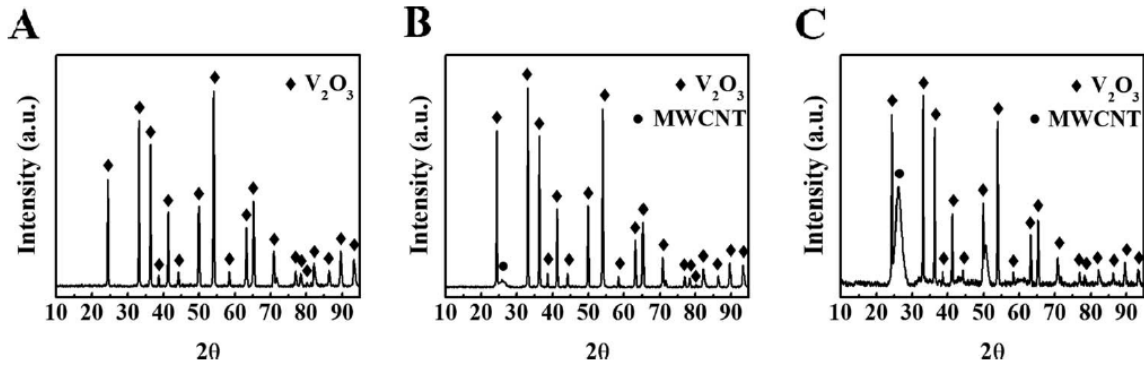


Figure 10.11: X-Ray diffraction patterns of (A) $V_2O_3(r)$, (B, C) $V_2O_3(r)$ -MWCNT composites: (A, B) before AP and (C) after AP.

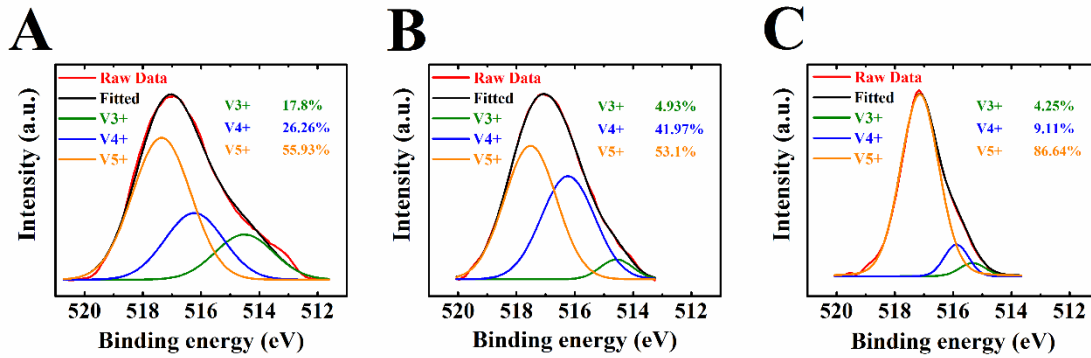


Figure 10.12: XPS data for (A) $V_2O_3(r)$, (B, C) $V_2O_3(r)$ -MWCNT composites: (A, B) before AP and (C) after AP.

The XPS studies (Figure 10.12A) of $V_2O_3(r)$ revealed V^{4+} and V^{5+} species in the material surface in addition to V^{3+} . This result is in agreement with other XPS studies [61,62], which showed that V_2O_3 materials, regardless of purity and storage conditions, were always covered by a thin VO_x layer, containing V^{4+} and V^{5+} . The electrode fabrication procedure

resulted in further oxidation of the $V_2O_3(r)$ surface (Figure 10.12B), as indicated by the significant increase in the V^{4+} content. The AP resulted in significant increase of the V^{5+} and reduction in V^{3+} and V^{4+} content in the surface layer (Figure 10.12C). Therefore, the results of XPS and XRD indicated that the AP resulted in the oxidation of $V_2O_3(r)$ surface.

The analysis of the electrochemical behavior of $V_2O_3(m)$ -MWCNT provided additional information, which allowed for a better understanding of the electrochemical behavior of the V_2O_3 -MWCNT composites. Figure 10.13A shows CVs for $V_2O_3(m)$ -MWCNT composites after AP at scan rates of 5, 10 and 20 $mV s^{-1}$. The comparison with the data for $V_2O_3(r)$ -MWCNT, shown in Figure 10.6A indicated that ball milling resulted in lower charge-discharge current and lower capacitances at low scan rates (Figure 10.13B). The C_S at 2 $mV s^{-1}$ was found to be 3.0 $F cm^{-2}$ (capacity 70 $C g^{-1}$) However, the $V_2O_3(m)$ -MWCNT electrodes showed improved capacitance retention at 100 $mV s^{-1}$, compared to $V_2O_3(r)$ -MWCNT electrodes. The capacitance retention of $V_2O_3(m)$ -MWCNT was 49%.

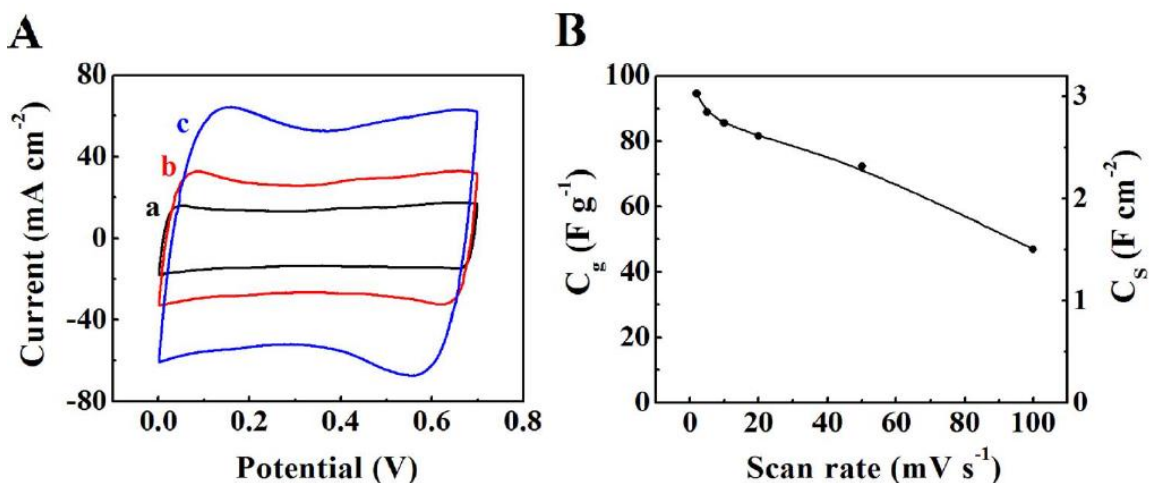


Figure 10.13: (A) CVs at scan rates of (a) 5, (b) 10 and (c) 20 mV s⁻¹ and (B) C_g and C_s versus scan rate for V₂O₃(m)-MWCNT composites, prepared using LG, after AP.

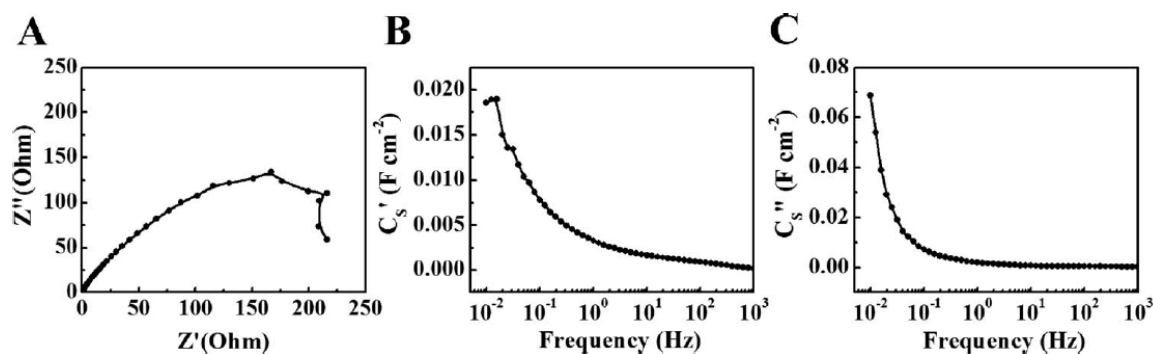


Figure 10.14: (A) Nyquist plot of complex impedance, (B,C) frequency dependences of components of complex capacitance (B) C_s' and (C) C_s'', calculated from the EIS data for V₂O₃(m)-MWCNT composites, prepared using LG, before AP.

The analysis of impedance data (Figure 10.14A) for V₂O₃(m)-MWCNT before the AP showed relatively high electrode resistance $R = Z'$. The high Z'' resulted from low capacitance. Indeed, C_s' calculated from the impedance data (Figure 10.14B) was below 20 mF cm⁻² at low frequencies and decreased rapidly with increasing frequency. It was found

that C_s'' decreased rapidly in the frequency range of 10–100 mHz (Figure 10.14C). The AP resulted in significant changes of the electrode impedance. The resistance R of the $V_2O_3(m)$ -MWCNT electrodes decreased by two orders of magnitude after the AP.

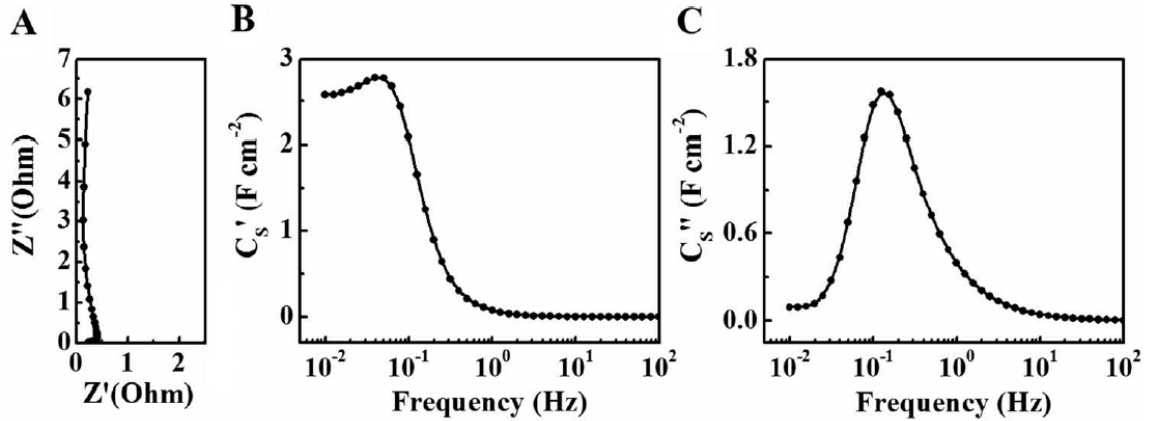


Figure 10.15: (A) Nyquist plot of complex impedance, (B,C) frequency dependences of components of complex capacitance (B) C_s' and (C) C_s'' , calculated from the EIS data for $V_2O_3(m)$ -MWCNT composites, prepared using LG, after AP.

Figure 10.15A indicates that the electrode resistance was below 0.5 Ohm in the entire tested frequency range. The Nyquist plot is represented by a nearly vertical line, indicating capacitive behavior. The reduction of Z'' after the AP resulted in an increase in C_s' by two orders of magnitude. The C_s' was in the range of 2.6–2.8 $F\ cm^{-2}$ at frequencies below 100 mHz and decreased drastically at higher frequencies, showing a relaxation type dispersion. The corresponding C_s'' dependence showed a relaxation maximum. The comparison of the frequency dependences of C_s'' for $V_2O_3(m)$ -MWCNT (Figure 10.15C) and $V_2O_3(r)$ -MWCNT (Figure 10.9C) showed that the relaxation peak of $V_2O_3(m)$ -MWCNT occurred at a higher frequency. The relaxation frequency, corresponding to the C_s'' maximum was found to be 70 and 110 mHz for $V_2O_3(r)$ -MWCNT and $V_2O_3(m)$ -MWCNT electrodes,

respectively. The higher relaxation frequency indicates better capacitance retention at high charge-discharge frequencies of the $V_2O_3(m)$ -MWCNT electrodes. This result correlates with improved capacitance retention of $V_2O_3(m)$ -MWCNT at high scan rates in the CV experiments. The analysis of cyclic behavior of the $V_2O_3(m)$ -MWCNT electrodes after the AP showed a capacitance reduction of about 22% after 1000 cycles (Figure 10.16).

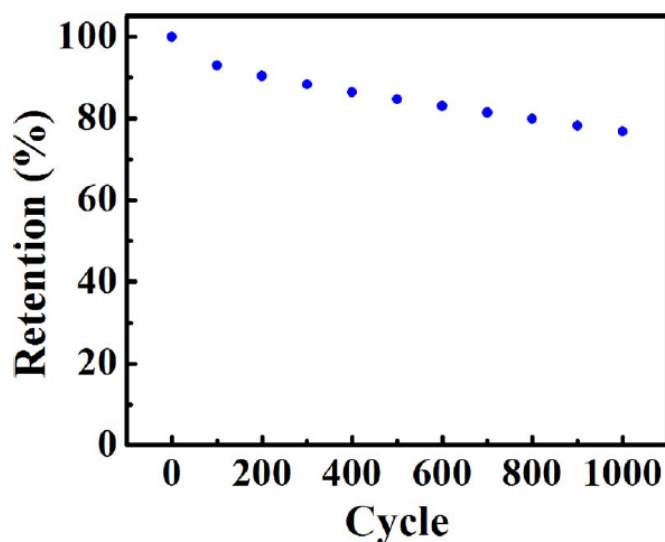


Figure 10.16: Capacitance retention versus cycle number for $V_2O_3(m)$ -MWCNT composites, prepared using LG, after AP.

This study showed that milling of V_2O_3 powder resulted in reduced capacitance. The result is surprising, because the reduction of particle size and corresponding increase in the surface area are beneficial for electrochemical charge storage reactions. It should be noted that several investigations [63–66] have shown that the specific capacitance does not correlate with the surface area, since some very small pores are inaccessible by the electrolyte.

It is suggested that there are two competing phenomena in the $V_2O_3(r)$ -MWCNT and $V_2O_3(m)$ -MWCNT materials to explain these observations. The first is that the capacitance increases due to an enrichment of V^{5+} on the surface with an increased pseudocapacitive contribution from the V^{5+}/V^{4+} couple[50], as well as an etching effect due to partial dissolution. This etching effect could result in the formation of channels in the active surface layer, improving electrolyte access and reducing the overall system impedance, despite the surface layer material likely being electrically insulating. The increased area afforded by these etched channels would also have the effect of boosting the capacitance. The result is a core-shell structure with a porous, oxidized surface layer and conductive V_2O_3 core. It is likely that, because of the much smaller particle size, the $V_2O_3(m)$ is far more susceptible to complete dissolution during the activation, leading to a drop in gravimetric capacitance when normalized by the initial mass. This might also explain why the $V_2O_3(r)$ -MWCNT composite is more stable during cycling than $V_2O_3(m)$ -MWCNT, as is seen in Figure 10.10 and Figure 10.16. The second is the quality of mixing between the V_2O_3 particles and MWCNT. The ball milled $V_2O_3(m)$, because of the smaller particle size, had far superior mixing with the MWCNT, compared to $V_2O_3(r)$. Despite being a conductive oxide, V_2O_3 is not nearly as conductive as MWCNT. The better mixing between $V_2O_3(m)$ -MWCNT, based on a particle size argument resulted in a boost in rate performance over $V_2O_3(r)$ -MWCNT. It is important to note that active mass of the electrodes, studied in our investigation was 20 times larger, compared to reference [50]. Further advances in the development of V_2O_3 -MWCNT electrodes and understanding of

charging and activation mechanisms will result in better utilization of V_2O_3 in the electrodes of electrochemical supercapacitors.

10.5 Conclusions

LG is an efficient dispersant, which allowed for the dispersion of V_2O_3 and MWCNT and improved their mixing. The use of LG facilitated the fabrication of V_2O_3 -MWCNT composites with high active mass loading (30 mg cm^{-2}) and high R_m (33%). An AP allowed for significant increase in capacitance and reduction of resistance of $V_2O_3(r)$ -MWCNT and $V_2O_3(m)$ -MWCNT electrodes. The highest C_s of 4.4 F cm^{-2} (capacity 102.7 C g^{-1}) was achieved using $V_2O_3(r)$ -MWCNT electrodes. Cyclic voltammetry and impedance spectroscopy data showed that $V_2O_3(m)$ -MWCNT electrodes exhibited improved capacitance retention at high charge-discharge rates. However, $V_2O_3(r)$ -MWCNT offers the advantage of greater cyclic stability. XPS and XRD studies revealed changes in composition and microstructure of the activated electrode material, which contained V^{4+} and V^{5+} species, involved in the charge-discharge process. The remarkably high C_s , and low resistance make $V_2O_3(r)$ -MWCNT composite a material of choice for practical applications in electrodes of electrochemical supercapacitors.

10.6 Acknowledgements

The authors gratefully acknowledge the Natural Sciences and Engineering Research Council of Canada for the financial support and Vale Canada for the donation of Ni foam.

10.7 References

- [1] L. Coustan, A. Le Comte, T. Brousse, and F. Favier, "MnO₂ as ink material for the fabrication of supercapacitor electrodes," *Electrochimica Acta*, vol. 152, pp. 520-529, 2015.
- [2] E. Macheaux, T. Brousse, D. Belanger, and D. Guyomard, "Supercapacitor behavior of new substituted manganese dioxides," *Journal of Power Sources*, vol. 165, no.2, pp 651-655, 2007.
- [3] Y. Lei, B. Daffos, P.L. Taberna, P. Simon, and F. Favier, "MnO₂-coated Ni nanorods: Enhanced high rate behavior in pseudo-capacitive supercapacitor," *Electrochimica Acta*, vol. 55, pp. 7454-7459, 2010.
- [4] L. Demarconnay, E. Raymundo- Piñero, and F. Béguin, "A symmetric carbon/carbon supercapacitor operating at 1.6 V by using a neutral aqueous solution," *Electrochemistry Communications*, vol. 12, no.10, pp. 1275-1278, 2010.
- [5] H.S. Kim, J. B. Cook, S. H. Tolbert, and B. Dunn, "The development of pseudocapacitive properties in nanosized-MoO₂," *Journal of The Electrochemical Society*, vol. 162, no.5 A5083-A5090, 2015.
- [6] F. Grote, R.S. Kühnel, A. Balducci, and Y. Lei, "Template assisted fabrication of free-standing MnO₂ nanotube and nanowire arrays and their application in supercapacitors," *Applied Physics Letters*, vol. 104, pp. 053904, 2014.
- [7] N. Goubard-Bretesché, O. Crosnier, G. Buvat, F. Favier, and T. Brousse, "Electrochemical study of aqueous asymmetric FeWO₄/MnO₂ supercapacitor," *Journal of Power Sources*, vol. 326, pp. 695-701, 2016.
- [8] A. Balducci, "Electrolytes for high voltage electrochemical double layer capacitors: A perspective article," *Journal of Power Sources*, vol. 326, pp. 534-540, 2016.
- [9] M. B. Sassin, S. G. Greenbaum, P. E. Stallworth, A. N. Mansour, B. P. Hahn, K. A. Pettigrew, D. R. Rolison, and J. W. Long, "Achieving electrochemical capacitor functionality from nanoscale LiMn₂O₄ coatings on 3-D carbon nanoarchitectures," *Journal of Materials Chemistry A*, vol. 1, no.7, pp. 2431-2440, 2013.
- [10] C. A. Beasley, M. B. Sassin, and J. W. Long, "Extending electrochemical quartz crystal microbalance techniques to macroscale electrodes: Insights on pseudocapacitance mechanisms in MnO_x-coated carbon nanofoams," *Journal of The Electrochemical Society*, vol. 162, no.5, pp. A5060-A5064, 2015.
- [11] V. Khomenko, E. Raymundo- Piñero, E. Frackowiak, and F. Béguin, "High-voltage asymmetric supercapacitors operating in aqueous electrolyte," *Applied Physics A*, vol. 82, no.4, pp. 567-573, 2006.

- [12] A. Balducci, D. Belanger, T. Brousse, J. Long, and W. Sugimoto, "Perspective—a guideline for reporting performance metrics with electrochemical capacitors: from electrode materials to full devices," *Journal of The Electrochemical Society*, vol. 164, no.7, pp. A1487-A1488, 2017.
- [13] R. Chen, R. Poon, R. P. Sahu, I. K. Puri, and I. Zhitomirsky, "MnO₂-carbon nanotube electrodes for supercapacitors with high active mass loadings," *Journal of The Electrochemical Society*, vol. 164, no.7, pp. A1673-A1678, 2017.
- [14] C. Wu, F. Feng, and Y. Xie, "Design of vanadium oxide structures with controllable electrical properties for energy applications," *Chemical Society Reviews*, vol. 42, no.12, pp. 5157-5183, 2013.
- [15] Y. Yan, B. Li, W. Guo, H. Pang, and H. Xue, "Vanadium based materials as electrode materials for high performance supercapacitors," *Journal of Power Sources*, vol. 329, pp. 148-169, 2016.
- [16] S. Boukhalifa, K. Evanoff, and G. Yushin, "Atomic layer deposition of vanadium oxide on carbon nanotubes for high-power supercapacitor electrodes," *Energy & Environmental Science*, vol. 5, no.5, pp. 6872-6879, 2012.
- [17] G. Li, X. Wang, F. M. Hassan, M. Li, R. Batmaz, X. Xiao, and A. Yu, "Vanadium Pentoxide Nanorods Anchored to and Wrapped with Graphene Nanosheets for High-Power Asymmetric Supercapacitors," *ChemElectroChem*, vol. 2, no.9, pp. 1264-1269, 2015.
- [18] V. Augustyn, P. Simon, and B. Dunn, "Pseudocapacitive oxide materials for high-rate electrochemical energy storage," *Energy & Environmental Science*, vol. 7, no. 5, pp. 1597-1614, 2014.
- [19] H. Y. Lee and J. Goodenough, "Ideal supercapacitor behavior of amorphous V₂O₅·nH₂O in potassium chloride (KCl) aqueous solution," *Journal of Solid State Chemistry*, vol. 148, no. 1, pp. 81-84, 1999.
- [20] B. Saravanakumar, K. K. Purushothaman, and G. Muralidharan, "Interconnected V₂O₅ nanoporous network for high-performance supercapacitors," *ACS Applied Materials & Interfaces*, vol. 4, no.9, pp. 4484-4490, 2012.
- [21] Z. Chen, V. Augustyn, J. Wen, Y. Zhang, M. Shen, B. Dunn, and Y. Lu, "High-performance supercapacitors based on intertwined CNT/V₂O₅ nanowire nanocomposites," *Advanced Materials*, vol. 23, no.6, pp. 791-795, 2011.
- [22] M. P. Yeager, W. Du, B. Bishop, M. Sullivan, W. Xu, D. Su, S. D. Senanayake, J. Hanson, and X. Teng, "Storage of potassium ions in layered vanadium pentoxide nanofiber electrodes for aqueous pseudocapacitors," *ChemSusChem*, vol. 6, no.12, pp. 2231-2235, 2013.

- [23] K. Jeyalakshmi, S. Vijayakumar, S. Nagamuthu, and G. Muralidharan, "Effect of annealing temperature on the supercapacitor behaviour of β - V_2O_5 thin films," *Materials Research Bulletin*, vol. 48, no.2, pp. 760-766, 2013.
- [24] R. Ingole, S. Kondawar, and B. Lokhande, "Substrate dependent morphological and electrochemical properties of V_2O_5 thin films prepared by spray pyrolysis," *Journal of Materials Science: Materials in Electronics*, vol. 28, no.3, pp. 2385-2391, 2017.
- [25] Z. Li, F. Wang, and X. Wang, "Hierarchical branched vanadium oxide nanorod@ Si nanowire architecture for high performance supercapacitors," *Small*, vol. 13, no.1, pp. 1603076, 2017.
- [26] S. D. Perera, B. Patel, N. Nijem, K. Roodenko, O. Seitz, J. P. Ferraris, Y. J. Chabal, and K. J. Balkus, "Vanadium Oxide Nanowire–Carbon Nanotube Binder-Free Flexible Electrodes for Supercapacitors," *Advanced Energy Materials*, vol. 1, no.5, pp. 936-945, 2011.
- [27] I. Shakir, Z. Ali, J. Bae, J. Park, and D. J. Kang, "Layer by layer assembly of ultrathin V_2O_5 anchored MWCNTs and graphene on textile fabrics for fabrication of high energy density flexible supercapacitor electrodes," *Nanoscale*, vol. 6, no.8, pp. 4125-4130, 2014.
- [28] J. Zhu, L. Cao, Y. Wu, Y. Gong, Z. Liu, H. E. Hoster, Y. Zhang, S. Zhang, S. Yang, and Q. Yan, "Building 3D structures of vanadium pentoxide nanosheets and application as electrodes in supercapacitors," *Nano Letters*, vol. 13, no.11, pp. 5408-5413, 2013.
- [29] C.J. Cheng, S.J. Bao, and C. M. Li, "A facile and well-tailored vanadium oxide porous network for high-capacity electrochemical capacitive energy storage," *Materials Letters*, vol. 120, pp. 283-286, 2014.
- [30] H.Y. Li, C. Wei, L. Wang, Q.S. Zuo, X. Li, and B. Xie, "Hierarchical vanadium oxide microspheres forming from hyperbranched nanoribbons as remarkably high performance electrode materials for supercapacitors," *Journal of Materials Chemistry A*, vol. 3, no.45, pp. 22892-22901, 2015.
- [31] S. D. Perera, B. Patel, J. Bonso, M. Grunewald, J. P. Ferraris, and K. J. Balkus Jr, "Vanadium oxide nanotube spherical clusters prepared on carbon fabrics for energy storage applications," *ACS Applied Materials & Interfaces*, vol. 3, no.11, pp. 4512-4517, 2011.
- [32] J. Yang, T. Lan, J. Liu, Y. Song, and M. Wei, "Supercapacitor electrode of hollow spherical V_2O_5 with a high pseudocapacitance in aqueous solution," *Electrochimica Acta*, vol. 105, pp. 489-495, 2013.
- [33] J. Shao, X. Li, Q. Qu, and H. Zheng, "One-step hydrothermal synthesis of hexangular starfruit-like vanadium oxide for high power aqueous supercapacitors," *Journal of Power Sources*, vol. 219, pp. 253-257, 2012.
- [34] L. Hua, Z. Ma, P. Shi, L. Li, K. Rui, J. Zhou, X. Huang, X. Liu, J. Zhu, and G. Sun, "Ultrathin and large-sized vanadium oxide nanosheets mildly prepared at room temperature

for high performance fiber-based supercapacitors,” *Journal of Materials Chemistry A*, vol. 5, no.6, pp. 2483-2487, 2017.

[35] Z. Lin, X. Yan, J. Lang, R. Wang, and L.-B. Kong, “Adjusting electrode initial potential to obtain high-performance asymmetric supercapacitor based on porous vanadium pentoxide nanotubes and activated carbon nanorods,” *Journal of Power Sources*, vol. 279, pp. 358-364, 2015.

[36] C. Zhu, D. Hu, and Z. Liu, “Interconnected three-dimensionally hierarchical heterostructures with homogeneously-dispersed V_2O_5 nanocrystals and carbon for high performance supercapacitor electrodes,” *Electrochimica Acta*, vol. 229, pp. 155-165, 2017.

[37] M.H. Bai, L.J. Bian, Y. Song, and X.X. Liu, “Electrochemical codeposition of vanadium oxide and polypyrrole for high-performance supercapacitor with high working voltage,” *ACS Applied Materials & Interfaces*, vol. 6, no.15, pp. 12656-12664, 2014.

[38] Q. H. Do, C. Zeng, C. Zhang, B. Wang, and J. Zheng, “Supercritical fluid deposition of vanadium oxide on multi-walled carbon nanotube buckypaper for supercapacitor electrode application,” *Nanotechnology*, vol. 22, no. 36, pp. 365402, 2011.

[39] T. Kudo, Y. Ikeda, T. Watanabe, M. Hibino, M. Miyayama, H. Abe, and K. Kajita, “Amorphous V_2O_5 /carbon composites as electrochemical supercapacitor electrodes,” *Solid State Ionics*, vol. 152, pp. 833-841, 2002.

[40] T. Watanabe, Y. Ikeda, T. Ono, M. Hibino, M. Hosoda, K. Sakai, and T. Kudo, “Characterization of vanadium oxide sol as a starting material for high rate intercalation cathodes,” *Solid State Ionics*, vol. 151, no. 1-4, pp. 313-320, 2002.

[41] I.H. Kim, J.H. Kim, B.W. Cho, Y.H. Lee, and K.B. Kim, “Synthesis and electrochemical characterization of vanadium oxide on carbon nanotube film substrate for pseudocapacitor applications,” *Journal of The Electrochemical Society*, vol. 153, no.6, pp. A989-A996, 2006.

[42] C.H. Lai, C.K. Lin, S.W. Lee, H.Y. Li, J.K. Chang, and M.J. Deng, “Nanostructured Na-doped vanadium oxide synthesized using an anodic deposition technique for supercapacitor applications,” *Journal of Alloys and Compounds*, vol. 536, pp. S428-S431, 2012. (2012).

[43] Z. Huang, H. Zeng, L. Xue, X. Zhou, Y. Zhao, and Q. Lai, “Synthesis of vanadium oxide, V_6O_{13} hollow-flowers materials and their application in electrochemical supercapacitors,” *Journal of Alloys and Compounds*, vol. 509, no. 41, pp. 10080-10085, 2011.

[44] C.M. Huang, C.C. Hu, K.H. Chang, J.M. Li, and Y.F. Li, “Pseudocapacitive characteristics of vanadium oxide deposits with a three-dimensional porous structure,” *Journal of The Electrochemical Society*, vol. 156, no.8, pp. A667-A671, 2009.

- [45] B. Saravanakumar, K. K. Purushothaman, and G. Muralidharan, "High performance supercapacitor based on carbon coated V_2O_5 nanorods," *Journal of Electroanalytical Chemistry*, vol. 758, pp. 111-116, 2015.
- [46] Y. Gogotsi and P. Simon, "True performance metrics in electrochemical energy storage," *Science*, vol. 334, no. 6058, pp. 917-918, 2011.
- [47] P. H. Jampani, K. Kadakia, D. H. Hong, R. Epur, J. A. Poston, A. Manivannan, and P. N. Kumta, "CVD derived vanadium oxide nano-sphere-carbon nanotube (CNT) nano-composite hetero-structures: high energy supercapacitors," *Journal of The Electrochemical Society*, vol. 160, no.8, pp. A1118-A1127, 2013.
- [48] W.C. Fang, "Synthesis and electrochemical characterization of vanadium oxide/carbon nanotube composites for supercapacitors," *The Journal of Physical Chemistry C*, vol. 112, no. 30, pp. 11552-11555, 2008.
- [49] G. Wang, X. Lu, Y. Ling, T. Zhai, H. Wang, Y. Tong, and Y. Li, "LiCl/PVA gel electrolyte stabilizes vanadium oxide nanowire electrodes for pseudocapacitors," *ACS Nano*, vol. 6, no. 11, pp. 10296-10302, 2012.
- [50] M. Yu, Y. Zeng, Y. Han, X. Cheng, W. Zhao, C. Liang, Y. Tong, H. Tang, and X. Lu, "Valence-Optimized Vanadium Oxide Supercapacitor Electrodes Exhibit Ultrahigh Capacitance and Super-Long Cyclic Durability of 100 000 Cycles," *Advanced Functional Materials*, vol. 25, no. 23, pp. 3534-3540, 2015.
- [51] J. Zheng, Y. Zhang, X. Jing, X. Liu, T. Hu, T. Lv, S. Zhang, and C. Meng, "Synthesis of amorphous carbon coated on V_2O_3 core-shell composites for enhancing the electrochemical properties of V_2O_3 as supercapacitor electrode," *Colloids and Surfaces A: Physicochemical and Engineering Aspects*, vol. 518, pp. 188-196, 2017.
- [52] K. Shi and I. Zhitomirsky, "Influence of current collector on capacitive behavior and cycling stability of Tiron doped polypyrrole electrodes," *Journal of Power Sources*, vol. 240, pp. 42-49, 2013.
- [53] Y. Su and I. Zhitomirsky, "Hybrid MnO_2 /carbon nanotube-VN/carbon nanotube supercapacitors," *Journal of Power Sources*, vol. 267, pp. 235-242, 2014.
- [54] M. Ata, Y. Liu, and I. Zhitomirsky, "A review of new methods of surface chemical modification, dispersion and electrophoretic deposition of metal oxide particles," *RSC Advances*, vol. 4, no. 43, pp. 22716-22732, 2014.
- [55] H. Lee, S. M. Dellatore, W. M. Miller, and P. B. Messersmith, "Mussel-inspired surface chemistry for multifunctional coatings," *Science*, vol. 318, no. 5849, pp. 426-430, 2007.
- [56] H. Lee, B. P. Lee, and P. B. Messersmith, "A reversible wet/dry adhesive inspired by mussels and geckos," *Nature*, vol. 448, no.7151, pp. 338, 2007.

- [57] B. Vigolo, C. Coulon, M. Maugey, C. Zakri, and P. Poulin, "An experimental approach to the percolation of sticky nanotubes," *Science*, vol. 309, no.5736, pp. 920-923, 2005.
- [58] B. Vigolo, A. Penicaud, C. Coulon, C. Sauder, R. Pailler, C. Journet, P. Bernier, and P. Poulin, "Macroscopic fibers and ribbons of oriented carbon nanotubes," *Science*, vol. 290, no. 5495, pp. 1331-1334, 2000.
- [59] C. Ramirez-Castro, O. Crosnier, L. Athouël, R. Retoux, D. Belanger, and T. Brousse, "Electrochemical performance of carbon/MnO₂ nanocomposites prepared via molecular bridging as supercapacitor electrode materials," *Journal of The Electrochemical Society*, vol. 162, no.5, pp. A5179-A5184, 2015.
- [60] Y. Wang, Y. Liu, and I. Zhitomirsky, "Surface modification of MnO₂ and carbon nanotubes using organic dyes for nanotechnology of electrochemical supercapacitors," *Journal of Materials Chemistry A*, vol. 1, no.40, pp. 12519-12526, 2013.
- [61] E. Hryha, E. Rutqvist, and L. Nyborg, "Stoichiometric vanadium oxides studied by XPS," *Surface and Interface Analysis*, vol. 44, no.8, pp. 1022-1025, 2012.
- [62] G. Silversmit, D. Depla, H. Poelman, G. B. Marin, and R. De Gryse, "Determination of the V2p XPS binding energies for different vanadium oxidation states (V⁵⁺ to V⁰⁺)," *Journal of Electron Spectroscopy and Related Phenomena*, vol. 135, no. 2-3, pp. 167-175, 2004.
- [63] W. Dong, J. S. Sakamoto, and B. Dunn, "Electrochemical properties of vanadium oxide aerogels," *Science and Technology of Advanced Materials*, vol. 4, no.1, pp. 3, 2003.
- [64] W. Dong, D. R. Rolison, and B. Dunn, "Electrochemical properties of high surface area vanadium oxide aerogels," *Electrochemical and Solid-State Letters*, vol. 3, no.10, pp. 457-459, 2000.
- [65] Y. U. Jeong and A. Manthiram, "Nanocrystalline manganese oxides for electrochemical capacitors with neutral electrolytes," *Journal of The Electrochemical Society*, vol. 149, no.11, pp. A1419-A1422, 2002.
- [66] R. N. Reddy and R. G. Reddy, "'Sol-gel MnO₂ as an electrode material for electrochemical capacitors," *Journal of Power Sources*, vol. 124, no. 1, pp. 330-337, 2003.

Chapter 11 Conclusions and Future Works

Conceptually new colloidal processing techniques and advanced dispersants from different families were developed and employed to fabricate high performance nanocomposite electrodes with high active mass loadings for ES applications. The major achievements of this dissertation can be summarized as follows:

1. The use of CPC as a multifunctional dispersant allowed the phase transfer of MnO_4^- to an organic solvent and the formation of MnO_2 coated MWCNTs, which have reduced agglomeration of particles and improved mixing of the composite components. The composite electrodes showed remarkable areal capacitances and low resistance at high active mass loadings between 42 to 61 mg cm^{-2} .
2. New scalable process for the fabrication of MnO_2 -MWCNTs composite has been developed using highly soluble NaMnO_4 precursor. The new process avoided the drying procedure to prevent formation of agglomerates and was able to produce a high concentration slurry for direct impregnation of current collector. The fabricated composite electrode showed superior electrochemical performance compared to electrodes fabricated by other colloidal techniques at the same active mass loading. The electrode was also used to fabricate asymmetric device with Zn-doped $\text{FeOOH-PPy-coated-MWCNTs}$ and have shown excellent performance.
3. Liquid-liquid extraction was employed for the fabrication of Mn_3O_4 -MWCNTs composite using LG as an extractor and dispersant. The strong catecholic adsorption of LG has promoted phase transfer of Mn_3O_4 particles to 1-butanol. Moreover, LG

allowed efficient dispersion of MWCNTs and Mn_3O_4 . Agglomeration was avoided and mixing of MWCNTs and Mn_3O_4 was improved using this approach. Enhanced electrochemical performance has been achieved at high active mass loading.

4. Advanced dispersant from BAS and organic dyes families were investigated, and they have proven to be effective for the dispersion of MWCNTs in aqueous solutions. Mn_3O_4 -MWCNTs composite electrodes were fabricated using TD and TL as MWCNTs dispersants, which allowed for improved mixing between Mn_3O_4 and MWCNTs. An activation procedure was developed to enhance of capacitance of Mn_3O_4 -MWCNTs electrode by generation of surface MnO_2 layer. The fabricated electrodes showed excellent capacitive performance after activation and generated new direction for alternative active materials in ESs.
5. New colloidal processing technique based on Schiff base formation between TL and DHB has enhanced the mixing of Mn_3O_4 and MWCNTs, and allowed good electrochemical performance achievable at high active mass loading.
6. Alternative metal oxide V_2O_3 was also investigated for applications in ES. It was demonstrated that an appropriate activation procedure was necessary for V_2O_3 , as the capacitance increased drastically after activation due to the formation of capacitive V_2O_5 . The results showed that electrode fabricated using LG as a co-dispersant and commercial V_2O_3 powder showed better cyclic stability, while electrode fabricated using ball-milled V_2O_3 showed improved capacitance retention. The enhanced conductivity and the high areal capacitance achieved for V_2O_3 makes it a promising candidate as active material for practical ESs application.

The results of this dissertation have addressed several problems related to ESs fabrication, and further attention should be given to the development of new colloidal techniques and scalable production of composites for ESs application. Future works should continue the investigation of new dispersants, particularly from the BAS and organic dyes families for the development of novel colloidal processing techniques. V_2O_3 has shown promising results without complex processing, and further development or modification should be investigated as there are still room for improvement for V_2O_3 as active material for ESs application.